Laser-Induced Breakdown Spectroscopy for the Exploration of Mars: Analysis of Molecular Emissions and Spatial Characterization of the Plasma

DISSERTATION

zur Erlangung des akademischen Grades
doctor rerum naturalium (Dr. rer. nat.)
im Fach Physik (Spezialisierung Experimentalphysik)

eingereicht an der
Mathematisch-Naturwissenschaftlichen Fakultät
der Humboldt-Universität zu Berlin
von

David Sebastian Vogt, M.Sc.

Präsidentin der Humboldt-Universität zu Berlin:
Prof. Dr.-Ing. Dr. Sabine Kunst

Dekan der Mathematisch-Naturwissenschaftlichen Fakultät:
Prof. Dr. Elmar Kulke

Gutachter:
1. Prof. Dr. Heinz-Wilhelm Hübers
2. Prof. Dr. Reinhard Noll
3. Olivier Forni, HDR

Tag der mündlichen Prüfung: 14. November 2019

Kurzfassung

Diese Arbeit beschäftigt sich mit laser-induzierter Plasmaspektroskopie (LIBS) im Kontext der robotischen Mars-Erkundung. LIBS ist eine Art der Atomemissionsspektroskopie, in der Plasma analysiert wird, das durch Laserablation von Probenmaterial gebildet wird. Seit 2012 wird die Methode von dem Instrument ChemCam an Bord des Mars-Rovers Curiosity eingesetzt, um das Gestein und den Boden der Marsoberfläche zu untersuchen. Sie wird auch in der NASA-Mission Mars 2020 und in der chinesischen Mission HX-1 eingesetzt werden, welche beide im Jahr 2020 zum Mars starten sollen.

Die ersten beiden Studien dieser Arbeit betrachten Molekülemissionen von Monohalogeniden, die sich im Plasma bilden. Diese können zur Detektion der Elemente Chlor und Fluor eingesetzt werden, die von besonderem geologischem Interesse für Mars sind. In der ersten Studie werden Emissionen von MgCl und CaCl in simulierten Marsbedingungen untersucht auf ihre Eignung zur Analyse der Chlorkonzentration. Nur das Signal von CaCl wird als stark genug befunden für diesen Zweck. Das CaCl-Signal ist am stärksten bei vergleichsweise geringen Chlorkonzentrationen, was nur durch einen Nichtgleichgewichtszustand des Plasmas erklärt werden kann. In der zweiten Studie werden die Emissionen von CaCl und CaF im Vergleich miteinander untersucht. Beide Emissionen können mit demselben Nichtgleichgewichtsmodell in Abhängigkeit der Konzentrationen der Reaktionspartner beschrieben werden. Allerdings werden auch starke Matrixeffekte beobachtet, welche die Intensitäten der Emissionen unabhängig von den Konzentrationen der Reaktionspartner beeinträchtigen können.

Im letzten Teil der Arbeit wird der Plasma-Imaging-Aufbau beschrieben, der im Rahmen dieser Arbeit aufgebaut wurde, und erste Ergebnisse werden vorgestellt, die mit diesem Aufbau erzielt wurden. Der Aufbau ermöglicht räumlich, zeitlich und spektral aufgelöste Messungen der Plasmaemission unter simulierten Marsbedingungen. Die Ergebnisse zeigen, dass CaCl und CaF nur im Plasmazentrum emittieren, was mit einer Verdünnung und Ausbildung eines Niedertemperaturbereichs im Plasmazentrum erklärt werden kann. Atomare Emissionen von Wasserstoff, Kohlenstoff und Sauerstoff sind dagegen intensiver an der Plasmafront und zeigen Verwirbelungen auf, was auf komplexe Temperaturverteilungen und auf einen starken Einfluss von Strömungen im Plasma hinweist.

Abstract

In this thesis, laser-induced breakdown spectroscopy (LIBS) is investigated in the context of the robotic exploration of Mars. LIBS is a type of atomic emission spectroscopy in which the plasma formed by laser-ablated sample material is analyzed spectroscopically. Since 2012, it is employed by the ChemCam instrument on board the Mars rover Curiosity to analyze the composition of rocks and soil on the Martian surface. The technique will also be used in NASA's Mars 2020 mission and in the Chinese HX-1 mission, which are both scheduled to launch to Mars in 2020.

The first two studies presented here are concerned with molecular emissions of monohalides that form in the laser-induced plasma. These can be used for the detection of chlorine and fluorine, which are of special geological interest for Mars. In the first study, MgCl and CaCl emissions are investigated for the detection and quantification of chlorine in simulated Martian atmospheric conditions, but only the CaCl signal is found to be intense enough for this purpose. The CaCl signal is found to be skewed towards low chlorine concentrations, which can only be explained by a non-equilibrium model of the laser-induced plasma. In the second study, CaCl and CaF emissions are investigated in comparison. The same non-equilibrium model is used to describe the dependence of both molecular emissions on the respective reactant concentrations. However, strong matrix effects are also observed that affect the observed intensities in ways that are unrelated to the reactant concentrations in the sample.

In the final part of the thesis the plasma imaging setup that was developed in the context of this thesis is presented, as well as first results that were obtained with it. The setup enables spatially, temporally, and spectrally resolved measurements of the laser-induced plasma in simulated Martian atmospheric conditions. The results show that CaCl and CaF emissions are confined close to the plasma center, likely because rarefaction leads to a low-temperature center in which molecules can form. Atomic emissions of hydrogen, carbon, and oxygen are more stable at the plasma front and show signs of vorticity, indicating a complex temperature distribution and a strong influence of flows within the plasma.

Contents

List of Abbreviations

CNSA	China National Space Administration
DLR	Deutsches Zentrum für Luft- und Raumfahrt
FWHM	Full width at half maximum
ICCD	Intensified charge-coupled device
ISRO	Indian Space Research Organisation
JSC	JSC Mars-1A
LIBS	Laser-induced breakdown spectroscopy
LOD	Limit of detection
LTB	Lasertechnik Berlin
LTE	Local thermodynamic equilibrium
MarsCoDe	Mars Surface Composition Detection Package
MOLA	Mars Orbiter Laser Altimeter
MSL	Mars Science Laboratory
NASA	National Aeronautics and Space Administration
Nd:YAG	Neodymium-doped yttrium aluminium garnet
NIR	Near-infrared
RMI	Remote Micro-Imager
SNR	Signal-to-noise ratio
TE	Thermodynamic equilibrium
THEMIS	Thermal Emission Imaging System
UV	Ultraviolet
VIS	Visible
VUV	Vacuum ultraviolet

List of Symbols

A	Spin-orbit coupling constant
A_{ul}	Einstein coefficient of spontaneous emission
B_e	Rotational constant
c	Speed of light in vacuum
D_e^0	Dissociation energy of the electronic state
D_e	Quartic centrifugal distortion constant
E_i	Energy level i
E_{ij}	Energy difference between E_i and E_j
$E_{s,z}$	Ionization energy of the z-th ion of species s
e	Elementary charge
g_i	Degeneracy of E_i
h	Planck constant
J	Rotational quantum number
K	Equilibrium rate constant
k	Reaction rate constant
k_B	Boltzmann constant
m_e	Electron rest mass
n_e	Electron density
s	Plasma species, either element or molecule
t_d	Delay time of ICCD camera
t_g	Gate width of ICCD camera
$U_{s,z}$	Internal partition function of the z-th ion of species s
z	Ionization stage

α_e	Rotation-vibration interaction constant
ϵ	Emission coefficient
ε_0	Permittivity of free space
ζ	Fit parameter, see Eq. (4.25)
η	Fit parameter, see Eq. (4.26)
$\Delta\lambda_D$	FWHM related to Doppler broadening
$\Delta\lambda_S$	FWHM related to Stark broadening
λ_e	Thermal de Broglie wavelength of an electron
ν	Wavenumber or frequency

ν_p	Plasma resonant frequency
υ	Vibrational quantum number
υ'	Upper vibrational level
υ''	Lower vibrational level
Φ_G	Gaussian distribution
Φ_L	Lorentz distribution
Φ_V	Voigt profile

C	Carbon
Ca	Calcium
$CaCO_3$	Calcium carbonate
CaCl	Calcium monochloride
$CaCl_2$	Calcium dichloride
CaF	Calcium monofluoride
CaF_2	Calcium difluoride
$CaSO_4$	Calcium sulfate
CaO	Calcium oxide
Cl	Chlorine
F	Fluorine
H	Hydrogen
H_2O	Water
K	Potassium
KCl	Potassium chloride
K_2SO_4	Potassium sulfate
Mg	Magnesium
MgCl	Magnesium monochloride
$MgCl_2$	Magnesium dichloride
MgF	Magnesium monofluoride
MgF_2	Magnesium difluoride
$MgSO_4$	Magnesium sulfate
NaCl	Sodium chloride
O	Oxygen

1. Introduction

Laser-induced breakdown spectroscopy (LIBS) is a type of atomic emission spectroscopy that has gained a lot of attention in the planetary science community. The basic idea behind LIBS is that a pulsed laser is used to ablate material from the surface of the sample under investigation. From the ablated material a plasma plume is generated with a lifetime of several microseconds, depending on the ambient conditions. Inside the laser-induced plasma there are excited atoms, ions, and molecules, which emit light at characteristic wavelengths. These so-called emission lines can be detected by a spectrometer. The spectrum of the emitted light can then be used to calculate the concentrations of the detected elements in the investigated sample. While LIBS is most commonly used with solid samples, it can also be used to investigate liquids and gases. The only requirement is that the laser irradiance is sufficient to generate a plasma. The experimental setup for a LIBS measurement is straightforward: the pulsed laser is focused onto the sample to create a high irradiance on a small spot. Collection optics then focus a fraction of the emitted light into a spectrometer. Since many of the strongest atomic and ionic emission lines can be found in the ultraviolet (UV) to near-infrared (NIR) spectral range, well-suited spectrometers are commercially available. Depending on the collection setup, a single laser shot is often enough for a spectrum with a high signal-to-noise ratio, but the measurement can also be integrated over multiple laser shots in order to improve the signal. If the laser pulse is synchronized with the exposure time of the detector, time-resolved measurements with a temporal resolution of several nanoseconds can be realized as well.

In comparison to many other spectroscopic techniques, LIBS is a relatively new technology. While other types of atomic emission spectroscopy such as flame spectroscopy and spark/arc spectroscopy had already been known for a long time, the pulsed lasers that are required for LIBS only became available in the 1960s [25]. With the availability of high-energy pulsed lasers, LIBS quickly rose to prominence in the 1980s and 1990s as a new type of spectroscopy that was especially interesting for remote analysis [25]. The potential of quantitative LIBS for space applications was recognized very soon. In 1992, first studies were presented that demonstrated the viability of a LIBS instrument for the *in situ* analysis of planetary surfaces [11, 76, 77]. In 2000, an influential and widely-cited paper was published by Knight et al. [79] that described the capabilities of LIBS as a technology for planetary exploration in detail. Five major advantages of LIBS for planetary exploration were listed: (1) the capability for stand-off analysis from a distance of several meters, (2) the rapid sample acquisition that does not require

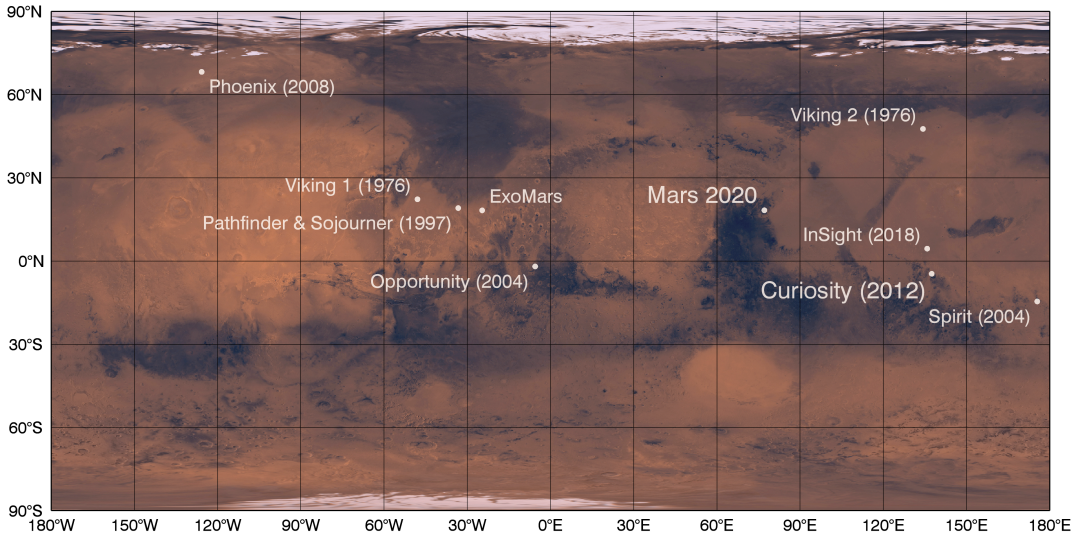

Figure 1.1: Map of Mars showing the landing sites and dates of landers and rovers from past successful missions and of the two upcoming Mars rover missions ExoMars and Mars 2020. No landing site has been announced yet for the Chinese HX-1 mission. The map of Mars is a mosaic based on Viking orbiter images in Simple Cylindrical projection (credit: USGS Astrogeology [146]).

new positioning of the rover, as the instrument only needs to be aimed and focused at a new target, (3) the capability to clean and prepare the sample by repeated laser ablation, which can be used to remove dust, desert varnish, or weathered surface layers in order to get access to the bulk material, (4) the rapid analysis of a sample that is mostly determined by the number of laser shots that are integrated, and (5) the sensitive detection of nearly all naturally occurring elements, including hydrogen [79]. In summary, a planetary rover equipped with a LIBS instrument can analyze more targets in a shorter period of time than a rover that only uses contact and analytical laboratory instruments, thus greatly increasing the scientific return of a mission.

The atmospheric conditions on Mars are especially well-suited for LIBS. The influence of the ambient gas and its pressure on the vaporization process and on LIBS signal intensities was first studied by Iida [73], who showed that a high optical density of the plasma reduces the amount of ablated material. At high pressures, for example at the standard atmospheric pressure of 101.3 kPa, the plasma is optically dense because it is more confined. The plasma itself then shields the sample surface from the later portion of the laser pulse, so that less material is ablated. At the same time, the absorbed laser energy and the higher number of collisions in the plasma at high pressures result in more excitation of species in the plasma. This trade-off leads to maximum LIBS signal intensities at ambient pressures of about 1–50 kPa. These findings were later reproduced in the context of space application [65, 79] and specifically for Mars [15]. The typical ambient pressures at which LIBS intensities are at their maximum are close

to the atmospheric pressure of Mars, which is about 0.8 kPa at the surface but varies depending on location and season [64, 133].

The advantages of LIBS in planetary exploration and the near-optimal conditions on Mars increased interest in a LIBS instrument for a mission to Mars. After successful field studies with a rover mast-based LIBS instrument by Wiens et al. [156], the ChemCam ("Chemical Camera") instrument suite was developed and in 2004 was proposed as a science payload for NASA's Mars Science Laboratory (MSL) mission. It was selected as a science payload in the same year [103]. The MSL spacecraft launched on November 26, 2011, and the Curiosity rover landed successfully in Gale crater on Mars on August 6, 2012 (see Fig. 1.1) [102]. The final design of the ChemCam instrument and its science objectives were reported in the same year [90, 157]. The instrument uses LIBS to analyze samples at distances from 1.3 m to 7 m with a laser energy of about 15 mJ/pulse and a spot size of 50–500 micrometers. Its three spectrometers cover the wavelengths of 240–850 nm, with gaps at 340–385 nm and 469–492 nm [91]. In addition to LIBS spectra of selected targets, it also provides high-resolution images with the Remote Micro-Imager (RMI) instrument, which help to contextualize the measurements [86, 90, 100]. Since the start of the mission, ChemCam has acquired more than 700,000 spectra, enabling the qualitative and quantitative analysis of major, minor, and trace elements along the path of Curiosity [85, 91]. It was the first instrument to detect fluorine and boron on Mars [44, 51]. As planned [58], ChemCam is also used to select samples for the contact and analytical laboratory instruments of the Mars Science Laboratory, so that more relevant scientific data can be obtained from these instruments.

The success of ChemCam has firmly put LIBS on the map of planetary science and increased interest in LIBS for other planetary missions. LIBS instruments have been proposed for planetary missions to Venus [19, 20], to the Moon [139, 143], to Jupiter's and Saturn's moons [112, 139], and to smaller Solar System bodies like asteroids and comets [26, 82, 113, 152]. The lunar exploration mission Chandrayaan-2 of the Indian Space Research Organisation (ISRO), which was launched in July 2019 but failed to achieve a soft landing of its lander on the lunar surface in September 2019, was supposed to employ a LIBS instrument on board its rover to perform chemical analysis of the lunar surface [143]. Furthermore, there will be two more missions to Mars with LIBS instruments in their science payload set to launch in 2020. One is the *Mars Global Remote Sensing Orbiter and Small Rover* (HX-1) by the China National Space Administration (CNSA), which will do LIBS analysis with the *Mars Surface Composition Detection Package* (MarsCoDe) [122]. The other is NASA's Mars 2020 mission, which will include the SuperCam instrument suite, a successor of the ChemCam instrument suite. SuperCam will be a new and highly evolved version of ChemCam [158]. It will incorporate a Remote Micro Imager (RMI) and a remote LIBS instrument again, but

will also be able to perform remote analysis using Raman spectroscopy and visible and infrared (VISIR) passive reflectance spectroscopy. In order to achieve a good signal-to-noise ratio for remote Raman spectroscopy, the spectral range of 535–855 nm will be detected with an intensified charge-coupled device (ICCD). This will technically also allow for time-resolved LIBS measurements in this spectral range, which could improve the signal-to-noise ratio and could be used to filter out signals from the early plasma stages, such as ionic carbon signals that interfere with the quantification of hydrogen [120].

With LIBS having been established as an important technique for planetary science, it is crucial to investigate the specific challenges of LIBS data analysis in this field. Since Mars is already being analyzed with LIBS, and two more LIBS instruments are set to operate on Mars in the near future, investigations of LIBS on Mars are of foremost importance. Chemometrics and machine learning can already be used to distinguish very effectively between various minerals and to reduce the influence of matrix effects on the analysis [155], but there are still limits to the applicability of these statistical approaches [38]. For the detection and quantification of minor and trace elements in the samples, which reveal important information about the Martian geological history, the best results are achieved with a univariate analysis of the spectral features. By taking into account the theoretical models describing the laser-induced plasma emission, the elemental concentrations can be obtained from the intensities and the spectral profiles of the emission lines.

The analysis of some geologically important elements such as chlorine and fluorine is challenging, however. The strongest emission lines of chlorine and fluorine are in the vacuum-ultraviolet (VUV) spectral range [24], which is not covered by ChemCam or SuperCam. With the weaker emission lines in the visible (VIS) to near-infrared (NIR) wavelength range, the limits of detection (LOD) of chlorine and fluorine are relatively high at several weight percentages [24, 91]. In order to improve the LOD for these elements, emissions of diatomic molecules in the plasma have gained more attention in the last few years [50]. In particular, molecular bands of CaCl and CaF have been used to lower the LOD for chlorine and fluorine significantly, enabling the first detection of fluorine on Mars [44, 92]. Since magnesium has also been detected in Martian LIBS spectra, bands of MgCl and MgF could also be of interest.

Only few studies on molecular emissions in LIBS have been made. Some have showcased specific applications [4, 5, 92], and there have been excellent theoretical publications on the modeling of chemical reactions in plasma [29, 135, 136]. However, the relation between the concentrations in the sample and the intensities of the molecular bands has not been investigated, which is crucial for a better understanding of the formation of molecules in the laser-induced plasma. There are also open questions with regards to the spatial distributions of molecular emissions in the laser-induced plasma.

Simulations predict that they should only form in the colder periphery of the plasma [29, 135, 136], while first low-resolution results indicate that they could be found closer to the plasma center, which could not be explained by typically used plasma models [50].

This thesis investigates the molecular emissions that can be used to detect chlorine and fluorine in LIBS spectra as well as in spatially resolved measurements of the plasma emission. Furthermore, the spatial distributions of calcium, hydrogen, carbon, and oxygen are investigated, which are of special interest for LIBS on Mars. The primary goal of the thesis is to provide answers to the following questions:

- Which of the molecular emissions that could be observed in Martian LIBS spectra are well-suited for the detection and quantification of chlorine and fluorine?
- What is the relation between the intensity of a molecular emission in LIBS and the concentrations of the reacting elements?
- How are atomic, ionic, and molecular emissions distributed within the laser-induced plasma, and which processes determine these spatial distributions?

These questions are explored theoretically and experimentally. In both cases, Martian atmospheric conditions are simulated in order to obtain results that are relevant to Martian LIBS data. Two different experimental setups are used: the first is the high-resolution LIBS setup at DLR Berlin, and the second is a new plasma imaging setup that I designed in the course of this thesis, which enables spectrally, spatially, and temporally resolved measurements of the plasma emission. In the following, the structure of this thesis and the studies that were conducted are outlined briefly.

In Chapter 2, a summary of the theoretical background of LIBS is given. This includes the breakdown and ablation of the sample surface, the evolution of the laser-induced plasma over time, and the emission spectra of the plasma. The formation of molecules in the plasma, their energy levels, and their emission spectra are described in detail. The chapter concludes with a description of the model of a plasma in LTE, which is commonly used to simulate the plasma composition in dependence of the temperature. In Chapter 3, the high-resolution LIBS setup at DLR Berlin is presented and characterized. Furthermore, the preparation of the samples is described and an overview of the data analysis and the software that I used is given. In Chapter 4, the emissions of MgCl and CaCl molecules in the laser-induced plasma are investigated for the detection and quantification of chlorine. Experimental studies are compared with theoretical calculations of the emission spectra and of the plasma composition in LTE. A new non-equilibrium model is derived to describe the intensity of the molecular emissions in dependence of the reactant concentrations. The model is successfully applied to the CaCl emission in various sets of samples with different concentrations

of calcium and chlorine. Chapter 5 introduces the MgF and CaF emissions for the detection and quantification of fluorine. The MgF emission is quickly found to be of low intensity. The CaF emission is investigated theoretically and experimentally, this time in direct comparison to the CaCl emission. Equivalent series of samples are made for the investigation of CaCl and CaF in order to obtain comparable results. The non-equilibrium model that was derived in the previous chapter is used for both molecular emissions. The accuracy of the quantification of chlorine and fluorine via molecular emission is evaluated. Furthermore, the influence of matrix effects, i.e. of changes in the sample matrix that are not considered in the non-equilibrium model, is investigated as well. In Chapter 6, the new plasma imaging setup that was developed in the course of this thesis is presented and characterized. The calibration of the setup is shown, two different measurement modes are explained, and the Abel inversion that is used for the deconvolution of the measured signal distributions is described. The plasma imaging setup is then used in Chapter 7 for first spatially resolved studies of the emissions of CaCl, CaF, calcium, hydrogen, carbon, and oxygen. Chapter 8 summarizes the main results of this thesis and the conclusions that can be drawn from them.

2. Theoretical Background

In this chapter, the theoretical background of LIBS and of the plasma emissions that are investigated in this thesis are described in more detail. I first introduce the basics of LIBS, which include the electric breakdown in the sample, the ablation of the sample surface, the formation of the plasma, and the characteristics and the time evolution of the plasma emission. The next section focuses on the molecules in the laser-induced plasma and their emission spectra, which are determined by the energy levels of the molecules. In the final section, I describe how the number densities of electrons, atoms, ions, and molecules inside the plasma can be modeled based on the assumption of local thermal equilibrium (LTE).

2.1 Basics of LIBS

The LIBS technique relies on an electric breakdown in the sample, which is caused by the interaction with a pulsed laser. The electric breakdown causes the formation of a plasma plume which emits light that can be analyzed with a spectrometer. The plasma is transient and its emission changes over time as the temperature changes and as the plasma expands into the environment of the sample. Figure 2.1 shows the laser ablation process and the formation and evolution of the plasma plume in the ambient gas for a solid sample in chronological order, based on a similar depiction by Vadillo and Laserna [147]. In the following a brief description of the most important processes is given. The focus here will be on solid samples, since LIBS is only used for the analysis of rocks and soils in planetary exploration. Most of the fundamental principles apply for LIBS in gases and liquids as well, however [25]. Additionally it will be assumed that the plasma expands into an ambient gas at a low pressure, as is the case on Mars.

2.1.1 Breakdown and ablation

Laser-induced electric breakdown in the sample material is a necessary step for the formation of an emissive plasma that can be analyzed with a spectrometer. For solids, the removal of material from the sample surface following the laser-induced breakdown is called laser ablation. The ablation rate measures the removed mass per laser pulse [60], or sometimes the depth or volume of the crater that is generated by a pulse [148].

In the surface of the solid, the electric breakdown occurs if an electron avalanche is initiated, which only happens if the laser irradiance reaches a critical level [12].

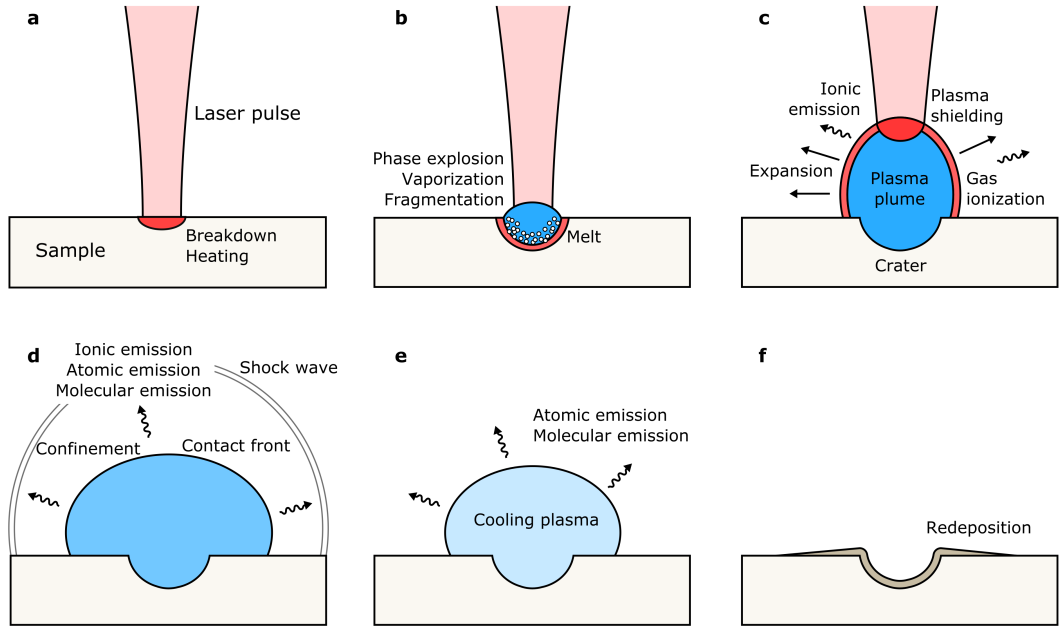

Figure 2.1: Laser ablation and evolution of the plasma plume in the ambient gas for a solid sample. a) Laser-matter interaction leads to breakdown followed by rapid heating. b) Surface material is ablated by phase explosion, vaporization, or fragmentation, and a crater is formed. c) The plasma plume expands at a supersonic speed. The plasma partially shields the surface from the incoming laser pulse and is heated up further. The compressed ambient gas is ionized as well. d) The ambient gas pressure confines the plasma, which starts to cool. The shock wave detaches from the plasma. e) As the plasma cools, ions and electrons recombine. Atomic and molecular emissions now dominate the emission. f) As the plasma loses energy, the material is deposited on the sample surface in and around the crater again.

This threshold value depends on several properties of the investigated sample and on the laser wavelength, but typical values in the range of 10^8–$10^9\,\mathrm{W/cm^2}$ have been reported for many materials [25]. The laser-material interaction consists of multiple highly complex processes, especially in the case of laser pulses that are longer than about 20 picoseconds [142]. Some of these processes are still unidentified [127]. The generally accepted description of breakdown in solids is a twofold process, where an initial number of electrons is first brought into the conduction band, and then initiates an avalanche of electrons [12, 141, 142]. The initial number of electrons is brought into the conduction band by multiphoton ionization [12]. The electrons in the conduction band then gain energy through interaction with the laser field in free-free transitions, also called inverse bremsstrahlung [12]. The energy is then transferred to the lattice by scattering with phonons [141]. If the energy of single electrons exceeds the band gap energy, they may promote valence electrons to the conduction band by impact ionization, which enhances the avalanche effect [142]. Breakdown occurs if the energy

transferred to the lattice is high enough to cause vaporization, melting, and plasma formation.

Following the electric breakdown, material from the surface of the solid is ablated. This is because the scattering of electrons from the electron avalanche with lattice phonons rapidly heats up the material. There are different mechanisms that are involved in the ablation process, of which phase explosion, also called explosive boiling, is considered to be the most efficient mechanism [94]. In this case the rapid heating causes homogeneous nucleation and a subsequent rapid transition to a mixture of vapor and liquid droplets [94, 115]. Another process is vaporization, which is defined here as a complete atomization of the surface layer that only occurs at high irradiances [115]. The third important process is fragmentation, which occurs if the mechanical stress due to the thermal expansion of the surface is very high [14, 114]. In this case spatially nonuniform strain rates and inhomogeneities in the expansion speed first lead to fracturing and then to the formation of clusters and fragments, which are rapidly ejected. All three ablation mechanisms can occur at the same time and may have different relevance for different materials [94, 114, 115]. Bogaerts et al. [14] suggest that fragmentation could be especially important for geological samples. In general, the ablated atoms are ejected perpendicular to the sample surface, regardless of the incidence angle of the laser pulse [99].

Stoichiometric ablation For the spectroscopic analysis of a sample, it is not only important how much mass is ablated and how intense the plasma emission is. The relative concentrations of the elements in the plasma should also be equal to those in the sample. If that is the case, the ablation is said to be stoichiometric. It is an ideal case that is not always fulfilled. At non-stoichiometric ablation, also called elemental fractionation, the composition of the plasma does not accurately represent the composition of the solid [109]. Elemental fractionation has been linked to the different volatilization efficiencies of different elements [75, 109], to transport mechanisms inside the plasma [109], and to the latent heat of vaporization of the substance [126], i.e. bonds with high bond dissociation energies are less likely to be broken by thermal effects. This can lead to the presence of fragments in the plasma and to strong elemental fractionation especially for samples in which different types of bonds are present. The fragmentation mechanism has also been linked to increased elemental fractionation [14].

2.1.2 Plasma evolution

The plasma plume that is formed by the ablated material initially expands at a supersonic speed, which in ambient gas produces a shock wave and an audible crack [25]. At low laser irradiances, the shock wave directly detaches from the propagating plasma, but at higher laser irradiances the plasma initially propagates at the same speed as

the shock wave, so that the shock front and the plasma edge are the same. The latter is called a laser-supported detonation (LSD) wave [116], which is the model that best describes the plasma propagation at the laser irradiances used in this thesis. Since the ablated material is ejected in a cone perpendicular to the sample surface [99], the plasma expands with a cylindrical symmetry into the ambient gas and the shock front has a nearly hemispherical shape [30, 134]. At 500 Pa in ambient helium gas, plasma expansion velocities of the order of 10^4 m/s have been reported [57].

After the initial expansion, the plasma plume is slowed down by collisions with the ambient gas and eventually stops expanding. The shock wave then detaches from the contact front between the ambient gas and the plasma and later degenerates into the sound wave [8]. The collisions between plasma and ambient gas during the plasma expansion compress and heat the ambient gas, so that some of it close to the shock front is ionized as well and contributes to the plasma emission. The collision also produces an internal shock wave inside the plasma plume due to backscattered material. The internal shock wave starts at the contact surface between ambient gas and plasma plume and propagates inwards towards the plasma center and plays a role in homogenizing the plasma [8]. The pressure and composition of the ambient gas define the strength of the confinement and therefore the size of the plasma plume. In terrestrial atmospheric conditions, i.e. in air at around 101.3 kPa, the plasma is significantly more confined than in Martian ambient conditions of an atmosphere consisting mostly of CO_2 at around 800 Pa, so that the plasma plume in Martian atmospheric conditions is much larger [84].

In the initial stage of the plasma, the plasma plume is already expanding while the later part of the laser pulse is still incoming. Due to a high electron density, the plasma resonant frequency ν_p is higher than the laser frequency, which causes the plasma to become opaque to the laser pulse. The laser pulse is then partially absorbed and reflected by the plasma plume and only a fraction of it reaches the surface. This effect is called plasma shielding [25, 148]. It occurs even for ultrashort pulses in the femtosecond regime [142]. The plasma resonant frequency ν_p is given by

$$\nu_p = \frac{1}{2\pi}\sqrt{\frac{e^2 n_e}{m_e \varepsilon_0}}\,, \tag{2.1}$$

so that the plasma shielding effect increases with the square root of the electron density n_e [116]. The electron density is higher for higher densities of the ambient gas due to the stronger confinement of the plasma, so that a higher pressure of a given ambient gas also generally leads to more pronounced plasma shielding and a reduced ablation rate [73, 79, 88, 148]. However, plasma shielding also causes the direct heating of the plasma plume by the laser pulse, which increases the excitation of the plasma species and leads to stronger plasma emission [79, 113]. The trade-off between a stronger excitation of the plasma itself at high pressures and a higher ablation rate at lower pressures is one

of the reasons why moderate ambient pressures of 0.5–1.5 kPa, such as those found on Mars, are ideal for LIBS [15, 79, 84, 113].

After the laser pulse has ended, the plasma plume does not gain additional energy anymore and slowly loses energy through thermal conduction, radiative losses, and recombination [25]. As the plasma cools, electron-ion recombination increases and atomic instead of ionic emission begins to dominate the plasma spectrum. Simple molecules form as well, enabling the observation of molecular emission that is the focus of this thesis. Eventually, larger particles form that deposit in and around the ablation crater. The particles that form in the plasma plume can be different from the composition of the sample itself, causing laser-induced alteration of the sample surface around the crater [132].

The lifetime of the plasma is generally longer at high pressures [25]. In terrestrial atmospheric conditions, a laser-induced plasma can often still emit after more than 100 µs, while the signal in Mars atmospheric conditions will already be weak after about 10 µs. In vacuum, the plasma is not confined at all, leading to fast expansion and a short lifetime [84, 113, 128].

2.1.3 Plasma emission

The laser-induced plasma consists of atoms, ions, simple molecules, and free electrons. They all contribute to the spectral radiance of the plasma. The free electrons are responsible for the plasma continuum emission, which is produced by bremsstrahlung and radiative recombination. Bremsstrahlung in plasma is mostly caused by the deceleration of electrons that interact with ions in the initial stages of the plasma [31]. Radiative recombination is the recombination of free electrons and ions, which dominates the later part of the continuum [31]. The spectral distribution of both processes can be described by Planck-like spectral distributions [31]. The plasma continuum is usually regarded as an unwanted side effect. Since it quickly declines in intensity, time-resolved setups are often used with a delay time between the laser pulse and the time gate in order to gate out the continuum emission. If this is not possible, background removal algorithms are used to remove the plasma continuum from LIBS spectra. In the data processing routine of ChemCam, a continuous wavelet transform algorithm for noise and continuum removal is used [155].

The emissions of atoms, ions, and molecules are based on the transitions from higher energy levels E_u to lower energy levels E_l. They appear as emission lines in the spectra. The energy of the emitted photons is

$$E_{ul} = E_u - E_l = \frac{hc}{\lambda_{ul}} \,. \tag{2.2}$$

The line emission coefficient is given by

$$\epsilon_{ul} = \frac{hc}{4\pi\lambda_{ul}} n_u A_{ul} \,, \tag{2.3}$$

where n_u is the population density of the upper level and A_{ul} is the Einstein coefficient of spontaneous emission [7, 60, 104]. The Einstein coefficient A_{ul} gives the rate of the spontaneous transition from the upper level to the lower level and is typically of the order of $10^8\,\mathrm{s}^{-1}$ [67]. Tabulated values of transition probabilities A_{ul} can be found in databases for spectral lines such as the NIST Atomic Spectra Database [118]. The line emission coefficient ϵ_{ul} is sometimes also called the intensity of the line, e.g. [67]. In this thesis, the intensity of an emission is defined as the number of photons corresponding to a given transition as measured by the experimental setup, as is commonly done in the LIBS community. For an optically thin plasma, this intensity is proportional to the *spatial integral* of the line emission coefficient along the line-of-sight of the setup, but not necessarily to the line emission coefficient itself. In order to obtain the line emission coefficient, a spatial deconvolution has to be applied, which requires spatially resolved measurements [7].

In addition to spontaneous emission, absorption also occurs in the plasma. Specifically, photons emitted by a transition from the upper state E_u to the lower energy state E_l can be absorbed again by particles of the same species that are in the lower state E_l, in which case they are excited to the upper state E_u. This effect is called self-absorption [7, 60]. In LIBS spectra, it leads to a broadening of the emission line and a reduction of the measured intensity. If the absorption happens due to a temperature gradient within the plasma, it can also lead to a dip in the center of the emission line, in which case the effect is called self-reversal [60, 104]. Both effects are especially strong for transitions where the lower energy level is the ground state E_0 or an energy level close to it. Due to the nonlinearity of their intensity in dependence of the elemental concentration, self-absorbed and self-reversed lines are less suited for quantitative univariate analysis. Emission lines that have a high lower energy level relative to the ground state are less prone to self-absorption, i.e. they are optically thin [60, 104].

For molecules, the fundamental process is the same as for atoms and ions, but in addition to electronic energy levels, molecules also have vibrational and rotational energy levels [67]. Their spectra typically feature "bands" of many rotational lines close together that come from the same electronic and vibrational transition. Their spectra are discussed in more detail in Section 2.2.

2.1.4 Broadening of emission lines

Due to Heisenberg's uncertainty principle, the emission lines have a natural linewidth that is larger than zero. For typical lifetimes of the excited energy levels of about 10 ns, the natural linewidth is of the order of 10^{-5} nm and cannot be resolved at the spectral

resolutions used in LIBS. Other broadening mechanisms are significantly stronger, of which Doppler broadening and the Stark effect are the dominant ones [25, 104].

The Doppler broadening is based on the velocity distribution of the emitting species. For a Maxwell-Boltzmann distribution of the velocities, the full width at half maximum (FWHM) is given by

$$\Delta\lambda_D = \lambda_c \sqrt{\frac{8\ln(2) k_B T}{mc^2}}\,, \tag{2.4}$$

where λ_c is the central wavelength and m is the mass of the emitting species [25]. The Doppler broadening of a Maxwell-Boltzmann velocity distribution is described by a Gaussian function. For the H_α emission line at 656.3 nm and a plasma temperature of 20 000 K, it is about 0.07 nm.

The Stark effect describes the shifting and splitting of energy levels in an external electric field [25, 56, 104]. This electric field exists in the presence of other charged particles, so that a high pressure increases the Stark effect. This is called pressure broadening or Stark broadening, which is accompanied by a Stark shift of the central wavelength. The broadening is described by a Lorentzian distribution. An empirical formula that relates the FWHM of the linear Stark effect for the H_α emission line to the electron density n_e is given by Gigosos et al. [53]:

$$\Delta\lambda_S = 0.549\,\text{nm} \times \left(\frac{n_e}{10^{17}\,\text{cm}^{-3}}\right)^{0.67965} \tag{2.5}$$

For an electron density $n_e = 10^{16}\,\text{cm}^{-3}$, which is a typical value for laser-induced plasmas in Martian atmospheric conditions, the Stark broadening of the H_α line is about 0.3 nm. Relations similar to Eq. (2.5) are found for the other hydrogen lines as well, so that measuring the Stark broadening of hydrogen lines is a very common method to calculate the electron density [39, 111]. For other elements and non-hydrogenic ions, the Stark effect is quadratic and the calculation of the broadening is more complicated [7, 25].

In addition to Doppler broadening and Stark broadening, the instrumental broadening of the spectrometer also plays an important role and has to be measured. Usually it is approximated by a Gaussian profile [60]. The FWHM of the instrumental broadening of the high-resolution LIBS setup used in this thesis is about 0.06 nm in the VIS range, while the FWHM of the plasma imaging setup is about 0.13 nm in the VIS range. The three broadening mechanisms result in a convolution of a Gaussian distribution $\Phi_G(x)$ and a Lorentz distribution $\Phi_L(x)$ that is described by a Voigt profile

$$\Phi_V(x) = \int \Phi_G(x')\Phi_L(x - x')\,\mathrm{d}x'\,, \tag{2.6}$$

which is usually used to fit spectral lines in LIBS [25, 60].

2.1.5 Local thermodynamic equilibrium (LTE)

The existence of a local thermodynamic (or thermal) equilibrium is an essential condition for most of the analytical techniques that are used in LIBS [7, 27, 104]. LTE is similar to thermodynamic equilibrium (TE), in which the complete system can be described by a single plasma temperature [60]. However, TE requires a complete balance of all processes inside the plasma, including a radiative equilibrium that is only possible for an optically thick black body [149]. Since a laser-induced plasma plume emits light, it loses energy by radiation and a radiative equilibrium cannot be attained. While this means a deviation from TE, the energy exchange between the plasma particles still remains effective so that electrons, atoms, ions, and molecules can be described by the same temperature [27, 149]. This new equilibrium, in which particles and radiation are decoupled and must be described by different temperatures, is the LTE. A consequence of the LTE is that spatial gradients of the temperature within the plasma are possible, leading to different regions within the plasma that are described by their individual local plasma parameters [149].

In LTE, the same statistical relations as in TE can be used to describe the energy distributions for the plasma particles. The relative population of the excited energy levels of atoms, ions, and molecules is described by the Boltzmann distribution [27]

$$n_{s,z,i} = n_{s,z} \frac{g_i}{U_{s,z}(T)} \exp\left(\frac{-E_i}{k_B T}\right) , \tag{2.7}$$

where $n_{s,z,i}$ is the population density of the energy level i of species s in the ionization stage z, $n_{s,z}$ is the total number density of the species s in the ionization stage z, g_i is the degeneracy of the energy level E_i, and $U_{s,z}(T)$ is the internal partition function

$$U_{s,z}(T) = \sum_i g_i \exp\left(\frac{-E_i}{k_B T}\right) . \tag{2.8}$$

Eq. (2.7) can be inserted into Eq. (2.3) to obtain the relative emission coefficients of the transition lines of a species in dependence of the temperature. By rearranging the equation and taking the logarithm of both sides, the following equation is obtained:

$$\ln\left(\frac{\epsilon_{ul}\lambda_{ul}}{g_u A_{ul} c_B}\right) = \ln\left(\frac{hcn_{s,z}}{4\pi U_{s,z}(T) c_B}\right) - \frac{1}{k_B T} E_u \tag{2.9}$$

The correction factor c_B, in J/m^2, is introduced here so that the terms inside the logarithms are dimensionless. If the argument on the left side of Eq. (2.9) is plotted in dependence of the upper energy level E_u, a linear relationship can be observed with the slope $-(k_B T)^{-1}$. By fitting the slope, the plasma temperature T can be determined. This type of plot is called a Boltzmann plot [7, 25, 29]. Since the temperature varies within the plasma, local emission coefficients ϵ_{ul} should ideally be used in the Boltzmann plot in order to gain the temperature distribution in the plasma plume [7]. However,

in typical LIBS measurements the local emission coefficients are not available. The spatially integrated intensities are therefore used instead of the local emission coefficients. In this case, the calculated temperature values are spatially averaged. They will be lower for atomic species and higher for ionic species, since these species are mostly found at different temperatures. The obtained temperature values should therefore be used with caution, and ionic species should be used for more accurate estimates of the highest temperatures in the plasma.

The relative number densities of subsequent ionization stages of the same species in LTE can be calculated with the Saha (or Saha-Eggert) equation:

$$\frac{n_e n_{s,z+1}}{n_{s,z}} = \frac{1}{\lambda_e^3} \frac{2U_{s,z+1}(T)}{U_{s,z}(T)} \exp\left(-\frac{E_{s,z+1} - E_{s,z}}{k_B T}\right) \tag{2.10}$$

Here $E_{s,z}$ is the ionization energy of the ionization stage z and λ_e is the thermal de Broglie wavelength of an electron,

$$\lambda_e = \sqrt{\frac{h^2}{2\pi m_e k_B T}}\,. \tag{2.11}$$

The Saha equation can be used to make a so-called Saha-Boltzmann plot, which enables the calculation of the temperature from more than one ionization stage [7, 160]. As for the Boltzmann plot, this method is only applicable for homogeneous plasma plumes or if the local emission coefficients of the spectral lines were obtained by deconvolution of the measured intensities. Otherwise the measured intensities of atomic and ionic lines will represent different regions in the plasma and the calculate temperature will be significantly lower than the highest temperature in the plasma [7]. For the same reason the most accurate calculations of the highest temperature in the plasma are obtained from Boltzmann plots with ionic lines [31, 160].

Whether LTE exists depends on several criteria, of which the McWhirter criterion is the one that is used most often [27]. It defines a critical electron density above which collisional rates are at least ten times higher than radiative rates and is formulated as

$$n_e[\mathrm{cm}^{-3}] > 1.6 \times 10^{12} \sqrt{T[\mathrm{K}]} (\Delta E_{\max}[\mathrm{eV}])^3\,. \tag{2.12}$$

Here $\Delta E_{\max}$ is the largest gap between two adjacent energy levels of all species in the plasma, which is usually the energy gap between the ground state and the first excited state [27]. The McWhirter criterion is not a sufficient condition for LTE. Additional criteria for LTE are the linearity of the Boltzmann plot and comparisons of the excitation and ionization temperatures as obtained from the Boltzmann plot and the Saha-Boltzmann plot, respectively [7].

It has been questioned whether LTE really exists in a transient laser-induced plasma [16, 27]. However, since the alternative approaches are complex collisional-radiative models, the assumption of LTE conditions generally prevails in the LIBS community

[29]. Even if LTE is only an approximation, plasma parameters such as the temperature and the electron density that are calculated from LTE equations can still be useful as estimates of the real values, and changes of these values between different LIBS measurements can be indicative of changes in the matrix effects that affect the LIBS spectra.

2.2 Molecules in the laser-induced plasma

Molecular emission spectra have been observed in many LIBS measurements [29]. In the UV/VIS/NIR spectral range usually investigated in LIBS, the most common molecular signals are those of electronic transitions within diatomic molecules [67]. Since they can be quite intense, there is a high interest in utilizing these emissions for the detection and quantification of elements that produce only weak atomic and ionic emission [29, 50, 62]. Molecular emissions in LIBS can also be used to quantify the isotopes of elements, since the isotopic shift of molecular emissions is larger than the shift of atomic lines [61].

In this section, the reaction kinetics that determine the molecular concentrations in the plasma are briefly introduced. Subsequently an overview of the electronic, vibrational, and rotational energy levels of diatomic as well as linear and quasi-linear triatomic molecules is provided and the resulting molecular emission spectra in the UV/VIS/NIR spectral range are derived.

2.2.1 Molecule formation

The laser-induced plasma is initially too hot for chemical reactions that lead to the formation of molecules. As the temperature decreases over time, collisions between heavy particles become more likely and molecular species are formed [29]. The elementary reactions between atoms A and B in a plasma are three-body reactions in which a third particle M enables the reaction by taking up the excess energy [83]:

$$\mathrm{A} + \mathrm{B} + \mathrm{M} \rightleftarrows \mathrm{AB} + \mathrm{M}^* \tag{2.13}$$

In the forward direction, A and B form the diatomic molecule AB while M takes up the excess energy. In the backward direction, the collision of molecule AB and an energetic particle M* leads to the dissociation of AB into the atoms A and B. The rates at which the concentrations of A, B, AB, and M change are given by reaction kinetics [83]:

$$\frac{dn_{AB}}{dt} = k^{+} n_A n_B n_M - k^{-} n_{AB} n_M \,, \tag{2.14}$$

$$\frac{dn_A}{dt} = \frac{dn_B}{dt} = -\frac{dn_{AB}}{dt} \tag{2.15}$$

$$\frac{dn_M}{dt} = 0 \,. \tag{2.16}$$

Here n_{AB} is the number density of AB molecules, n_A and n_B are the number densities of the reactants, and n_M is the number density of the third collisional body. The forward direction has the rate constant k^+ and the backward direction has the rate constant k^-. The concentration of the third body M does not change, since it only takes up excess energy.

In TE or in LTE, the forward and backward direction are in equilibrium and the concentrations do not change over time. In that case, $dn_{AB}/dt = 0$ and

$$K \equiv \frac{k^-}{k^+} = \frac{n_A n_B}{n_{AB}} \tag{2.17}$$

is the so-called equilibrium constant that relates the number densities of atoms A and B to the number density of the diatomic molecule AB.

Chemical reactions are not the only possible mechanism that leads to the presence of molecules in the plasma. If fragmentation is a relevant ablation process, they can also form as fragments of the sample matrix [34, 114]. These fragments are directly ejected from the sample surface and correspond to the native bonds that are found in the sample itself [29]. Polyatomic fragments quickly decompose in the hot early plasma, leading to the formation of diatomic molecules that may be observed in LIBS spectra [9]. In most plasma models, the formation of molecules during fragmentation is neglected, as it is assumed that these fragments and molecules are quickly atomized in the initial plasma stages and play no significant role for the total plasma emission. Models used to describe the chemistry in the plasma are either based on a kinetic approach or on an equilibrium approach [9, 29, 135]. The fully kinetic approach requires three-dimensional modeling of the spatial, temporal and chemical plasma evolution and therefore goes beyond the scope of this thesis. The calculations for the chemical equilibrium model are presented in Section 2.3.

2.2.2 Molecular energy levels

For the calculation of the spectra of diatomic molecules and of the internal partition functions in a plasma at equilibrium, it is necessary to have an accurate description of the energy levels of molecules. They are usually calculated with the help of experimentally measured spectroscopic constants, which will be introduced here. The description is based on Herzberg [67].

The internal energy of the diatomic molecule can be separated into an electronic term, a vibrational term, and a rotational term. In molecular spectroscopy, it is common to express energies and frequencies in terms of wavenumbers, which is the reciprocal wavelength of the emission in cm^{-1}. The energy is then written as

$$T = T_e + G + F\,, \tag{2.18}$$

where T is the total internal energy, T_e is the electronic term value, G is the vibrational term, and F is the rotational term, all given in wavenumbers. T_e is a constant representing the minimum of the potential curve for the electronic state. The vibrational and rotational terms G and F can be approximated by using the model of a vibrating rotator, in which the vibrational potential is that of an anharmonic oscillator. In that case, the vibrational term is

$$G = \omega_e \left(\upsilon + \tfrac{1}{2}\right) - \omega_e x_e \left(\upsilon + \tfrac{1}{2}\right)^2 + \dots \tag{2.19}$$

with the *vibrational frequency* ω_e and the *anharmonic constant* $\omega_e x_e$. The anharmonic constant is

$$\omega_e x_e = \frac{\omega_e^2}{4E_e}\,, \tag{2.20}$$

where $E_e = D_e^0 + \frac{1}{2}\omega_e$ is the depth of the potential well in wavenumbers. D_e^0 is the dissociation energy of the electronic state in wavenumbers, which can be calculated from the dissociation energy of the electronic ground state by

$$D_e^0 = D_0^0 - T_e + \tfrac{1}{2}\omega_e\,, \tag{2.21}$$

as long as the given electronic state dissociates into the same atomic state as the ground state [135].

The rotational term of a vibrating rotator also depends on the vibrational state υ, because the internuclear distance and therefore the moment of inertia and the centrifugal force change with the vibrational state. It is given by

$$F = B_\upsilon J(J+1) - D_\upsilon J^2(J+1)^2 + \dots\,, \tag{2.22}$$

with the quantum number J of the total angular momentum and with the vibration-dependent constants

$$B_\upsilon = B_e - \alpha_e \left(\upsilon + \tfrac{1}{2}\right) + \dots \tag{2.23}$$

and

$$D_\upsilon = D_e - \beta_e \left(\upsilon + \tfrac{1}{2}\right) + \dots\,. \tag{2.24}$$

B_υ is the vibration-dependent rotational constant, with the *rotational constant* B_e and the *rotation-vibration interaction constant* α_e. D_υ is associated with the influence of the centrifugal force. Because it is very small, the vibration-dependent correction factor is usually neglected and D_υ is approximated by D_e alone.

In the model of a vibrating rotator, $J = 0, 1, 2, \dots$, which is often a sufficient approximation. If the orbital angular momentum of the electrons about the internuclear axis L and the electron electron spin S are considered as well, then the possible values of J are

$$J = \Omega,\, \Omega+1,\, \Omega+2,\, \dots\,, \tag{2.25}$$

where Ω is the component of the total electronic angular momentum along the internuclear axis. The value of Ω depends on the components of L and S along the internuclear axis. The component of L along the internuclear axis is

$$\Lambda = 0,\, 1,\, 2,\, \ldots,\, L\,, \tag{2.26}$$

and the component of S along the internuclear axis is

$$\Sigma = -S,\, -S+1,\, \ldots,\, S\,. \tag{2.27}$$

The values of Ω are then given by

$$\Omega = |\Lambda + \Sigma|\,. \tag{2.28}$$

For a given electronic state with $\Lambda > 0$, Ω can have $2S+1$ different values due to the electron spin, i.e. for $\Lambda = 1$ and $S = \frac{1}{2}$ there are two possible values $\Omega = \frac{1}{2}, \frac{3}{2}$. This leads to a splitting of the electronic term into $2S+1$ components in the internal magnetic field, and the electronic term is called a multiplet. The electronic energy of a multiplet is given by

$$T_e = T_0 + A\Lambda\Sigma\,, \tag{2.29}$$

where the constant A is called the *spin-orbit coupling constant*. The multiplicity $2S+1$ and the quantum numbers Λ and Ω are denoted in the international molecular term symbol

$$^{2S+1}\Lambda_\Omega\,, \tag{2.30}$$

in which $\Lambda = 0,\, 1,\, 2,\, \ldots$ are denoted as Σ, Π, Δ, ..., respectively. The splitting of the electronic term due to A is shown in Fig. 2.2 (Section 2.2.3) for a $^2\Pi$ doublet state, which splits into $^2\Pi_{1/2}$ and $^2\Pi_{3/2}$.

Using Eqs. 2.18, 2.19, 2.22, and 2.29 with experimentally obtained literature values for the spectroscopic constants T_e, ω_e, $\omega_e x_e$, B_e, α_e, D_e, and A, the energy levels of many diatomic molecules can be calculated quite accurately. For a more accurate description of the molecular energy levels, the coupling of the electronic motion and the rotation needs to be considered as well. This interaction leads to Λ-type doubling, which causes a splitting of $F(J)$ into two components for each J value, $F_c(J)$ and $F_d(J)$ [67]. The effect is very small, and is neglected for the calculation of molecular energy levels in this thesis. However, it is implemented in the software that I used to simulate molecular emission spectra [154], and can be seen in Fig. 2.3 (Section 2.2.3).

Notation In this thesis the standard notation for the electronic states of diatomic molecules is used, which is a letter denoting the position of the electronic state followed by the molecular term symbol [67, 72]. The letter in front of the term symbol is usually an X for the electronic ground state, an A for the first excited electronic state, and a B

for the second excited electronic state. The quantum number Ω is omitted unless it is of importance. For the Σ states, the reflection symmetry along a plane containing the internuclear axis is denoted by a $+$ for symmetry and a $-$ for antisymmetry. For the molecules investigated in this thesis, the first excited state is $A^2\Pi$, i.e. a doublet state with $S = \frac{1}{2}$, $\Lambda = 1$, and $\Omega = \frac{1}{2}, \frac{3}{2}$. The ground state is $X^2\Sigma^+$, i.e. $S = \frac{1}{2}$, $\Lambda = 0$, and symmetric.

Energy levels of triatomic molecules The energy levels of triatomic molecules are generally more complex than those of diatomic molecules due to the greater number of degrees of freedom for vibration and rotation [98]. In the simplest case of symmetrical linear triatomic molecules, there are four fundamental vibrational modes: one symmetric mode, one antisymmetric mode, and two degenerate bending modes. Accordingly, there are three vibrational quantum numbers υ_1, υ_2, and υ_3. The vibrational term is then

$$G = \sum_{i=1}^{3} \omega_i \left(\upsilon_i + \tfrac{1}{2}\right) + \sum_{i=1}^{3}\sum_{j=1}^{3} x_{ij} \left(\upsilon_i + \tfrac{1}{2}\right)\left(\upsilon_j + \tfrac{1}{2}\right) , \tag{2.31}$$

with the vibrational frequencies ω_i and the anharmonic constants x_{ij}. The rotational term is

$$F = \left(B_e - \sum_{i=1}^{3} \alpha_i \left(\upsilon_i + \tfrac{1}{2}\right)\right)\left(J(J+1) - \ell^2\right) + \dots , \tag{2.32}$$

with the three rotation-vibration interaction constants α_i and the angular momentum quantum number ℓ. It is not always possible to calculate this term accurately. For many triatomic molecules, the data about the electronic states is incomplete, and the quantum number of the angular momentum as well as the rotation-vibration interaction constants are unknown. However, for the calculation of an internal partition function it is often sufficient to use the rotational temperature as a measure of the rotational energy levels.

The energy levels of linear triatomic molecules are also a reasonable approximation for the energy levels of quasilinear triatomic molecules, i.e. triatomic molecules with a bond angle close to 180° [81]. The triatomic molecules considered in this thesis are either linear ($CaCl_2$) or quasilinear (CaF_2) [80, 81].

2.2.3 Emission spectra

The emission spectra of diatomic molecules in laser-induced plasma are given by the transitions between the electronic, vibrational, and rotational energy levels and their respective intensities [67]. In the UV and visible range, electronic transitions can be observed. However, these transitions in the electronic state are accompanied by transitions in the vibrational and rotational levels. This means that instead of a single electronic transition line, *band systems* can be observed. These band systems contain

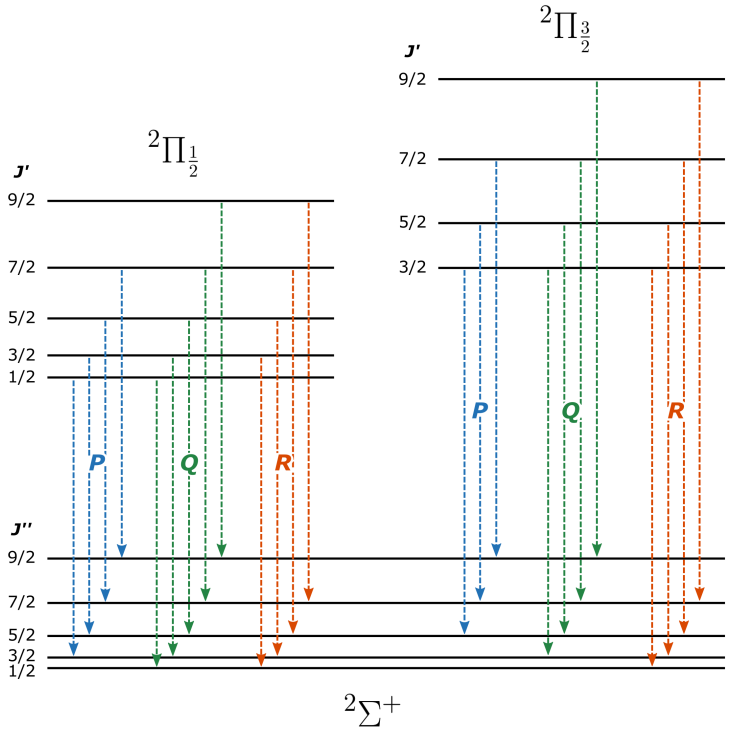

Figure 2.2: Energy level diagram showing the rotational levels $J = 0.5 \ldots 4.5$ of a single vibrational level υ' in the electronic $^2\Pi$ state and of a single vibrational level υ'' in the $^2\Sigma^+$ state. The $^2\Pi$ state splits into $^2\Pi_{1/2}$ and $^2\Pi_{3/2}$ due to spin-orbit coupling. The allowed transitions from rotational levels of the upper states to rotational levels of the lower states are $\Delta J = -1$ (P), $\Delta J = 0$ (Q), and $\Delta J = +1$ (R).

lines of all possible transitions between the vibrational and rotational levels of the upper and lower electronic state. A single band is the series of rotational lines of a single vibrational transition υ' to υ'', with υ' being the vibrational level in the upper electronic state and υ'' being the vibrational level in the lower electronic state. Since the distances between the rotational lines are very small, they appear as a continuous band if the dispersion of the spectrometer is not high enough.

All bands investigated in this thesis are bands of $^2\Pi - ^2\Sigma$ transitions, so that a focus is placed on these transitions. The energy level diagram of a $^2\Pi - ^2\Sigma$ transition is shown in Fig. 2.2, with the allowed transitions grouped into P, Q, and R branches. These branches are shown in Fig. 2.3a for a hypothetical molecular band, Fig. 2.3b. The spin-orbit coupling was neglected in this case, i.e. $A = 0$. The three branches and their intensities define the molecular band, as will be explained in the following.

The energy of a photon that is emitted during the transition from the upper electronic state to the lower electronic state is equal to the difference between the energy of the upper and the lower state. Accordingly, the wavenumber of the corresponding

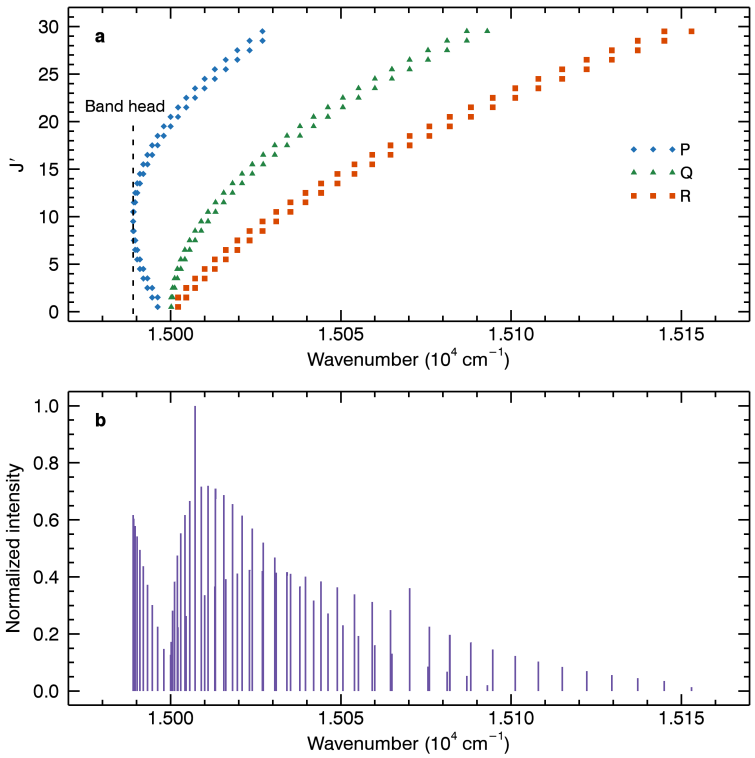

Figure 2.3: Simulated band spectrum of a hypothetical molecule for a vibrational transition from a $^2\Pi$ state to a $^2\Sigma^+$ state at $T = 300\,\mathrm{K}$. The band origin is at $\nu_0 = 15\,000\,\mathrm{cm}^{-1}$, the upper and lower rotational constants are $B'_v = 1.1\,\mathrm{cm}^{-1}$ and $B''_v = 1\,\mathrm{cm}^{-1}$, respectively, and $J = 0.5 \ldots 29.5$. The spin-orbit coupling constant was set to $A = 0$. a) Fortrat diagram showing the P, Q, and R branches of the rotational structure. Λ-type doubling can be observed in each branch. b) Band spectrum of the transition, consisting of rotational lines with different intensities according to the population density of the upper state $F(J')$ and the Hönl-London factors.

spectral line is given by

$$\nu = T' - T'' = (T'_e - T''_e) + (G' - G'') + (F' - F''), \tag{2.33}$$

with the upper state marked by a single prime and the lower state marked by a double prime. The difference of the upper and lower electronic terms is constant for a given electronic transition, while the vibrational and the rotational term vary depending on the initial and final vibrational and rotational states. If the electronic state changes, there is no general selection rule for the vibrational transitions, meaning that they are all allowed in principle. By contrast, only specific rotational transitions are allowed.

A band is the spectrum of rotational lines belonging to a specific vibrational transition. The band origin ν_0 is given by the part of Eq. (2.33) that does not depend on

the rotational quantum number J:

$$\begin{aligned}\nu_0 =&(T_e' - T_e'') + (G' - G'')\\ =&(T_0' - T_0'') + (A'\Lambda'\Sigma' - A''\Lambda''\Sigma'')\\ &+ \omega_e'(\upsilon' + \tfrac{1}{2}) - \omega_e x_e'(\upsilon' + \tfrac{1}{2})^2\\ &- \omega_e''(\upsilon'' + \tfrac{1}{2}) + \omega_e x_e''(\upsilon'' + \tfrac{1}{2})^2\end{aligned} \tag{2.34}$$

It is worth noting that the transitions between low-lying vibrational levels with equal $\Delta\upsilon = \upsilon' - \upsilon''$ will be very close together if ω_e and $\omega_e x_e$ are similar for the upper and the lower state. There can be a significant overlap between bands of these band sequences, so that they sometimes appear as a single band.

Positions of rotational lines Only rotational transitions that fulfill the selection rules appear in the band spectrum. The selection rules for the rotational transitions depend on the quantum numbers of the electronic angular momentum in the upper and lower state, Λ' and Λ''. If at least one of them is non-zero, the difference between the quantum numbers J' and J'' can take on three values:

$$\Delta J = J' - J'' = 0, \pm 1 \tag{2.35}$$

The spectral lines are categorized into three branches depending on the value of ΔJ. The series of lines with $\Delta J = -1$ are the *P branch*, those with $\Delta J = 0$ are the *Q branch*, and those with $\Delta J = +1$ are the *R branch*. If both $\Lambda' = 0$ and $\Lambda'' = 0$, then the Q branch is not allowed. The Q branch is allowed for all transitions considered in this thesis.

Neglecting the small influence of the rotational constant D_υ, the wavenumbers of the lines of the P, Q, and R branches are approximately:

$$\nu_P = \nu_0 + \Delta B_\upsilon(J'' + J''^2) - 2B_\upsilon' J'' \tag{2.36}$$

$$\nu_Q = \nu_0 + \Delta B_\upsilon(J'' + J''^2) \tag{2.37}$$

$$\nu_R = \nu_0 + \Delta B_\upsilon(J'' + J''^2) + 2B_\upsilon'(J'' + 1) \tag{2.38}$$

They can be displayed in a Fortrat diagram, see Fig. 2.3a. The value of $\Delta B_\upsilon = B_\upsilon' - B_\upsilon''$ determines the appearance of the band. Importantly, it determines in which branch the *band head* is formed, which is the sharp edge of the band with a high intensity that is characteristic for many molecular bands. If ΔB_υ is positive, the band head will form in the P branch, if it is negative, the band head will form in the R branch. In both cases, the wavenumber of the band head is given by

$$\nu_{BH} = \nu_0 - \frac{(B_\upsilon' + B_\upsilon'')^2}{4(B_\upsilon' - B_\upsilon'')}\,. \tag{2.39}$$

The value of the second term is negative if $B_\upsilon' - B_\upsilon''$ is positive, which means that the band head is at a longer wavelength than the band origin if it is formed in the P

branch. In this case the band is *degraded toward the violet*, i.e. the band intensity will decrease towards shorter wavelengths. This is the case in Fig. 2.3b. If the band head forms in the R branch, $B'_\upsilon - B''_\upsilon$ is negative and so the band head marks the shortest wavelength of the band. In this case the band is *degraded toward the red*. For the bands investigated in this thesis, the heads of the individual P, Q, and R branches can often be observed very clearly in the spectrum and can even be more intense than the band head. Since there is no specific term for these heads, I will refer to them as *branch heads*, and the band head is simply the branch head at the edge of the band.

Emission coefficient calculation The Franck-Condon principle states that the electronic transition in a molecule is much faster than the vibrational motion, so that the nuclei are approximately still in the same position and have the same velocity as before. In a potential energy diagram, this means that the most intense transitions occur vertically from those positions at which the molecule is most likely found. In emission, these are the turning points of the vibrational motion, so that the most intense transitions are those that occur vertically downwards from the turning points in the upper state. The quantum mechanical formulation of this principle is that the electronic transition moment R_e only varies slowly with the internuclear distance r and can be approximated by an average value $\overline{R_e}$ [54]. The transition probability $P_{\upsilon',\upsilon''}$ then only depends on the overlap integral of the vibrational eigenfunctions ψ_υ,

$$P_{\upsilon',\upsilon''} = \overline{R_e}^2 \left(\int {\psi'_\upsilon}^* \psi''_\upsilon \, \mathrm{d}r \right)^2 . \tag{2.40}$$

The square term in this equation is the Franck-Condon factor $f_{\upsilon',\upsilon''}$ of the transition,

$$f_{\upsilon',\upsilon''} = \left(\int {\psi'_\upsilon}^* \psi''_\upsilon \, \mathrm{d}r \right)^2 . \tag{2.41}$$

Using this, the emission coefficient of the band corresponding to the transition $\upsilon' \to \upsilon''$ is [67, p. 200]

$$\epsilon_{\upsilon',\upsilon''} = \frac{64}{3} \pi^4 c n_{\upsilon'} \nu^4 \overline{R_e}^2 f_{\upsilon',\upsilon''} . \tag{2.42}$$

Here $n_{\upsilon'}$ is the number of molecules in the upper vibrational state, which can be calculated with Eq. (2.7). The vibrational eigenfunctions ψ_υ are determined by the formulation of the potential energy. A simple and yet quite accurate approximation is the Morse potential [97]. The Morse potential is described by the potential well depth E_e, the equilibrium internuclear distance r_e, and the decay constant in the exponential term $a = \sqrt{k_e/2E_e}$, where k_e is the force constant of the molecule in the given electronic state. The vibrational eigenfunctions are then given by [28]

$$\psi_\upsilon(z) = N(\upsilon, \lambda) z^{\lambda - \upsilon - \frac{1}{2}} e^{-\frac{1}{2}z} L_\upsilon^{(2\lambda - 2\upsilon - 1)}(z) , \tag{2.43}$$

with the new coordinate $z = 2\lambda e^{-a(r-r_e)}$, with the dimensionless parameter

$$\lambda = \frac{2\pi\sqrt{2\mu E_e}}{ah}\,, \tag{2.44}$$

where μ is the reduced mass of the molecule, and with the normalization factor

$$N(\upsilon,\lambda) = \sqrt{\frac{(2\lambda - 2\upsilon - 1)\Gamma(\upsilon+1)}{\Gamma(2\lambda-\upsilon)}}\,. \tag{2.45}$$

$L_\upsilon^{(2\lambda-2\upsilon-1)}(z)$ is a generalized Laguerre polynomial [140], and $\Gamma(x)$ is the gamma function. The overlap integral of two vibrational eigenfunctions can be solved numerically.

The relative intensities of the rotational lines of the band can be calculated from the product of the Boltzmann factor $e^{-F(J)/k_BT}$ of the rotational levels and the Hönl-London factors [71]. For $\Delta\Lambda = 1$, which is the case for $^2\Pi - {}^2\Sigma$ transitions, the Hönl-London factors are:

$$S_J{}^P = \frac{(J'+1-\Lambda')(J'+2-\Lambda')}{4(J'+1)} \tag{2.46}$$

$$S_J{}^Q = \frac{(J'+\Lambda')(J'+1-\Lambda')(2J'+1)}{4J'(J'+1)} \tag{2.47}$$

$$S_J{}^R = \frac{(J'+\Lambda')(J'-1+\Lambda')}{4J'} \tag{2.48}$$

The superscripts indicate that the formulae are for the P branch, the Q branch, and the R branch, respectively. Here the Λ-type splitting of the rotational levels of multiplet states is neglected, but accurate theoretical descriptions for doublet transitions can be found in [10].

2.3 Modeling the equilibrium plasma

For the investigation of LIBS spectra and of the spatial distributions of elements in a laser-induced plasma, it can be important to model the laser-induced plasma numerically. There are many possible models of varying complexity. For the most complete description of the plasma, many different effects have to be considered, including the ablation process [14], non-equilibrium effects [74], the radiative loss of energy [134], and the expansion of the plasma plume [13, 23]. A complete model also needs to consider the time evolution of the plasma. It is obvious that such a description requires a lot of processing power, takes a lot of time, and depends on too many parameters to be viable as a model for the analysis of measurement data. Typically, the models that are made are specialized for a specific task, such as the investigation of the ablation process in dependence of parameters of the laser and the solid [142], or the investigation of the plasma plume expansion in different ambient gases and pressures [13]. For the investigation of the plasma emission, collisional-radiative models are sometimes used, but

most commonly variations of the equilibrium approach are used [29]. The condition of LTE is assumed to be fulfilled during a significant portion of the plasma lifetime, and transport mechanisms are assumed to be significantly slower than the establishment of equilibrium. In this case a non-stationary and inhomogeneous plasma can be approximated by small homogeneous plasma regions that slowly interact with each other. In this section, the equations that are necessary to describe a plasma in this way are presented. The model will also be expanded to include chemical reactions in the plasma as well. The description is based on the work by Shabanov and Gornushkin [135, 136].

2.3.1 Atomic and ionic number densities

For a stationary plasma in equilibrium, the number densities of the atomic and ionic species can be numerically calculated in dependence of the temperature of the plasma and of the total number densities of nuclei of each element. For this it is assumed that the plasma behaves similar to an ideal gas in LTE, which allows for the use of the Boltzmann distribution, Eq. (2.7), and the Saha equation, Eq. (2.10). The latter can be shortened to

$$\frac{n_e n_{s,z+1}}{n_{s,z}} \equiv S_{s,z+1}(n_e, T)\,, \tag{2.49}$$

so that the number density of $n_{s,z}$ can be expressed as $n_{s,z} = S_{s,z} n_{s,z-1}/n_e$. The total number density of particles belonging to species s can then be written as

$$n_s = \sum_{i=0}^{z} n_{s,i} = \left(1 + \sum_{z\geq 1} \frac{\prod_{i=1}^{z} S_{s,j}}{n_e^z}\right) n_{s,0}\,. \tag{2.50}$$

Since n_s is an input parameter, and the individual Saha equations $S_{s,z+1}$ can be calculated for a given temperature, Eq. (2.50) defines $n_{s,0}$, and subsequently all $n_{s,z}$, as functions of the temperature and the electron density. In order to calculate the electron density, the law of charge conservation is used, which states that the number of electrons in the plasma has to be equal to the number of electrons that have been released during ionization:

$$n_e = \sum_{s,z} z n_{s,z} \tag{2.51}$$

The number densities in this equation are obtained from Eq. (2.50) by using an initial estimate of the electron density. The correct electron density can then be found by iteration. The upper limit for the electron density is $n_e^{max} = \sum_s z_{max} n_s$, where z_{max} is the highest ionization stage of species s. This is a good initial estimate of the electron density at high temperatures.

2.3.2 Molecular number densities

At low temperatures, molecular species need to be considered in the calculation of the composition of the equilibrium plasma. In TE or in LTE, the forward and backward

directions of all reactions are in equilibrium, see Section 2.2.1. In the case of a laser-induced plasma, the reactants are usually neutral atoms or ions and there is only one product, which is a diatomic or triatomic molecule. It is sufficient to consider only reactions between neutral atoms and molecules, as the Saha equation relates the number densities of ionic species to those of the neutral species, so that the number density of molecular ions can be determined independently. Equivalently to the Saha equation, a description of the equilibrium constant K of the reaction can be found that relates the number densities n of the species that participate in the reaction to their partition functions U [161]:

$$K = \frac{\prod_p n_p^{C_{pq}}}{n_q} = \frac{\lambda_q^3}{\prod_p \lambda_p^{3C_{pq}}} \frac{\prod_p U_p^{C_{pq}}}{U_q} e^{\frac{-D_q}{k_B T}} \tag{2.52}$$

Here the subscripts p and q denote elemental and molecular species, respectively, C_{pq} is the stoichiometric number of atoms of the type p that are bound in a single molecule q, and D_q is the dissociation energy of the molecule q. The thermal de Broglie wavelengths λ are given by

$$\lambda = \sqrt{\frac{h^2}{2\pi m k_B T}}\,, \tag{2.53}$$

with the mass m of the species in question. Equation (2.52) is sometimes called the Guldberg-Waage equation due to its origin in the law of mass action [29, 135]. The internal partition functions of the elemental species U_p are given by Eq. (2.8), while the internal partition function of a molecule q is given by the product of the electronic, vibrational, and rotational partition functions,

$$\begin{aligned} U_q &= U_{\mathrm{el}} U_{\mathrm{vib}} U_{\mathrm{rot}} \\ &= \sum_e \sum_v \sum_J g_e g_J \exp\left(-\frac{hc\,(T_e + G(v) + F(J,v))}{k_B T}\right)\,, \end{aligned} \tag{2.54}$$

with the statistical weight of the electronic state $g_e = (2S+1)(2-\delta_{0,\Lambda})$ and with the statistical weight of the rotational state $g_J = g_n(2J+1)$, where g_n is the statistical weight of the nuclei [105]. At sufficiently high temperatures, the rotational partition function can be integrated over J and expressed as the temperature divided by a characteristic rotational temperature $\theta_{\mathrm{rot}} = hcB_v/k_B$, with B_v given by Eq. (2.23). The partition function for diatomic and linear triatomic molecules can then be written as [105]

$$U_q = \sum_{e,v} \frac{g_e T}{\sigma \theta_{\mathrm{rot}}} \exp\left(-\frac{T_e + G(v)}{k_B T}\right)\,. \tag{2.55}$$

Here $\sigma = 1$ for heteronuclear molecules and $\sigma = 2$ for homonuclear molecules and symmetric linear triatomic molecules. The energy levels may not exceed the dissociation energy that is needed to remove the first atom from the molecule.

With the partition functions, the equilibrium constants K can be calculated from Eq. (2.52) for all molecules in dependence of the temperature. Subsequently the equilibrium number densities can be found numerically using the law of mass conservation, which states that the number of nuclei of the element p must stay the same:

$$n_p = \sum_z n_{p,z} + \sum_q C_{pq} n_q \tag{2.56}$$

For simple plasmas in which only a few molecules can form, the problem can often be reduced to a relatively simple iterative approach, where the main problem is choosing the correct algorithm to reduce numerical errors. Shabanov and Gornushkin describe one algorithm for a system of the elemental species A and B in which the molecules A_2, B_2, and AB can form [135], and another where the molecules B_2, AB, and AB_2 can form [136]. If more chemical reactions are added, it becomes more difficult to calculate the chemical equilibrium. In such a case, a hierarchical algorithm can be used, in which the number densities are iteratively solved for the reaction that is furthest from equilibrium until all reactions are close to equilibrium [22]. While relatively simple, this type of algorithm can easily get stuck in a very slowly converging loop and works best for reactions with similar equilibrium constants.

3. LIBS Setup and Methods

The experiments of this thesis were conducted with two separate LIBS setups. The first one is the high-resolution LIBS system at the Institute of Optical Sensor Systems of the German Aerospace Center (DLR). Its main advantages are a high spectral resolution combined with a high spectral coverage and time-resolved measurement capabilities. This is the setup that was used for measurements where a spatially integrated spectrum was sufficient and high resolution and spectral range were required. The second LIBS setup is the plasma imaging setup that I have developed during my work for this thesis, which allows for spatially resolved measurements of the plasma emission. Both setups use a simulation chamber in order to simulate the ambient pressure and the ambient gas found in extraterrestrial environments.

In this chapter, the first experimental setup will be described, as well as the methods that were used in the preparation of samples and in the calculation of the elemental compositions of the samples. The design and the characterization of the plasma imaging setup are found in Chapter 6.

3.1 LIBS setup

The high-resolution LIBS setup at DLR Berlin was used for the measurements in Chapter 4 and Chapter 5. A schematic of the setup is shown in Fig. 3.1. The main components of the setup are the Q-switched Nd:YAG laser (Continuum Inlite II-20), the echelle spectrometer (LTB Aryelle Butterfly) with a time-gated intensified charge-coupled device (ICCD) camera (Andor iStar), and the simulation chamber in which the ambient gas and the ambient pressure can be adjusted for the simulation of extraterrestrial environments. The laser is synchronized with the camera by a control unit with an internal clock generator that is part of the spectrometer system. In its optical path, the laser beam traverses a filter cascade with up to five filters that can attenuate the pulse energy. After the filter cascade, the beam is diverged by a plano-concave lens with a focal length of $-75\,\mathrm{mm}$ and then focused with a plano-convex lens with a focal length of $150\,\mathrm{mm}$. A mirror directs the laser beam into the simulation chamber through a window at the top of the chamber. Inside the chamber, the laser beam hits the sample, which is placed on a motorized translation stage, at an incidence angle of about 5°. The translation stage enables the positioning of the sample so that its surface is in the focus of the laser beam, where the beam diameter is about $300\,\mu\mathrm{m}$. The pulsed laser beam ablates the sample surface and initiates the plasma formation. The emitted light

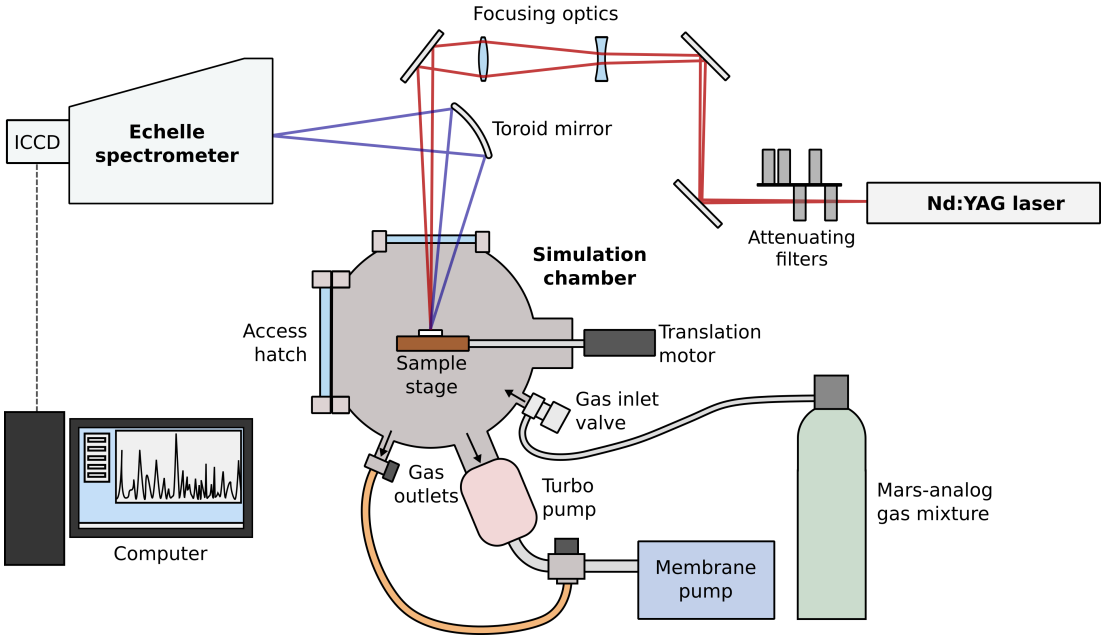

Figure 3.1: Schematic of the LIBS setup.

from the plasma is collected with a toroid mirror and focused onto the entrance slit of the echelle spectrometer.

3.1.1 Laser

The Q-switched Nd:YAG laser (Continuum Inlite II-20) operates at its fundamental wavelength of 1064 nm with a repetition rate of 10 Hz and a pulse width of 6 ns. At the focus position inside the simulation chamber, it has a maximum pulse energy of 120.5 mJ, which can be reduced down to 0.4 mJ using the filter cascade in the optical path. For this thesis, pulse energies in the range of 15–35 mJ were used, which is a realistic range of pulse energies that could be achieved by LIBS instruments in planetary exploration, cf. [90].

3.1.2 Spectrometer

The echelle spectrometer (LTB Aryelle Butterfly) can be switched between two spectral ranges, the UV spectral range from 190 nm to 350 nm, and the UV/VIS/NIR spectral range from 270 nm to 850 nm. Switching between the two wavelength ranges is done internally by turning a mirror so that the collected light goes through a different optical system within the spectrometer before reaching the same detector. All measurements for this thesis were made with the UV/VIS/NIR spectral range, which has a spectral resolution of about 0.03 nm in the UV and a spectral resolution of about 0.09 nm in the NIR.

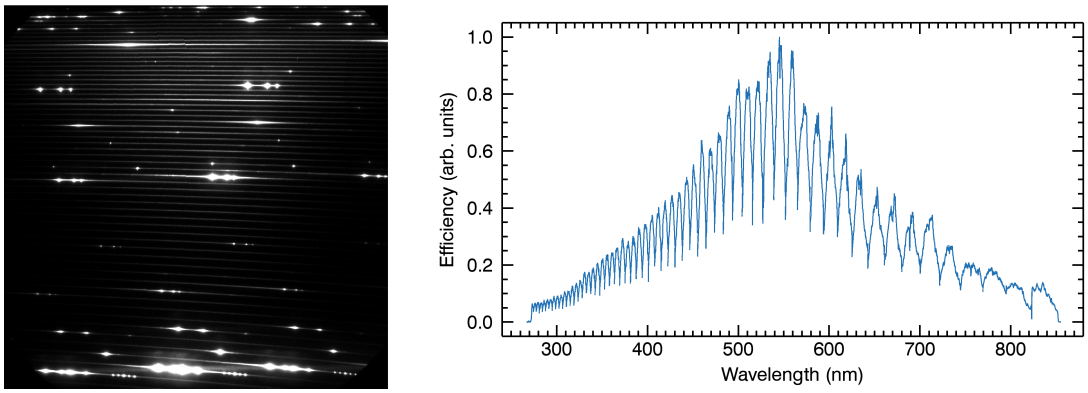

Figure 3.2: Left: Image of a LIBS spectrum as seen by the ICCD camera of the echelle spectrometer. The diffraction orders m are spatially separated in the vertical direction, while the spectrum within one diffraction order is dispersed in the horizontal direction. Right: Spectral efficiency of the LIBS setup in the UV/VIS/NIR wavelength range. Within each diffraction order, the efficiency can be seen to rise towards the blaze wavelength.

The advantage of an echelle spectrometer is that it is able to cover a wide spectral range while still offering a very high spectral resolution. This is achieved by using a combination of a prism and an echelle grating, where the echelle grating separates the diffraction orders in one dimension of the detector, while the prism disperses the spectrum within each single diffraction order along the other dimension of the detector. An example of the resulting camera image is shown in Fig. 3.2 (left). The different diffraction orders can be seen as nearly horizontal lines across the image that are above one another. At the bottom of the image, the diffraction orders in the UV regime can be seen, while the NIR wavelengths are in the diffraction orders at the top. To obtain a spectrum, the diffraction orders are extracted from the image and fitted with a wavelength calibration function, whereupon any overlapping wavelength ranges are removed. Since each diffraction order has its highest efficiency close to the blaze wavelength, the combined spectrum has a spectral efficiency consisting of many local maxima, which can be seen in Fig. 3.2 (right). This spectral efficiency, which was measured with a calibrated light source (Energetiq EQ LDLS), is that of the whole LIBS setup and includes losses in the optical path before the spectrometer. It is used for the calibration of the relative intensities of spectral features at different wavelengths, which is important for the temperature calculation from Boltzmann plots.

3.1.3 Simulation chamber

The simulation chamber has a volume of about 5000 cm^3 and can be used to simulate extraterrestrial environments at lower pressures and with a different atmospheric composition than Earth. The pressure inside the chamber can be reduced to less than 1 Pa with a turbo pump, and different ambient gases can be inserted with a fine ad-

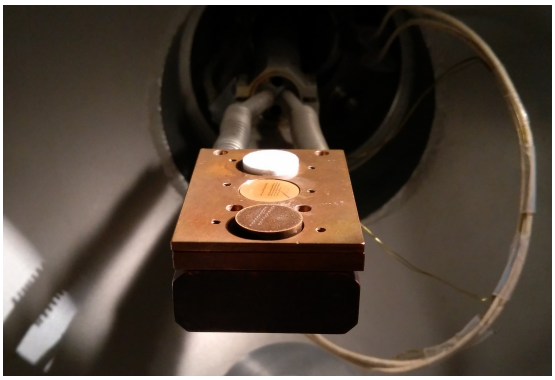

Figure 3.3: Three pellets on the motorized stage of the simulation chamber.

justment valve. For this thesis, Martian atmospheric conditions are simulated by filling the simulation chamber with Mars-analog gas and keeping the pressure constant at 650 Pa. The Mars-analog gas consists of 95.55 vol% CO_2, 2.7 vol% N_2, 1.6 vol% Ar, and 0.15 vol% O_2, which closely resembles the composition of the lower Martian atmosphere [110]. The pressure of 650 Pa is slightly lower than the average atmospheric pressure on the surface of Mars, which is closer to 750–800 Pa [64, 68]. The lower pressure was chosen for comparability with other measurements at the same LIBS setup [121, 129]. In order to achieve a good simulation of Martian atmospheric conditions, the pressure inside the chamber was first reduced to less than 200 Pa, then flooded with 2000 Pa of Mars-analog gas before adjusting the pressure to 650 Pa. A constant gas flow of approximately 40 L/ min inside the simulation chamber was used to maintain the composition and the pressure of the ambient gas over time.

Inside the simulation chamber, samples are placed on a motorized stage that can be translated in three dimensions, see Fig. 3.3. This allows for the adjustment of the height of the sample surface in relation to the focus of the laser beam and makes it possible to move to a new position on the sample surface or to a new sample. A camera above the stage that has its focus in the same plane as the laser beam allows for the controlled positioning of the sample. Three pellets of 1.4 cm diameter can be placed next to each other on the stage, enabling consecutive measurements on three samples before the simulation chamber needs to be pressurized and opened to change samples.

3.2 Sample preparation

All investigated samples were pressed pellets with a diameter of 1.4 cm, which is large enough for a grid of at least 10×10 measurements with a distance of 1 mm between adjacent positions. The mass of the pellets was about 1 g. Before pressing the sample material into a pellet, it was ground into a fine powder using a mortar and pestle. Based on investigations of several samples under a microscope, the typical grain size

after this procedure was less than 40 µm. The material was then pressed into pellets by applying a pressure of 0.25 GPa for at least 10 minutes.

If samples were mixed from different materials, the mixing ratio was determined by measuring the weight of the substances with a scientific scale. Then the substances were mixed using the mortar and pestle as before. The uncertainty of the scale is conservatively estimated as $\Delta m = 0.01\,\mathrm{g}$ from the observed variance between repeated measurements. Additional sources of uncertainty for the molar fractions are losses during the mixing process, for example due to residues in the mortar or because some materials formed dust and were lost in this way, which changes the mixing ratio. I attempted to minimize all sources of uncertainty by increasing the total amount of mixed material significantly, so that the lowest weight of a substance was still at least 0.1 g.

Samples made from hygroscopic materials were placed inside a desiccator before and after the measurements in order to avoid deliquescence of the samples and to reduce the adsorption of atmospheric water. Before measuring hygroscopic samples, they were kept at a low pressure of less than 200 Pa inside the simulation chamber for up to 30 minutes in order to reduce the influence of adsorbed water.

3.3 Software and data analysis

The data analysis in this thesis as well as the simulations of the laser-induced plasma were made with custom scripts written in the programming language IDL. For all fits, the MPFIT package for IDL was used [89]. It is an implementation of the Levenberg-Marquardt algorithm for non-linear least-squares fitting and allows user-defined fit functions.

The intensities and linewidths of emission lines in the measured LIBS spectra were obtained by fitting them with a Voigt profile (Eq. 2.6). If multiple emission lines were present and were partially superimposed, the whole spectral interval was fitted with multiple Voigt profiles in a single fit in order to obtain the individual linewidths and intensities. Since this can increase the uncertainty of the solutions for the fit parameters, it was only done if necessary. A special case is that of the O(I) triplet around 777.4 nm. Since the initial energy levels are nearly equal for the three emission lines, they can for all purposes be considered to be a single signal, which was done here whenever these lines were investigated.

Molecular bands are similar to the case of multiple atomic emission lines from similar upper energy levels, with the difference that the number of rotational lines in a band is very high. Since the line broadening is usually much larger than the distance between adjacent rotational lines, they can not be fitted individually. While it would be possible to simulate the molecular spectrum and use this simulated band profile as a

fit, this requires very precise knowledge of the spectroscopic constants of the molecule. For the investigated bands, the available data was not sufficient for this approach (see Section 4.3.1 and Section 5.2.1). Instead, the molecular band intensities were obtained by summing up the total intensity within a small wavelength range where no other spectral features could be detected. In some cases, the molecular bands were completely superimposed by other spectral features, for example from other molecular bands. In this case, the spectrum was fitted with a linear combination of several different spectra within a given wavelength range. The spectra used for the linear combination were taken from measurements where the superimposed signals did not appear.

For the simulation of molecular band spectra, the software PGOPHER was used [154]. With this software, the rotational spectra of multiple vibrational transitions can be simulated. The correct values of the constants need to be calculated manually beforehand from the equations given in Section 2.2.3. For the simulations a maximum rotational quantum number $J_{\mathrm{max}} = 300$ was used. For lower values, the simulated spectrum often did not resemble the measured spectra, while higher values could not improve it further. A Boltzmann population distribution was assumed in which vibrational and rotational temperatures are the same and are equal to the plasma temperature. For the simultaneous simulation of several vibrational transitions, the relative transition strengths have to be known as well. For a single molecule these are given by the Franck-Condon factors $f_{v',v''}$, which were obtained from the literature or from my own numerical calculations using the vibrational eigenfunctions of the Morse potential.

4. Detection of Chlorine by Molecular Emission

Chlorine plays an important role in the geological and aqueous history of Mars. It was first detected in the Martian regolith by the two Viking landers at concentrations of 0.5–1.5 wt%, indicating a strong enrichment in the Martian regolith [17, 18]. High chlorine concentrations have also been found in Martian meteorites, leading to the hypothesis that Mars could be richer in volatiles than Earth [35, 36]. Remote sensing measurements of the Martian surface with the 2001 Mars Odyssey Gamma Ray Spectrometer confirmed that chlorine is indeed enriched at the Martian surface [78, 144]. The observed heterogeneous distribution of chlorine on the Martian surface has been linked to hydrothermal and volcanic activity [78], with Filiberto and Treiman [42] suggesting that chlorine may have been the dominant volatile species in Martian magmas. In the thermal infrared images of the 2001 Mars Odyssey Thermal Emission Imaging System (THEMIS), chloride-bearing minerals were identified that were mostly found within the highlands of the southern hemisphere, see Fig. 4.1 [107, 108]. The geological context was found to be consistent with water-related formation processes [108]. In-

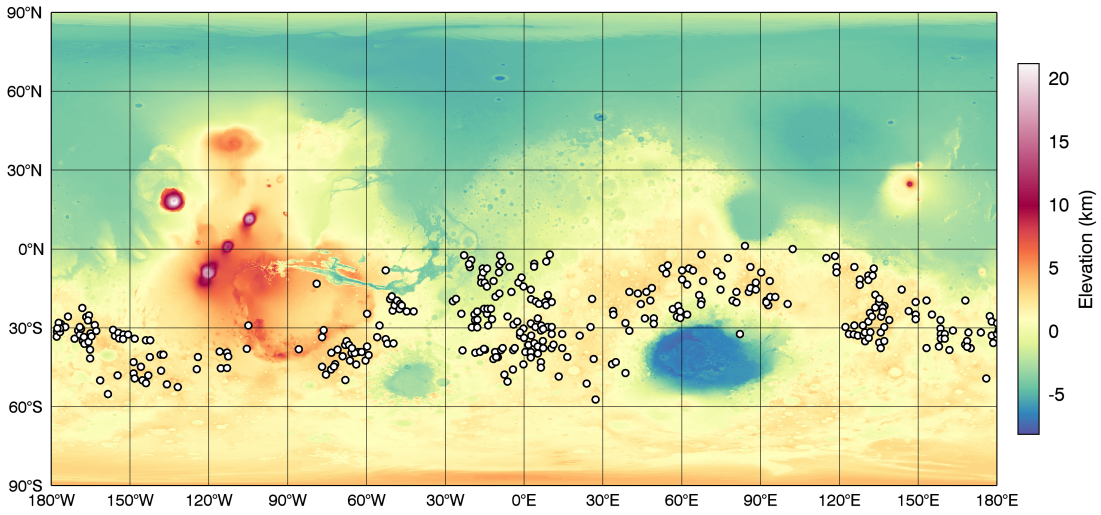

Figure 4.1: Global distribution of chloride-bearing minerals (white circles) on Mars as identified in THEMIS data by Osterloo et al. [108]. They are mostly found in the southern highlands. The topographic map was created from the Mars Global Surveyor's MOLA altimetry data obtained via NASA's Planetary Data System [93, 137].

deed, chlorine-bearing salts are strongly connected to the aqueous history of Mars and to the presence of liquid water today. Perchlorates, which have been detected by the Phoenix Mars Lander mission's Wet Chemistry Laboratory, lower the freezing point of aqueous solutions significantly, enabling the presence of liquid water even at cold Martian temperatures [59, 123, 138]. The detection of chlorine is therefore important for a more complete understanding of past and present Martian environments as well as the history and the presence of liquid water on Mars.

As mentioned in Chapter 1, halogens generally have very high excited electronic levels, so that their strongest emission lines are often in the VUV spectral range that is not covered by ChemCam and SuperCam. The detection of chlorine with ChemCam has therefore been challenging [6], and the presence of chlorides in Martian targets could sometimes only be inferred from the detection of a potential cation [21]. Molecular emissions have been a promising alternative for the detection of halogens. Gaft et al. [50] investigated many potential molecular bands that could be used for the detection of halogens. For the detection of chlorine in a Martian environment, the most promising molecular bands are MgCl and CaCl, since both magnesium and calcium are ubiquitous on Mars and have been found in water-related materials such as sulfates, chlorides, and perchlorates [37]. Indeed, molecular bands of CaCl have already been found in LIBS spectra of ChemCam [44, 92]. However, the number of Martian targets showing CaCl emission in the LIBS spectra was significantly lower than that of targets which showed CaF emission, and the Cl emission lines appeared to be the more robust signal for Cl despite the high detection limit [91]. It has been suggested that the Ca concentration of the investigated samples might have been too low, or that Cl prefers to recombine with Mg instead of Ca [91]. In order to understand the formation of CaCl in laser-induced plasma under Martian conditions, it is therefore necessary to investigate the dependence on the concentrations of Ca and Cl, but also a possible interference of MgCl.

If MgCl emits at a similar intensity as CaCl, MgCl bands would be interesting alternative signals for the detection of Cl. The strongest MgCl band is at about 380 nm, which is outside of the spectral range of ChemCam and SuperCam, but might be within range of the MarsCoDe instrument of the CNSA's HX-1 rover. It is also worthwhile to investigate MgCl in order to find out whether the spectral range around 380 nm should be included in future LIBS instruments for planetary exploration.

In this chapter, the molecular emissions of MgCl and CaCl are investigated for samples of varying composition and in simulated Martian conditions. First, pure samples of $MgCl_2$ and $CaCl_2$ are investigated in order to study the MgCl and CaCl emission for samples that offer ideal conditions due to the high concentrations of the reactants. The MgCl band is found to be too weak for the detection of Cl even in the LIBS spectrum of the pure $MgCl_2$ sample. In order to explain this observation, the formation of

Table 4.1: Overview of the test series with varying Ca and Cl concentrations. The variable α indicates the varying weight fractions of the two substances in the mixtures.

Series	Mixture	χ_{Ca} (at%)	χ_{Cl} (at%)	# samples
$KCl + CaSO_4$	$\alpha KCl + (1\text{-}\alpha)\, CaSO_4 \cdot 2\,H_2O$	8.3 ... 3.4	0 ... 29.3	15
$NaCl + CaSO_4$	$\alpha NaCl + (1\text{-}\alpha)\, CaSO_4 \cdot 2\,H_2O$	8.3 ... 2.9	0 ... 32.9	12
$CaCl_2 + MgSO_4$	$\alpha CaCl_2 \cdot 2\,H_2O + (1\text{-}\alpha)\, MgSO_4 \cdot 7\,H_2O$	0 ... 7.7	0 ... 15.4	17
$CaCl_2$ + JSC	$\alpha CaCl_2 \cdot 2\,H_2O + (1\text{-}\alpha)$ JSC Mars-1A	2.6 ... 5.1	0.3 ... 6.7	7
KCl + JSC	$\alpha KCl + (1\text{-}\alpha)$ JSC Mars-1A	2.4 ... 2.2	0.3 ... 5.4	9
NaCl + JSC	$\alpha NaCl + (1\text{-}\alpha)$ JSC Mars-1A	2.4 ... 1.1	0 ... 26.8	9

MgCl in laser-induced plasma is investigated theoretically. By contrast, the CaCl band is clearly observed for the pure $CaCl_2$ sample and exceeds the intensity of the Cl(I) signal, making it well-suited for an improved detection of chlorine. The dependence of the CaCl emission on the laser energy and the time evolution of the CaCl emission are investigated. Additionally, the laser-induced plasma is simulated numerically in order to find the temperature at which the CaCl emission is expected to appear. In the next section, the dependence of the CaCl band intensity on the concentrations of Ca and Cl in the sample is investigated in six different test series and for different measurement parameters. A model for the band intensity based on the chemical reactions of Ca, Cl, and CaCl in the plasma is derived and applied to the six test series.

A majority of the results shown in this chapter have been published in [150].

4.1 Samples and experiments

4.1.1 Samples

Various pure and mixed samples were made to investigate the molecular emissions of MgCl and CaCl. For the investigation of the MgCl emission in a sample with high concentrations of Mg and Cl, the hexahydrate of magnesium chloride was used, $MgCl_2 \cdot 6\,H_2O$. For the investigation of CaCl emission in a sample with high concentrations of Ca and Cl, the dihydrate of calcium chloride was used, $CaCl_2 \cdot 2\,H_2O$. Both substances are highly hygroscopic, so that the samples needed to be stored in a desiccator in order to avoid deliquescence of the samples.

For the investigation of the CaCl band intensity in dependence on the reactant concentrations, six test series were made, each consisting of several samples with different concentrations of Ca and Cl. An overview of the test series is given in Table 4.1. The chlorides KCl and NaCl, the sulfates $MgSO_4$ and $CaSO_4$, and the Martian regolith simulant JSC Mars-1A were selected for the mixtures. JSC Mars-1A simulates the

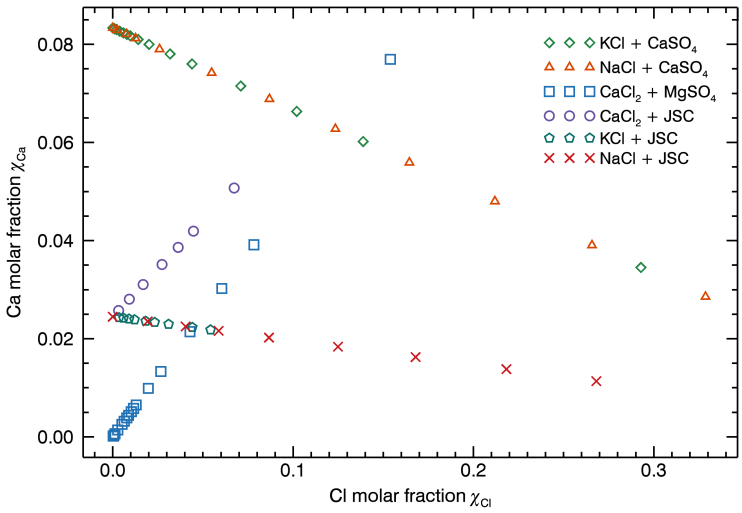

Figure 4.2: Molar fractions of Ca and Cl in the samples of the six test series, as calculated from the weight ratios of the mixed substances and their elemental compositions. In the two test series with $CaCl_2$, the molar fractions of Ca and Cl increase at the same time. For the remaining test series, the Ca molar fraction decreases for increasing Cl.

regolith found on Mars and contains feldspar that provides the equivalent of about 6.2 wt% CaO [3]. It is therefore plausible that the calcium concentration of Martian regolith alone is enough to produce CaCl emission in Martian LIBS spectra.

The series can be categorized into four *anti-correlated* and two *correlated* series. In the anti-correlated series, the Ca concentrations decrease linearly as the Cl concentrations increase, while the concentrations increase simultaneously in the correlated series (Fig. 4.2). The first anti-correlated series consists of 15 samples mixed from KCl and $CaSO_4 \cdot 2\,H_2O$ at different mixing ratios from 0 wt% to 80 wt% KCl. In order to determine whether the results are consistent for different chlorine-bearing salts, the second anti-correlated series consists of 12 mixtures of NaCl and $CaSO_4 \cdot 2\,H_2O$, in which the NaCl concentration is also varied from 0 wt% to 80 wt%. For the remaining two anti-correlated series, KCl and NaCl are again used as the chlorine-bearing salts, but the calcium-bearing component of the mixture is JSC Mars-1A instead of $CaSO_4 \cdot 2\,H_2O$. Nine samples were made for the series containing KCl, with KCl concentrations between one and 17 wt% to investigate the case of low chlorine concentrations more closely. The series consisting of NaCl and JSC Mars-1A consists of nine samples with NaCl ranging from 0 to 60 wt% in order to observe the general trend of the CaCl band intensity.

The two correlated series both contain $CaCl_2 \cdot 2\,H_2O$ at varying concentrations. In the first series it is mixed with $MgSO_4 \cdot 7\,H_2O$ in 17 samples with concentrations from zero to 80 wt%. In the second series it is mixed with JSC Mars-1A in seven samples with concentrations from one to 24 wt%. Due to the hygroscopy of the samples in

the two series, they were stored in a desiccator. Samples in the $CaCl_2 + MgSO_4$ series showed signs of deliquescence throughout the production process.

4.1.2 Measurement parameters

Measurements were made with the setup described in Chapter 3. The UV/VIS/NIR spectral range of the Aryelle Butterfly was used for all measurements. The laser repetition rate was set to 10 Hz. The laser energy was set to 22 mJ/pulse, except for the experiments in which the influence of the laser energy is investigated. Unless specified otherwise, all measurements were made under Martian atmospheric conditions in the simulation chamber, which means that the CO_2-dominant Mars-analog gas described in Chapter 3 was used as the ambient gas in the simulation chamber, with a constant pressure of about 650 Pa.

The pure $MgCl_2 \cdot 6\,H_2O$ sample was measured with different parameters in order to improve the detection of the MgCl emission. The best results were obtained by integrating over 500 laser shots while slowly moving the sample, so that each shot was on a new position on the sample. The pure $CaCl_2 \cdot 2\,H_2O$ sample and the mixtures of $CaCl_2 \cdot 2\,H_2O$ and $MgSO_4 \cdot 7\,H_2O$ were measured at three different positions on the sample for each measurement setting, with the exception of the time-resolved measurements of $CaCl_2 \cdot 2\,H_2O$, for which one measurement per delay time was made. In each measurement, 30 laser shots on the same spot were integrated spot in order to obtain a good SNR.

Due to the high uncertainties of the measurements in the $CaCl_2 + MgSO_4$ series (up to 70%, see Fig. 4.22c), the number of measurements was increased to 10 measurements per sample and per measurement setting for the remaining samples. As before, each individual measurement was integrated over 30 laser shots on the same spot.

The default settings for the time gate of the ICCD used in this thesis are a delay time of 350 ns between the laser pulse and the start of the measurement, and a gate width of 10 µs. The delay time was chosen in order to gate out the continuum emission in the early stages of the plasma, which increases the noise level considerably. The gate width was chosen because no change in the signal intensities in the LIBS spectra could be observed after 10 µs in the measurements of pure $CaCl_2 \cdot 2\,H_2O$, as will be seen in Section 4.3.5. For the time-resolved measurements in Section 4.3.5, a gate width of 500 ns was used and the delay time was varied from 150 ns before plasma initiation up to 10 µs after plasma initiation.

The six test series for the investigation of the relationship between the CaCl band intensity and the reactant concentrations were measured with an additional setting of the time gate, where no delay time was used and the gate width was increased to 3 ms. These settings are similar to those of the ChemCam instrument, which cannot make temporally resolved measurements. The purpose of these additional measurements

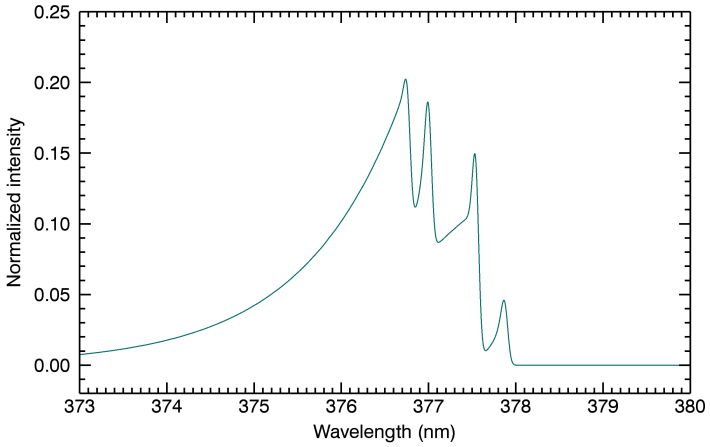

Figure 4.3: Simulated spectrum of the MgCl $A^2\Pi - X^2\Sigma^+$ (0-0) band for a temperature of 4000 K and a spectral resolution of 0.08 nm. Four branch heads can be seen at 376.7 nm, 377.0 nm, 377.5 nm, and 377.9 nm.

was to find out whether the relationship between the band intensity and the reactant concentrations changes in dependence on the measurement setting that was used, and specifically if the early plasma stages play an important role.

4.2 MgCl emission

In this study the emission of MgCl in LIBS is investigated. While there have been many spectroscopic investigations of MgCl, e.g. [70, 125, 153], there have only been few studies on its emission in LIBS. It is mentioned in a study by Gaft et al. [50] as a promising signal for the detection of Cl. A LIBS spectrum of a $MgCl_2$ sample with what the authors identified as the MgCl $A^2\Pi - X^2\Sigma^+$ band system is shown in the study. The study was performed in Earth conditions with a long delay time of 15 µs. Our publication on the detection of Cl using molecular emissions is, to my knowledge, the only other LIBS study in which the MgCl emission is investigated [150].

The primary goal of my study was to find out whether MgCl can also be observed in Martian conditions in spectra with shorter delay times than the ones used by Gaft et al. [50], and whether it can be used for the detection and quantification of Cl. The secondary goal was to confirm that the spectral features shown in their study are indeed MgCl bands, since they used a low-resolution spectrometer that could not resolve the profiles of the bands. With the high-resolution DLR LIBS setup, the rotational band structure can be resolved in more detail. By comparison to a simulated MgCl spectrum, the band can then be identified to a higher degree of certainty.

Table 4.2: Spectroscopic constants used in the simulation of the MgCl $A^2\Pi - X^2\Sigma^+$ (0-0) band, taken from Hirao et al. [70].

Constant (cm^{-1})	$X^2\Sigma^+$	$A^2\Pi$
T_0	0	26 739.9
B_0	0.244 805	0.250 826
D_0	$2.725\,81 \times 10^{-7}$	$2.669\,32 \times 10^{-7}$
A	0	54.4681

4.2.1 Simulation of the $A^2\Pi - X^2\Sigma^+$ (0-0) band

Spectroscopic constants of the $A^2\Pi$ state and the $X^2\Sigma^+$ state of MgCl have been calculated by Rostas et al. [125] and Hirao et al. [70] from investigations of the $A^2\Pi - X^2\Sigma^+$ band system, of which the (0-0) vibrational transition is the most intense and therefore most useful for the detection of Cl. In Fig. 4.3, the simulated emission spectrum of the (0-0) band is shown that was simulated using the values given by Hirao et al. [70], which are given in Table 4.2. A spectral broadening is simulated here by setting the Gaussian width to 0.08 nm. The plasma temperature used for the simulation is 4000 K, but the spectrum looks similar for temperatures of 1000 K to 8000 K. The maxima remain at the same wavelengths and only changes in the intensity distributions occur. As will be seen from the calculation of the chemical equilibrium (Fig. 4.6), the MgCl molecule is not expected to form at higher or lower temperatures.

The spectrum looks very similar to the measured spectrum by Hirao et al. [70]. It is degraded to the violet and has four intense peaks at 376.7 nm, 377.0 nm, 377.5 nm, and 377.9 nm which correspond to the four expected branch heads of a $^2\Pi - ^2\Sigma$ transition. In a LIBS measurement, the band can look slightly more complex due to the overlap of multiple $\Delta v = 0$ transitions in this wavelength range and due to the influence of MgCl isotopes [125], but the basic rotational structure should look similar to the simulated spectrum shown in Fig. 4.3. Since the closest peak observed by Gaft et al. [50] is at 375.8 nm instead of 376.7 nm, it is likely that the observed signals are not emissions of MgCl.

4.2.2 LIBS spectrum

In order to detect a clear signal of MgCl in a LIBS spectrum, a pure sample of $MgCl_2 \cdot 6\,H_2O$ was investigated, see Fig. 4.4. The measurement was conducted in Martian atmospheric conditions with a laser energy of 35 mJ/pulse. Since no MgCl bands could be identified in measurements that were averaged over 30 laser shots, the shown spectrum was averaged over 500 laser shots. The sample was moved slowly during the measurement so that each laser shot was on a new position on the sample, which prevents drilling into the sample and increases the detected intensity. This way, very

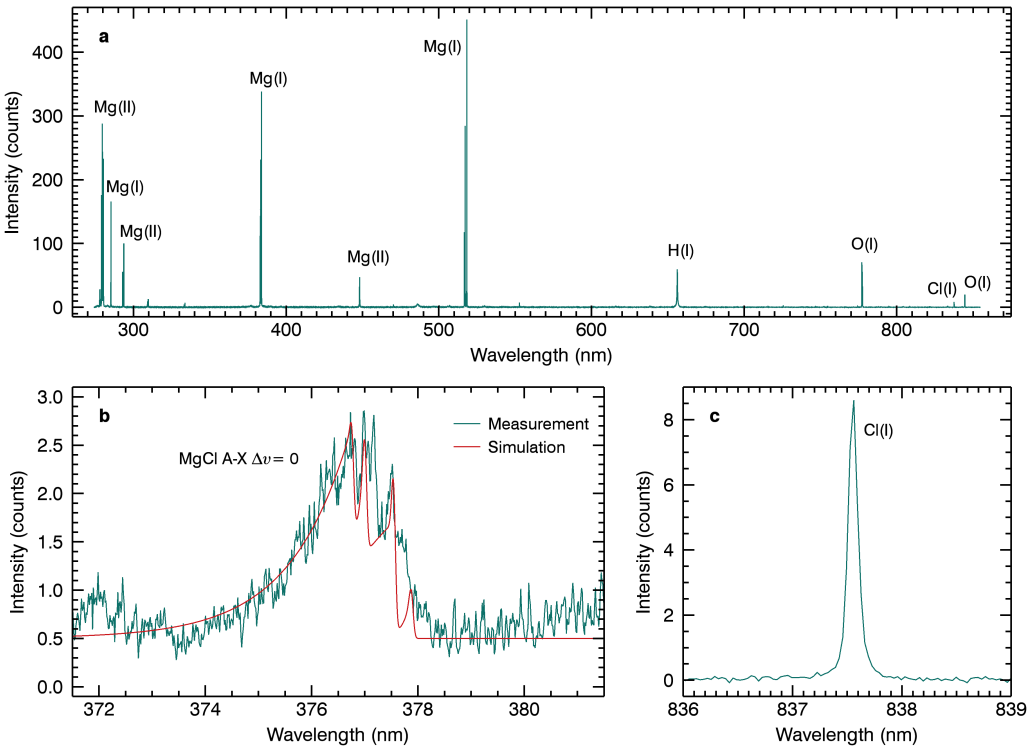

Figure 4.4: LIBS spectrum of $MgCl_2 \cdot 6\,H_2O$ in simulated Martian ambient conditions. The delay time was 350 ns and the gate width was 10 µs. In order to get a clear signal, the spectrum was averaged over 500 laser shots at different positions. a) Full measured spectrum (270–850 nm) showing strong emission lines of Mg as well as weaker lines from Cl, O, and H. b) Close-up of the MgCl band at 377 nm in comparison with the simulated spectrum. c) Cl(I) line at 837.6 nm. The maximum of the Cl(I) line is about three times higher than the that of the MgCl band.

high SNRs are achieved for the emission lines in the spectrum. The intensity values in Fig. 4.4 correspond to the average intensity counts per laser shot.

The MgCl $A^2\Pi - X^2\Sigma^+$ $\Delta\upsilon = 0$ band sequence, called the MgCl band from now on, appears in the expected wavelength range, showing signs of the four branch heads that can also be seen in the simulated spectrum. Despite the high concentration of Mg and Cl in the sample, the band is very weak, however, and the signal is very noisy. Its intensity maximum is at about 2.8 counts, whereas the Cl(I) line has a maximum value of 8.5 counts. This is despite the fact that the efficiency of the spectrometer is about three times higher at 378 nm than it is at 838 nm (see Fig. 3.2). The MgCl band is therefore clearly not useful for an improved detection of Cl in Martian atmospheric conditions. Since the study by Gaft et al. [50] was made in terrestrial atmospheric conditions, additional measurements in terrestrial atmospheric conditions were made as well in order to investigate whether the MgCl emission is stronger at a higher ambient pressure. However, no improvement of the MgCl band intensity could be observed.

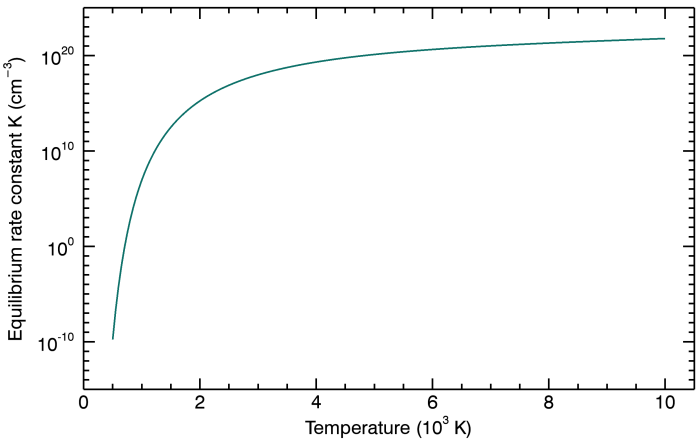

Figure 4.5: Equilibrium constant of the reaction Mg + Cl $\rightleftharpoons$ MgCl in dependence of the plasma temperature as calculated from Eq. (2.52).

4.2.3 Equilibrium plasma composition

In order to investigate why the MgCl band has a low intensity, I have calculated its number density in an idealized plasma at LTE that contains only Mg and Cl for temperatures from 500 K to 20 000 K. The molecules Mg_2 and Cl_2 are considered here as well, though their dissociation energy is lower than that of MgCl and their formation will only be relevant at low temperatures. The formation of $MgCl_2$ is neglected because no description of its energy levels was found, and because it only affects the calculation at low temperatures.

The equilibrium rate constants of the reactions were calculated from the partition functions using Eq. (2.52). The spectroscopic constants given by Huber and Herzberg [72] were used to calculate the molecular energy levels. The dissociation energies are $D_0^0(Mg_2) = 0.05\,\text{eV}$ for Mg_2 [72], $D_0^0(Cl_2) = 2.48\,\text{eV}$ for Cl_2 [72], and $D_0^0(MgCl) = 3.26\,\text{eV}$ for MgCl [69]. The equilibrium rate constant for Mg + Cl $\rightleftharpoons$ MgCl is shown in Fig. 4.5 in dependence of the temperature. It strongly increases for increasing temperatures, especially in the range between 500 K and 4000 K, indicating a shift of the equilibrium from favoring the MgCl molecule to favoring the atomic species Mg and Cl which mostly takes place in this temperature region. The equilibrium rate constant is independent from the plasma composition and from other reactions.

For the simulation of the plasma, I set the ratio of Mg to Cl to 1:2 and defined the total number density of nuclei in the plasma. According to the ideal gas law, the number density of particles in the ambient gas at a pressure of 650 Pa and at a temperature of 300 K is

$$N/V = p/(k_B T) = 650\,\text{Pa}/(1.38 \times 10^{-23}\,\text{J/K} \times 300\,\text{K}) = 1.57 \times 10^{17}\,\text{cm}^{-3}\,. \quad (4.1)$$

Since the total number density of particles in the plasma n_{tot} should be slightly higher

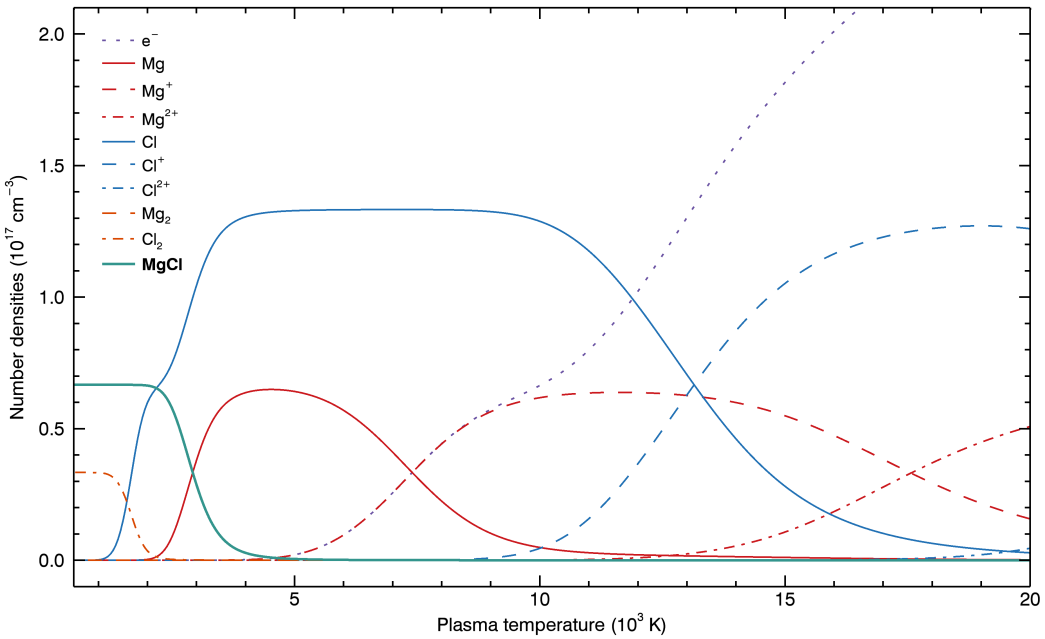

Figure 4.6: Number densities in chemical equilibrium for a simulated plasma consisting only of Mg and Cl at a ratio of 1:2, as calculated from Eqs. (2.49–2.56). The total number density of nuclei is $2 \times 10^{17}\,\mathrm{cm}^{-3}$. MgCl only forms at low temperatures below 5000 K. The formation of $MgCl_2$ at even lower temperatures is not considered here.

than the number density of particles in the ambient gas, the value of Eq. (4.1) was chosen as a lower boundary for n_{tot}. The typically observed electron densities are in the range of 10^{16}–$10^{17}\,\mathrm{cm}^{-3}$, indicating that n_{tot} should not be significantly larger than the lower boundary, so that an approximate value of $n_{\mathrm{tot}} = 2 \times 10^{17}\,\mathrm{cm}^{-3}$ was chosen for the simulation.

The calculated number densities of all considered species are shown in Fig. 4.6. The formation of Cl^- anions is not considered here, as their concentration in a simulated LTE plasma was found to be very small [136]. It can be seen that the highest concentrations of MgCl are found at low temperatures and strongly decrease between 2000 K and 5000 K, where the concentration has fallen to a negligible level. In a real plasma, the formation of $MgCl_2$ will also decrease the MgCl concentration at low temperatures, so that there is only a small temperature region in which MgCl is stable. There are also additional reactions that can take place, such as the reaction of Mg and O to MgO, which has a higher dissociation energy and should therefore be more stable than MgCl. These other reactions will reduce the number density of MgCl even further, so that the result here can be considered as an upper limit.

The intensity of the MgCl A-X band system is proportional to the number of MgCl molecules in the upper vibrational level, which is the vibrational level $v = 0$ of the $A^2\Pi$ state for the most intense band in the $\Delta v = 0$ band sequence. Figure 4.7 shows the

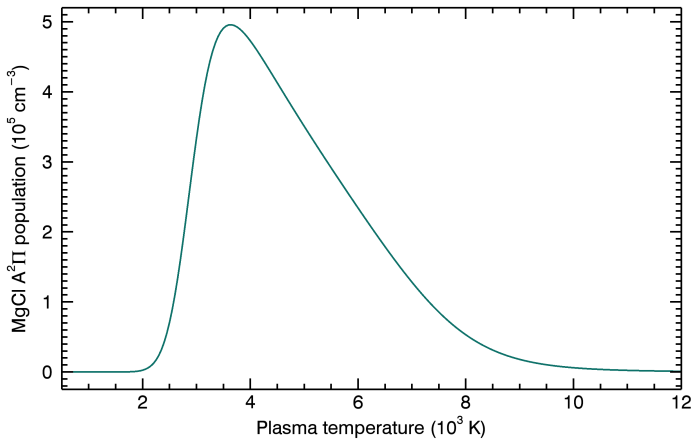

Figure 4.7: Population density of the MgCl $A^2\Pi$ $\upsilon = 0$ state as calculated from Eq. (2.7).

population density of this level in dependence of the temperature. Despite the higher number densities for MgCl at lower temperatures, the highest population densities of the upper level are found in a temperature range from 3000 K to 6000 K. A maximum value of $5 \times 10^5\,\mathrm{cm}^{-3}$ is reached at about 3500 K, which is quite low in comparison to typical plasma temperatures of more than 15 000 K. The population density of the upper level of the Cl(I) emission at 837.6 nm exceeds this value by orders of magnitude for higher temperatures, reaching $1.2 \times 10^{13}\,\mathrm{cm}^{-3}$ at 15 000 K. This indicates that the low number of molecules in the upper vibrational level of the MgCl band transition is partially responsible for the low intensity of the MgCl band. A potentially higher transition probability for the MgCl A-X emission might offset this to some extent, but I could not find any values for this in the literature.

4.3 CaCl emission for pure $CaCl_2 \cdot 2\,H_2O$

Here I investigate the emission of CaCl in LIBS spectra of pure $CaCl_2 \cdot 2\,H_2O$ with a focus on the $\Delta\upsilon = 0$ band sequence of the $A^2\Pi$–$X^2\Sigma^+$ band system. This band sequence is the CaCl emission with the highest intensity and is therefore the most suitable one for the detection of Cl. The individual bands within the sequence are superimposed, so that they appear as a single spectral feature. This spectral feature is simply called the *CaCl band* or the *CaCl A-X band* in this thesis as long as a more accurate distinction is not necessary.

In contrast to the MgCl band in Section 4.2, the CaCl band is quite intense. It has also been observed in Martian LIBS spectra by ChemCam [44, 50], and is often more intense than the atomic and ionic Cl emissions in the corresponding spectra. In this section, the CaCl band intensity is investigated in a simple $CaCl_2$ sample matrix in order to understand its dependence on the laser energy and its evolution over time.

Table 4.3: Spectroscopic constants used in the simulation of the CaCl A-X band spectrum.

Constant	$X^2\Sigma^+$	$A^2\Pi$	References
T_e (cm^{-1})	0	$1.613\,08 \times 10^4$	[41, 72]
ω_e (cm^{-1})	3.6753×10^2	$3.704\,78 \times 10^2$	[41, 72]
$\omega_e x_e$ (cm^{-1})	1.31	1.448	[41, 72]
B_e (cm^{-1})	0.152 230 17	0.154 239 3	[41, 72]
α_e (cm^{-1})	7.9896×10^{-4}	8.715×10^{-4}	[41, 72]
D_e (cm^{-1})	1.029×10^{-7}	1.0536×10^{-7}	[41, 72]
A (cm^{-1})	0	70.603	[41, 72]
r_e (Å)	2.4367	2.4219	[117]
k_e (Ncm^{-1})	1.52	1.54	[117]
E_e (cm^{-1})	3.3×10^4	1.7×10^4	[72]

4.3.1 Simulation of the CaCl A-X band

The spectroscopic constants of CaCl have been investigated in multiple studies, e.g. [41, 72, 95]. For the simulation of the CaCl A-X band, I have used the values for the $A^2\Pi$ state and the $X^2\Sigma^+$ state that were measured by Ernst et al. [41], which are to my knowledge the most recent experimental values available. However, since the vibrational constants were only given as differences between the A state and the X state, I have used the values by Huber and Herzberg [72] for the X state. The constants r_e and k_e were taken from Radzig and Smirnov [117] and $E_e \approx D_0^0/hc - T_e$ was calculated from the dissociation energy $D_0^0 = 4.1\,\text{eV}$ [72]. Based on these constants, the first seven vibrational transitions were calculated.

The result can be seen in Fig. 4.8a for a plasma temperature of 4000 K and a

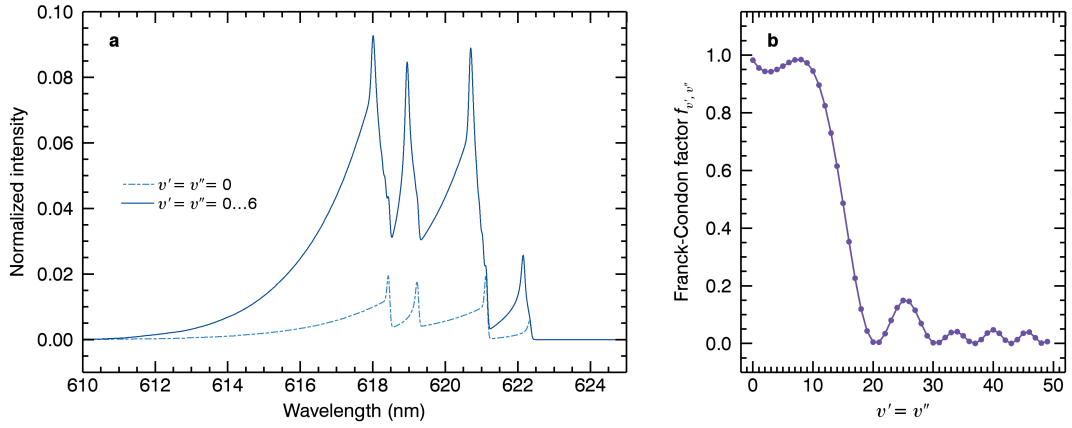

Figure 4.8: a) Simulated spectrum of the CaCl A-X (0-0) band and of the $\Delta v = 0$ band sequence up to $v' = v'' = 6$. A spectral resolution of 0.08 nm was simulated and the temperature was set to 4000 K. b) Calculated Franck-Condon factors for $\Delta v = 0$ transitions based on the overlap integral of the eigenfunctions of a Morse potential.

Gaussian width of 0.08 nm. The simulated spectra of the (0-0) band and of the $\Delta v = 0$ sequence up to $v' = v'' = 6$ are shown. The comparison makes it clear that it is not sufficient to just consider the (0-0) band alone. Since the Franck-Condon factors remain relatively high up to about $v' = v'' = 15$, as shown in Fig. 4.8b, the influence of the higher vibrational transitions on the band profile is strong and cannot be neglected. The peaks of the band sequence are shifted towards lower wavelengths and the band edges are less steep. Furthermore, the intensity of the band rises considerably.

Only seven vibrational transitions could be considered here, but Fig. 4.8 suggests that up to 15 vibrational transitions should be considered in order to get an accurate representation of the CaCl A-X $\Delta v = 0$ band sequence. However, this also increases the uncertainty of the simulation due to uncertainties in the spectroscopic constants, where the available data is usually only accurate for a small number of low-lying vibrational levels. The Franck-Condon factors will also be less accurate for higher vibrational transitions as the Morse potential becomes more inaccurate.

Since about 24% of all Cl on Earth occurs as the isotope ^{37}Cl, I considered including the molecular isotope Ca^{37}Cl in the simulations as well. However, ^{35}Cl is about 3.2 times more abundant than ^{37}Cl, so that the relative intensity of the strongest transition of the molecular isotope will also be weaker by that factor, which is equivalent to having a Franck-Condon factor of about 0.31. Since there are 16 vibrational transitions of Ca^{35}Cl with a higher Franck-Condon factor according to Fig. 4.8b, the effect of the isotope on the band profile is insignificant and can be neglected.

4.3.2 Equilibrium plasma composition

The equilibrium plasma composition of a $CaCl_2$ plasma was calculated in the temperature range from 500 K to 20 000 K. In addition to atomic and ionic species, the molecules Ca_2, Cl_2, CaCl, and $CaCl_2$ were considered as well. The constants used to calculate the energy levels of the diatomic molecules were taken from [72], while the constants for $CaCl_2$ were taken from [80]. The dissociation energies are $D_0^0(Ca_2) = 0.4\,\text{eV}$ for Ca_2 [159], $D_0^0(Cl_2) = 2.48\,\text{eV}$ for Cl_2 [72], $D_0^0(\text{CaCl}) = 4.08\,\text{eV}$ for CaCl [69], and $D_0^0(CaCl_2) = 9.1\,\text{eV}$ for the total dissociation of $CaCl_2 \longrightarrow Ca + 2\,Cl$ [69]. The ionization energies of Ca and Cl were taken from the NIST database [118].

The equilibrium constants for CaCl and $CaCl_2$ as calculated from Eq. (2.52) are shown in Fig. 4.9. As expected they both strongly increase for increasing temperatures, indicating that the equilibrium is closer to the original reactants instead of the product at high temperatures.

For the simulation of the plasma, the ratio between Ca and Cl was set to 1:2 and a total number density of nuclei of $2 \times 10^{17}\,\text{cm}^{-3}$ was chosen again as in Section 4.2.3. The calculated number densities in dependence of the temperature are shown in Fig. 4.10. Neither Ca_2 nor Cl_2 are formed in significant concentrations. In-

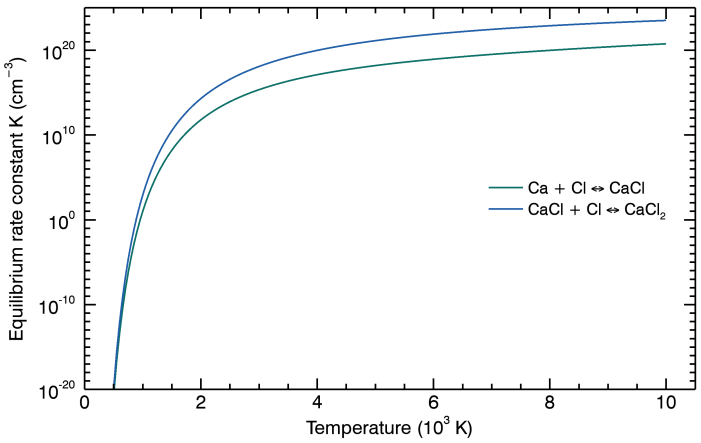

Figure 4.9: Equilibrium rate constants of the reactions Ca + Cl $\rightleftharpoons$ CaCl and CaCl + Cl $\rightleftharpoons$ $CaCl_2$ in dependence of the temperature as calculated from Eq. 2.52.

stead, all nuclei are bound in $CaCl_2$ molecules at low temperatures. Starting at about 2000 K, these molecules dissociate to CaCl and to free atomic species of Cl. The potential formation of Cl^- anions in the plasma is again neglected in accordance with the results by Shabanov and Gornushkin [136]. As the CaCl molecules dissociate, which

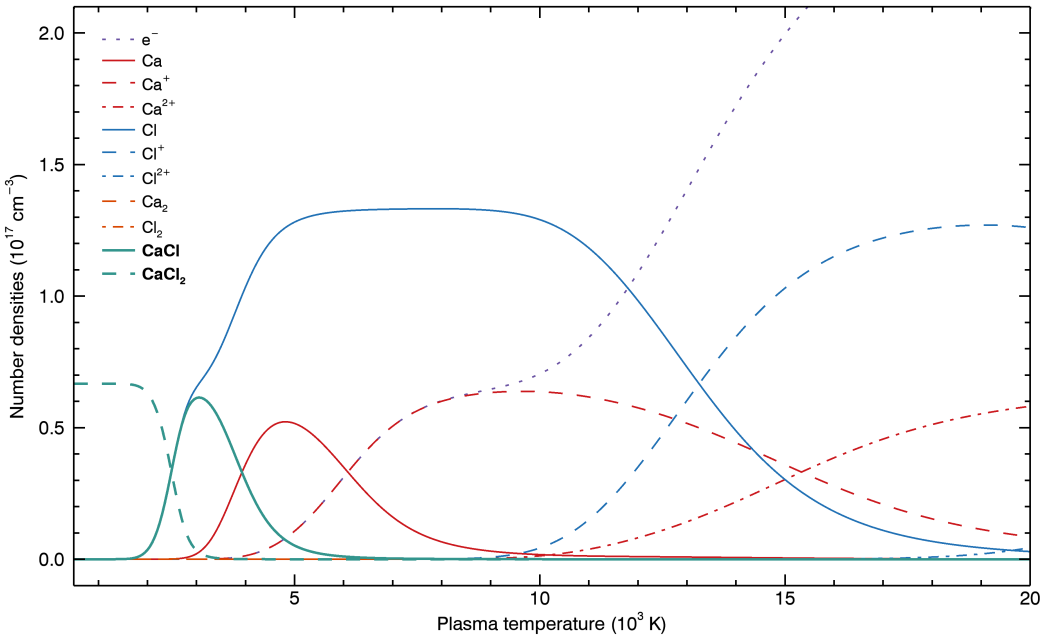

Figure 4.10: Number densities of species in a $CaCl_2$ plasma at equilibrium in dependence of the temperature, as calculated from Eqs. (2.49–2.56). The total number density of nuclei was set to $2 \times 10^{17}\,\mathrm{cm}^{-3}$. At low temperatures, all atoms are bound in $CaCl_2$ molecules. The highest CaCl concentrations are found between 2000 K and 5000 K.

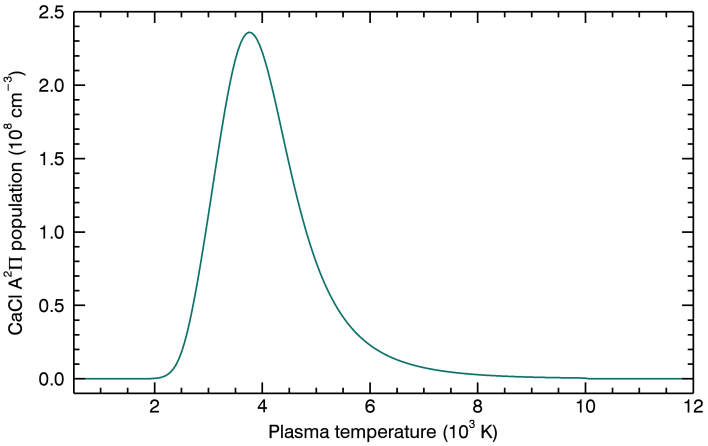

Figure 4.11: Population density of the $A^2\Pi$ $\upsilon = 0$ state of CaCl in dependence of the temperature as calculated from Eq. (2.7).

starts around 3000 K, free Ca atoms are formed in the plasma as well. Due to the low ionization energy of Ca, $I(\mathrm{Ca}) = 6.1\,\mathrm{eV}$, Ca^+ ions are formed very soon, so that the Ca^+ concentration exceeds the Ca concentration already at about 6000 K. By contrast, the high ionization energy of Cl, $I(\mathrm{Cl}) = 13.0\,\mathrm{eV}$, means that Cl^+ ions can only be observed at high temperatures, since the Cl^+ concentration exceeds the Cl concentration only above 10 000 K.

The population density of the vibrational level $\upsilon = 0$ of the $A^2\Pi$ state of CaCl is shown in Fig. 4.11 in dependence of the temperature. As in Section 4.2.3, this indicates at which temperatures the CaCl emission is expected according to equilibrium calculations. The corresponding temperature range roughly goes from 3000 K to 5000 K. The CaCl emission is therefore expected to appear only in the colder outer periphery of the plasma or in the later plasma stages when the temperature has decreased sufficiently. The maximum value of about $2.4 \times 10^8\,\mathrm{cm}^{-3}$ is almost 500 times higher than the maximum value that was calculated for MgCl (Fig. 4.7), indicating that the CaCl A-X band intensity will be significantly higher than the MgCl A-X band intensity and thus better suited for the detection and quantification of Cl.

4.3.3 Measured band spectrum of CaCl

Figure 4.12 shows the LIBS spectrum of pure $CaCl_2 \cdot 2\,H_2O$ measured in Martian atmospheric conditions. The most intense lines in the spectrum are Ca emission lines, with weaker lines from Cl, O, and H. Additionally, the A-X and B-X band systems of CaCl can be observed at 618 nm and at 593 nm, respectively. The CaCl A-X $\Delta\upsilon = 0$ band sequence is very intense, confirming the result from the simulation. The most intense CaCl B-X band sequence is weaker than the most intense CaCl A-X band sequence, which is in part due to the efficiency of the spectrometer which is 40% lower in the

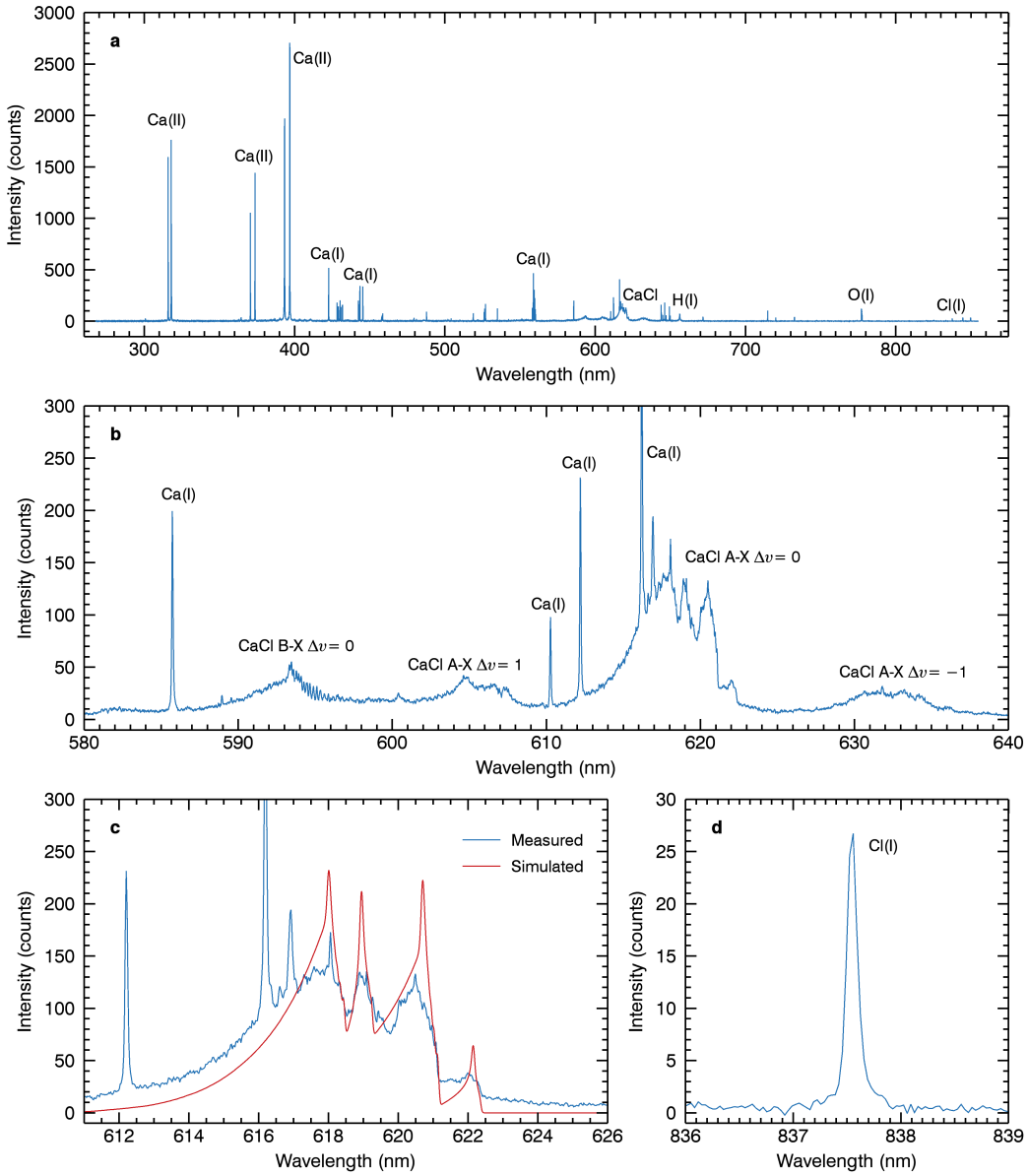

Figure 4.12: LIBS spectrum of pure $CaCl_2 \cdot 2\,H_2O$ measured in Martian atmospheric conditions with a pulse energy of 35 mJ, a delay time of 350 ns and a gate width of 10 µs. The spectrum is averaged over three measurements that were integrated over 30 shots each. a) Total spectrum from 270 nm to 850 nm showing strong Ca(I) and Ca(II) lines as well as the CaCl A-X band at 618 nm, the H_α line at 656.3 nm, and the O(I) triplet at 777 nm. b) CaCl A-X and B-X band systems. Of the A-X band system, the band sequences $\Delta v = 1$, $\Delta v = 0$, and $\Delta v = 1$ can be seen at 605 nm, 618 nm, and 632 nm, respectively. c) Comparison between the measured CaCl A-X band and the simulated one. d) Cl(I) line at 837.6 nm.

spectral range of the B-X band than it is around the A-X band. The lower SNR of the B-X band in these LIBS spectra is the main reason why I focus on the A-X band in this thesis.

The measured CaCl A-X band has a very similar structure to the simulated one (Fig. 4.12c). The total intensity of the simulated spectrum was increased here for the comparison. The edges towards higher wavelengths correspond especially well to the measurement, and the similar curve of the rising band at lower wavelengths as well as the similar relative intensities of the peaks could indicate that the temperature of the simulation is approximately correct. However, the exact shape of the measured band could not be predicted by the simulation. The peaks of the simulated spectrum are too steep, the valley at 619 nm is shifted to a lower wavelength, and in general there seem to be more irregularities in the measured band spectrum that cannot be explained by the noise of the measurement. The differences might be explained by slightly inaccurate spectroscopic constants or inaccurate values for the Franck-Condon factors, but the largest influence is likely the lack of additional vibrational transitions. This makes the CaCl A-X band ill-suited for fitting with a simulated spectrum, since a correct simulation requires a large number of parameters that are not well-known.

The Cl(I) line at 837.6 nm is significantly weaker than the CaCl A-X band, as can be seen in Fig. 4.12d. Its maximum is at nearly 27 counts, while the maximum of the CaCl band is at about 160 counts, so that the CaCl A-X band is roughly six times more intense. This shows the potential of using the CaCl band for Cl quantification.

4.3.4 Energy variation

The LIBS spectrum of $CaCl_2 \cdot 2\,H_2O$ was measured using different laser energies from 1.2 mJ/pulse to 50.7 mJ/pulse. The intensities of the CaCl A-X band, the Ca(I) line at 431.9 nm, the Cl(I) line at 837.6 nm, and the Ca(II) line at 373.7 nm are shown in Fig. 4.13, again measured with a delay time of 350 ns and a gate width of 10 µs. While the intensity increases for all signals as the energy is increased, a clear saturation effect can be observed for the CaCl band and the Ca(I) line. The Cl(I) line and the Ca(II) line do not seem to be affected by this saturation and show a nearly linear relationship. This suggests that the saturation is stronger for emissions at lower temperatures, where neutral Ca and CaCl are most abundant (see Fig. 4.10).

In order to investigate whether the plasma temperature rises for increasing laser energies, the plasma temperature was calculated from Boltzmann plots using the Ca(II) lines at 315.9 nm, 317.9 nm, 370.6 nm, 373.7 nm, and 849.8 nm. These lines were chosen because they are only minimally self-absorbed and because they are more intense than any Cl(II) lines. An example for a Boltzmann plot is shown in Fig. 4.14a, and the calculated temperature values for the different laser energies are shown in Fig. 4.14b, where the two laser energies below 2 mJ/pulse had to be omitted because no good line

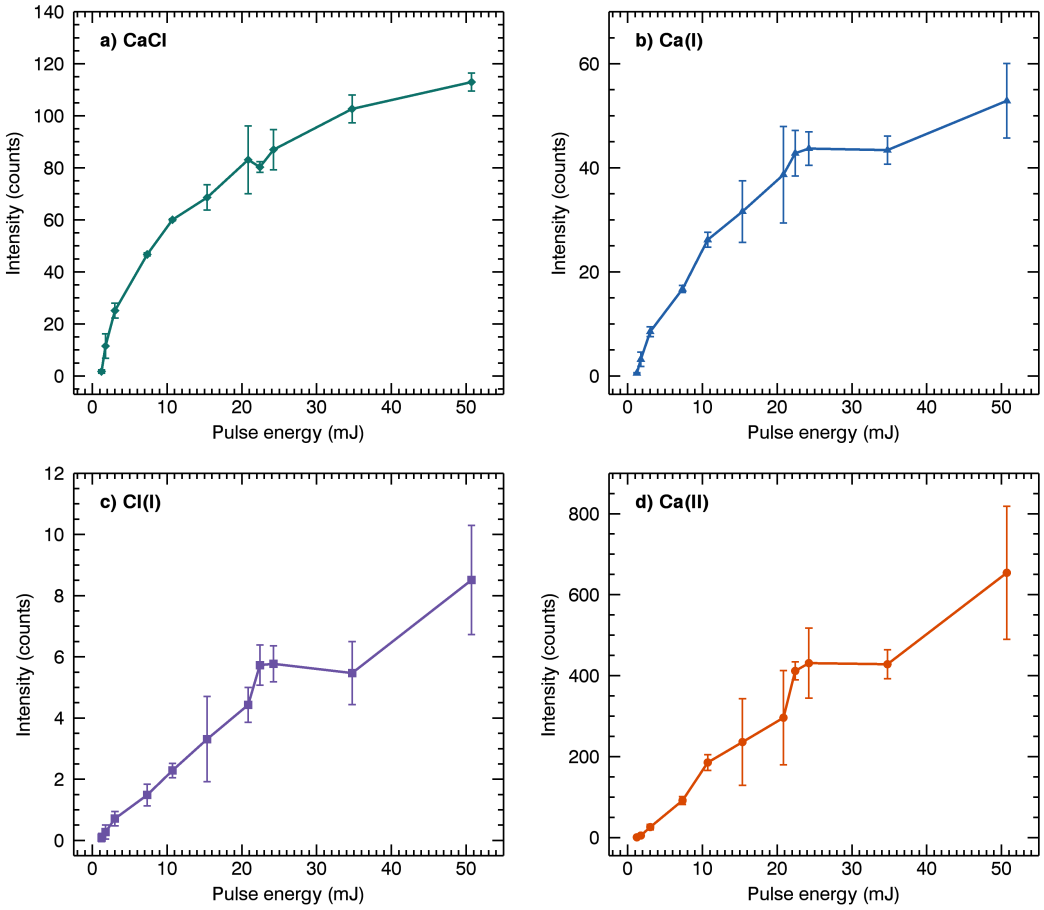

Figure 4.13: Dependence of signals in the spectrum of $CaCl_2 \cdot 2\,H_2O$ on the laser energy, measured with a delay time of 350 ns and a gate width of 10 µs. a) CaCl A-X band at 618 nm. b) Ca(I) line at 431.9 nm. c) Cl(I) line at 837.6 nm. d) Ca(II) line at 373.7 nm. The confidence intervals correspond to the standard deviations from three measurements per laser energy.

intensities could be obtained. The confidence intervals correspond to the 1σ uncertainties calculated from the linear fit of the Boltzmann plot. No trend can be observed for increasing laser energies. The temperature stays constant at $T = (14\,400 \pm 2200)\,\mathrm{K}$. While initially surprising, this result agrees with the results by Yalçin et al. [160], who also found that the plasma temperature is not strongly affected by the laser energy. The results indicate that the increasing laser energy mostly results in a stronger ablation rate and therefore a larger number of particles in the plasma.

The electron density n_e was calculated from the line width of the H_α line by fitting a Voigt profile to the line, see Fig. 4.14c. The results are shown in Fig. 4.14d, where the confidence intervals correspond to the 1σ uncertainties of the fit. The relative uncertainties are below 3% for all electron densities measured at laser energies above 7 mJ/pulse. The two lowest laser energies are omitted again, since no fit could be

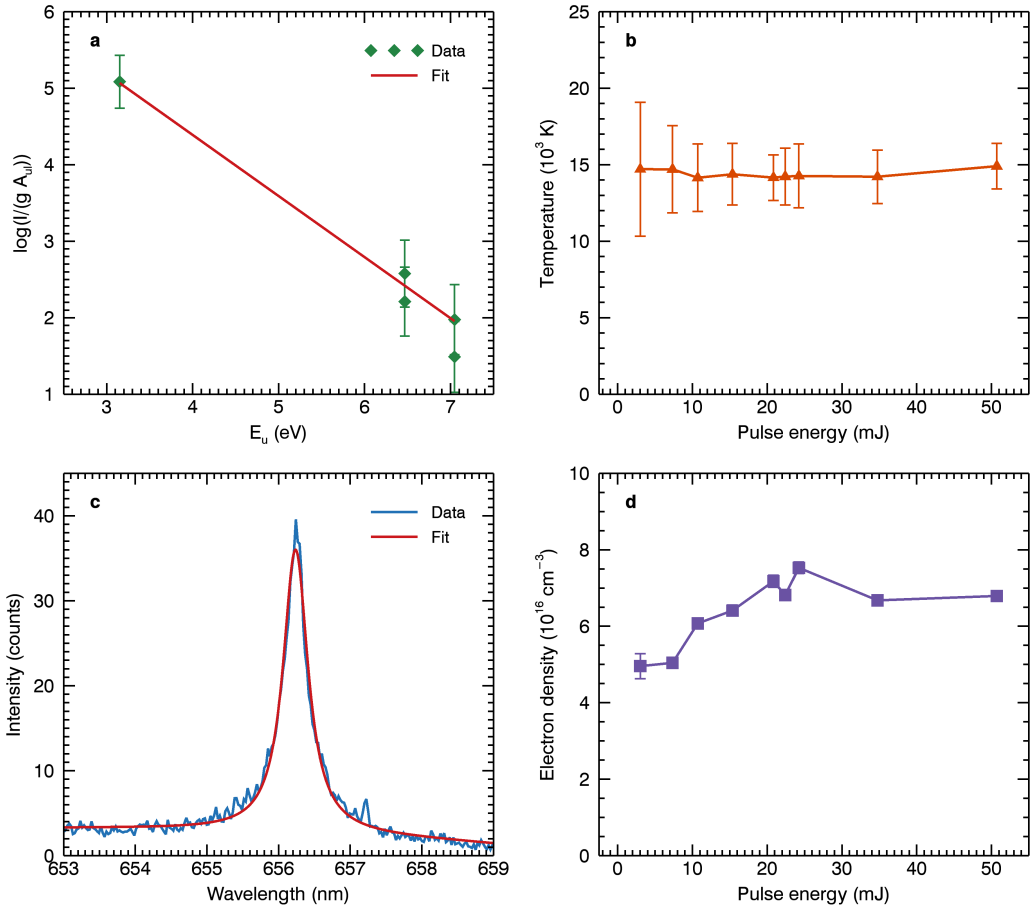

Figure 4.14: a) Example of a Boltzmann plot of five Ca(II) lines from the spectrum measured with a pulse energy of 15.4 mJ. The slope of the fit is proportional to the reciprocal of T, see Eq. (2.9). b) T values in dependence of the laser energy. No temperature values could be obtained for the two lowest pulse energies (1.2 mJ and 1.8 mJ). c) H_α line measured with a pulse energy of 15.4 mJ and fitted with a Voigt profile. From the width of the Lorentzian contribution, the electron density is calculated using Eq. (2.5). d) Electron density in dependence of the pulse energy. No electron densities could be obtained for the two lowest pulse energies (1.2 mJ and 1.8 mJ).

obtained. The electron density seems to increase slightly between 3 mJ/pulse and 24 mJ/pulse, but stays constant afterwards.

Since the temperature evaluation indicates that the ablation rate is higher at high laser energies, the electron density should increase for increasing laser energies if nothing else changes in the plasma plume. A nearly constant electron density instead means that the plasma volume has to increase. This is plausible since the pressure of the plasma plume during its expansion will be stronger for higher ablation rates. The equilibrium between the ambient pressure and the plasma pressure will then be attained at a larger plasma volume, in which the number densities are again similar to those of a plasma

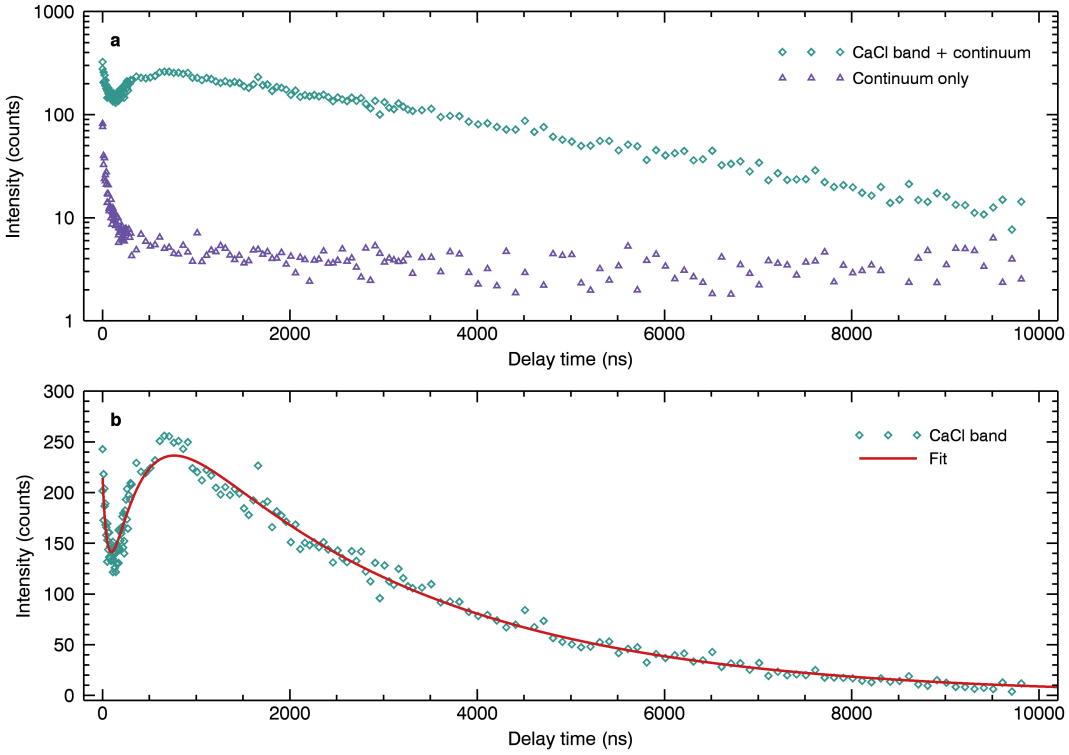

Figure 4.15: a) Time evolution of the CaCl band signal and the continuum signals from LIBS spectra of $CaCl_2 \cdot 2\,H_2O$. The delay time was varied in steps of 10 ns, the gate width was constant at 500 ns. b) CaCl band signal after subtracting the continuum signal. The signal is fitted with the sum of an exponential function and a reaction kinetics model, see Eqs. (4.4a)–(4.9).

plume that is created at lower laser energies. This hypothesis is supported by the study of Harilal et al. [63], who observed an increase of the plasma size in dependence of the laser energy. If it is mostly the hot plasma center that grows in size, the colder periphery where the neutral Ca and CaCl are formed will be relatively smaller. This might explain the observed saturation effect in Fig. 4.13 and why it mostly appears for signals which have their highest emission at low temperatures.

4.3.5 Time evolution

Figure 4.15a shows the time evolution of the measured CaCl band intensity in the LIBS spectrum of $CaCl_2 \cdot 2\,H_2O$ as well as the time evolution of the continuum signal, which was measured in the range of 685–695 nm. The time shown on the x-axis is the delay time of the ICCD gate, with the origin set to the time of the laser ablation. The CaCl band intensity shown here still includes a contribution from the continuum, but it can be seen in the logarithmic representation of the two signals that the time evolution of the CaCl band signal is different from that of the continuum. This means that the

decreasing band intensity in the first 100 ns is not caused by the decreasing continuum, but instead is the CaCl band intensity itself that is decreasing. After subtracting the continuum intensity from the band intensity, the signal still shows a decreasing trend in the first 100 ns, as can be seen in Fig. 4.15b. Afterwards it starts increasing up until about 700 ns after plasma initiation, where it reaches its global maximum. The signal then proceeds to decrease slowly until it has nearly dropped to zero at 10 µs. This trend is interesting and seems to be related to several processes affecting the band intensity. It cannot be described by a simple model of a homogeneous plasma in LTE, in which the intensity would be strongly tied to the dependence of the CaCl concentration on the plasma temperature as described by the equilibrium plasma composition (Fig. 4.10). Instead, it suggests a dominant influence of reaction kinetics within the plasma on the CaCl band intensity.

The fit shown in Fig. 4.15b is the sum of two processes: the rapid diffusion of an initial high CaCl concentration, and the slow formation of CaCl via reaction kinetics. The former was modeled with an exponential term that describes the initial decay in the first 100 ns. The latter was modeled as a system of two successive reactions:

$$\mathrm{A} + \mathrm{B} \xrightarrow{\mathrm{k_1}} \mathrm{AB}^* \tag{4.2}$$

$$\mathrm{AB}^* \xrightarrow{\gamma \mathrm{k_2}} \mathrm{AB} \tag{4.3}$$

Here A and B are the reacting elements, and AB* is a highly energetic precursor of molecule AB which cannot be observed in the measurement, while AB is in a state that can be observed by the molecular emission, i.e. the $A^2\Pi$ electronic state in this experiment. The concentration of third bodies M that are involved in the reactions, which can be any plasma species, is assumed to be nearly constant within the time frame of the reactions, so that it is neglected here. The formation of AB* from A and B is dependent on the rate constant k_1, while the transition from AB* to AB is described by γk_2. The concentrations of all reactants and products decrease over time due to the diffusion of the plasma. Since the lines of Ca and Cl seem to decay with similar rate constants in the time-resolved measurements and the masses of Ca and Cl are similar, I assume that the diffusion of A and B is governed by the same rate constant k_0. Molecules AB* either diffuse or transition to AB, which in total is governed by a rate constant k_2. The fraction of k_2 that governs the diffusion of AB* is $(1-\gamma)k_2$. AB diffuses with the rate constant k_3. The corresponding rate equations are

$$\frac{d}{dt} n_A = -k_1 n_A n_B - k_0 n_A \,, \tag{4.4a}$$

$$\frac{d}{dt} n_B = -k_1 n_A n_B - k_0 n_B \,, \tag{4.4b}$$

$$\frac{d}{dt} n^*_{AB} = k_1 n_A n_B - k_2 n^*_{AB} \,, \tag{4.4c}$$

$$\frac{d}{dt} n_{AB} = \gamma k_2 n^*_{AB} - k_3 n_{AB} \,. \tag{4.4d}$$

Assuming that the formation of AB* has a negligible effect on the concentrations of A and B in comparison to the more dominant diffusion term with the constant k_0, their concentrations are approximated as

$$n_A(t) \approx A_0 e^{-k_0 t}\,, \tag{4.5a}$$

$$n_B(t) \approx B_0 e^{-k_0 t}\,. \tag{4.5b}$$

With these relations, Eq. (4.4c) can be solved, and the concentration of AB* is found to be

$$n^*_{AB}(t) = \frac{k_1 A_0 B_0}{2k_0 - k_2}\left(e^{-k_2 t} - e^{-2k_0 t}\right)\,. \tag{4.6}$$

The integration constant was chosen so that $n^*_{AB}(0) = 0$. Inserting Eq. (4.6) into Eq. (4.4d) yields

$$n_{AB}(t) = \frac{\gamma k_1 k_2 A_0 B_0}{2k_0 - k_2}\left(\frac{e^{-k_3 t} - e^{-k_2 t}}{k_2 - k_3} - \frac{e^{-k_3 t} - e^{-2k_0 t}}{2k_0 - k_3}\right)\,. \tag{4.7}$$

Again, the value of the integration constant was chosen so that $n_{AB}(0) = 0$. While $n_{AB}(0) > 0$ could also be assumed due to the observation of a non-zero CaCl concentration at $t = 0$, this does not lead to a good fit of the observed time evolution. The high initial CaCl band intensity decreases at a faster rate than the intensity in the later plasma stages does, so that it needs to be considered separately. This indicates that the CaCl molecules that are responsible for the initial high intensity do not interact with the chemical reactions, potentially due to a spatial separation within the plasma. The initial CaCl concentration is therefore modeled as an exponential decay

$$n_{\mathrm{exp}}(t) = c_0 e^{-k_4 t}\,, \tag{4.8}$$

and the CaCl band intensity is

$$I_{\mathrm{CaCl}}(t) \propto n_{AB}(t) + n_{\mathrm{exp}}\,. \tag{4.9}$$

The time t is the time after plasma initiation. Integrating Eq. (4.9) over the time gate of 500 ns then leads to a function that can be used to fit the measured band intensities as seen in Fig. 4.15b.

The obtained values for the fit parameters are shown in Table 4.4. Fig. 4.16a shows the resulting time evolution of the concentrations n^*_{AB} and n_{AB}, and the time evolution of the CaCl concentration is shown in Fig. 4.16b. Ca and Cl react quickly to CaCl*, as indicated by the early maximum of n^*_{AB} at about 240 ns after plasma initiation. However, the necessary transition to the $A^2\Pi$ state introduces a delay, so that the maximum intensity of the A-X emission is only reached at about 980 ns after plasma initiation. At that point, the concentrations of Ca and Cl have decreased so much that nearly no new CaCl molecules are formed. The subsequent time evolution of the

Table 4.4: Fit parameters for the time evolution of the CaCl band intensity.

Parameter	Value
$a\gamma k_1 A_0 B_0$ (counts/s)	$(2.7 \pm 0.2) \times 10^6$
ac_0 (counts/s)	$(2.6 \pm 0.3) \times 10^9$
k_0 (s^{-1})	$(2.1 \pm 0.2) \times 10^6$
$k_2 = 2k_0$ (s^{-1})	$(4.2 \pm 0.3) \times 10^6$
k_3 (s^{-1})	$(3.7 \pm 0.2) \times 10^5$
k_4 (s^{-1})	$(2.1 \pm 0.2) \times 10^7$

band intensity then only depends on the decay rate k_3, which is most likely related to the plasma expansion and cooling. The intensity from $n_{\mathrm{exp}}(t)$ accounts for about 7% of the total intensity of the CaCl band, indicating that CaCl molecules that were potentially formed due to fragmentation of the sample can have an influence on the measured signal intensity.

Within its uncertainty, $k_2 = 2k_0$. Indeed, the same results can be obtained if Eq. (4.7) is derived using this assumption. This result can be explained by the fact that the CaCl molecule has about twice the momentum of the Ca and Cl atoms, resulting in a diffusion rate that is twice as high. The rate constant γk_2 for the transition to the

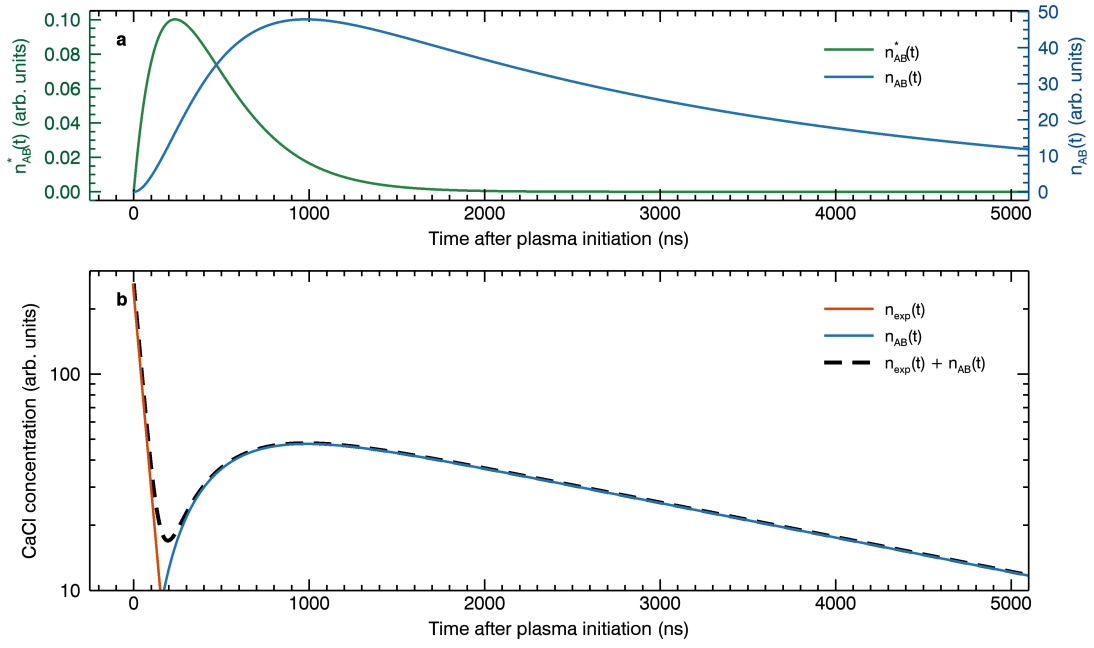

Figure 4.16: Time evolution of the CaCl concentration based on the fit of the CaCl A-X emission with Eq. (4.9). a) Formation of CaCl* and CaCl over time via chemical reactions. CaCl* reaches its highest population after 240 ns, while the highest CaCl population is reached after 980 ns. b) Total CaCl $A^2\Pi$ population from the sum of the exponential decay and the formation from chemical reactions.

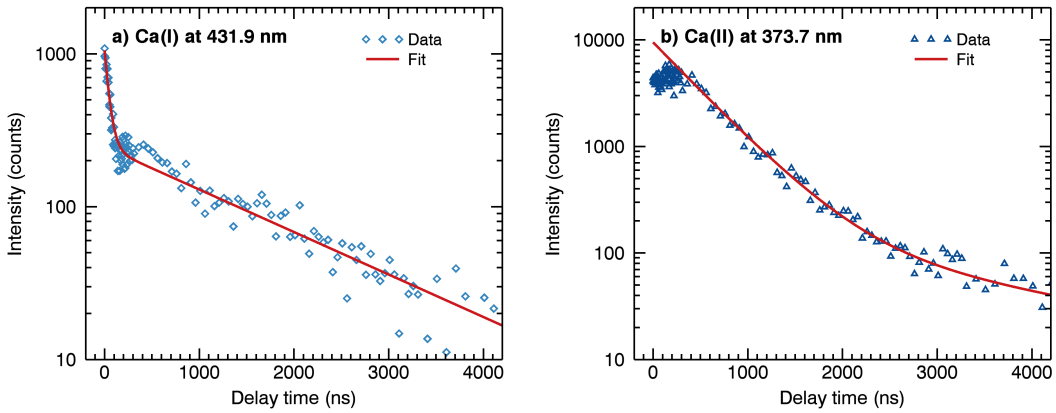

Figure 4.17: Time-resolved Ca line intensities fitted with the sum of two exponential functions. The rate constants k_0, k_3, and k_4 from the fit of the CaCl band intensity (Table 4.4) also describe the time evolution of these signals. a) Ca(I) line at 431.9 nm with a quick initial decay governed by the rate constant k_4 and a new rate constant k_5. b) Ca(II) line at 373.7 nm, which decreases with the rate constants k_0 and k_3.

lower state does not seem to influence this rate strongly, so that γ is likely relatively small. Molecules that transition to a lower energy state lose energy in the process, which could explain the slower decrease of the CaCl concentration with the rate k_3.

The rate constants obtained from the fit of the CaCl band intensity also describe the time evolution of the Ca lines, as shown in Fig. 4.17. Both the Ca(I) line at 431.9 nm and the Ca(II) line at 373.7 nm were fitted with the sum of two exponential decay functions. The same fast initial decay that was observed for the CaCl emission can also be seen for the Ca(I) line and is described by the same rate constant $k_4 = (2.1 \pm 0.2) \times 10^7\,\mathrm{s}^{-1}$. It is likely that the ablation process that produces a high initial CaCl concentration also produces a high initial concentration of neutral Ca. As the plasma then heats up rapidly, these species, which are only stable at low temperatures, disappear: the CaCl molecules dissociate and the Ca atoms are ionized. The dominant rate constant at larger delay times for Ca(I) is $k_5 = (6.4 \pm 0.4) \times 10^5\,\mathrm{s}^{-1}$, which does not seem to be related to a rate constant of the CaCl evolution and could instead be a general

Table 4.5: Fit parameters for the time evolution of the Ca(I) and Ca(II) lines, fitted with the sum of two exponential decay functions.

Line	Amplitudes (counts)	Decay constants (s^{-1})
Ca(I) at 431.9 nm	$(8.1 \pm 0.2) \times 10^2$	k_4
	$(2.5 \pm 0.1) \times 10^2$	$k_5 = (6.4 \pm 0.4) \times 10^5$
Ca(II) at 373.7 nm	$(9.3 \pm 0.2) \times 10^3$	k_0
	$(1.8 \pm 0.3) \times 10^2$	k_3

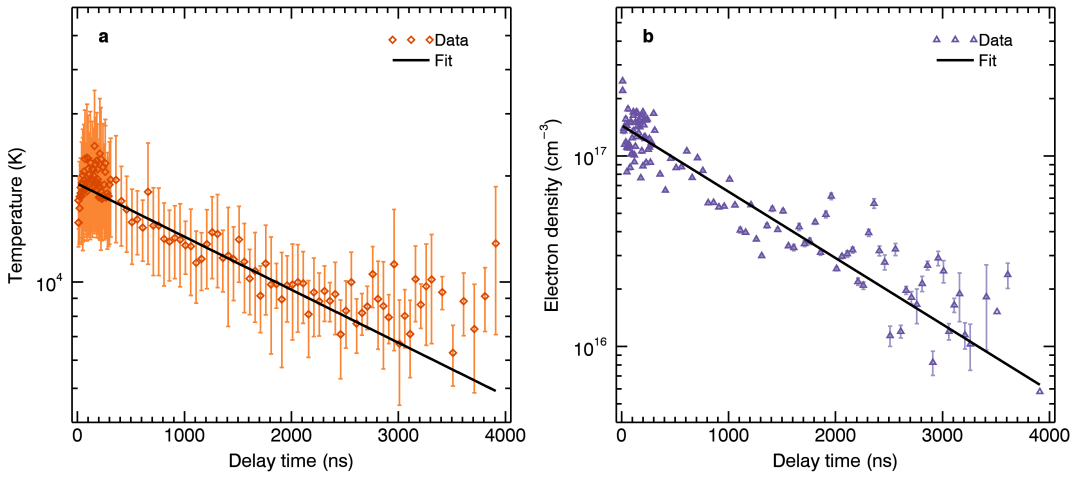

Figure 4.18: a) Time-resolved plasma temperature of $CaCl_2 \cdot 2\,H_2O$ as calculated from Boltzmann plots of Ca(II) lines. b) Time-resolved electron density as calculated from the H_α line width. Both are fitted with an exponential decay function.

diffusion and cooling process. However, the decrease of the Ca(II) line intensity can be fitted very accurately with the rate constants k_0 and k_3. In the model, k_0 determines the decay of the Ca and Cl concentrations. Since the CaCl formation takes place in the early plasma, it is reasonable that it mostly depends on the ionic concentrations. The good fit of k_3 for the later delay times could be an indication that k_3 represents a general process in the plasma after a pressure equilibrium with the ambient gas has been reached. This process could be a slow diffusion of the plasma plume or the cooling of a nearly stationary plasma. The fit constants for the Ca(I) line and for the Ca(II) line are summarized in Table 4.5.

Temperature and electron density Temperature T and electron density n_e were calculated for all time-resolved measurements in the same way as in Section 4.3.4. Their time evolution is shown in Fig. 4.18. The results could only be evaluated up to 4 µs because the SNR in spectra with higher delay times was too low. Both T and n_e were fitted with an exponential decay function to obtain the general trend. The fit parameters can be found in Table 4.6.

The order of magnitude of n_e relative to T is comparable to the values that were

Table 4.6: Fit parameters for the time evolution of the temperature and of the electron density, which were fitted with a single exponential decay function.

Plasma parameter	Amplitude	Decay constant (s^{-1})
Temperature T	$(1.90 \pm 0.07) \times 10^4$ K	$k_T = (3.5 \pm 0.2) \times 10^5$
Electron density n_e	$(1.45 \pm 0.08) \times 10^{17}\,cm^{-3}$	$k_e = (8.0 \pm 0.6) \times 10^5$

used in Section 4.3.2, indicating that the estimated total number density of particles in the simulation is also comparable to the experimental value. The rate constants that govern the time evolution of T and n_e (k_T and k_e in Table 4.6, respectively) are of the same magnitude as k_3, i.e. the decay constant of the CaCl and Ca(II) signals in the late plasma, and k_5, i.e. the decay constant of the Ca(I) signal in the late plasma. The cooling rate in particular is nearly the same value as k_3, which suggests that k_3 could be related to the cooling of the plasma plume.

4.4 Dependence on Ca and Cl concentrations

In the previous section the CaCl band signal was analyzed for a $CaCl_2$ sample with a 1:2 ratio of Ca and Cl atoms. However, the CaCl band also appears in samples with different concentrations of Ca and Cl. The dependence of the CaCl band on these concentrations is therefore investigated in this section. Studies on CaCl emission usually assume that there is a sufficiently high concentration of Ca present in the sample so that it does not influence the CaCl formation, or that the Ca concentration correlates with the Cl concentration. In both cases, a linear relationship between the Cl concentration and the CaCl band intensity is usually implicitly assumed. If Ca and Cl are supplied by different compounds which have uncorrelated concentrations within the sample, this assumption will not necessarily be valid anymore. Furthermore, the CaCl signal alone is not enough to distinguish between minerals such as $CaCl_2$ and chlorapatite ($Ca_5(PO_4)_3Cl$) in a sample, so that a univariate model that relates the CaCl band intensity to a specific Cl concentration might lead to wrong concentration estimates and wrong classification of the sample.

The primary goal of this study is to investigate the dependence of the CaCl band intensity on the sample composition and to develop a suitable calibration model with which the underlying Cl concentration can be calculated. The dependence on two separate elemental concentrations is a challenge here, as a univariate linear model is not sufficient anymore and a multivariate dependence has to be considered. The secondary goal is to find potential solutions to the problem that a multivariate intensity function cannot be used as an unambiguous calibration curve, i.e. that there are many sets of concentrations that could result in the observed intensity.

4.4.1 Spectra

In Fig. 4.19, examples of LIBS spectra for each test series are shown, with labels for the strongest emission lines and for the CaCl A-X band. The CaCl A-X band can be observed in nearly all spectra, though it is weak for the samples in which KCl and NaCl were mixed with JSC Mars-1A, since the concentrations of Ca and Cl are both low. The cations Na, K, Ca, and Mg of the salts generally have strong atomic and ionic

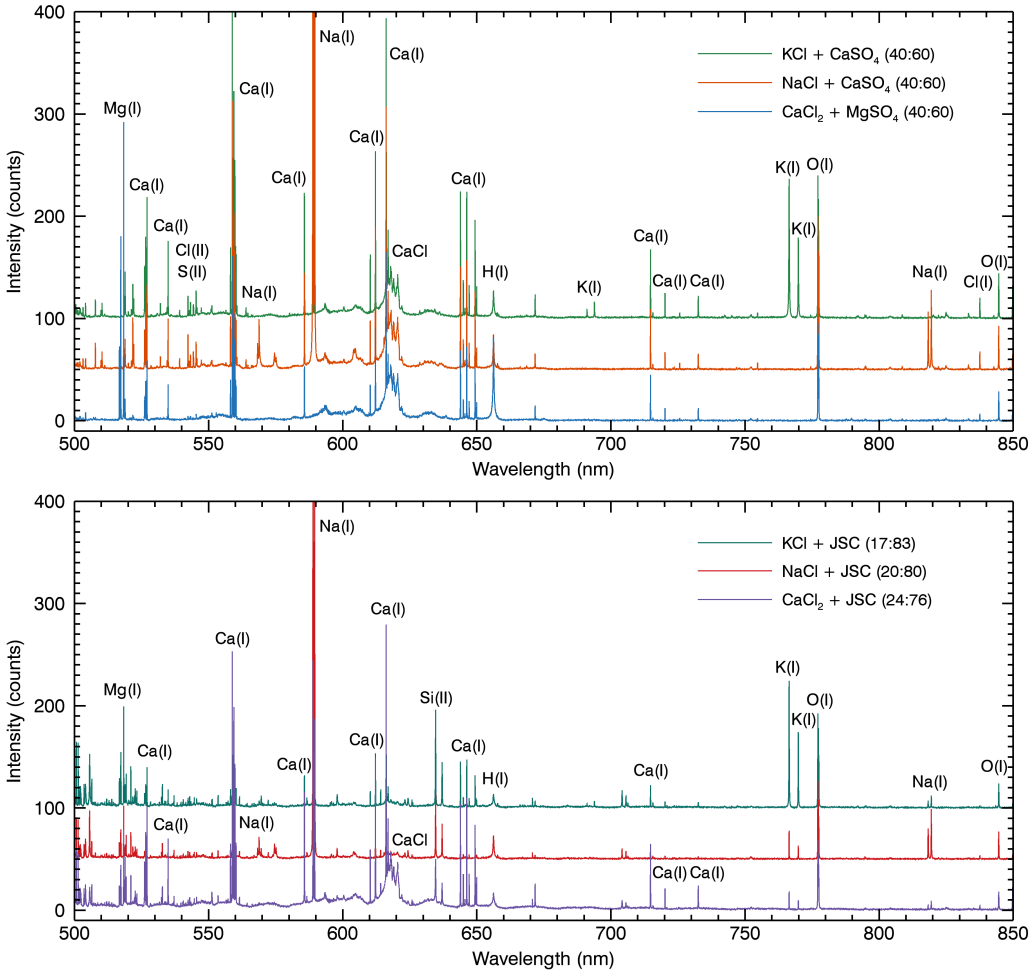

Figure 4.19: LIBS spectra of samples from each test series made for this study. The pulse energy was 35 mJ and the spectra were averaged over 30 shots.

emission lines, so that they are easily observed in Fig. 4.19. A small Na contamination can also be observed for the samples containing $CaSO_4 \cdot 2\,H_2O$.

In all spectra, the H_α line at 656.3 nm and the O(I) triplet at 777 nm can be observed, the latter being dominated by atmospheric oxygen [52]. The high intensity of the H_α line for samples containing $CaSO_4 \cdot 2\,H_2O$, $MgSO_4 \cdot 7\,H_2O$, or $CaCl_2 \cdot 2\,H_2O$ is partially due to the hydration state of these salts. In the two remaining samples of KCl and NaCl mixed with JSC Mars-1A, the H_α line is weaker and is most likely related to the adsorption of atmospheric water in the samples.

The strongest hydrogen emission can be observed for the spectrum of the sample with 30 wt% $CaCl_2 \cdot 2\,H_2O$ and 70 wt% $MgSO_4 \cdot 7\,H_2O$. The samples from this test series were challenging because of the hygroscopic nature of both substances, especially if the ratio of the two salts was close to one. It is likely that the salts reacted while being pressed and formed $CaSO_4 \cdot 2\,H_2O + MgCl_2 \cdot 6\,H_2O + H_2O$, where the high hygroscopy of

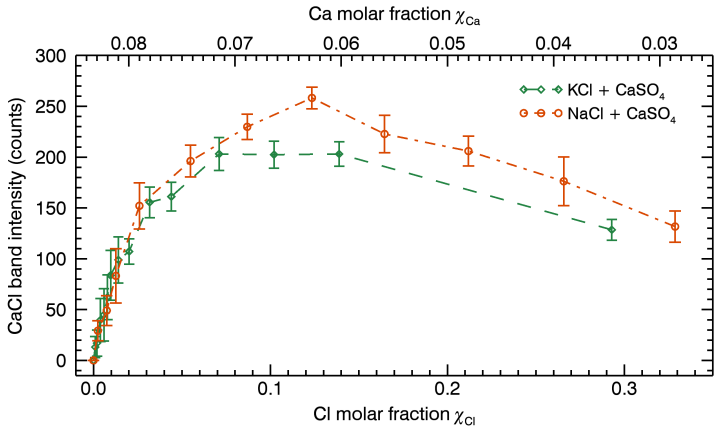

Figure 4.20: CaCl A–X band intensity in dependence of the Ca and Cl concentrations for the $KCl + CaSO_4$ series and the $NaCl + CaSO_4$ series. The highest intensities are found at a lower intensity than expected for both test series. The values are taken from measurements with a delay time of 350 ns and a gate width of 10 µs.

$MgCl_2 \cdot 6\,H_2O$ further increased deliquescence. As a result, the samples were translucent and often the formation of liquid water could be observed during LIBS measurements. This is likely the reason that the results from this test series have a higher uncertainty and vary more strongly than the results from the other test series. The effect did not occur for the samples mixed from $CaCl_2 \cdot 2\,H_2O$ and JSC Mars-1A.

4.4.2 CaCl band intensities

Fig. 4.20 shows the results of the CaCl band intensities for the anti-correlated $KCl + CaSO_4$ series and the anti-correlated $NaCl + CaSO_4$ series. As expected, there is no linear relationship between the Cl concentration and the CaCl band intensity due to the decreasing Ca concentration in these samples. The results are surprising, however, because the highest intensity is found at a relatively low Cl concentration of about 10 at%, which corresponds to a Ca concentration of about 6.7 at%. It was expected that the highest intensity would be found at the point where the product of the concentrations of Ca and Cl is at the maximum, which would be the case at 25 at% Cl and 4.2 at% Ca. Instead, the curve of the band intensity is asymmetrical and skewed towards lower Cl concentrations. In the following, the derivation of this theoretical prediction is given, which is based on the LTE model of the reactions in the plasma. I will also present potential explanations for the disagreement between the theoretical prediction and the presented measurements, before eventually deriving a new theoretical model that is able to describe the measurements very well.

LTE model The initial expectation to find the highest intensity at the point where the product of the two concentrations is highest is the result of considerations of the plasma in a chemical equilibrium. For high temperatures, only the formation of CaCl has to be considered, as high concentrations of $CaCl_2$ are only found below 3000 K in Fig. 4.10. The reactions that are important in the formation of CaCl are

$$\mathrm{Ca + Cl + M} \underset{\mathrm{k_2}}{\overset{\mathrm{k_1}}{\rightleftharpoons}} \mathrm{CaCl + M^*}\,, \tag{4.10}$$

where the forward reaction is the formation of CaCl by collision of Ca, Cl, and a third body M, and the backward direction is the dissociation of CaCl due to a collision with an energetic third body M*. The forward and backward rate constants are k_1 and k_2, respectively. At equilibrium, the rate equation, Eq. (2.14), is equal to zero. Then the relationship between the concentrations of CaCl, Ca, and Cl is

$$n_{\mathrm{CaCl}} = \frac{1}{K} n_{\mathrm{Ca}} n_{\mathrm{Cl}}\,, \tag{4.11}$$

where the equilibrium rate constant $K = k_2/k_1$ is the same as in Fig. 4.9. In order to find the relation to the molar fractions of Ca and Cl in the sample, n_{Ca} and n_{Cl} have to be related to the total number densities of Ca and Cl nuclei, $n_{\mathrm{Ca,tot}}$ and $n_{\mathrm{Cl,tot}}$. Since

$$n_{\mathrm{Ca,tot}} = n_{\mathrm{Ca}} + n_{\mathrm{CaCl}} = n_{\mathrm{Ca}} + \frac{1}{K} n_{\mathrm{Ca}} n_{\mathrm{Cl}} \text{ and} \tag{4.12}$$

$$n_{\mathrm{Cl,tot}} = n_{\mathrm{Cl}} + n_{\mathrm{CaCl}} = n_{\mathrm{Cl}} + \frac{1}{K} n_{\mathrm{Ca}} n_{\mathrm{Cl}}\,, \tag{4.13}$$

one finds by substituting the second equation into the first and solving for the physical solution $n_{\mathrm{Ca}} \geq 0$ that

$$\begin{aligned} n_{\mathrm{CaCl}} = & \frac{1}{2}\left(n_{\mathrm{Ca,tot}} + n_{\mathrm{Cl,tot}} + K \right. \\ & \left. - \sqrt{n_{\mathrm{Ca,tot}}^2 - 2n_{\mathrm{Ca,tot}}(n_{\mathrm{Cl,tot}} - K) + (n_{\mathrm{Cl,tot}} + K)^2}\right)\,. \end{aligned} \tag{4.14}$$

A series expansion for $K \to \infty$ finally results in

$$n_{\mathrm{CaCl}} = \frac{n_{\mathrm{Ca,tot}} n_{\mathrm{Cl,tot}}}{K} + \dots\,, \tag{4.15}$$

i.e. for high values of K the CaCl concentration is proportional to the product of the total number densities of Ca and Cl nuclei. As shown in Fig. 4.9, for most temperatures K is orders of magnitude bigger than the typical number densities of Ca and Cl in a laser-induced plasma in Martian ambient conditions, so that this equation should hold. Since under stoichiometric ablation the number densities of the nuclei are proportional to the molar fractions in the sample, the band intensity should therefore be proportional to the product of the molar fractions of Ca and Cl in the sample.

Fig. 4.20 is evidence that this model, derived from the assumption of LTE, is insufficient. One possible explanation is that the K values calculated from the partition

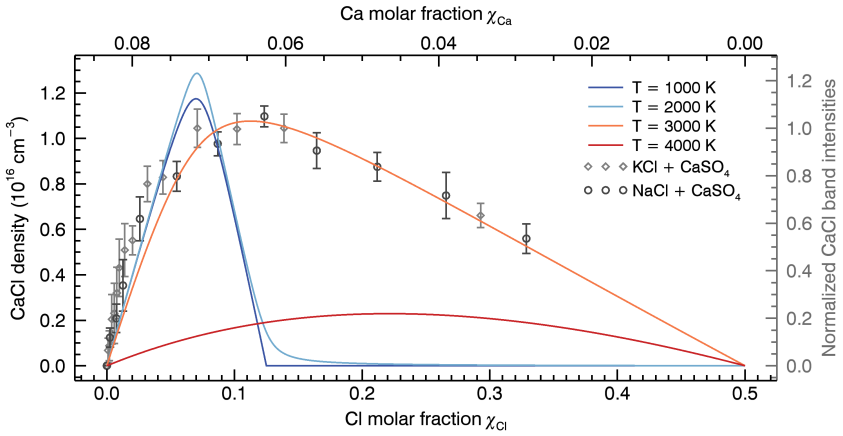

Figure 4.21: Numerical results for the CaCl concentration in dependence of the Ca and Cl atom densities in a plasma in chemical equilibrium at four different temperatures. For $T = 1000\,\mathrm{K}$ and $T = 2000\,\mathrm{K}$, the formation of $CaCl_2$ dominates the curves, while for $T = 3000\,\mathrm{K}$ and $T = 4000\,\mathrm{K}$ there is no visible influence of $CaCl_2$. None of the curves match the experimental data exactly.

functions of Ca, Cl, and CaCl need to be lower, either because the calculation is incorrect or because the reactions take place at low temperatures. In this case, Eq. (4.14) would slowly approach the value for $K = 0$,

$$n_{\mathrm{CaCl}}(K = 0) = \frac{1}{2}(n_{\mathrm{Ca,tot}} + n_{\mathrm{Cl,tot}} - |n_{\mathrm{Ca,tot}} - n_{\mathrm{Cl,tot}}|)\,, \tag{4.16}$$

and the maximum of the curve would approach the point where $n_{\mathrm{Ca,tot}} = n_{\mathrm{Cl,tot}}$.

Another explanation is that other reactions affect the concentration of CaCl in the plasma. Reactions with unrelated elements, such as the reaction of Ca and O to CaO, cannot be responsible, as these would only decrease the concentrations of Ca or Cl in the plasma, which would not change the position of the maximum product of the two concentrations. However, reactions of CaCl and Cl to $CaCl_2$ can explain a decrease of the CaCl concentration specifically for high Cl concentrations. In a plasma that is in LTE, these reactions are only important at low temperatures and should not play an important role, which is why they were neglected previously. If they are nevertheless introduced into the LTE model, the equations cannot be solved analytically anymore, but must be solved numerically with an iterative approach to find the set of number densities of the species that satisfies all equilibrium conditions at the same time.

This was done here to investigate the influence of $CaCl_2$ formation. I made simulations of the plasma in equilibrium with varying total number densities of the nuclei of Ca and Cl at four different temperatures ($T = 1000\,\mathrm{K}$, $T = 2000\,\mathrm{K}$, $T = 3000\,\mathrm{K}$, and $T = 4000\,\mathrm{K}$) and included the formation of Cl_2, CaCl, and $CaCl_2$. The total number density of nuclei in the plasma was set to $n_{\mathrm{tot}} = 2 \times 10^{17}\,\mathrm{cm}^{-3}$ as in earlier simulations.

The total number densities of Ca and Cl nuclei, $n_{\mathrm{Ca}}^{\mathrm{tot}}$ and $n_{\mathrm{Cl}}^{\mathrm{tot}}$, are fractions of n_{tot} that correspond to the molar fractions in the two anti-correlated test series $\mathrm{KCl} + \mathrm{CaSO_4}$ and $\mathrm{NaCl} + \mathrm{CaSO_4}$.

The results can be seen in Fig. 4.21 along with the curve described by the CaCl band intensities of the $\mathrm{KCl} + \mathrm{CaSO_4}$ and the $\mathrm{NaCl} + \mathrm{CaSO_4}$ series. At the two lowest temperatures, the formation of $\mathrm{CaCl_2}$ affects the CaCl concentration, resulting in a strong cut-off point where the concentration of Cl is higher than twice the Ca concentration. The curves do not resemble the curve described by the measurements, so that the formation of $\mathrm{CaCl_2}$ at equilibrium cannot be used to explain the measurements. For $T = 4000\,\mathrm{K}$, the curve follows Eq. (4.15), which cannot describe the measurements either. Only the curve for $T = 3000\,\mathrm{K}$ is similar to the measurements. At this temperature the equilibrium rate constant of the CaCl reaction is low enough that the curve is in between the two extremes given by Eq. (4.15) and Eq. (4.16). However, the curve does not match the measurements exactly. At low Cl concentrations, the measured values are higher than those predicted by the LTE model, which cannot be resolved by changing the temperature. My results in Chapter 5 will show that the similarity between this curve and the curve described by the measurements cannot be reproduced for test series with different relationships between Ca and Cl.

Non-equilibrium model This model, which is able to describe the measurements well, is derived from a steady-state approach for the formation of CaCl, but does not require the plasma to be in LTE anymore. It is therefore similar to partial LTE (pLTE), in which the plasma in a small region is considered to be only *close* to equilibrium [149]. The new model was first presented in [151] and is based on a similar model by Ogryzlo et al. [106], who investigated the O_2 nightglow emission.

In the following, CaCl will be represented as a generic diatomic heteronuclear molecule AB made from the reactants A and B, which can react with a B atom to form $\mathrm{AB_2}$. The model considers the following reactions and processes:

$$\mathrm{A} + \mathrm{B} \xrightarrow{\mathrm{k_1}} \mathrm{AB^*} \tag{4.17a}$$

$$\mathrm{AB^*} \xrightarrow{\mathrm{k_2}} \mathrm{A} + \mathrm{B} \tag{4.17b}$$

$$\mathrm{AB^*} + \mathrm{B} + \mathrm{M} \xrightarrow{\mathrm{k_3}} \mathrm{AB_2} + \mathrm{M} \tag{4.17c}$$

$$\mathrm{AB^*} + \mathrm{M} \xrightarrow{\mathrm{k_4}} \mathrm{AB} + \mathrm{M} \tag{4.17d}$$

$$\mathrm{AB^*} + \mathrm{M} \xrightarrow{\gamma\mathrm{k_4}} \mathrm{AB(A)} + \mathrm{M} \tag{4.17e}$$

$$\mathrm{AB(A)} + \mathrm{M} \xrightarrow{\mathrm{k_5}} \mathrm{AB(X)} + \mathrm{M} \tag{4.17f}$$

$$\mathrm{AB(A)} \xrightarrow{\mathrm{k_6}} \mathrm{AB(X)} + \mathrm{h}\nu \tag{4.17g}$$

The constants above the arrows are the rate constants of the reactions. Equation (4.17a) describes a collision of A and B that forms an excited precursor $\mathrm{AB^*}$ of the molecule

AB. The precursor can easily dissociate again if no third body is available to take up the excess energy (4.17b). It can also recombine with a B atom to form AB_2 via a three-body reaction with B and another species M (4.17c). The backward reaction $AB_2 \longrightarrow AB + B$ as a way of forming AB is neglected here, as it is assumed that the reaction to AB_2 only happens as the CaCl molecule moves out of the hot plasma into the cold periphery. Since no initial AB_2 molecules are present in the plasma, the backward reaction can therefore be neglected.

Equation (4.17d) describes a collision of AB* and M that causes the recombination to a more stable energy state. A fraction γ will then recombine to the $A^2\Pi$ state, notated as AB(A) in (4.17e), which relaxes to the ground state $X^2\Sigma^+$ either by collision (4.17f) or by emitting a photon (4.17g).

The rate of the radiative transition from the $A^2\Pi$ state to the $X^2\Sigma^+$ state is given by

$$\frac{dn_{h\nu}}{dt} = k_6 n_{AB(A)}\,, \tag{4.18}$$

where $n_{AB(A)}$ is the number density of AB molecules in the $A^2\Pi$ state, and $n_{h\nu}$ is the number density of emitted photons with the transition frequency ν (neglecting the spectral width of the transition). The emission coefficient of the A-X band is then proportional to the transition rate of the emission:

$$\epsilon_{A-X} = \frac{h\nu}{4\pi} k_6 n_A \tag{4.19}$$

Using the steady-state approximation for AB* and AB(A), their concentrations can be written as:

$$n_{AB^*} = \frac{k_1 n_A n_B}{k_2 + k_3 n_B n_M + k_4 n_M} \tag{4.20}$$

$$n_{AB(A)} = \frac{\gamma k_4 n_M}{k_5 n_M + k_6} n_{AB^*} \tag{4.21}$$

Since the exact values for the various parameters in Eqs. 4.19–4.21 are not known and cannot be measured directly, the equations need to be simplified. The first step is to exchange the number densities n_A and n_B of elemental species A and B in the plasma for their molar fractions χ_A and χ_B in the sample:

$$n_A = n_{\mathrm{tot}} \chi_A \tag{4.22}$$

$$n_B = n_{\mathrm{tot}} \chi_B \tag{4.23}$$

Here n_{tot} is the total number density of nuclei in the plasma that were ablated from the sample surface. The assumption here is that the ablation was stoichiometric and that the ratio of A and B in the plasma is not significantly affected by the formation of AB molecules, which seems likely as this was already the case in total equilibrium. Finally, by grouping the parameters together and by introducing a parameter F for the

detection efficiency of the experimental setup (in counts/photon) as well as a parameter Δt for the integration time, the intensity (in counts) can be formulated as:

$$I_{\text{A-X}} = \zeta \frac{\chi_A \chi_B}{(1 + \eta \chi_B)} \tag{4.24}$$

$$\zeta = F \Delta t \, n_{\text{tot}}^2 \frac{k_6 k_1 \gamma k_4 n_M}{(k_5 n_M + k_6)(k_2 + k_4 n_M)} \tag{4.25}$$

$$\eta = n_{\text{tot}} \frac{k_3 n_M}{k_2 + k_4 n_M} \tag{4.26}$$

The parameter ζ is given in counts of the spectrometer, while η is dimensionless. Equation (4.24) shows that a high concentration of reactant B reduces the molecular emission if the molecule AB_2 is formed at a high rate. If $\eta \chi_B \ll 1$, the formula approaches the result of Eq. (4.15). The parameter η is therefore a measure of how strongly the band intensity is affected by non-equilibrium processes.

Application to all test series Figure 4.22 shows the CaCl band intensities for all six test series that were created for this experiment and for the two different time gate settings. The anti-correlated series in Fig. 4.22a and b show the asymmetric band intensities that were already discussed. In the two correlated series shown in Fig. 4.22c and d, the CaCl band intensity increases nearly linearly for increasing concentrations of Ca and Cl, so that the highest band intensities can be observed in these two series. However, the data for the $CaCl_2 + MgSO_4$ series varies a lot, which is likely related to the deliquescence that was observed during the production of these samples. The MgCl band cannot be observed at all in the spectra of the $CaCl_2 + MgSO_4$ series, which suggests that CaCl formation is favored over MgCl formation.

For the mixtures of KCl and NaCl with JSC Mars-1A shown in Fig. 4.22e and f, CaCl band intensities could only be obtained from the measurements with a delay time of 350 ns. The continuum emission was particularly strong for samples containing JSC Mars-1A, leading to high background intensities and an increased noise level as well as measurement artifacts that appeared only at high continuum intensities. Therefore the CaCl emission, which was already less intense in these spectra, dropped below the detection limit for the shorter delay time. The measurements with a delay time of 350 ns show a similar behavior to that observed for the other two anti-correlated series, but the band intensity does not increase as strongly for low Cl concentrations. A small offset can be observed as well for the sample where no Cl concentration was added, indicating that the CaCl band can already be observed in the spectrum of pure JSC Mars-1A, for example because of a small contamination with NaCl.

The fit curves were all made using the non-equilibrium model described by Eq. (4.24), where an offset parameter was added to account for the background signal. The model is able to describe the anti-correlated and the correlated series accurately for both time gate settings. The fit parameters are listed in Table 4.7. For the two test series of KCl

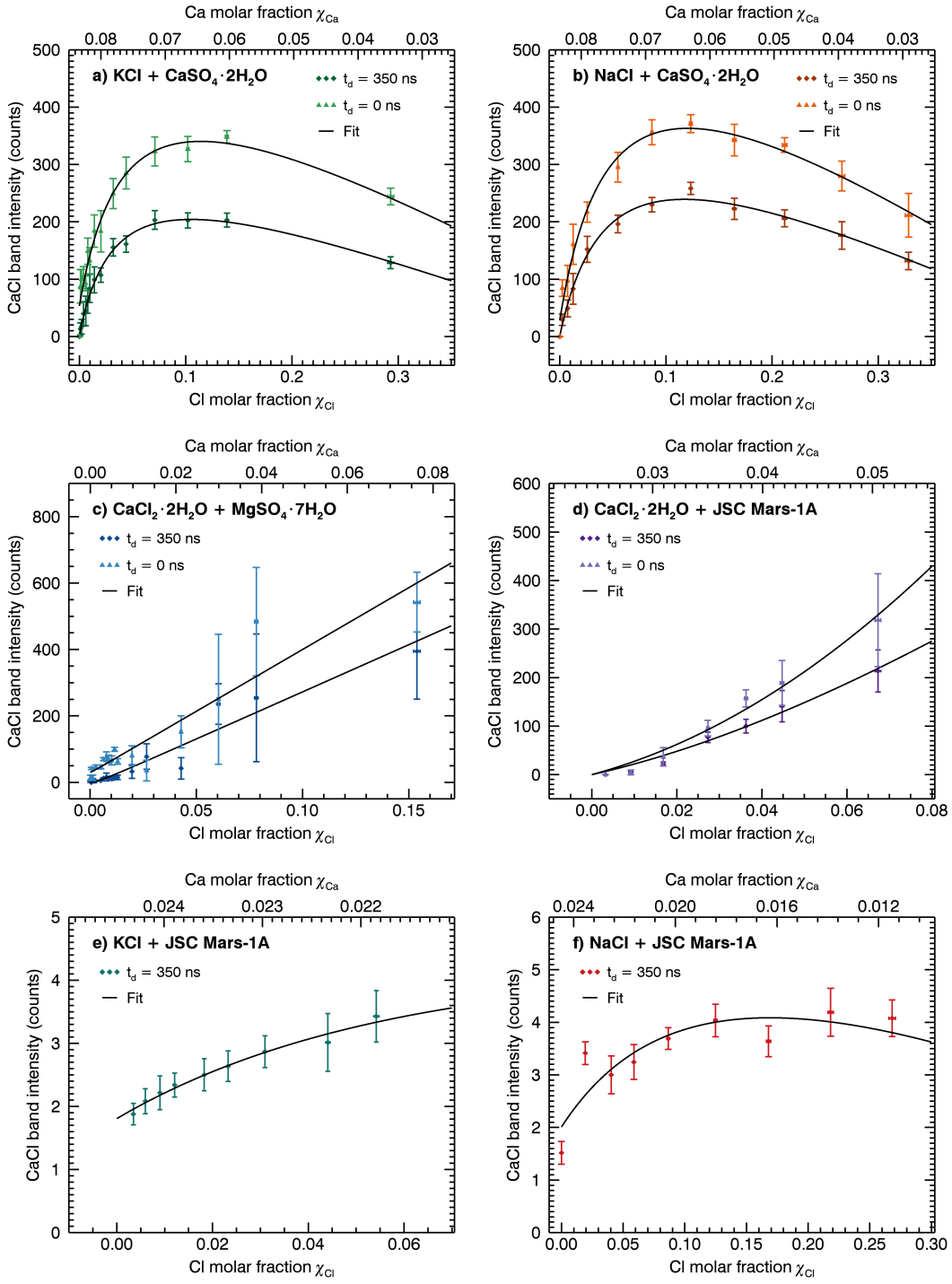

Figure 4.22: CaCl A–X band intensity in dependence of the Ca and Cl concentrations for all six test series and for the two time gate settings, indicated here by the delay time t_d. The fits are made with the non-equilibrium model. The confidence intervals correspond to the 1σ uncertainties calculated from all measurements per sample.

Table 4.7: Fit parameters ζ and η for all six test series and for both time gate settings.

Test series	350 ns delay time		0 ns delay time	
	ζ (counts)	η	ζ (counts)	η
$KCl + CaSO_4$	$10.9 \pm 0.7 \times 10^4$	26 ± 2	$13 \pm 1 \times 10^4$	21 ± 2
$NaCl + CaSO_4$	$10.4 \pm 0.6 \times 10^4$	19 ± 2	$13.8 \pm 0.9 \times 10^4$	18 ± 2
$CaCl_2 + MgSO_4$	$1 \pm 3 \times 10^6$	200 ± 500	$0 \pm 2 \times 10^8$	$0 \pm 2 \times 10^4$
$CaCl_2$ + JSC	$8.0 \pm 0.9 \times 10^4$	4 ± 3	$9.6 \pm 0.4 \times 10^4$	0 ± 1
KCl + JSC	$1.8 \pm 0.5 \times 10^3$	8 ± 7		
NaCl + JSC	$1.5 \pm 0.3 \times 10^3$	6 ± 2		

and NaCl mixed with $CaSO_4 \cdot 2\,H_2O$, they are nearly identical, which corresponds well to their general similarity. The parameters for the two correlated series are different from each other, but this could be caused by the higher uncertainty of the data from the samples of $CaCl_2$ mixed with $MgSO_4 \cdot 7\,H_2O$, which also causes a high uncertainty in the fit parameters. Another explanation is that using JSC Mars-1A as a component in the mixture results in a matrix that differs more strongly from that of the pure salt mixtures, so that the parameters are different. The parameters found for the measurements of mixtures of KCl and NaCl with JSC Mars-1A are also lower than the ones found for mixtures of KCl and NaCl with $CaSO_4 \cdot 2\,H_2O$, but are again similar to one another. This supports the idea that the change of the second component from a pure sulfate ($CaSO_4$ or $MgSO_4$) to JSC Mars-1A lowers the fit parameters. It should be noted, however, that a contamination of Cl in JSC Mars-1A will also influence these parameters, since the molar fractions calculated from the weight ratios of the components will be slightly off.

Fit parameter ζ is consistently larger for the measurements without a delay time. This is expected, since ζ functions as a scaling factor. Fit parameter η is lower for the measurements without a delay time in the test series of KCl and NaCl mixed with $CaSO_4 \cdot 2\,H_2O$, indicating that the influence of the reaction to $CaCl_2$ is reduced in this case. This trend can also be observed for $CaCl_2 \cdot 2\,H_2O$ mixed with JSC Mars-1A, but the values of the two fit parameters for the two correlated series are generally quite uncertain. A decrease of η indicates that the influence of the formation of $CaCl_2$ is reduced. This is a reasonable result, since the additional intensity in the measurements without a delay time of 350 ns mostly comes from the early plasma stages between 0 and 350 ns, in which the plasma temperature is high and $CaCl_2$ formation is expected to be reduced.

4.5 Summary and discussion

The MgCl band at 377 nm is not suited for the detection or quantification of Cl. It has a very low intensity even in the LIBS spectrum of a pure $MgCl_2 \cdot 6\,H_2O$ sample. The LTE simulations of the plasma show that the population density of the $A^2\Pi$ state of MgCl is very low for all temperatures due to the low dissociation energy of MgCl and the high excitation energy of the $A^2\Pi$ state. The formation of CaCl also seems to be favored over the formation of MgCl, so that the presence of Mg in a sample should not affect the formation of CaCl molecules.

The CaCl band in LIBS spectra of pure $CaCl_2 \cdot 2\,H_2O$ is significantly more intense than the Cl(I) line at 837.6 nm, making it an interesting signal for the detection and quantification of Cl. It is actually a band sequence of many superimposed bands, which leads to a complex band profile that is difficult to simulate. It is also the reason for the high intensity of the band. LTE simulations of the $CaCl_2$ plasma composition show that CaCl is only stable at low temperatures between 2000–5000 K, but the low-lying $A^2\Pi$ state still has a relatively high population density in a narrow temperature range around 4000 K.

LIBS spectra of $CaCl_2 \cdot 2\,H_2O$ at different laser energies show a saturation effect for the CaCl band intensity and the Ca(I) line intensity for high laser energies, which is likely related to the low temperatures at which CaCl and Ca are stable in the plasma. For neutral Cl and the Ca^+ ion, which are both stable within a larger temperature range, the dependence on the laser energy was more linear. This shows that the saturation is not caused by a reduced ablation rate. The plasma temperature that was calculated from Ca(II) lines remained constant for increasing laser energies, which suggests that the plasma does not get hotter at higher laser energies, but instead increases in size. If the colder regions of the plasma do not increase in a similar fashion, the signals of neutral Ca and CaCl would appear to saturate.

Time-resolved measurements of the CaCl band indicate a high concentration of CaCl molecules shortly after plasma initiation, which dissociate within the first 100 ns. Afterwards the majority of CaCl molecules are formed by slower chemical reactions. These separate processes could be modeled theoretically. The decay of the band intensity at long delay times seems to be related to the diffusion and the cooling of the plasma, so that no reactions are observed anymore after about 1 µs. Therefore calculations with a steady-state approach for CaCl seem to be justified in first approximation. Still, the behavior of the CaCl band intensity at low delay times indicates that the equilibrium approach has its limits. The plasma seems to be highly dynamic in these early stages. The high initial CaCl concentration indicates that chemical reactions are not the only processes that produces CaCl molecules. Fragmentation during the ablation process could be responsible for this early maximum, which accounts for about 7% of the total time-integrated band intensity.

The CaCl band intensities in test series with anti-correlated concentrations could not be described by an LTE model, which predicts the maximum band intensity to be found in the sample with the largest product of the reactant concentrations. Instead the band intensities are skewed towards lower Cl concentrations. It could be shown that an extension of the LTE model that also considers the formation of $CaCl_2$ cannot account for this asymmetry either. One explanation that could not yet be ruled out is that the reactions occur at a lower temperature where the equilibrium constant K is closer to zero. In this case the maximum band intensity would be shifted towards the equilibrium point of the Ca and Cl concentrations, which is close to the point where the maximum is observed in the measurements. This possibility will be investigated in the next chapter with a new test series in which the sum of the reactant concentrations is conserved.

The non-equilibrium model that I introduced here describes all measurements accurately, even for different delay times. The model still assumes that the CaCl concentration in the plasma is stable for most of the plasma lifetime. The reaction of CaCl to $CaCl_2$ plays an important role, since it reduces the CaCl band intensity for high Cl concentrations. In contrast to the LTE model, the reaction is not in balance with its backward reaction, however. Instead I assume that the reaction takes place while the molecule is moving towards a colder region where $CaCl_2$ is more stable, so that the backward reaction becomes more unlikely. This model is more in line with a laser-induced plasma that is known to be highly dynamic in nature while still offering a simple way of modeling the band intensity without resorting to complex simulations of the plasma dynamics.

The development of a theoretical model that can accurately describe the molecular band intensity for different reactant concentrations is an important step towards using molecular bands for the quantification of elements in the sample. However, there are still unresolved questions that need to be addressed. The nonlinearity of the CaCl band intensity for increasing laser energies suggests that the laser energy is an important parameter that needs to be investigated in the context of the dependence of the band intensity on the reactant concentrations as well. The effect of fragmentation, which has likely been observed in the time-resolved $CaCl_2 \cdot 2\,H_2O$ measurements, also needs to be investigated more closely, since it could affect the band intensity as a chemical matrix effect that only occurs for specific samples. The formation of other molecules by one of the reactants might be another important matrix effect. Furthermore, the theoretical model that was developed here might only work for CaCl, but not for other molecules, so that it should be applied to other molecules in order to investigate its generality.

5. Comparison of CaCl and CaF Emission

Like chlorine, fluorine has been hypothesized to play an important role in Martian geology. Concentrations of fluorine found in Martian meteorites have led to the estimation that Martian basalts and the bulk Martian mantle could contain about two to three times more fluorine than terrestrial basalts and Earth's mantle [36, 145]. A high concentration of fluorine could have a significant influence on basalt generation on Mars, since it lowers the liquidus temperature of basalts and impacts the chemistry of crystallizing minerals [43].

The first detection of fluorine on Mars was made possible by CaF emissions in Martian LIBS spectra measured by ChemCam [44, 50]. While the F(I) line at 685.6 nm can also be observed by ChemCam, it is not very intense, limiting the detection of fluorine to concentrations higher than about 5 wt% [91]. The presence of intense CaF bands in Martian LIBS spectra allowed for the unambiguous detection of fluorine-bearing phases that were identified to be micas, amphiboles, apatites, topaz, or fluorite [44]. The CaF bands have since been used to detect and quantify fluorine in many different locations along the traverse of Curiosity [45–48].

Molecular emissions of CaF are also of interest for terrestrial LIBS applications. It was shown that they can be used for the detection of fluorine even in samples that did not contain calcium if a calcium solution is nebulized over the fluorine-bearing sample [4, 5]. However, no studies on the exact dependence of the CaF concentration on the concentrations of calcium and fluorine in the sample have been made so far. This is especially relevant for the quantification of fluorine on Mars, since the calcium content in fluorine-bearing Martian rocks may differ greatly and cannot be adjusted by the addition calcium-bearing solutions.

In this chapter, I focus on the comparison of the CaF emission and the CaCl emission in order to investigate similarities and differences. The MgF emission as a potential alternative for fluorine detection is also discussed briefly, but it is found to be of low intensity. The CaF A-X band spectrum and emission coefficient are simulated equivalently to the simulations for CaCl in Chapter 4. The CaCl and CaF band intensities are compared in dependence of the reactant concentrations (Ca and Cl for CaCl, Ca and F for CaF) and it is shown that the fit model from last chapter, Eq. (4.24), is also applicable to the CaF band. The new test series also prove that LTE calculations

cannot describe the band intensities correctly. Calibration curves for the quantification of Cl and F based on Eq. (4.24) are shown. In the next experiment, the influence of the native bonds in the sample on the band intensities of CaCl and CaF is investigated. The native bonds are only expected to have an influence if strong fragmentation occurs and if the plasma is in non-equilibrium [29]. In that case, samples containing Ca−Cl bonds or Ca−F bonds should have stronger band intensities than samples with the same reactant concentrations in different bonds. The time-resolved measurements of $CaCl_2 \cdot 2\,H_2O$ in Section 4.3.5 have already indicated that fragmentation plays an important role for this sample. In the last experiment, the effect of the competing formation of CaCl and CaF in the laser-induced plasma is investigated. It is observed that CaF is favored over CaCl. In Martian LIBS spectra, this could be relevant if the analyzed target rock contains both fluorapatite, $Ca_5(PO_4)_3F$, and chlorapatite, $Ca_5(PO_4)_3Cl$), for example.

As before, all measurements were made in simulated Martian atmospheric conditions. The majority of the results were published in [151].

5.1 Samples and experiments

Reagent-grade salts were used for the samples in this study: K_2SO_4, $CaCO_3$, KCl, MgF_2, CaF_2, $CaSO_4 \cdot 2\,H_2O$, and $CaCl_2 \cdot 2\,H_2O$ were used either as pure samples or in mixtures. An overview of the five different test series is given in Table 5.1. In the following, the experiments that were conducted are described in more detail. All LIBS spectra were measured in Mars-analog gas at 650 Pa. 30 laser shots on the same sample position were averaged for a single LIBS spectrum. For most experiments the samples were measured at 10 different positions with the same time gate settings, where a delay time of 350 ns and a gate width of 10 µs were used. The exceptions are the time-resolved measurements, which were measured at varying delay times with a gate width of 500 ns.

Investigation of the CaF emission In the first part of this study, the CaF emission in LIBS is investigated. The CaF $A^2\Pi - X^2\Sigma$ $\Delta v = 0$ band sequence, called CaF A-X band or CaF band in the following, is compared to a simulated spectrum. As for the MgCl band and the CaCl band, the goal is to confirm the correct identification of the observed spectral feature and to investigate how easily the molecular band can be modeled. The LIBS spectrum of the sample of the *native bond series* that consists of 38.6 wt% CaF_2 and 61.4 wt% K_2SO_4 (12.5 at% Ca and 25.0 at% F) is used for the comparison. In the second part, the CaF concentration and emission in the laser-induced plasma of a CaF_2 sample are simulated in dependence of the plasma temperature. As in earlier calculations for MgCl and CaCl, the LTE model is used.

Table 5.1: Overview of the test series made for this study, showing the fundamental formulae for the mixtures and for the molar fractions of the investigated reactants Ca, Cl, and F. The variable α indicates the varying weight fractions of the two substances in the mixtures. Mix 1 is a 1:1 mixture of K_2SO_4 and KCl, Mix 2 is a 2.8:1 mixture of K_2SO_4 and MgF_2.

Series	Mixture	Molar fractions (Ca, Cl, F)	# samples
CaCl band series	α Mix 1 + $(1-\alpha)$ $CaCO_3$	$\chi_{Ca} = 0 \ldots 0.2$, $\chi_{Cl} = 0.2 - \chi_{Ca}$	20
CaF band series	α Mix 2 + $(1-\alpha)$ $CaCO_3$	$\chi_{Ca} = 0 \ldots 0.2$, $\chi_{F} = 0.2 - \chi_{Ca}$	15
Native bond series	Different mixtures	$2\chi_{Ca} = \chi_{Cl} = 0.22$ or $2\chi_{Ca} = \chi_{F} = 0.25$	4
Cl variation series	α CaF_2 + β KCl + $(1-\alpha-\beta)$ K_2SO_4	$2\chi_{Ca} = \chi_{F} = 0.03$, $\chi_{Cl} = 0 \ldots 0.087$	15
F variation series	α $CaCl_2 \cdot 2\,H_2O$ + β MgF_2 + $(1-\alpha-\beta)$ K_2SO_4	$2\chi_{Ca} = \chi_{Cl} = 0.03$, $\chi_{F} = 0 \ldots 0.155$	9

Dependence on reactant concentrations In this experiment I study the dependence of the molecular emission on the concentrations of the two reactants at three different laser energies: 17 mJ/pulse, 23 mJ/pulse, and 35 mJ/pulse. Two separate test series with anti-correlated reactant concentrations were made for this experiment, which are called *CaCl band series* and *CaF band series* in Table 5.1. The CaCl band series is for the investigation of the CaCl A-X band intensity in dependence of the Ca

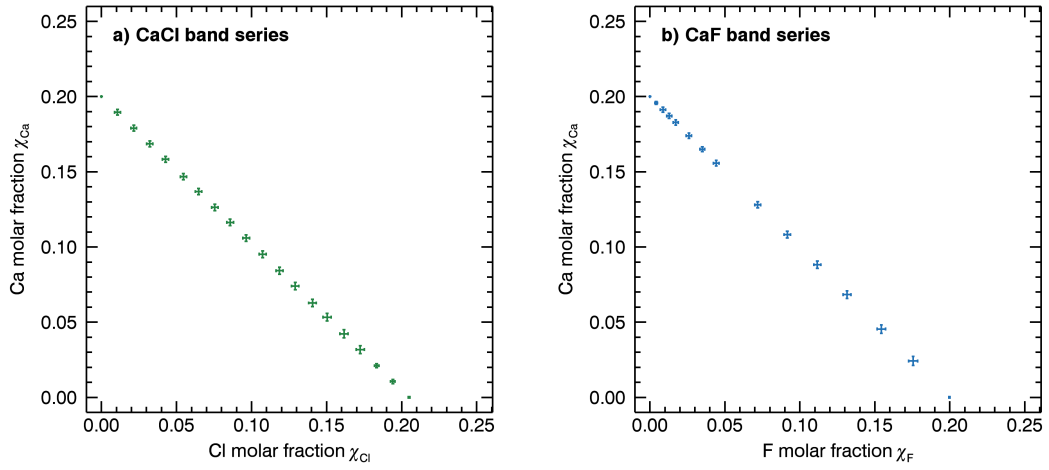

Figure 5.1: a) Molar fractions of Ca and Cl in the samples of the CaCl band series. b) Molar fractions of Ca and F in the samples of the CaF band series. In both series, the sum of the two reactants is nearly constant for all samples.

and Cl concentrations in the sample. In contrast to previous experiments, the series was prepared so that the sum of the concentrations of Ca and Cl was conserved at $\chi_{Ca} + \chi_{Cl} = 0.2$ (20 at%), see Fig. 5.1a. This is achieved by mixing a 1:1 mixture of K_2SO_4 and KCl, called *Mix 1* ($\chi_{Cl} = 0.2$), with $CaCO_3$ ($\chi_{Ca} = 0.2$) at different ratios.

The CaF band series is for the equivalent investigation of the CaF band intensity and its dependence on the Ca and F concentrations. The molar fractions of Ca and F for the individual samples are shown in Fig. 5.1b. Again, the sum is kept constant at 20 at%, this time by mixing a 2.8:1 mixture of K_2SO_4 and MgF_2 called *Mix 2* ($\chi_F = 0.2$) with $CaCO_3$. Due to the MgF_2 content of Mix 2, samples of this series were also used to investigate the MgF emission. Only 15 samples instead of 20 samples were produced for this series because of the difficulties during sample preparation. The mixed samples were very brittle due to the hardness of the MgF_2 crystals and did not hold together well. Some of the variation of the measurements in this series can be explained by these difficulties.

Influence of native bonds Four samples were made to analyze the influence of the native bonds in the sample due to fragmentation during laser ablation and non-equilibrium kinetics in the early plasma [29, 34]. They will be called the *native bond series*. Two samples contain the same concentrations of Ca and Cl in different chemical bonds, with one being made of pure $CaCl_2 \cdot 2\,H_2O$ while the other is mixed from 59.7 wt% KCl and 40.3 wt% $CaCO_3$. They both contain 11.1 at% Ca and 22.2 at% Cl ($\chi_{Ca} = 0.111$, $\chi_{Cl} = 0.222$). The next two samples both contain 12.5 at% Ca and 25.0 at% F ($\chi_{Ca} = 0.125$, $\chi_F = 0.250$). The first sample consists of 38.6 wt% CaF_2 and 61.4 wt% K_2SO_4, and the second sample consists of 38.4 wt% MgF_2 and 61.6 wt% $CaCO_3$. For all elemental concentrations the uncertainties are lower than 0.65 at%. Measurements were done with a laser energy of 23 mJ/pulse. In order to see potential differences in the time evolution of the band intensities, time-resolved measurements with varying delay times and a small gate width of 500 ns were made as well.

Influence of competing reactants If both Cl and F are present in the plasma, then CaCl formation and CaF formation are in direct competition with one another. This should affect the intensity of both molecular emissions. In order to study this effect, two sets of samples were made. In the *Cl variation series*, the concentrations of Ca and F were kept at nearly constant values of about 1.5 at% and 3 at%, respectively, while the Cl concentration was varied between 0 and 8.7 at% (Fig. 5.2a). This was achieved with ternary mixtures of CaF_2, KCl, and K_2SO_4 at different ratios. 15 samples were made for this series. The second series is the *F variation series*, for which $CaCl_2 \cdot 2\,H_2O$ was mixed with MgF_2 and K_2SO_4. In this series the Ca and Cl concentrations remain

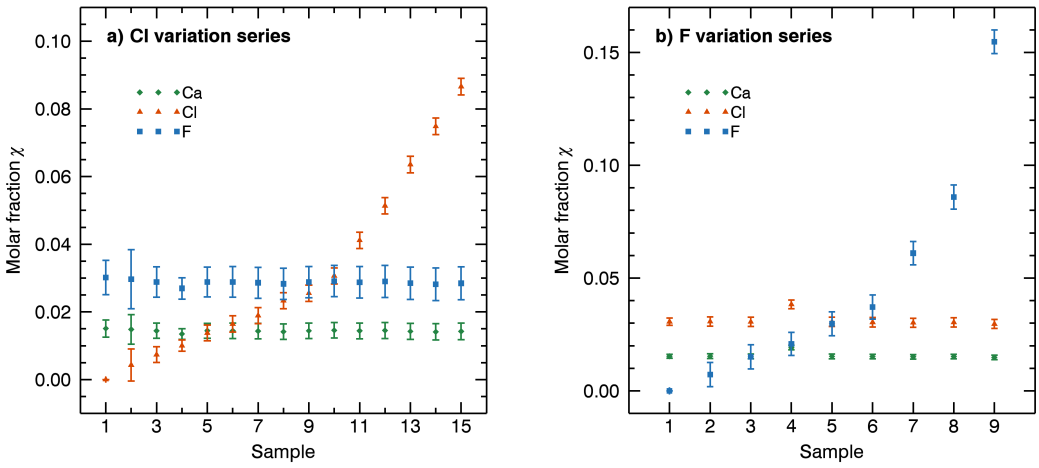

Figure 5.2: Molar fractions of Ca, Cl, and F in the samples of a) the Cl variation series and b) the F variation series.

close to 1.5 at% and 3 at%, respectively, while the F concentration is varied from 0 at% to 15.5 at% (Fig. 5.2b). The number of samples was reduced to 9 for this series since the results from the first series indicated that a lower number of samples would be sufficient to detect changes in the molecular band intensities. At the same time, the uncertainties of the elemental concentrations could be improved by increasing the total mass of the mixtures from which the samples were made.

5.2 CaF emission

In this section, the CaF emission is investigated closely. The same simulations that were used to investigate the MgCl emission and the CaCl emission in the last chapter are applied here to the CaF emission, i.e. the spectrum of the most intense A-X band sequence and the number density of CaF molecules in dependence of the temperature are calculated. Additionally, a LIBS spectrum of a sample containing CaF_2 is shown, in which the CaF B-X band and the CaF A-X band can be observed in comparison to the strongest F(I) emission line at 685.6 nm. The simulated spectrum of the CaF A-X band is compared with the measured one.

5.2.1 Simulation of the CaF A-X band

The spectroscopic constants of the $A^2\Pi$ state and the $X^2\Sigma^+$ state that were used for the simulation are listed in Table 5.2. The first seven constants were taken from Nakagawa et al. [101], r_e and k_e were taken from Radzig and Smirnov [117] and $E_e \approx D_0^0/hc - T_e$ was calculated from the dissociation energy $D_0^0 = 5.5\,\text{eV}$ [72]. Based on these constants, the first nine vibrational transitions were calculated, as before with $J_{\text{max}} = 300$.

Table 5.2: Spectroscopic constants used in the simulation of the CaF A-X band spectrum.

Constant	$X^2\Sigma^+$	$A^2\Pi$	References
T_e (cm^{-1})	0	$1.652\,68 \times 10^4$	[101]
ω_e (cm^{-1})	5.874×10^2	5.934×10^2	[101]
$\omega_e x_e$ (cm^{-1})	2.84	3.11	[101]
B_e (cm^{-1})	0.343 704	0.348 744	[101]
D_e ($10^{-7}\,cm^{-1}$)	4.5	4.4	[101]
α_e (cm^{-1})	2.436×10^{-3}	2.529×10^{-3}	[101]
A (cm^{-1})	0	71.475	[101]
r_e (Å)	1.967	1.95	[117]
k_e (N/cm−1)	2.61	2.67	[117]
E_e (cm^{-1})	4.4×10^4	2.8×10^4	[72]

The result can be seen in Fig. 5.3a for a plasma temperature of 5000 K and a Gaussian width of 0.08 nm. Again the single (0-0) transition is given as a comparison. The band sequence changes even more drastically than it does for CaCl (Fig. 4.8). The branch heads of each band can be seen as separate peaks that shift to lower wavelengths for increasing v, creating a comb-like structure. The strong difference to the (0-0) band shows that the simulation of many vibrational transitions is vital to correctly simulate the measured CaF A-X band sequence. The Franck-Condon factors in Fig. 5.3b support this, since they stay at high values up to $v' = v'' = 20$. Simulating only a low number of vibrational transitions will not lead to a good resemblance between simulation and measurement. However, considering more vibrational transitions also introduces uncertainties due to increasing inaccuracies of the Morse potential and of the spectroscopic constants for higher vibrational levels.

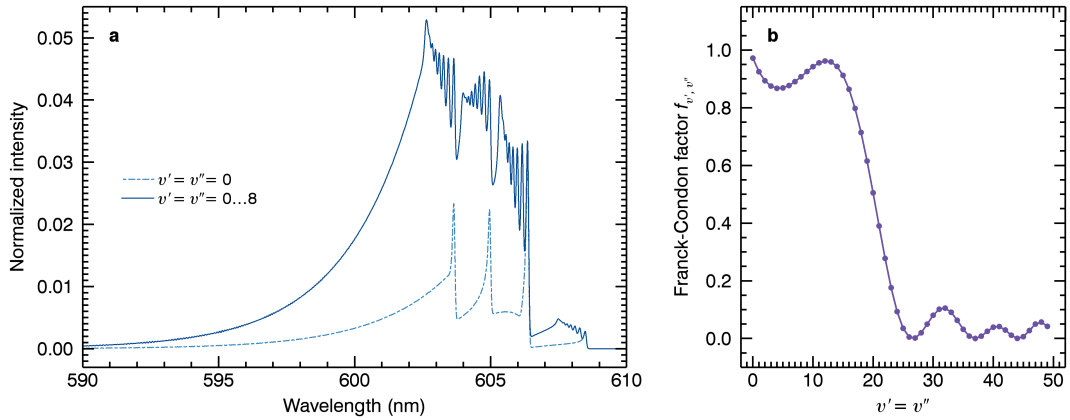

Figure 5.3: a) Simulated spectrum of the CaF A-X (0-0) band and of the $\Delta v = 0$ band sequence up to $v' = v'' = 8$. A spectral resolution of 0.08 nm was simulated and the temperature was set to 5000 K. b) Calculated Franck-Condon factors for $\Delta v = 0$ transitions.

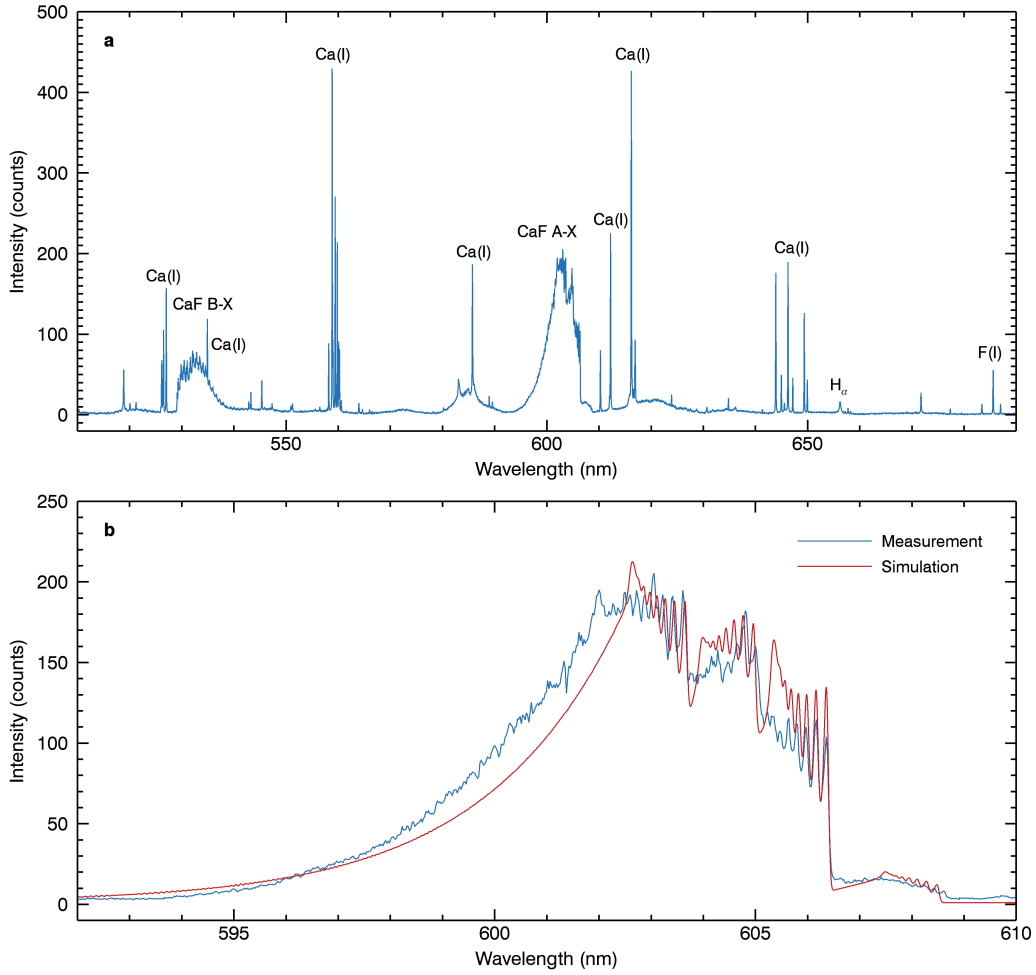

Figure 5.4: a) LIBS spectrum of a sample containing 38.6 wt% CaF_2 and 61.4 wt% K_2SO_4, measured with a delay time of 350 ns and a gate width of 10 µs. b) Comparison of the measured CaF A-X band and the simulated spectrum.

5.2.2 Comparison to LIBS spectrum

In Fig. 5.4a the measured LIBS spectrum of a sample containing CaF_2 is shown. The strongest emission lines in the shown spectral range are Ca(I) lines, but a weak H_α line at 656.3 nm and a moderately strong F(I) line at 685.6 nm can be observed as well. While the F(I) line is relatively intense and could likely be used to quantify the fluorine concentration in this specific sample quite well, the CaF bands are still more intense and offer a significantly improved SNR. Especially the A-X band with its peak at about 603 nm is unusually intense in contrast to the MgCl band and the CaCl band that were investigated in the last chapter. One explanation for this is the high number of intense vibrational transitions that are superimposed here. This effect, which was already predicted by the simulated spectrum, can be observed directly in the LIBS spectrum, see Fig. 5.4b. By increasing its total intensity, the simulated spectrum can be fitted

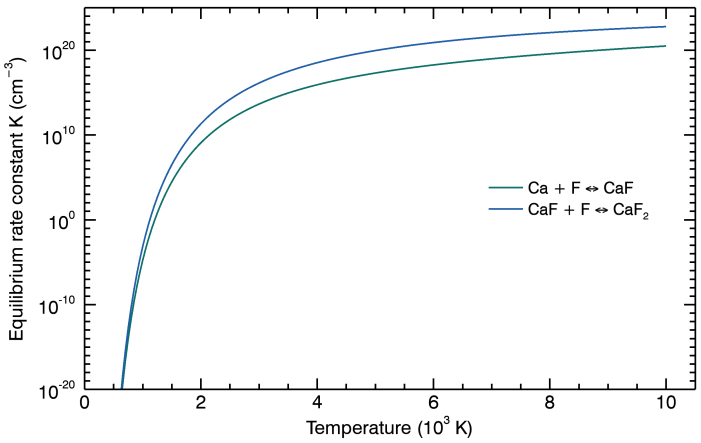

Figure 5.5: Equilibrium rate constants of the reactions $\mathrm{Ca} + \mathrm{F} \rightleftharpoons \mathrm{CaF}$ and $\mathrm{CaF} + \mathrm{F} \rightleftharpoons \mathrm{CaF_2}$ in dependence of the temperature as calculated from Eq. (2.52).

very closely to the measured spectrum, which also shows the shifted branch heads of the different vibrational transitions as a comb-like structure. The temperature seems to be approximately the same with about 5000 K according to the rise of the band at lower wavelengths and the relative intensities of the peaks. However, there are still some differences that seem to be related to the reduced number of vibrational transitions that are considered in the simulation and potentially to inaccurate Franck-Condon factors, since the simulation has some intense peaks that do not appear this way in the measurement. The simulation is still much closer to the measurement than it was in the case of the CaCl A-X band, which might also indicate that the spectroscopic constants that were used for this simulation are more accurate.

5.2.3 Equilibrium plasma composition

The equilibrium plasma composition of a $\mathrm{CaF_2}$ plasma was calculated in the temperature range from 500 K to 20 000 K under consideration of atomic and ionic species as well as the molecules $\mathrm{Ca_2}$, $\mathrm{F_2}$, CaF, and $\mathrm{CaF_2}$. The constants used to calculate the energy levels of the diatomic molecules were taken from [72], while the constants for $\mathrm{CaF_2}$ were taken from [81]. The dissociation energies are $D_0^0(\mathrm{Ca_2}) = 0.4\,\mathrm{eV}$ for $\mathrm{Ca_2}$ [159], $D_0^0(\mathrm{F_2}) = 1.60\,\mathrm{eV}$ for $\mathrm{F_2}$ [72], $D_0^0(\mathrm{CaF}) = 5.5\,\mathrm{eV}$ for CaF [124], and $D_0^0(\mathrm{CaF_2}) = 11.4\,\mathrm{eV}$ for the total dissociation of $\mathrm{CaF_2} \longrightarrow \mathrm{Ca} + 2\,\mathrm{F}$ [32]. The ionization energies of Ca and F were taken from the NIST database.

The equilibrium constants for CaF and $\mathrm{CaF_2}$ as calculated from Eq. (2.52) are shown in Fig. 5.5. They are slightly lower than the equilibrium constants calculated for CaCl and $\mathrm{CaCl_2}$ throughout the temperature range, indicating an equilibrium composition with higher molecular concentrations.

Equivalently to the $\mathrm{MgCl_2}$ and the $\mathrm{CaCl_2}$ plasma simulation, the ratio between Ca

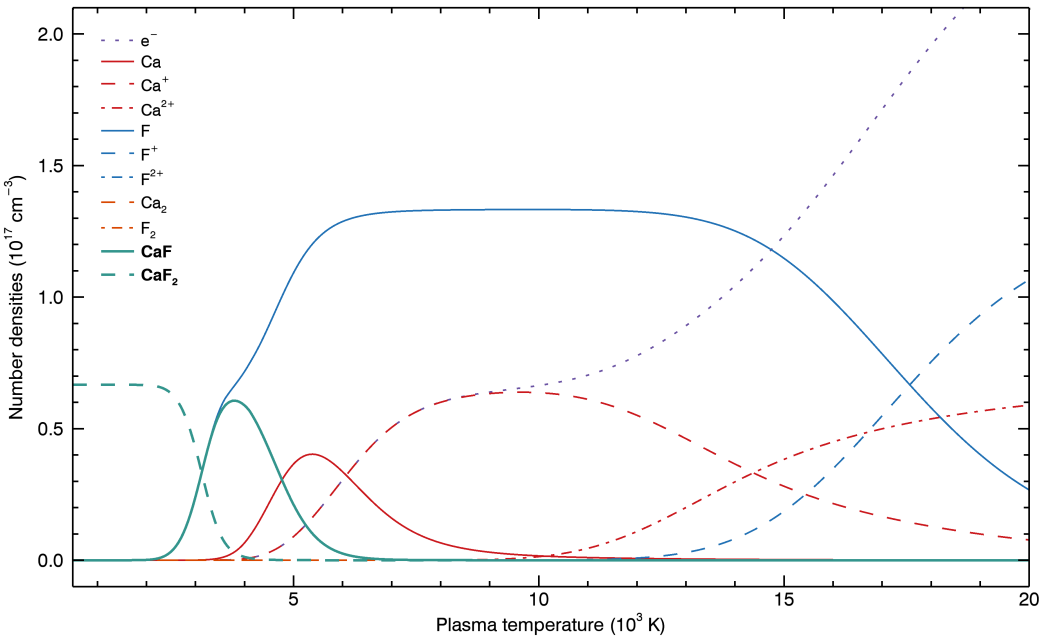

Figure 5.6: Number densities of species in a CaF_2 plasma at equilibrium in dependence of the temperature, as calculated from Eqs. (2.49–2.56). The total number density of nuclei was set to $2 \times 10^{17}\,\mathrm{cm}^{-3}$. At low temperatures, all atoms are bound in CaF_2 molecules. The highest CaF concentrations are found between 2500 K and 6000 K.

and F in the plasma simulation was set to 1:2 and a total number density of nuclei of $2 \times 10^{17}\,\mathrm{cm}^{-3}$ was chosen. The result is shown in Fig. 5.6. As before, the homonuclear molecules, here Ca_2 and F_2, are not formed in significant concentrations. All nuclei are bound in CaF_2 molecules at low temperatures, which dissociate into CaF + F at about 2000 K. The CaF molecules dissociate at around 3500 K, resulting in free Ca atoms which are soon ionized. The F atoms are not ionized until temperatures of about 13 000 K are reached.

Figure 5.7 shows the population density of the vibrational level $v = 0$ of the $A^2\Pi$ state of CaF for the CaF_2 plasma simulation in dependence of the temperature. In comparison to the equivalent population density for CaCl, Fig. 4.11, the peak is shifted towards higher temperatures by about 500 K, so that the highest emission is expected at around 4500 K. If the population of higher vibrational levels was considered as well, the peak emission of the CaF A-X band might shift slightly towards higher temperatures, but this effect would be small since the population at higher temperatures is limited by the higher dissociation rate of the CaF molecules. Accordingly, the simulated band spectrum with a temperature of 5000 K seems to be a good approximation.

The maximum population density of about $6.8 \times 10^8\,\mathrm{cm}^{-3}$ is almost three times higher than the maximum population density that was calculated for CaCl. Together with the higher number of contributing vibrational transitions, this indicates that the

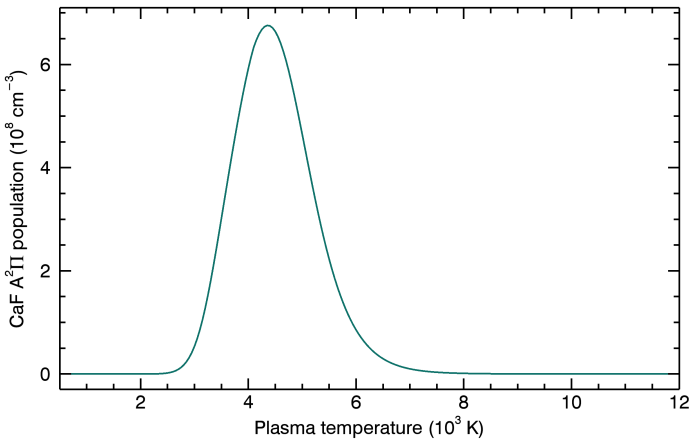

Figure 5.7: Population density of the $A^2\Pi$ $v = 0$ state of CaF in dependence of the temperature as calculated from Eq. (2.7).

CaF A-X band is more intense than the CaCl A-X band in equivalent conditions.

5.3 Dependence on reactant concentrations

Here the dependence of the CaCl band intensity and the CaF band intensity on the reactant concentrations is investigated. The two test series that were made for this study were made to have the same relationship between the reactants and a similar composition. The goal is to investigate whether the CaF band intensity can be described by the same formula that was derived for the CaCl band intensity in the last chapter, Eq. (4.24), and to analyze the differences that can be observed for the two molecular bands. Prior to that, the LIBS spectra of the samples as well as the plasma temperatures and the electron densities are compared, in order to rule out a significant influence of matrix effects and resulting differences in the plasma parameters. After using the derived model to describe the band intensities, calibration curves are presented where the molecular bands are used to quantify the chlorine and fluorine concentrations in the sample without requiring the evaluation of any atomic or ionic emission lines of the two halogens.

5.3.1 Spectra

Figure 5.8 shows the LIBS spectra of the three pure samples $CaCO_3$, Mix 1, and Mix 2. They were averaged from the 10 measurements that were made of each sample with a laser pulse energy of 35 mJ. For the $CaCO_3$ sample, strong lines of Ca(I) and Ca(II) dominate the spectrum. A slight contamination with sodium can be observed by the Na(I) line doublet at 589.0 nm and 589.6 nm. The orange bands of CaO appear between 590 nm and 630 nm, see the inset of Fig. 5.8a.

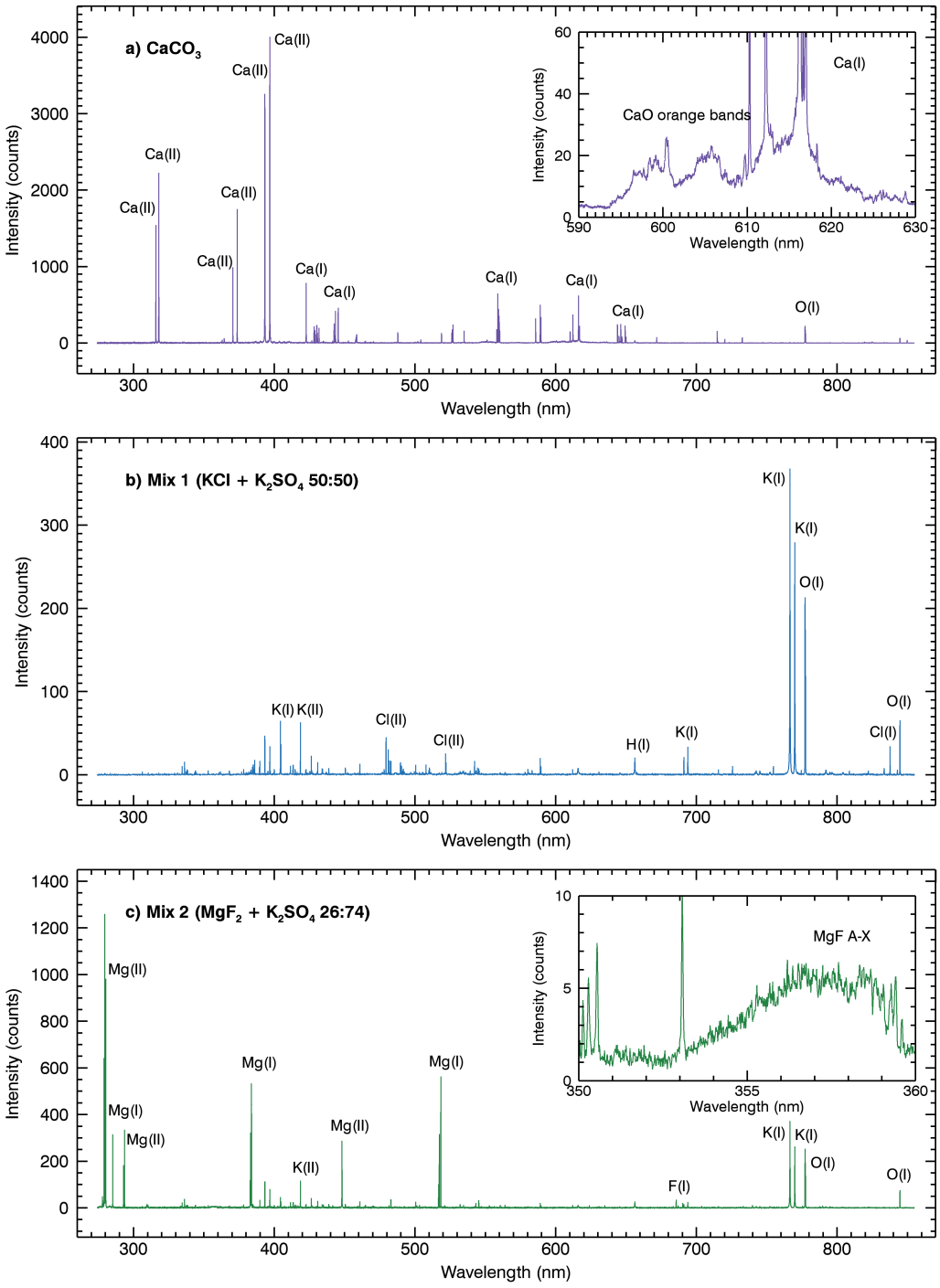

Figure 5.8: LIBS spectra of (a) $CaCO_3$, (b) Mix 1, and (c) Mix 2 showing characteristic emission lines. The $CaCO_3$ spectrum features molecular emissions CaO like the A-X band between 590 nm and 630 nm. In the spectrum of Mix 2, a weak MgF A-X band can be observed. The spectra have been averaged from 10 measurements per sample. The laser pulse energy was 35 mJ.

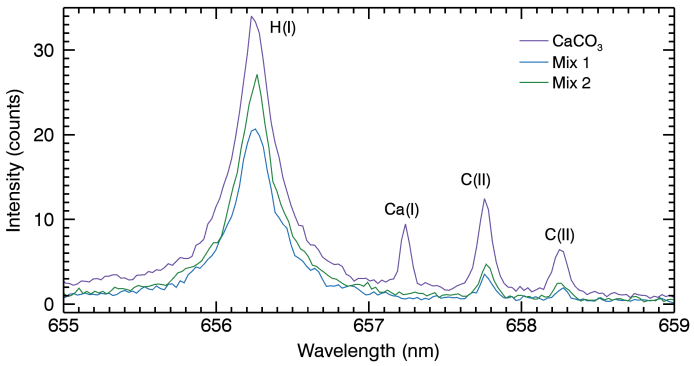

Figure 5.9: H_α line in the spectra of $CaCO_3$, Mix 1, and Mix 2. The Stark broadening is similar for all spectra. Additionally the two C(II) lines can be observed in all spectra. In the spectrum of the $CaCO_3$ sample, a Ca(I) line appears as well.

The spectrum of Mix 1 in Fig. 5.8b is dominated by weak emission lines of K(I), K(II), Cl(I), and Cl(II), with the exception of the strong K(I) lines at 766.5 nm and 769.9 nm. After these two lines, the O(I) triplet at 777.4 nm is the third most intense emission line. The O(I) triplet is at a similar intensity as in Fig. 5.8a, however, indicating that the low overall intensity is not due to a weaker plasma but due to lower transition probabilities of the observed emission lines. The large variation of the total intensity in dependence of the sample composition is a strong argument against a normalization using the total intensity of the spectrum, which is currently done for ChemCam spectra [100, 155].

Mix 2 has a LIBS spectrum with intense Mg(I) and Mg(II) lines as well as emission lines of K(I), K(II), O(I), and F(I) (Fig. 5.8c). The K(I) lines and especially the K(II) line at 418.6 nm are stronger than for Mix 1, even though the K concentration is lower. An explanation for this could be a higher plasma temperature due to the easily ionized Mg in the sample. Another signal of interest is the MgF A-X band between 353 nm and 360 nm, which can be seen in the inset. Since it can be observed for this sample with only 26 wt% MgF_2, it is more intense than the MgCl band at 377 nm. However, it is still weaker than the F(I) line at 658.6 nm and is therefore not suited for the quantification of fluorine. It also seems to be unstable with respect to the formation of CaF, since the MgF band intensity sharply decreased for samples with even small concentrations of Ca. This indicates that the formation of CaF is favored over the formation of MgF, so that the CaF emission is a more robust signal for the detection and quantification of fluorine. The MgF emission was therefore not studied further.

The spectra of all three samples feature the H_α line at 656.3 nm, see Fig. 5.9. Its appearance can be explained by adsorbed water in the samples, and its Stark broadening is used in the following section for the calculation of the electron densities. Since the linewidth does not change significantly for the three different samples, the calculated

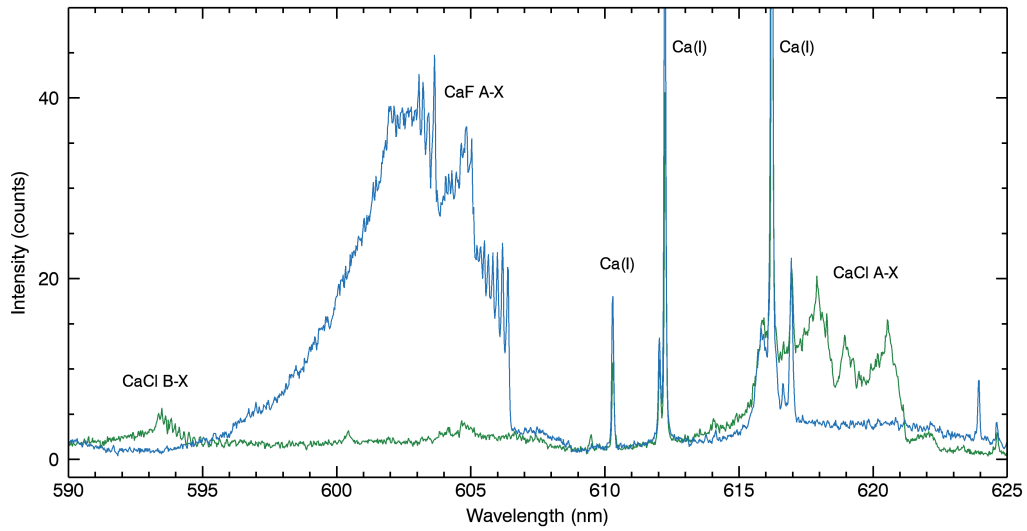

Figure 5.10: Spectra showing the CaF band and the CaCl band for low Ca concentrations and high concentrations of F and Cl, respectively (2.1 at% Ca and 18.3 at% Cl for the CaCl band spectrum, 2.4 at% Ca and 17.6 at% F for the CaF band spectrum).

electron densities will be similar as well.

Close to the H_α line, two weak C(II) lines at 657.8 nm and 658.3 nm appear in Fig. 5.9. They come from the CO_2-dominant Mars-analog ambient gas in the case of Mix 1 and Mix 2, but are especially intense for the carbon-bearing $CaCO_3$ sample. It is surprising that no C_2 bands can be observed in the spectrum of $CaCO_3$, for example the Swan system, which is the most intense C_2 emission. It is possible that the formation of CO is favored over the formation of C_2, so that the latter will only be observed if the oxygen concentration in the plasma is very low.

In the spectra of mixtures of $CaCO_3$ and Mix 1 or Mix 2, respectively, the molecular emissions appear, see Fig. 5.10. The shown spectra are from samples with low concentrations of Ca, but high concentrations of Cl and F (2.1 at% Ca and 18.3 at% Cl for the CaCl band spectrum, 2.4 at% Ca and 17.6 at% F for the CaF band spectrum). The concentrations of Cl and F are similar in these spectra, but the CaF band can be seen to have a much higher intensity than the CaCl band, as predicted by the simulations.

Since the CaCl band and the CaF band are superimposed by the CaO orange bands for high $CaCO_3$ concentrations, the band intensities were obtained by fitting the spectra with linear combinations of normalized pure band spectra of the CaO bands and of either the CaCl or the CaF band. The spectrum of pure $CaCO_3$ (Fig. 5.8a) was used to obtain a spectrum of the CaO orange bands, while the CaCl and CaF band spectra for the linear combination were the ones shown in Fig. 5.10. The band profiles did not change noticeably for different samples, indicating that the temperature at which the molecules were formed was constant for all samples.

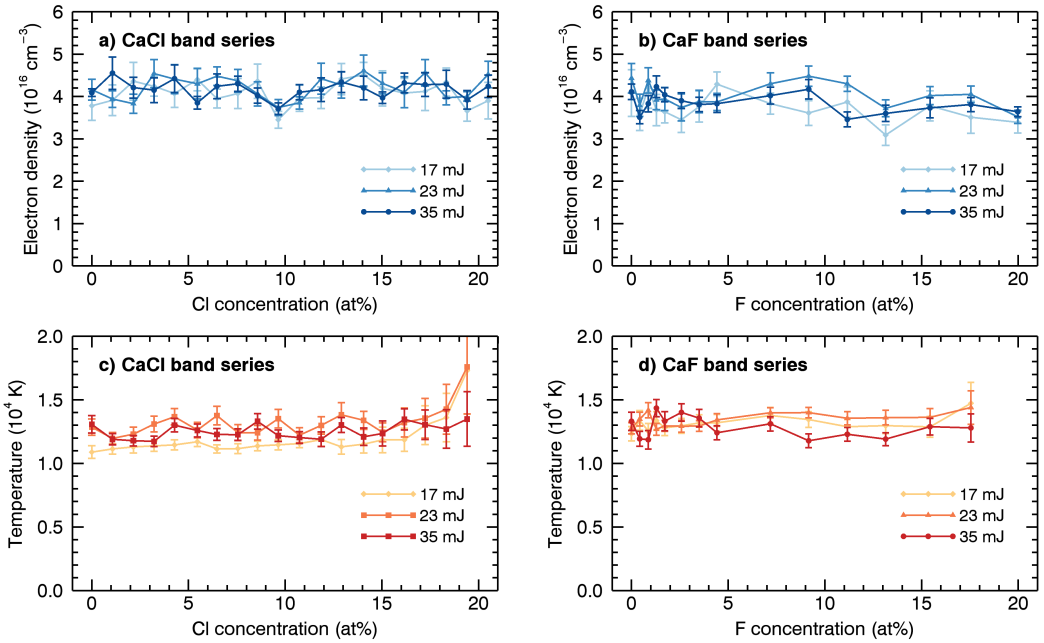

Figure 5.11: Electron densities for (a) the CaCl band series and (b) the CaF band series as well as temperatures for (c) the CaCl band series and (d) the CaF band series. The values do not change significantly for the three laser energies.

5.3.2 Electron density and temperature

If the electron density or the temperature change significantly for the samples within one test series, it is an indication that additional matrix effects occur that need to be considered in the evaluation of the results. Therefore it is important to monitor their values. The gate width of 10 µs that was used for most measurements in this chapter is similar to the plasma lifetime, so that the obtained values for the electron density and the temperature represent average values. If there are significant changes in these plasma parameters, they can be observed with these time-integrated measurements.

For the temperature calculation, Boltzmann plots of the Ca(II) lines at 315.9 nm, 317.9 nm, 370.6 nm, 373.7 nm, and 849.8 nm were used again as in Section 4.3. The electron densities were calculated from Eq. (2.5) after obtaining the Stark broadening of the H_α line as the Lorentzian linewidth of the Voigt fit. Figure 5.11 shows the results for all three laser energies and for both test series. The electron density remains nearly constant at an average value of around $(4.0 \pm 0.3) \times 10^{16}\,\mathrm{cm}^{-3}$ for both test series and for all laser energies. The temperature also does not show a clear trend, though it seems to be lower for 17 mJ/pulse than for the other laser energies in the case of the CaCl band series. As the Ca concentration decreases, the temperature values become less accurate due to the lower intensities of the Ca(II) lines, which explains the sudden increase of the temperature for the CaCl band series close to 20 at% Cl. Generally,

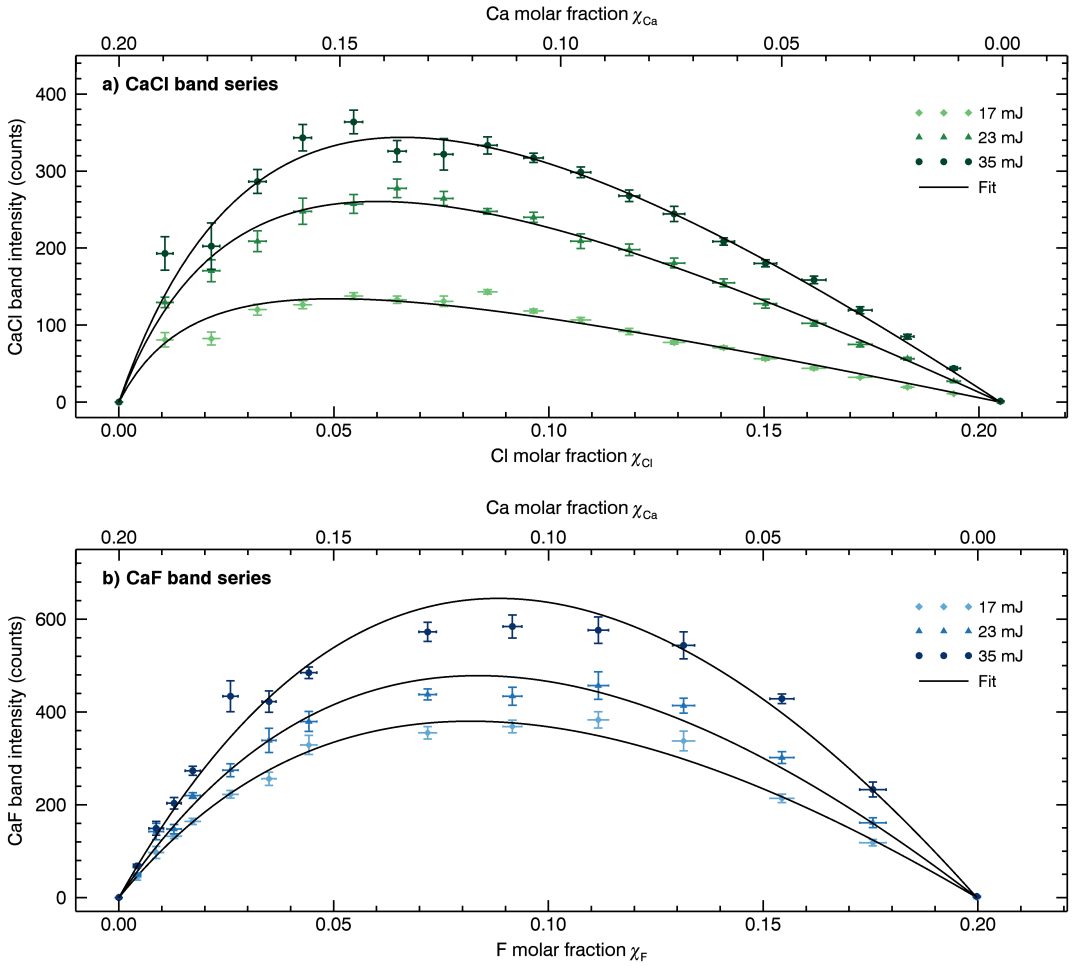

Figure 5.12: a) CaCl band intensity in the CaCl band series. b) CaF band intensity in the CaF band series. The fit based on Eq. (4.24) follows the measured values closely.

the temperature stays close to its average value of about $(13\,000 \pm 1000)\,\mathrm{K}$, however. These results are very similar to those of Section 4.3.4, which supports the theory that plasma plumes generated by laser pulses with higher energy will reach a higher volume, so that the number densities and temperatures within are again similar to those of plasma plumes generated by low-energy pulses.

Since neither the electron densities nor the temperatures change significantly for the different samples and for the different laser energies, it can be concluded that the differences in the measured signal intensities are mostly due to the changes in the sample composition and are not the result of changing plasma parameters.

5.3.3 Band intensities

Figure 5.12 shows the band intensities of the CaCl band and the CaF band for all samples in their respective test series and for all three laser energies. The fit functions

Table 5.3: Fit parameters for the calculation of the band intensity of CaCl and CaF in the CaCl band series and in the CaF band series for all three laser energies.

Laser energy (mJ/pulse)	CaCl band series ζ (counts)	CaCl band series η	CaF band series ζ (counts)	CaF band series η
17	$6 \pm 2 \times 10^4$	43 ± 10	$5.7 \pm 0.2 \times 10^4$	5.4 ± 0.6
23	$7.5 \pm 0.4 \times 10^4$	24 ± 2	$6.8 \pm 0.3 \times 10^4$	4.7 ± 0.8
35	$8.3 \pm 0.6 \times 10^4$	17 ± 2	$8.2 \pm 0.4 \times 10^4$	2.9 ± 0.7

based on the non-equilibrium model presented in Section 4.4.2, Eq. (4.24), are able to describe the band intensities very well in all cases, although there is a slight deviation from the fit function for the CaF band series close to the center of the curve. The curves described by the band intensities of the CaF band series are still slightly skewed towards low F concentrations, but they are closer to a symmetrical shape.

The LTE model described by Eq. (4.14) cannot describe the band intensities in Figure 5.12 correctly. Whereas the measured values of the CaCl band intensities in Section 4.4.2 still matched the LTE model for $T = 3000\,\mathrm{K}$ quite well (Fig. 4.21), the LTE model predicts a maximum intensity at $\chi_{\mathrm{Ca}} = \chi_{\mathrm{Cl}} = 0.1$ for the CaCl band series and at $\chi_{\mathrm{Ca}} = \chi_{\mathrm{F}} = 0.1$ for the CaF band series, regardless of the value of the equilibrium constant K in Eq. (4.14). The model can therefore not explain the asymmetry observed in the curves of both test series, proving that it is an insufficient model to describe the band intensities.

The fit parameters for Eq. (4.24) are shown in Table 5.3. The results for ζ are very similar for both test series. The main difference is in η, which is higher for CaCl, indicating that the reaction from CaCl* to $CaCl_2$ happens at a higher rate than the reaction from CaF* to CaF_2. This could potentially be related to the higher dissociation energy of CaF, which causes it to be more stable at higher temperatures. The intensity of the CaF band is then only slightly reduced by the $\eta\chi_{\mathrm{F}}$ term at high concentrations of F, leading to higher intensities than those of the CaCl band. Another interesting observation is that η declines for the CaCl band and for the CaF band alike if the laser energy is increased. A smaller η means that the dependence on the reactant concentrations approaches the curve predicted by the LTE model. This could indicate that at higher laser energies the formation of the triatomic molecules $CaCl_2$ and CaF_2 has less influence on the band intensity.

5.3.4 Quantification of Cl and F via molecular emission

In order to use the molecular bands of CaCl and CaF for the quantification of Cl and F, respectively, Eq. (4.24) needs to be solved for χ_B, which represents the concentration

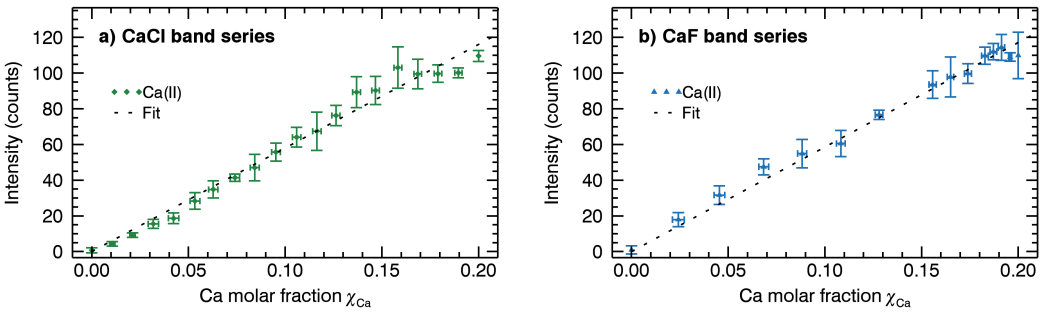

Figure 5.13: Calibration curves for the Ca(II) line at 373.7 nm in a) the CaCl band series and b) the CaF band series, measured at a laser energy of 23 mJ/pulse. The confidence intervals show the 1σ uncertainty calculated from the ten measurements per sample.

of Cl or F in the sample:

$$\chi_B = \frac{I_{\text{A-X}}}{\zeta\chi_A - \eta I_{\text{A-X}}} \tag{5.1}$$

The parameters ζ and η can be obtained from a calibration curve for the corresponding molecular band, and χ_A can be obtained from a calibration curve for the second reactant, in this case Ca. If a proportional calibration curve is used for the calibration of Ca, we get

$$I_{\text{Ca}} = m\chi_A\,, \tag{5.2}$$

where I_{Ca} is the measured intensity of the Ca emission that is used for the calibration, and m is the slope of the calibration curve. This can be inserted into Eq. (5.1) to obtain

$$\chi_B = \frac{I_{\text{A-X}}}{\zeta I_{\text{Ca}}/m - \eta I_{\text{A-X}}}\,, \tag{5.3}$$

so that χ_B is now only dependent on the measured intensities of the Ca emission and of the molecular band, and on the calibration parameters ζ, η, and m.

To investigate how well this method of quantification works, I used the measurements of the CaCl band series and the CaF band series that were made with a laser energy of 23 mJ/pulse, and calculated the molar fractions of Cl and F from them. First, the Ca(II) line at 373.7 nm is used for the calibration of the Ca emission, see Fig. 5.13. From the linear fits the same slope $m = (585 \pm 5)$ counts is obtained. The parameters ζ and η are taken from Table 5.3. Next, I inserted the 10 different measurements of the intensities of the Ca(II) line and of the respective molecular band for each sample into Eq. (5.3) to obtain values for χ_{Cl} and χ_{F}.

The final results can be seen in Fig. 5.14, where the shown values are the mean values of the calculated molar fractions in dependence of the molar fractions that had been obtained from the sample preparation. The confidence intervals correspond to the standard deviations of the 10 calculated values for each sample. For low molar fractions, the calculated values are close to the expected values, which are shown here

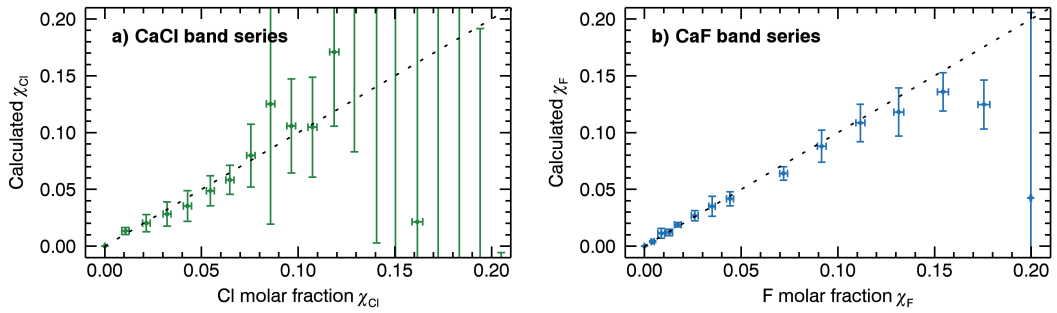

Figure 5.14: Experimentally derived molar fractions of a) Cl in the CaCl band series and b) F in the CaF band series. The intensities and the parameters ζ and η are taken from the measurements at a laser energy of 23 mJ/pulse. The confidence intervals show the standard deviation of ten measurements per sample. The calculated values are most accurate for low Cl and F concentrations.

as a dotted line. The accuracy is lower in the case of the CaCl band series. Here the variation between the different calculated values can be up to 5 at%, while it is closer to 2 at% in the case of the CaF band series. At higher molar fractions, the calculated values become even more inaccurate, again especially for the CaCl band series. The reason is that the denominator in Eq. (5.1) approaches zero for low molar fractions of Ca, so that even small uncertainties in $I_{\text{A-X}}$ will result in large deviations from the real value of χ_B. A high value for η will increase the variance of the results even further, which is why the calculated molar fractions of Cl are less accurate than those of F despite a generally better fit of the band intensities for the CaCl band series.

In general, a *high molar fraction of Ca* and a *low molar fraction of Cl or F* are the ideal case for the quantification of Cl and F via molecular emission. If Cl or F are too high, the quantification will always be more inaccurate. However, at higher molar fractions the Cl(I) line at 837.6 nm and the F(I) line at 685.6 nm can be used for the quantification, so that a combination of these two methods should lead to the most accurate results. If the molar fraction of Ca is too low, no accurate quantification via molecular emission is possible.

5.4 Influence of native bonds

The native bond series that was made for this study consists of four different samples, two for the investigation of the CaCl band and two for the investigation of the CaF band. My hypothesis was that fragmentation during laser ablation will lead to a higher concentration of molecules in the laser-induced plasma plume, since an unexpected high intensity of the CaCl band was observed shortly after plasma initiation in Fig. 4.15. Therefore one sample was made for each molecular band in which the molecular band

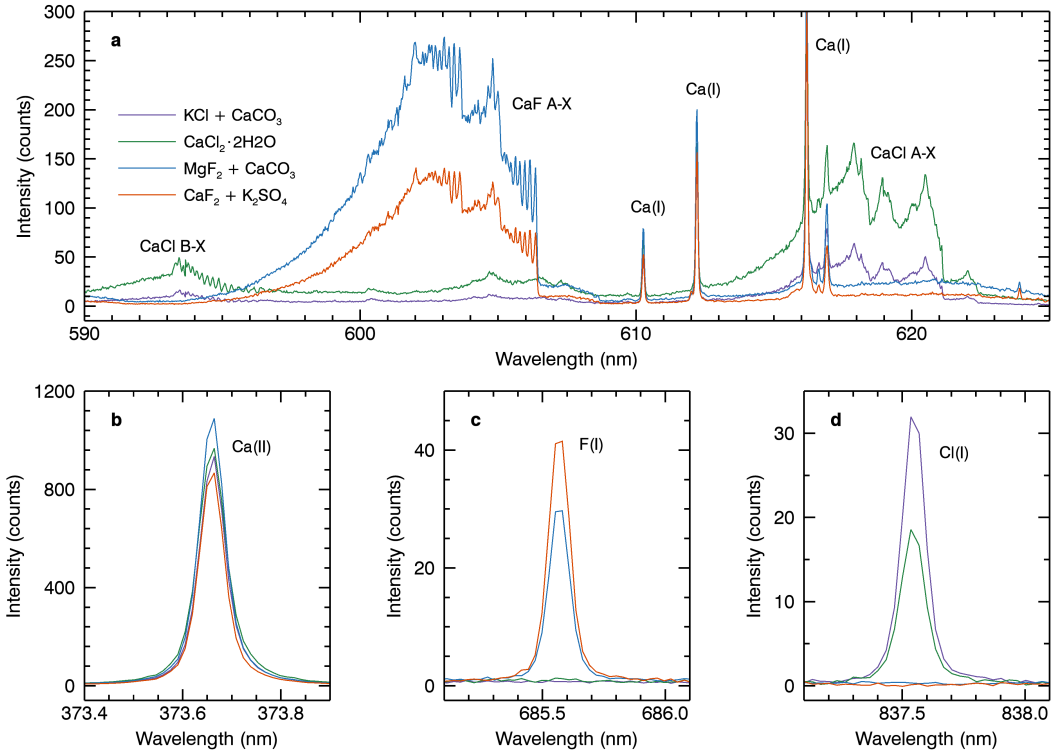

Figure 5.15: LIBS spectra of the samples of the native bond series measured with a laser energy 23 mJ/pulse, averaged from ten different measurements per sample. The CaF A-X band is stronger for the sample without a native Ca–F bond, while the CaCl A-X band is stronger for the sample with a native Ca–Cl bond.

was already present in the sample, and one comparison sample was made where no native bond between the reactants was present. LIBS measurements of the samples were first made with a large gate width of 10 µs, then time-resolved measurements with different delay times and a small gate width of 500 ns were made in order to see whether the time evolution changes in dependence of the sample composition.

5.4.1 Spectra

The spectra of the native bond series that were measured with a delay time of 350 ns and a gate width of 10 µs are shown in Fig. 5.15. The molecular bands change significantly between the two samples that are compared for each band, even though the reactant concentrations (Ca and F for the CaF band, Ca and Cl for the CaCl band) were kept at the same values. The expectation was that the intensity would increase due to an influence of fragmentation leading to the direct formation of CaCl and CaF molecules as fragments of the sample during ablation. This expectation is met in the case of the CaCl band, where the stronger emission can be observed for the sample containing $CaCl_2$. However, the opposite effect can be observed for the CaF band: here the much

more intense band can be observed for the sample that does *not* contain CaF_2. This result is surprising and cannot be explained by a simple fragmentation effect, though it is likely still related to matrix effects due to the different sample compositions. The uncertainties of the elemental concentrations in the samples are too small to play a role here.

The intensity of the CaCl band increases by a factor of 2.8 for the sample containing $CaCl_2$ in comparison to the sample without bonds between Ca and Cl. If this increase was simply the result of higher number densities of the species in the plasma, then the Ca(II) line at 373.7 nm and the Cl(I) line at 837.6 nm should also increase by a significant factor. However, only the Ca(II) increases slightly, and not by a large amount (Fig. 5.15b). The Cl(I) line instead decreases significantly as the band intensity increases (Fig. 5.15d), which could indicate that more Cl is bound in CaCl molecules.

For the CaF band, the intensity is about 1.9 times lower for the sample containing CaF_2 than it is for the sample containing no CaF_2. The same effect as for the CaCl band can be observed, however, where the spectrum with the stronger molecular emission also has a stronger Ca(II) line intensity (Fig. 5.15b), but a weaker F(I) line intensity (Fig. 5.15c). It is interesting that this relationship is similar in both cases despite the reversed effect for the CaF band intensity. For the CaCl band alone, where the intensity was stronger for the sample with Ca–Cl bonds, the reduction of the Cl(I) signal could have been an indication of fragmentation leading to a higher CaCl density and to less Cl atoms in the sample. However, since the F(I) line is also reduced here for the sample in which fragmentation cannot be a formation process for CaF, it seems more likely that the formation of molecular bands generally leads to a reduction of the halogenic line intensities, regardless of the formation process of the molecule. This is surprising considering Fig. 4.10 and Fig. 5.6, where the number densities of neutral Cl and F atoms were found to be consistently high over a large temperature range, so that the halogenic emission should not be strongly affected by molecular formation in the low-temperature regions of the plasma.

5.4.2 Time-resolved measurements

In order to investigate the observed differences between the influence of the sample composition on the CaF band intensity and on the CaCl band intensity, time-resolved measurements were made with a small gate width of 500 ns. The time-resolved CaCl and CaF band intensities can be seen in Fig. 5.16. It can be seen that the two weaker molecular emissions of the $KCl + CaCO_3$ mixture and of the $CaF_2 + K_2SO_4$ mixture (a and d, respectively) have a very different time evolution than the more intense emissions (b and c). For the $CaCl_2 \cdot 2\,H_2O$ sample and the $MgF_2 + CaCO_3$ sample, the band intensity starts at a high intensity early in the plasma and then quickly increases further until the maximum is reached for a delay of about 1 µs, at which point the

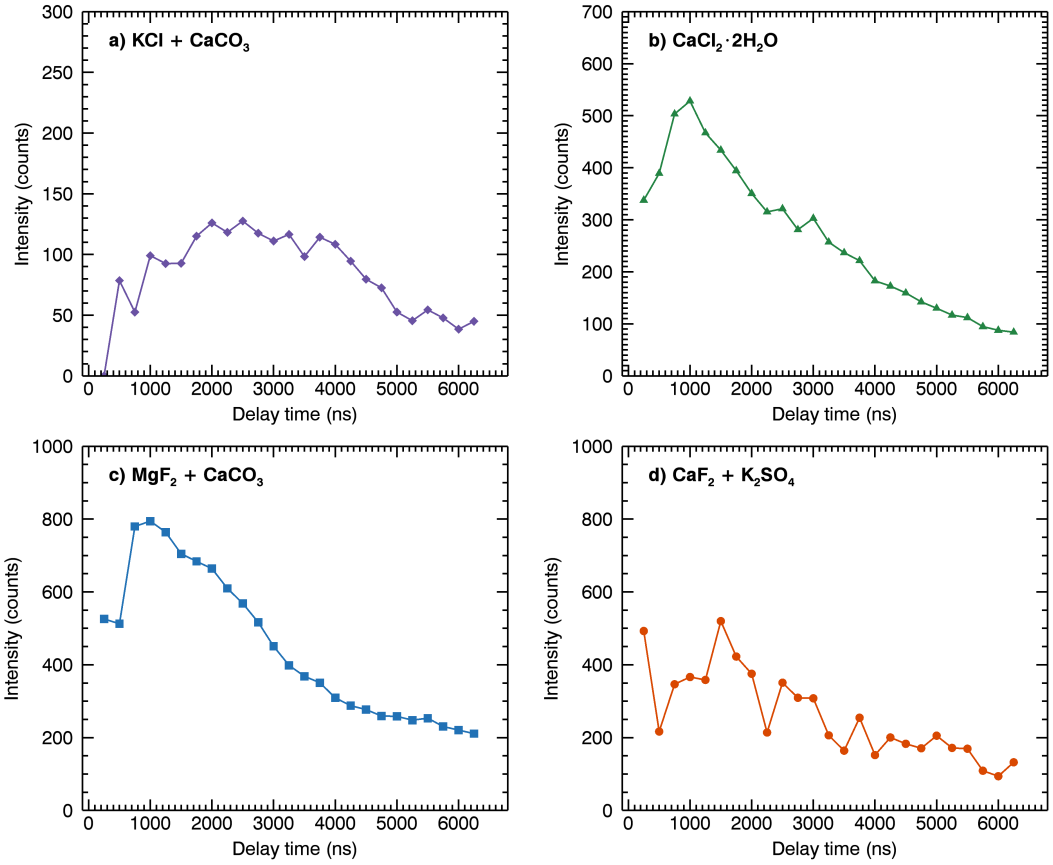

Figure 5.16: Band intensities of CaCl and CaF in the native bond series in dependence of the delay time.

intensity decreases relatively quickly. Both resemble the more detailed time evolution of $CaCl_2 \cdot 2\,H_2O$ shown in Fig. 4.15. For the $KCl + CaCO_3$ mixture, the band intensity is zero at the shortest delay time and only increases slowly, reaching a maximum after 2 µs that is maintained for a relatively long time before the intensity decreases more quickly after 4 µs. This time evolution seems to be that of molecules that are being formed in chemical reactions over time. The time evolution of the CaF band intensity for the sample containing CaF_2 is very irregular, starting at a relatively high value but then falling and rising several times. It is unlikely that this result accurately represents the time evolution of the CaF emission in a single plasma. Instead, it is likely that the CaF signal changed a lot in between measurements, which might indicate that the CaF_2 in the sample is not ablated efficiently, causing a high variation of the LIBS signals. Since a high band intensity is measured at the lowest delay time, it is possible that fragmentation does actually occur in the sample, but causes a higher variation of the LIBS signals instead of a consistently increased CaF band intensity.

The differences in the time evolution of the signals in dependence of the sample

composition generally support the idea that strong matrix effects are responsible. If the differences were caused by different reactant concentrations, the time evolution of the band intensities would not change as much as it does here. Whether the native bonds in the samples and fragmentation during the ablation process play a role here is not clear, but it seems that other physical matrix effects could be more dominant.

5.5 Influence of competing molecules

The goal of this study was to investigate potential matrix effects resulting from the competing formation of different molecules in the laser-induced plasma, specifically the influence that the formation of CaCl and CaF in the same plasma has on their intensities. In the two test series, the reactants of one of the molecules were kept at nearly constant concentrations while the concentration of the third potential reactant was increased.

The results are shown in Fig. 5.17, where some intensities have been normalized due to a strong variance of the signals around the observed trend. The variance of the molecular emissions was found to be correlated with that of signals corresponding to specific salts in the mixtures, indicating that the concentrations of these salts varied more than intended in between samples. This is likely due to the higher uncertainty of the mixing process for this study. The variance of the CaF band intensity in Fig. 5.17b was correlated with the variance of the Ca lines, so that the effect was normalized with the intensity variation of the Ca(II) line at 373.7 nm, i.e. the CaF signal was divided by the Ca(II) signal and then multiplied by the linear fit for the Ca(II) signal, so that the variance was significantly reduced without changing the general trend of the measurements. Equivalently the CaF band in Fig. 5.17c was normalized with the Mg(II) line at 293.6 nm, and the CaCl band in Fig. 5.17d was normalized with the Ca(II) line at 373.7 nm.

In the case of the Cl variation series, Fig. 5.17a and b, the CaCl band intensity can be seen to increase steadily in intensity as the Cl concentration is increased, but the CaF band intensity is not strongly affected. The sample with the highest Cl concentration contains three times more Cl than F, but the CaF emission is still close to its average value. A different observation can be made for the F variation series, Fig. 5.17c and d, where the CaCl band intensity can be seen to decrease strongly as the CaF band intensity increases.

The non-equilibrium model based on Eq. (4.24) that was used successfully in Section 5.3 was also used to fit the increasing band intensities in Fig. 5.17a and Fig. 5.17c. However, the parameters from Table 5.3 for the CaCl band and for the CaF band do not fit well in this case. The new fit parameters for the CaCl band in Fig. 5.17a are $\zeta = (3.6 \pm 0.3) \times 10^4$ counts and $\eta = 5.7 \pm 2.2$. If there were no other influences, a

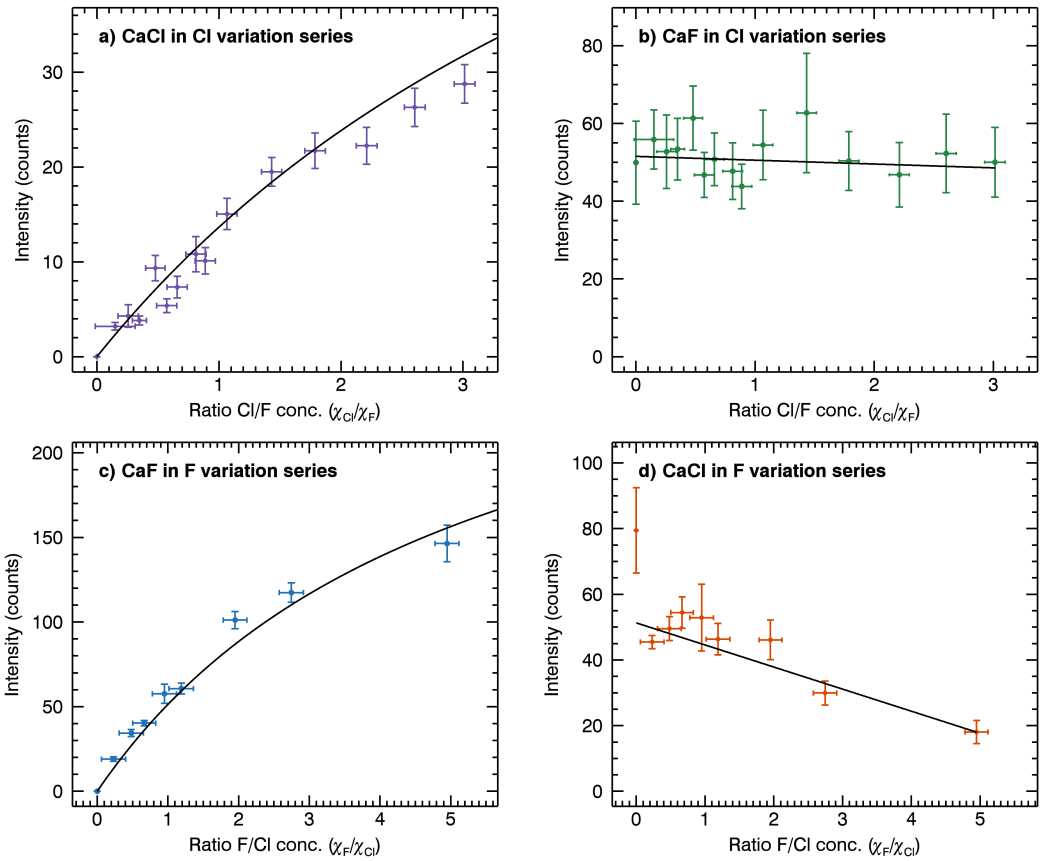

Figure 5.17: Intensities of the CaCl band and the CaF band in the samples of the Cl variation series (top) and the F variation series (bottom), measured with a laser energy of 23 mJ/pulse. Due to a high variance of the data, 15 measurements per sample were made. The CaF band intensity is not affected by the addition of more Cl, while the CaCl band intensity decreases for increasing F concentrations. The intensities in (b) and (d) have been normalized with the intensity variation of the Ca(II) line at 373.7 nm, while (c) has been normalized with the intensity variation of the Mg(II) line at 293.6 nm.

smaller η would indicate that the plasma parameters have changed considerably, so that the reaction rates have changed. However, given the setup of the experiment it is more likely that the reaction rates are actually similar to the ones given in Table 5.3, but that the concurrent formation of CaF molecules reduces the Ca concentration in the plasma. This would result in reduction of the fit parameters because the condition of a stoichiometric plasma, in which the number densities of the species are proportional to their molar fractions in the sample, is not fulfilled anymore.

In the case of the CaF band in Fig. 5.17c, the fit parameters are higher than they are in Table 5.3. They are $\zeta = (1.4 \pm 0.1) \times 10^5$ counts and $\eta = 6.4 \pm 2.2$. The parameter ζ is about twice as high as in the earlier measurement, implying an increased rate of CaF formation or an increased ablation rate that results in higher number densities in

the plasma. Since η also depends on the number densities in the plasma, the higher values of both parameters could be related to this kind of matrix effect. An increased formation of CaF molecules seems unlikely, since there is still the concurrent formation of CaCl molecules taking place in the plasma, even if it seems to be less favored than the CaF formation.

5.6 Summary and discussion

Different studies were made in order to compare the CaCl emission and the CaF emission in LIBS and to improve the understanding of the processes that influence the intensity of molecular emissions in LIBS in general. The CaF A-X band was analyzed with the help of simulations of the CaF A-X spectrum and of the plasma in equilibrium for a CaF_2 sample. The dependence of the CaCl band intensity and the CaF band intensity were investigated in two dedicated test series and were fitted with the non-equilibrium model that was introduced in the last chapter. The influence that native bonds in the sample between the reactants might have on the band intensities of CaCl and CaF was investigated in samples with equal concentrations of the reactants, but with different compositions. And finally, the influence of the competing formation of CaCl and CaF molecules in the same plasma was investigated in two dedicated series.

The simulated CaF A-X band spectrum matched the measured LIBS spectrum closely. However, a large number of 15–20 vibrational transitions needs to be considered to achieve the accuracy that is needed for the fit of a measured band spectrum. This increases the importance of accurate spectroscopic constants for the higher vibrational states as well as accurate Franck-Condon factors. The differences between the simulated spectrum and the measured spectrum are the result of using only the first nine vibrational transitions, approximating the potential curves as Morse potentials, and using available spectroscopic constants that are often only accurate for lower vibrational levels [67]. While the large number of superimposed, intense vibrational transitions makes fitting the CaF band spectrum more challenging than for other molecular emissions with fewer superimposed vibrational transitions, it is also responsible for the high intensity of the CaF band that makes it interesting for spectroscopic analysis.

The simulation of the CaF emission in dependence of the temperature showed that the temperature range for intense CaF emissions is slightly higher than that for intense CaCl emissions. The maximum population density of the CaF $A^2\Pi$ state was found to be about three times higher than for CaCl, which in addition to the higher number of vibrational transitions that are superimposed in the CaF A-X band explains the higher intensity of the CaF A-X band.

The non-equilibrium model that was derived in the last chapter has been shown to accurately describe the band intensities of both CaCl and CaF in the test series that

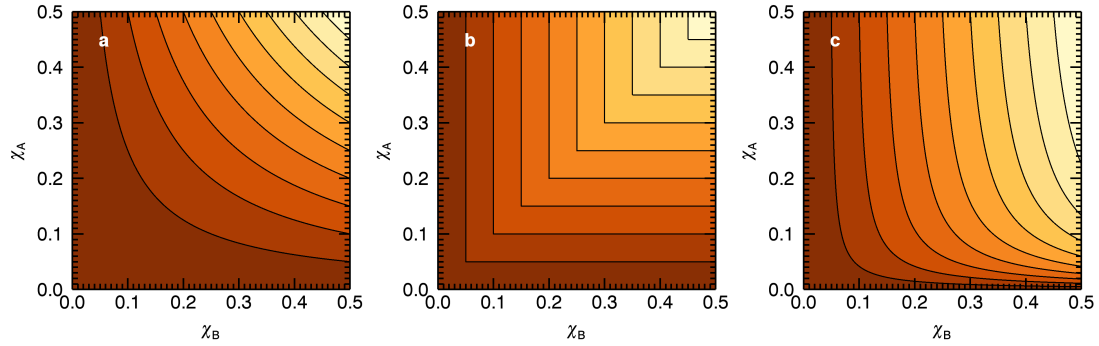

Figure 5.18: Theoretical intensity of the emission of molecule AB in dependence of the molar fractions χ_B and χ_A for different models, where B represents the halogen. a) LTE model with $K \to \infty$. b) LTE model with $K = 0$. c) Non-equilibrium model with $\eta = 20$. Lighter colors represent higher intensities.

were made. In the direct comparison with nearly equivalent test series, the CaCl band exhibited the same strong asymmetry as in the last chapter, while the asymmetry found for the CaF band was significantly less pronounced. The maximum CaF band intensity was still slightly skewed towards a higher Ca concentration and a lower F concentration, however. An open question from the last chapter was whether the LTE model could describe the band intensities correctly if the equilibrium constant K was changed to be closer to $K \to \infty$ or to $K \to 0$. These extreme cases are shown conceptually in Fig. 5.18a and b, while Fig. 5.18c shows the non-equilibrium model. In the LTE model with $K \to \infty$, the maximum intensity would be found where the product of the concentrations is maximized (Fig. 5.18a). In the equilibrium model with $K = 0$, it would be where the concentrations are equal (Fig. 5.18b). For the two new test series, both of these cases would lead to a maximum at $\chi_B = chi_A = 0.1$, in the center of the curves, so that no asymmetry would be observed. The asymmetry of the intensities in these test series is therefore a clear indication of non-equilibrium effects that can be approximated with my non-equilibrium model (Fig. 5.18c).

The influence of these non-equilibrium effects seems to decrease for increasing laser energies, since η decreased for both the CaCl band and the CaF band as the laser energy was increased. A potential explanation for this is that the plasma plume becomes more homogeneous at higher laser energies and is therefore closer to the equilibrium case. If the reason for this change is related to the higher total number density of species in the plasma at higher laser energies, it might even be possible that the non-equilibrium effects would also decrease as the ambient pressure increases and the plasma is more confined. In that case the observed non-equilibrium effects would only be as strong because of the special experimental conditions in Martian exploration with LIBS, making dedicated studies for LIBS in Martian exploration even more important. The conditions that affect ζ and η should be investigated more closely in future studies.

Using the non-equilibrium model and the fit parameters, the molar fractions of Cl and F in the two test series were calculated. The results are especially accurate for high fractions of Ca and low fractions of Cl and F, while they are highly inaccurate for high Cl and F fractions. This initially surprising observation is actually a statistical result of the multivariate nature of the band intensity. If the molar fraction of Ca is too low or the molar fraction of Cl or F is too high, the uncertainty of the band intensity has a much stronger impact on the quantification result. On the other hand, even very low Cl or F fractions can be accurately calculated as long as the Ca fraction is high enough. The accuracy is strongly decreased for high η values and low band intensities, which makes the quantification of Cl via CaCl less accurate than the quantification of F via CaF.

In the study on the influence of the native bonds, I found that the chemical composition of the sample can have a strong impact on the band intensities even if the molar fractions of Ca and Cl/F stay the same. The initial hypothesis that fragmentation during the ablation might increase the number of molecules in the plasma, which would result in higher band intensities for both CaCl and CaF, could not be confirmed completely. While the CaCl band intensity strongly increased for the sample containing Ca−Cl bonds in comparison to the sample without these bonds, the opposite effect could be observed for the CaF band, which was much stronger for the sample containing no Ca−F bonds. In the time-resolved measurements of the samples it was found that the time evolution of the weaker molecular emissions looked different from that of the stronger molecular emissions. It is clear that strong matrix effects are observed here, but the origin is not certain. It is possible that physical matrix effects like the hardness of the materials and the looseness of the grains in the pressed samples play a more important role than fragmentation in the case of the CaF band. For the CaCl band, the observations were exactly as they would be expected if fragmentation played an important role, however. In the sample without Ca−Cl bonds, the band intensity increased much more slowly and stayed at a lower level over time, supporting the idea that in this case reactions in the plasma are the only formation process for the CaCl molecules. Since the strong matrix effects that were observed will have a large impact on the correct quantification of Cl and F, I believe that further studies on this subject are very important if molecular emissions are to be utilized for the quantification of halogens.

In the last study I investigated the influence of the simultaneous formation of CaCl and CaF in the plasma on their respective band intensities. I found that the CaF emission is barely affected by the formation of CaCl in the same plasma, while the CaCl emission was strongly affected by the formation of CaF. The CaCl band intensity decreased as more fluorine was added to the sample composition. This suggests that the formation of CaF is favored over the formation of CaCl, which is in line with the

higher dissociation energy of CaF and with the consistently lower equilibrium constant K of the CaF reaction. The results show that the hierarchy between different molecules has an influence on the band intensities. If CaCl and CaF bands appear in the same LIBS spectrum, the CaF band intensity can be used with the usual calibration, but for the CaCl band the intensity will be reduced, which needs to be considered for a correct quantification.

6. Plasma Imaging Setup

Spatially resolved measurements of the emission of the laser-induced plasma can improve the understanding of LIBS spectra [2, 7, 96]. In many LIBS studies, the plasma is approximated as an isothermal, uniform, and mostly stationary system. More advanced models that have been used to describe the plasma use two layers, a hot plasma core and a colder periphery [66, 104]. These approximations can be insufficient for complex plasmas. The dynamic nature of the plasma and the species within can lead to large differences in the spatial distributions of different species. Temperature gradients within the plasma can also occur, making the calculation of the plasma temperature challenging as different regions within the plasma will have different temperatures.

The model of an isothermal, uniform, and stationary plasma is also based on measurements in terrestrial conditions. The high atmospheric pressure on Earth confines the plasma, which equalizes the plasma temperature and increases the homogeneity of the plasma. In Martian atmospheric conditions or at even lower pressures, the lack of confinement leads to a large plasma plume with strong variations of the temperature and of the concentrations of the plasma species. The laser-induced plasma in these low-pressure ambient conditions has not been characterized in detail with regards to the influence of spatial variations.

In this chapter I present the plasma imaging setup that I developed at the DLR in Berlin. The setup enables spatially and temporally resolved measurements of the laser-induced plasma in simulated low-pressure environments, for example in simulated Martian atmospheric conditions or at low pressures down to 5 mPa, which can approximate the ambient conditions of planetary bodies without atmospheres. First the design is presented along with an overview of the instrumentation that was used in the setup. In the next section, the system is characterized by its image quality, its detection efficiency, and its spectral resolution. The final section describes how measurements are made with the setup.

6.1 Design and instrumentation

A schematic of the plasma imaging setup can be seen in Fig. 6.1. A pulsed laser is used to ablate material from the sample inside the simulation chamber, which causes the plasma formation. The plasma is imaged onto the slit of the imaging spectrometer, which images the selected spectral range onto the ICCD camera while keeping the spatial information along the slit. The ICCD camera enables time-resolved measurements

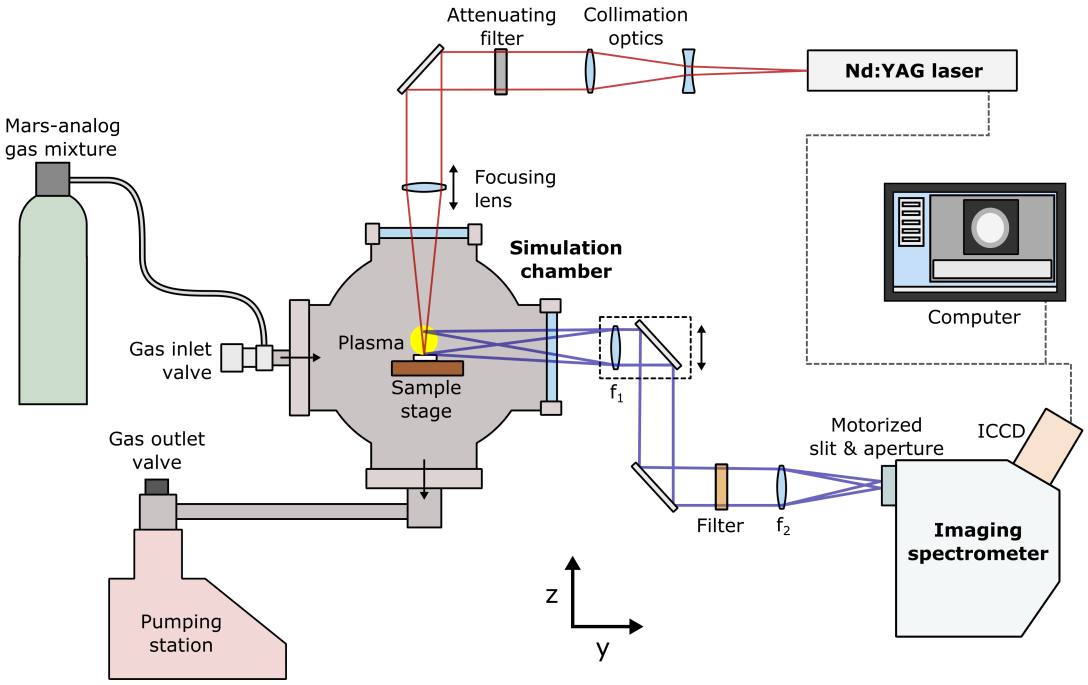

Figure 6.1: Schematic of the plasma imaging setup.

with its photocathode. The details of the design will be described in the following.

Laser The laser (Quantel Viron) is a Q-switched Nd:YAG laser with a wavelength of 1064 nm, a frequency of 1–22 Hz, a pulse width of 8.1 ns, and a pulse energy of 30.7 mJ. The pulse energy can be reduced with filters in the optical path where the beam is collimated. For plasma imaging measurements, a low frequency of 2 Hz is advantageous since the sample needs to be moved in between all measurements, so that previous ablation craters do not affect the results. The laser is synchronized with the camera by a pre-trigger signal that the laser transmits to the camera. In the optical path, the laser beam is first collimated, then redirected downward by a mirror above the chamber window. A focusing lens with $f = 150\,\text{mm}$ above the window focuses the beam into the simulation chamber. The position of the lens can be adjusted to change the vertical focus position of the laser beam inside the chamber. The laser beam is perpendicular to the sample surface, though the angle can be varied slightly by adjusting the mirror with its adjustment screw. This is used to change the position of the focal point on the sample, so that successive laser pulses do not hit the same position. These adjustments of the focal point are only made along the axis of the optical path of detection (i.e. in the left-right direction in Fig. 6.1), so that the plasma does not change its location on the camera image. The slight deviations from a perpendicular incidence do not affect the measurements noticeably.

Simulation chamber The simulation chamber is the central component of the setup. It is connected to a pumping station (Pfeiffer Vacuum HiCube 80 Eco) which can reduce the pressure in the chamber to less than 50 mPa. In order to insert ambient gas, it has a gas inlet with a fine adjustment valve that can be connected to different sources of ambient gas, for example to the Mars-analog gas described in Chapter 3. The chamber contains a stage on which the samples are placed and has one window at the top and one window at the side. The laser beam is directed vertically into the chamber through the top window, while the light of the plasma is collected through the side window. If the plasma is axisymmetrical about the normal of the sample surface or about the optical axis of the laser, this configuration makes it possible to obtain a symmetrical side view of the plasma, from which the intensity of the emission along the radius can be calculated. An external micrometer screw enables the lateral translation of the sample stage by about 25 mm in the direction normal to the paper plane in Fig. 6.1. This enables measuring the sample at different lateral positions or moving to a second sample without having to open the simulation chamber.

Collection optics The collection optics image the object in focus onto the slit of the spectrometer. They consist of two UV grade fused silica singlet lenses and two UV-enhanced aluminum mirrors. The lens and the mirror in front of the window of the simulation chamber can be vertically translated by about 25 mm with a micrometer screw in order to scan different heights of the plasma. The lens collimates the light so that this vertical translation does not affect the focus at the slit. It has a focal length of $f_1 = 200\,\mathrm{mm}$ at the design wavelength of 588 nm. In order to be able to detect the full plasma, a focal length of $f_2 = 150\,\mathrm{mm}$ was chosen for the second lens, so that the magnification of the collection optics is $M_C = f_2/f_1 = 0.75$ if both lenses are in their focus positions, i.e. if the distance from the object to the first lens is $d_1 = 200\,\mathrm{mm}$ and the distance between the second lens and the slit is $d_2 = 150\,\mathrm{mm}$. However, due to the chromatic aberration of the lenses it can be preferable to adjust the positions of the lenses for the specific spectral range that is investigated. For the measurements in this thesis, a compromise was attempted by optimizing the lens positions for a wavelength of $\lambda = 400\,\mathrm{nm}$. The distance between object and first lens was set to $d_1 = 185\,\mathrm{mm}$ while the distance from the second lens to the slit was kept equal to its focal length with $d_2 = 150\,\mathrm{mm}$, so that the magnification should be $M_C = d_2/d_1 = 0.81$.

Spectrometer and camera The spectrometer (Andor Kymera 328i) is an imaging Czerny-Turner spectrometer with the focal length $f = 328\,\mathrm{mm}$ and the f-number $f/\# = 4.1$. It has a motorized slit with an adjustable width of 10–2500 µm. Behind the slit there is a motorized aperture which can be adjusted to reduce or increase the cone angle of the light that is imaged onto the detector. The gratings are mounted on a

Table 6.1: Gratings of the spectrometer with their number of lines per millimeter and their blaze wavelength.

	Lines/mm	Blaze wavelength (nm)
Grating 1	1200	500
Grating 2	1200	750
Grating 3	2400	240

grating turret, which can be rotated to select different wavelength ranges. The three different gratings that are installed are listed in Table 6.1. The camera (Andor iStar 334T) is an ICCD with a 1024×1024 pixel detector and a photocathode that is sensitive from 180 nm to 850 nm. It can be gated with a time resolution of less than 2 ns. In order to reduce noise in the measurements, it can be cooled down to $-30\,^{\circ}\mathrm{C}$. The software Andor SOLIS was supplied with the spectrometer, which was used to control the measurement parameters such as the camera settings, the slit width, the grating, the selected wavelength range, and the size of the aperture.

Wavelength filters Several spectral filters can be inserted into the setup in the collimated part of the optical path of the detection. One is an edge filter which blocks wavelengths up to 450 nm. This filter is necessary for measurements at wavelengths longer than 450 nm, because the second order of shorter wavelengths can otherwise be observed in the spectra. With the edge filter, the shortest wavelength at which a second order can be observed is 900 nm, which is outside of the spectral range of interest. Below 450 nm, no filter is needed as the efficiency of all gratings drops quickly at 230 nm. In addition to the edge filter, various bandpass filters can be used as well. If the angle of the grating in the spectrometer is adjusted so that the zero-order is imaged onto the camera, the image is not spectrally resolved and a normal image of the object in the focus position is obtained. In this measurement mode, a bandpass filter can be used to look at a specific spectral range without losing the two-dimensional spatial information. Five bandpass filters are currently used: one at 780 nm (FWHM 10 nm) for the O(I) triplet at 777.4 nm, one at 770 nm (FWHM 10 nm) for the two K(I) lines at 766.5 nm and 769.9 nm, one at 656.3 nm (FWHM 1.2 nm) for the H_α line at 656.3 nm, one at 600 nm (FWHM 10 nm) for the CaF band at 603 nm, and one at 380 nm (FWHM 10 nm) for the investigation of the Mg(I) lines at 382.9 nm, 383.2 nm, and 383.8 nm.

Synchronization of laser and camera For precise time-resolved measurements, the ICCD needs to be synchronized with the laser with a precision in the nanosecond range. This is challenging because the two instruments have different internal clocks, and because the ICCD needs to do frequent cleaning cycles and is only responsive at

certain times. To avoid this cleaning cycle, the ICCD has to be the master that controls the laser, but it is not possible to precisely time the laser pulse in this case. Therefore the laser is used as the master. The laser has a pre-trigger signal that is sent out at a precise time interval before the laser pulse, which can also be adjusted. This pre-trigger signal is used as the trigger for the ICCD. Measurements of the signals of the pre-trigger, the ICCD exposure, and the time gate of the ICCD show that the ICCD time gate can be synchronized with the laser with a precision of less than 10 ns, but only if the delay time of the ICCD and the time between the pre-trigger signal and the laser pulse are both larger than the fluctuations of the ICCD exposure time, which varies from 0 µs to 25 µs. Therefore the pre-trigger signal is set to be sent out 30 µs before the laser pulse, and the zero-delay of the ICCD is set to 29.96 µs, because there is a constant difference of 40 ns between the two signals. Apart from the variation of the camera's exposure time in relation to the trigger signal, no significant jitter was observed.

6.2 Characterization

Here several measurements are shown that were made to characterize the setup. First the sharpness of the image at different wavelengths is investigated and the magnification of the setup is calculated. Next the vignetting of the image is investigated with a uniform light source. Finally, measurements of the spectral resolution and the spectral efficiency are shown.

6.2.1 Sharpness and magnification

Figure 6.2 shows the image of a metal ruler that was placed in the focus of the setup. It was measured in normal room lighting in the zero-order of Grating 1 with a maximum aperture and a maximum slit width of 2500 µm. The image is quite sharp in the middle, but gets slightly more blurry at the edges. Based on the scale of the ruler, the spatial resolution of the setup is 64.8 pixels/mm or 15.4 µm/pixel. Since a pixel of the ICCD is 13.3 µm wide, this means that the actual magnification of the system is $M_{\text{tot}} = 0.86$ instead of the magnification of $M_C = 0.81$ that was calculated from the focal lengths of the collection optics. This is because the spectrometer also has a slight magnification. The 2500 µm slit is 200 pixels wide in the image, which corresponds to 2.66 mm on the image plane if the pixels are 13.3 µm wide. This means that the magnification of the spectrometer is $M_S = 1.064$, and the magnification of the collection optics is $M_C = M_{\text{tot}}/M_S = 0.81$, which is the same as the magnification that was calculated from the distances of the collection optics.

Since the image of the ruler was made in normal room lighting, it only shows that images taken in the visual range are in focus. For the UV range, measurements are

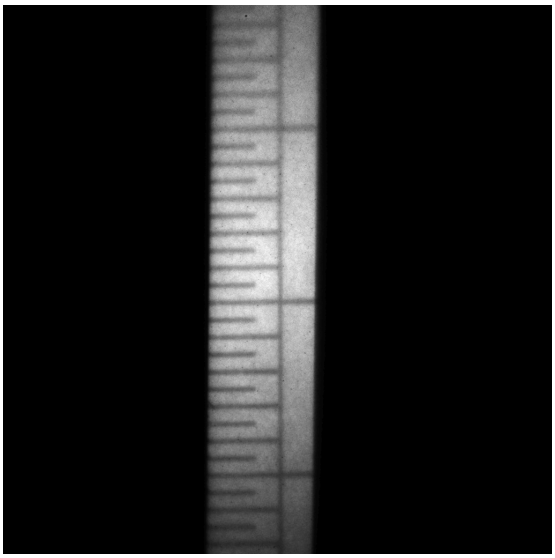

Figure 6.2: Image of a metal ruler in the focus, measured with a maximum slit width of 2500 µm and a maximum aperture in the zero-order of Grating 1. The three different intervals correspond to 5 mm, 1 mm, and 0.5 mm, respectively. The width of the image corresponds to 15.8 mm.

more difficult, since specific light sources as well as non-absorbing objects are required. Measurements were made with a thin metal plate with equidistant holes that was illuminated from the back by a mercury lamp, which has an intense Hg(I) line at 253.7 nm. Figure 6.3 shows images of the grid that were taken with Grating 3 by setting the center wavelength to 253.7 nm, so that only the light from this wavelength is captured. One measurement was made with a maximum aperture and another was made with a minimum aperture. A strong vignetting effect can be observed in Fig. 6.3b, but the sharpness is the same in both images. Despite the chromatic aberration of the lenses, the images are very sharp and the holes, which are 0.587 mm apart, can be resolved easily. However, the magnification in the UV is different from the magnification in the visual range. The distance between two holes is 44.8 pixels in the image, which

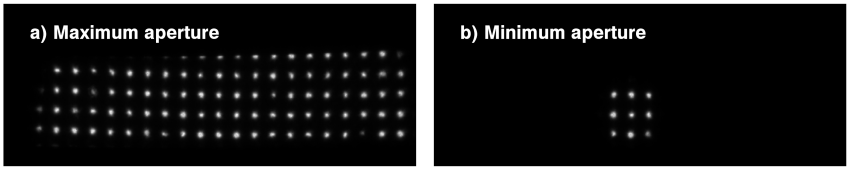

Figure 6.3: Metal grid illuminated from the back by a mercury lamp. Grating 3 was set to 253.7 nm so that the image only shows the image that is produced by the Hg(I) line at this wavelength. Measurements were made with a) maximum aperture and b) minimum aperture.

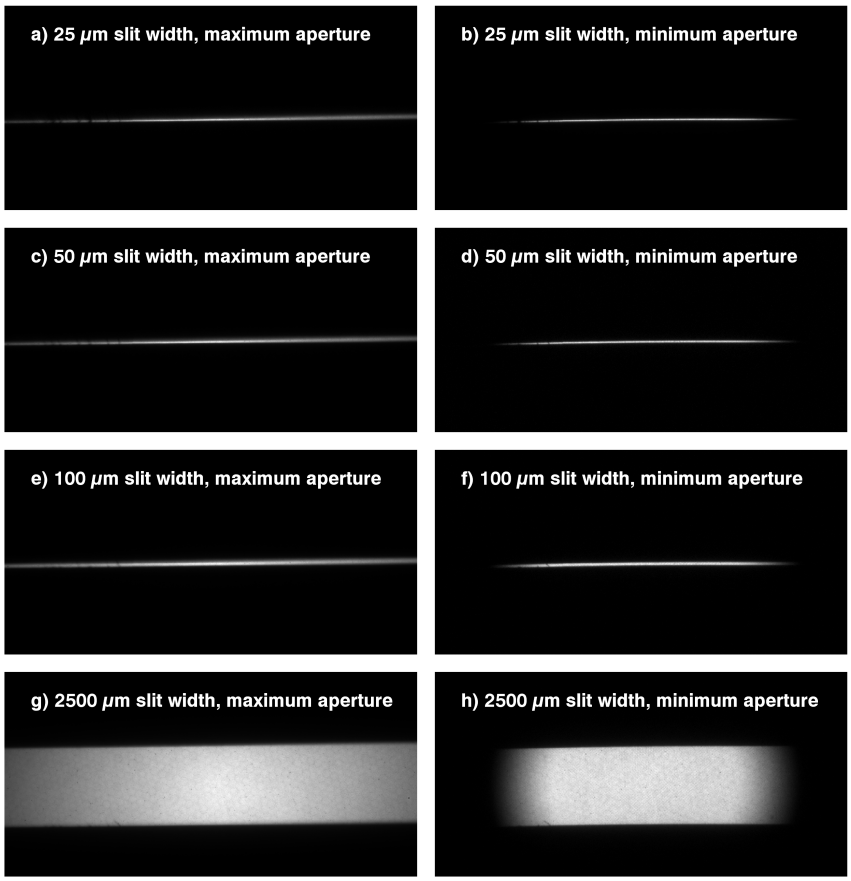

Figure 6.4: Images of a uniform light source in the focus of the setup measured with different slit widths and with a maximum/minimum aperture. The grating is Grating 1 in zero-order mode. At high slit widths (g and h), the hexagonal pattern resulting from the microchannel plate of the intensifier can be seen in the measurements.

amounts to 13 µm/pixel and a magnification of $M(253.7\,\mathrm{nm}) = 1.023$. This magnification is likely dependent on the positioning of the focus mirror in the spectrometer, which can be adjusted for optimum focus and has different default values for each grating.

6.2.2 Vignetting

In order to investigate the vignetting of the setup and the influence of the aperture, measurements of a uniform light source in the focus position were made for all three gratings at slit widths of 25 µm, 50 µm, 100 µm, and 2500 µm. Two measurements were made for each slit width, one with the maximum aperture and one with the minimum aperture. Figure 6.4 shows selected results for Grating 1, but equivalent measurements were made for the other gratings and for additional slit widths. Figure 6.5 shows corresponding plots of the intensity distribution along the slit for the maximum aperture

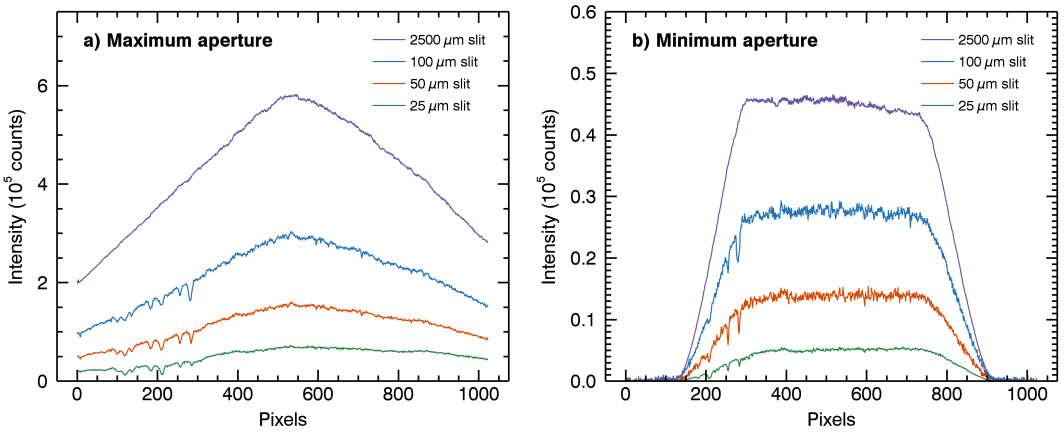

Figure 6.5: Intensity distribution along the slit with a) maximum aperture and b) minimum aperture. In comparison to the intensity at maximum aperture, the intensity at minimum aperture significantly decreases, but it also flattens in the center of the image.

and for the minimum aperture.

Vignetting can be seen for both the maximum and the minimum aperture, but it is stronger for the minimum aperture. In both cases, rough edges of the slit cause irregular intensity dips especially at small slit widths. The measurements shown in Fig. 6.5 can be used to correct both the vignetting and these intensity dips in plasma measurements. However, at a slit width of 25 µm the light is almost completely blocked at some points along the slit. If the spectral resolution is not important, the slit width should be increased to avoid this effect.

For the minimum aperture, the intensity in the center of the image flattens and the sharpness is increased. The reason is the higher depth of field and the lower contribution of large angles in the image. This is important for the Abel inversion, which requires a high depth of field and nearly parallel light in order to be a offer a good reconstruction of the radial plasma intensity. If an Abel inversion is to be applied to the measurements, it is therefore preferable to use the minimum aperture.

A pattern of hexagons can be observed in the illuminated area of the image if the slit is opened wide as in Fig. 6.4g and h. This pattern is caused by the microchannel plate of the intensifier of the ICCD, in which the channels are arranged in this way. Measurements of a uniform light source can be used to remove the pattern from measurement data, but ideally such measurements would be done with the light source directly in front of the camera so that vignetting and other interferences are avoided. For the measurements in this thesis a digital filter was sometimes used to smoothen the data, which blurs the hexagonal pattern.

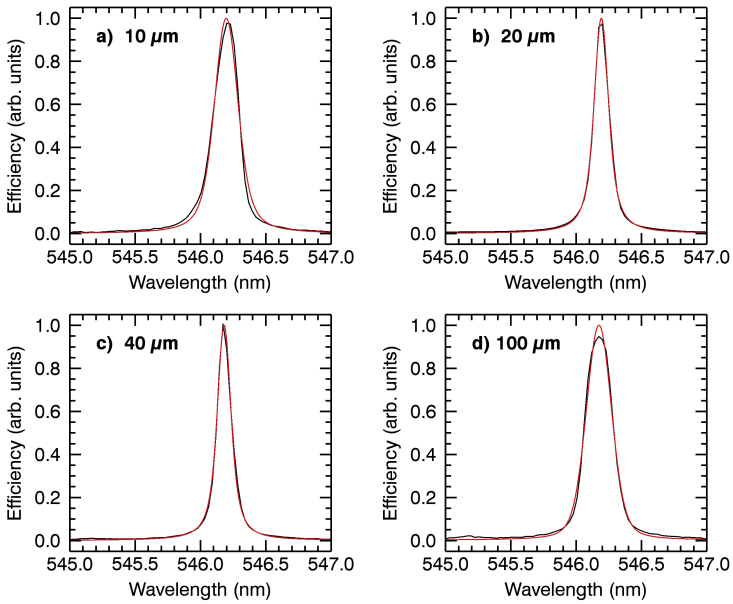

Figure 6.6: Spatially integrated spectra of the Hg(I) line at 546 nm of a mercury lamp for different slit widths. In red, Voigt profiles can be seen that were fitted to the measurements.

6.2.3 Spectral resolution

The spectral resolution at different slit widths was investigated using a mercury lamp and the Hg(I) line at 546.7 nm. The spatially integrated spectra of the line at four different slit widths can be seen in Fig. 6.6. They were fitted with Voigt profiles, from which the linewidths were obtained that are shown in Table 6.2. Surprisingly, the smallest linewidth is not found in the measurement with the minimum slit width of 10 µm, but in the one with a slit width of 40 µm. At the minimum slit width of 10 µm, the spectrum is actually slightly more blurred than at higher slit widths, resulting in a higher linewidth that is comparable to that of a slit width of 100 µm. This might be due to a small lateral offset between the slit blades that could allow more light to enter than intended. This is not a problem for most plasma imaging measurements, however, since light throughput is usually more important than spectral resolution and the slit is usually opened to at least 50 µm.

Table 6.2: Linewidth of the Hg(I) line at 546.7 nm for different slit widths.

Slit width (µm)	FWHM (nm)
10	0.216
20	0.135
40	0.127
100	0.230

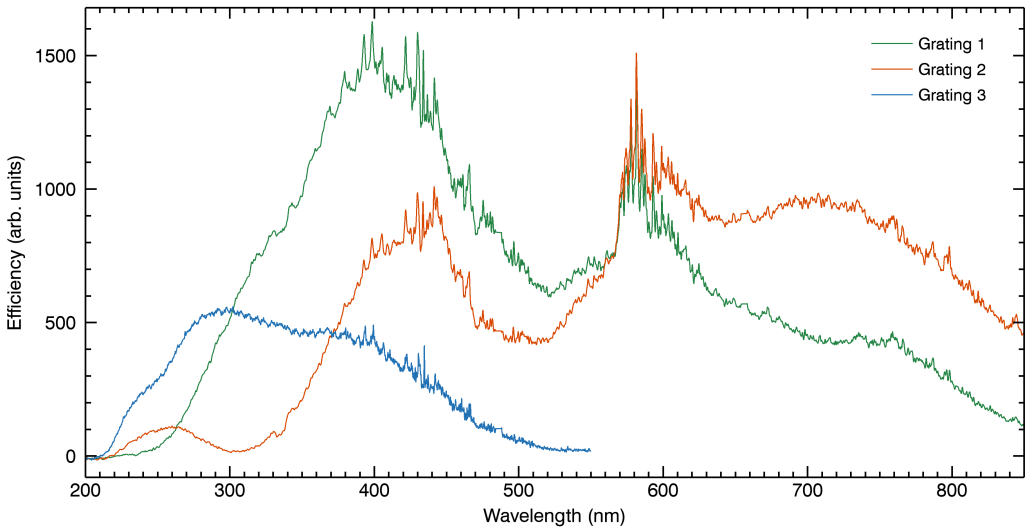

Figure 6.7: Spectral efficiency of the plasma imaging setup for the three gratings. Some of the observed spectral features come from the spectrum of the calibration lamp, but are still visible here because the data for the calibration lamp was only available in steps of 1 nm and with a low spectral resolution.

6.2.4 Spectral efficiency

Figure 6.7 shows the spectral efficiency of the setup, which was measured using a deuterium-halogen calibration lamp (AvaLight-D(H)-S) for all three gratings. The curves were obtained by dividing the measured intensities by the supplied calibration spectrum of the lamp. Grating 1 is efficient in nearly the complete spectral range and surpasses the other gratings from about 300 nm to about 580 nm. Grating 2 is the most efficient grating at wavelengths longer than 580 nm. Grating 3 is the most efficient grating from 200 nm to 300 nm, though it also provides a higher spectral resolution than the other gratings and is therefore useful at longer wavelengths as well.

The peaks in the spectra are mostly the result of peaks in the deuterium spectrum. The calibration spectrum for the lamp is only available at a low spectral resolution, so that many spectral features of the deuterium spectrum are not resolved. The two strongest deuterium lines at 486 nm and 656 nm were manually removed. For the normalization of the measured intensities, the spectra should be smoothed further to reduce the spectral features of the calibration lamp.

6.2.5 Summary

An overview of the parameters of the plasma imaging setup is given in Table 6.3. The plasma imaging setup is able to focus light within a high spectral range. Setting the aperture of the spectrometer to its minimum value significantly increases the depth of

Table 6.3: Summary of the instruments and the characteristic parameters of the plasma imaging setup.

Laser	Quantel Viron (Q-switched Nd:YAG)		
Laser wavelength (nm)	1064		
Laser pulse width (ns)	8.1		
Laser pulse energy (mJ)	30.7		
ICCD camera	Andor iStar 334T		
Pixels	1024×1024 ($13.3 \times 13.3\,\mu m^2$ pixel area)		
ICCD time resolution (ns)	< 2		
Jitter of synchronization of laser and camera (ns)	< 10		
Spectrometer	Andor Kymera 328i		
Gratings	Grating 1	Grating 2	Grating 3
Lines/mm	1200	1200	2400
Spectral coverage (nm)	260–900	330–900	220–500
Spectral resolution (nm)	approx. 0.13 ($\lambda = 546\,nm$)		
Magnification	$M(\mathrm{VIS}) = 0.86$, $M(254\,nm) = 1.023$		
Pressure range	approx. 50 mPa to 100 kPa		

field and sharpness of the setup, so that this should be done whenever light throughput is not as important. The magnification of the setup varies in dependence of the wavelength, which means that different calculations for the spatial dimension of the measurements need to be made for signals that are located at different wavelengths. Values for the UV at 253.7 nm and for the visual range have been calculated, from which the magnification at other wavelengths can be estimated.

The vignetting of the system has been measured for different slit widths and for all gratings, so that the plasma measurements can be corrected for it if necessary. At minimum aperture, it does not seem to be necessary as the intensity within the visible area is very uniform. Irregular intensity dips were observed at lower slit widths that were caused by rough edges of the slit blades. Since the effect can be quite strong and might cause problems for the correct measurement of spatial distributions of signals, the slit width should be increased slightly if possible. The highest spectral resolution was also obtained for slightly wider slit widths of 20–40 µm. Even at 100 µm, the resolution is still good enough for most purposes, as long as spectral lines are investigated that are not superimposed by other lines. Therefore there is no strong advantage in using a slit width of less than 40 µm.

The spectral efficiency of the setup was measured for all three gratings. The efficiencies of the gratings mostly correspond to their blaze wavelengths, i.e. Grating 2 is best for VIS/NIR above 580 nm and Grating 3 is best for UV up to 300 nm, while

Grating 1 covers the wavelengths in between. The spectral efficiency curves are important for comparisons of line intensities and for the calculation of the temperature from a Boltzmann plot. Since the efficiency curves still show spectral features from the deuterium light source, they should be smoothed before using them for the normalization of the measured intensities.

6.3 Experimental methods

Measurements of the laser-induced plasma with the plasma imaging setup are slightly different from LIBS measurements with the setup described in Chapter 3. One important difference is that the plasma imaging setup is designed to investigate the dynamic processes in the laser-induced plasma, which makes it important to use a short time gate for the measurements and to use many different delay times in order to observe the dynamic behavior of the inspected signals. If a long time gate is used, the spatial distributions of the different time regimes will be superimposed. In this case no accurate spatial information can be obtained, unless the signals are nearly stationary in time.

6.3.1 Samples

Due to the importance of the time evolution of the signals, more measurements have to be done of a single sample than in a standard LIBS measurement. The low spectral range may also increase the number of measurements if several different signals at different wavelengths are investigated. If measurements at different heights of the plasma are of interest as well, the number of measurements increases even further. Each measurement should be done on a new position of the sample, since craters from earlier measurements will cause distortions of the laser-induced plasma. Homogeneity of the sample and a flat surface are therefore even more important than in standard LIBS measurements. In order to achieve this, the samples are ground into fine powder and pressed into pellets, as described before.

6.3.2 Measurement modes

Two different types of plasma measurements were used in this thesis, which are shown in Fig. 6.8. The first method (Fig. 6.8a) is the measurement of a spatially-resolved LIBS spectrum within a small spectral range and at a selected height. The wavelength range is determined by the grating and the specified center wavelength. In order to obtain a high spectral resolution, the slit width should be 100 µm or less. Using the same measurement settings, different heights can be scanned to obtain a complete picture of the spatial distributions of the signals in the selected wavelength range. In the second method (Fig. 6.8b), the slit is opened to 2500 µm instead. The wavelength is selected

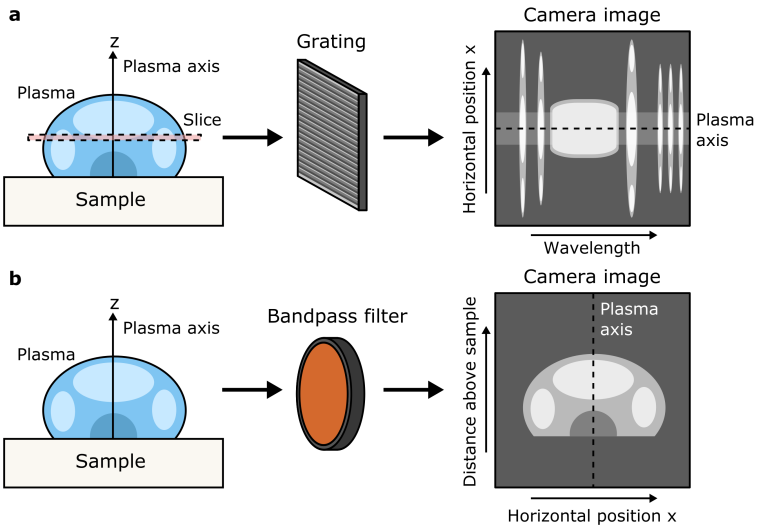

Figure 6.8: Types of plasma emission measurements. a) A height is selected and a spatially-resolved spectrum is measured with a slit width of 100 µm or less. b) An image of the plasma emission is made in the zero-order of the grating, with a bandpass filter inserted into the detection path to select a specific wavelength regime. A larger portion of the plasma can be measured at once, but the spectral resolution is lost. For spectrally isolated emission lines, the same effect can be achieved by setting the grating to the wavelength of the emission line and opening the slit.

with a bandpass filter in the optical path, and the grating is set to the zero-order. In this case the spectral information is lost, but more spatial information is obtained with a single measurement. Often only one or two different heights of the plasma have to be measured in order to obtain the full spatial distribution of the selected wavelength range. For specific spectrally isolated lines, this method can also be used without a bandpass filter by setting the grating to the wavelength of the emission line. If there is no interference from other spectral features, the spatial distribution of the selected emission in the plasma will be obtained. Grating 3 is especially useful for this method due to its high dispersion, which increases the distance between adjacent emission lines on the image.

6.3.3 Deconvolution by Abel inversion

If the observed plasma emission is axisymmetrical and optically thin, an Abel inversion can be applied to the spatially resolved intensity measurement to gain the emission coefficient $\epsilon(r)$ along the radius r [2, 40, 49, 55, 87]. The principle is illustrated in Fig. 6.9. The intensity $I(x)$ for the line of sight at the position x is given by

$$I(x) = \int_{-y_0}^{y_0} \epsilon(r)\,\mathrm{d}y = 2\int_x^R \frac{r\epsilon(r)}{\sqrt{r^2 - x^2}}\,\mathrm{d}r\,, \tag{6.1}$$

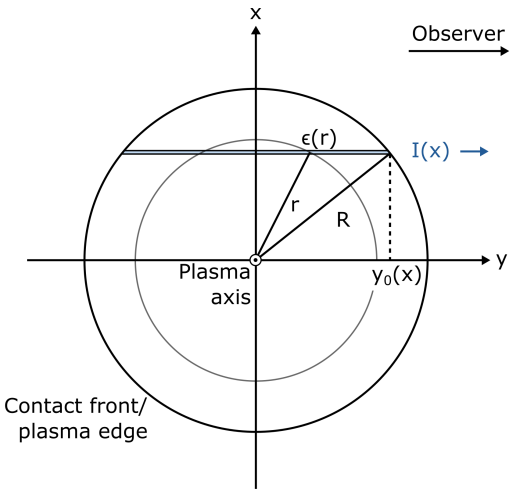

Figure 6.9: An axisymmetrical plasma that is observed from the side. The plasma axis is normal to the paper. The detected intensity at a certain position x is the integral over the emission coefficient $\epsilon(r)$ along the line of sight.

with $y_0(x) = \sqrt{R^2 - x^2}$ being the edge of the plasma at the maximum radius R, so that $\epsilon(r \geq R) = 0$. The Abel inversion of this equation is

$$\epsilon(r) = -\frac{1}{\pi} \int_{-x}^{R} \frac{\mathrm{d}I(x)}{\mathrm{d}x} \frac{1}{\sqrt{x^2 - r^2}} \, \mathrm{d}x \,. \tag{6.2}$$

For a general intensity distribution $I(x)$, the equation cannot be solved analytically. There are many different numerical techniques to calculate the solution of Eq. (6.2), however, e.g. [2, 55, 87]. For this thesis, the algorithm described by Liu et al. [87] was chosen because it is very fast and has been found to be very accurate for various synthetic data sets, even if noise was added. For all algorithms, the accuracy is lowest at the plasma axis, since the solution of the emission coefficient at the plasma center depends on the solutions for the outer layers, so that noise and numerical simplifications accumulate and increase the error of the solution.

The fundamental steps that are necessary to obtain the deconvoluted radial emission coefficient $\epsilon(r)$ by performing an Abel inversion on a spatial intensity distribution $I(x)$ are illustrated in Fig. 6.10. Since cylindrical symmetry is assumed, the first step after obtaining the intensity distribution is to calculate the average of the intensities $I(-x)$ and $I(x)$ for a plasma axis at $x = 0$ and to only consider positive x values. Due to the strong effect of noise on the result of the numerical Abel inversion, the data may also need to be smoothened and binned. In this thesis, a smoothing filter was applied and the spatial resolution was reduced by a factor of 2. Still, the Abel inversion sometimes leads to solutions that are clearly numerical artifacts, especially close to the plasma center. A maximum entropy reconstruction instead of the Abel inversion could potentially improve the calculated radial emission coefficients [33].

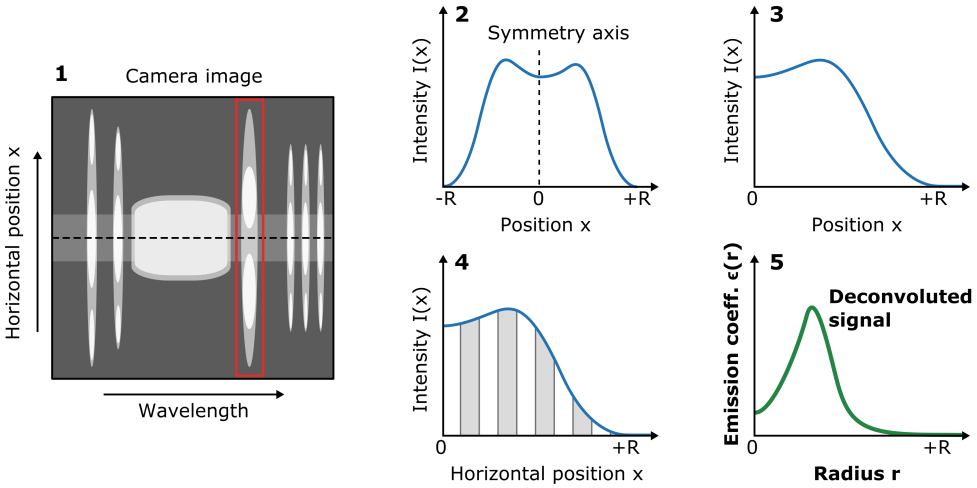

Figure 6.10: Process used to obtain the radial emission coefficient of a signal. 1) The spatial intensity distribution $I(x)$ is extracted from the measurement data. 2) The axis of symmetry is determined. The data is smoothed if necessary. 3) The two halves of the signal are averaged to obtain a representative intensity distribution from $I(0)$ to $I(R)$. 4) The signal is reduced to intervals of equal intensity corresponding to rings around the plasma axis. 5) The deconvolution is started in the outermost ring and iterated until the innermost ring is reached. The result is the radial emission coefficient $\epsilon(r)$.

7. Spatial Characterization of Plasma Emissions

In this chapter, the first results from measurements with the new plasma imaging setup in Martian atmospheric conditions are presented. Several studies were conducted in which the spatial distributions of various spectral features were investigated for a small selection of samples. The first study continues the research on the molecular emissions of CaCl and CaF from Chapter 4 and Chapter 5. The other studies are first examples of further potential applications for plasma imaging, with a focus on the hydrogen emission, calcium emissions, and atmospheric carbon and oxygen emissions in the laser-induced plasma.

The simulations of the CaCl and CaF emissions in the earlier chapters were based on a plasma in LTE, but the experimental results indicated that LTE was not sufficient to describe the observed band intensities. The need for a non-equilibrium model might indicate that the spatial distributions will also depend on plasma dynamics. The plasma simulations and the comparisons of the CaCl and CaF bands to simulated band spectra in Chapter 4 and Chapter 5 also indicate that the molecular emissions should appear at relatively low plasma temperatures of 3000–5000 K. In spatial characterizations of the plasma temperature, the temperature was typically hot at the plasma center and colder in the outer layers [1, 2]. Therefore, molecules would be expected to appear in the cold outer layers of the plasma, but measurements of the CaF distribution in terrestrial LIBS plasmas seem to contradict this prediction [50]. In this chapter I investigate the spatial distributions of CaCl and CaF in LIBS in Martian atmospheric conditions and find that they are actually located very close to the plasma center.

For Mars-relevant samples, the calcium emissions are often the strongest observable emissions. They are investigated here to understand the spatial and temporal evolution of these signals better. Another interesting aspect is that both atomic and ionic emissions can be studied with a good SNR. This enables the investigation of temperature gradients in the laser-induced plasma, since the differences in the spatial distributions of atomic and ionic calcium emissions will only depend on the local temperatures.

Hydrogen is important in the context of planetary science for the detection of water and hydrated minerals. However, hydrogen quantification has been challenging in Martian LIBS spectra due to a high variability of the sample [120]. One potential reason for this is that the surface geometry has a strong influence especially on the

Table 7.1: Overview of the analyzed signals and samples.

Emission	Samples
CaCl A-X at 618 nm	$CaCl_2 \cdot 2\,H_2O$, 80:20 NaCl + $CaSO_4 \cdot 2\,H_2O$
CaF A-X at 603 nm	CaF_2
Ca(I) at 612.2 nm	$CaCl_2 \cdot 2\,H_2O$, 80:20 NaCl + $CaSO_4 \cdot 2\,H_2O$
Ca(I) at 431.9 nm	$CaSO_4 \cdot 2\,H_2O$
Ca(II) at 373.7 nm	$CaSO_4 \cdot 2\,H_2O$
H_α at 656.3 nm	JSC Mars-1A, $CaSO_4 \cdot 2\,H_2O$
C(I) at 247.9 nm	$CaSO_4 \cdot 2\,H_2O$
C(III) at 229.7 nm	$CaSO_4 \cdot 2\,H_2O$
O(I) at 777.4 nm	$CaSO_4 \cdot 2\,H_2O$, NaCl

hydrogen signal due to the low mass and the high velocity of the hydrogen atoms [119]. The hydrogen signal was shown to increase up to seven times its initial value if the plasma was formed close to a vertical plate, while other signals such as the oxygen signal remained at a similar intensity. Here a similar experiment is made where the spatial distribution of the hydrogen emission is investigated as well. Additionally, the general distribution of the hydrogen emission is investigated for different samples. The results show that the hydrogen distribution is strongly influenced by pressure gradients within the plasma and indicate a vorticity of the lower plasma plume, but geometrical influences on the total intensity of the hydrogen signal cannot be observed.

The atmospheric carbon and oxygen in Martian LIBS spectra is of interest for the normalization of signal intensities, for example for the hydrogen signal [120, 131]. Their spatially resolved signals were investigated here to better understand the interaction of the ambient gas with the plasma. Studies have shown that the high pressure of the ablated material reduces the concentration of the elements from the ambient gas in the plasma center, which causes a strong separation between the hot plasma core that contains ablated sample material and a colder periphery that contains more atmospheric contributions [2]. For the samples that were investigated here and for Martian atmospheric conditions, this result could not be reproduced. Instead, the carbon emissions are found to be close to the plasma center.

7.1 Materials and methods

Table 7.1 gives an overview of the signals that were investigated. All measurements were done in simulated Martian atmospheric conditions with a laser energy of about 20 mJ/pulse. In order to observe the time evolution of the signals, all measurements were done at different delay times, usually in steps of 100 ns or 200 ns. A gate width of 100 ns and a small aperture were used unless stated otherwise.

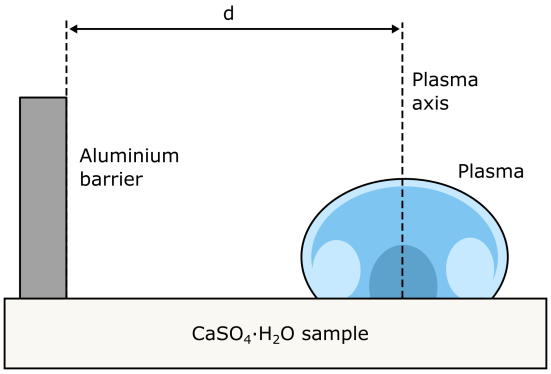

Figure 7.1: Illustration describing the measurements with a vertical aluminium barrier placed on top of a $CaSO_4 \cdot 2\,H_2O$ sample, similar to the experiment by Rapin et al. [119]. A plasma was generated at varying distances d from the barrier to investigate the influence on the plasma emissions.

Molecular emissions The spatially resolved emissions of CaCl and CaF were first investigated in pure samples of $CaCl_2 \cdot 2\,H_2O$ and CaF_2, respectively. For the CaCl emission, a 80:20 mixture of NaCl and $CaSO_4 \cdot 2\,H_2O$ ($\chi_{Cl} = 0.33$ and $\chi_{Ca} = 0.03$) was analyzed as well in order to investigate whether the spatial distribution of the CaCl signal changes in dependence of the sample, since the formation of additional CaCl molecules due to fragmentation is only expected to be observed for the $CaCl_2 \cdot 2\,H_2O$ sample. Spectrally resolved measurements of the CaCl band were made within the wavelength range from 605 nm to 635 nm with a slit width of 50 µm at 1.78 mm, 2.28 mm, and 2.78 mm above the sample. The CaF band in the plasma of pure CaF_2 was measured with a bandpass filter at 600 nm (FWHM 10 nm), so that the full distribution could be obtained in a single measurement.

Calcium emissions The spatial distribution of the Ca(I) signal at 612.2 nm in the measurements of the $CaCl_2 \cdot 2\,H_2O$ sample and of the 80:20 NaCl + $CaSO_4 \cdot 2\,H_2O$ sample was analyzed in order to compare the CaCl signal distribution with that of one of the reactants. Additionally, the two-dimensional distributions of Ca(I) at 431.9 nm and Ca(II) at 373.7 nm were measured for a $CaSO_4 \cdot 2\,H_2O$ sample in order to compare the spatial distributions of atomic and ionic calcium emissions. Since these lines are relatively isolated in the spectrum, the signals were measured with a wide open slit.

Hydrogen emission The H_α line at 656.3 nm was investigated with the bandpass filter at 656.3 nm (FWHM 1.2 nm). Samples of JSC Mars-1A and of $CaSO_4 \cdot 2\,H_2O$ were used in order to see the hydrogen signal for different materials. The hydrogen signal of JSC Mars-1A is mostly from adsorbed water. In addition to general time-resolved measurements, the hydrogen signal was also investigated close to a vertical barrier in order to investigate the increase in intensity that was reported for such a

geometry [119]. An aluminium plate was used as the barrier and was placed on top of the $CaSO_4 \cdot 2\,H_2O$ sample, see Fig. 7.1. The results will be shown separately in comparison with equivalent measurements of the oxygen signal, which did not become more intense in proximity to a vertical barrier in the experiments by Rapin et al. [119].

Atmospheric emissions The spatial distributions of C(I) at 247.9 nm and C(III) at 229.7 nm were investigated for a $CaSO_4 \cdot 2\,H_2O$ sample, while the O(I) triplet at 777.4 nm was investigated for a $CaSO_4 \cdot 2\,H_2O$ sample and a NaCl sample in order to investigate the difference between the oxygen distribution for samples with and without oxygen. The 780 nm bandpass filter was used for the O(I) triplet, while the C(I) and C(III) lines are spectrally isolated and can be measured with an open slit. The O(I) emission was also measured at varying proximity to a vertical aluminium barrier placed on top of a $CaSO_4 \cdot 2\,H_2O$ sample to compare it with the H_α emission.

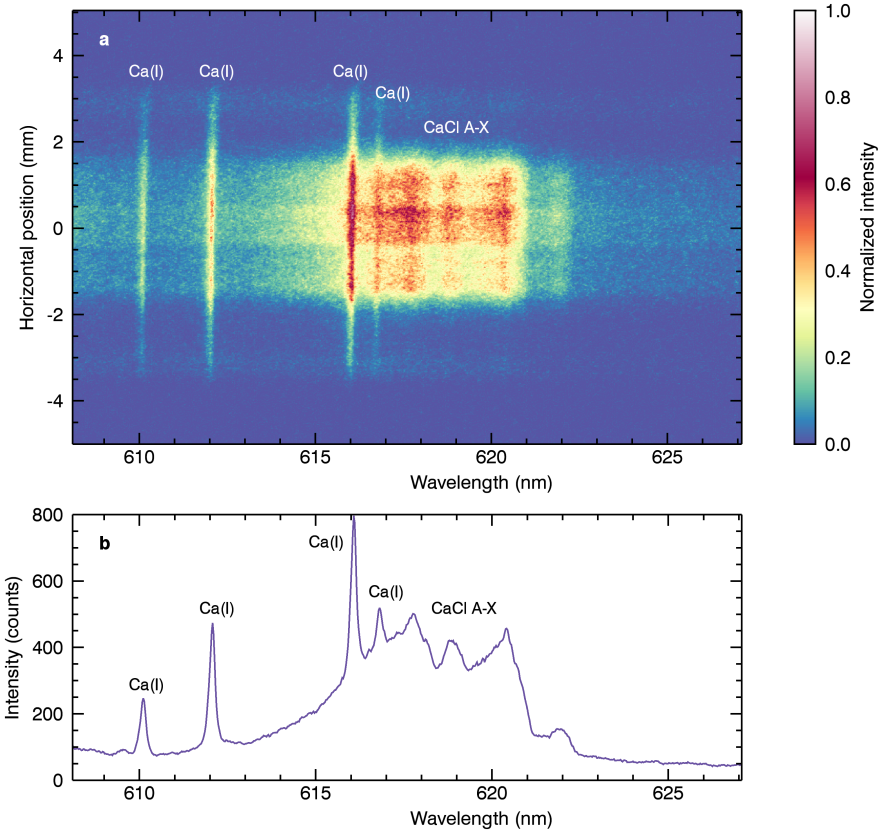

Figure 7.2: a) Spatially resolved CaCl band spectrum for the $CaCl_2 \cdot 2\,H_2O$ sample at 1.78 mm above the sample, measured at a delay of 2 µs. The spectrum is symmetrical about the plasma axis and shows distinct regions of different intensity. b) Spatially integrated representation of the same spectrum, clearly showing the Ca(I) lines and the CaCl A-X band.

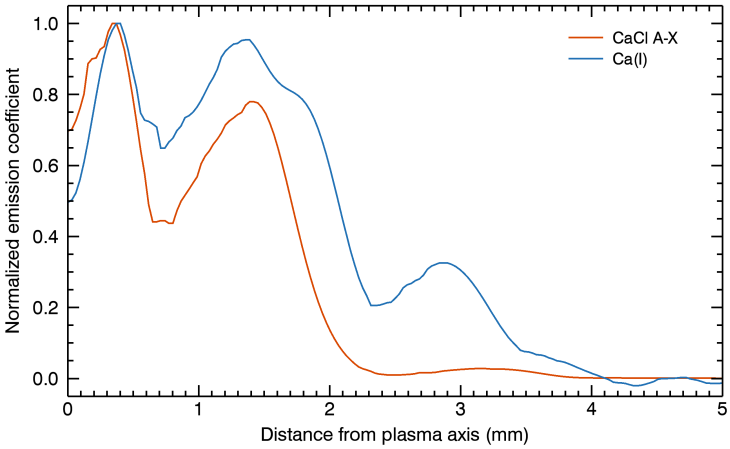

Figure 7.3: Normalized emission coefficient of the CaCl A-X band and the Ca(I) line at 612.2 nm in dependence of the distance to the plasma axis. The measurement was made 1.78 mm above the sample surface with a delay time of 2 µs.

7.2 Results

7.2.1 Molecular emissions

An example of a spatially resolved spectrum for the $CaCl_2$ sample is shown in Fig. 7.2a, with the spatially integrated version given as a reference in Fig. 7.2b. The delay time for this measurement was 2 µs. The Ca(I) lines and the CaCl band can be observed, with a clear symmetry about the plasma axis. The Ca(I) line remains intense within a large region, while different regions can be identified for the CaCl band, which are separated by sudden changes in the band intensity. A deconvolution of the intensity profiles reveals complex emission distributions along the radius of the plasma, which are shown in Fig. 7.3. The Ca(I) line emission is more evenly distributed than the CaCl band emission, but they both follow a similar pattern with a maximum at 0.4 mm distance from the plasma axis, a dip at 0.7 mm, and another maximum at 1.4 mm that is followed by the strongest decline of the emission coefficient. While both emission coefficients rise at a radius of about 3 mm again, this is much more pronounced for the Ca(I) line. The emission distributions therefore both have a shape that consists of three ring-like maxima around the plasma axis. This pattern suggests that dynamic processes and complex temperature distributions strongly influence these signals.

The high emission of CaCl close to the plasma center is surprising, since the temperature at the center was expected to be too high for stable CaCl molecules. The closeness of the CaCl band intensity to the plasma center is observed for all delay times and for all observed heights in the plasma plume, however. Figures 7.4a–c show the spatially integrated intensity of the CaCl band and the Ca(I) line at 612.2 nm for the three different heights, while Fig. 7.4d–f show the corresponding FWHM of the spatial

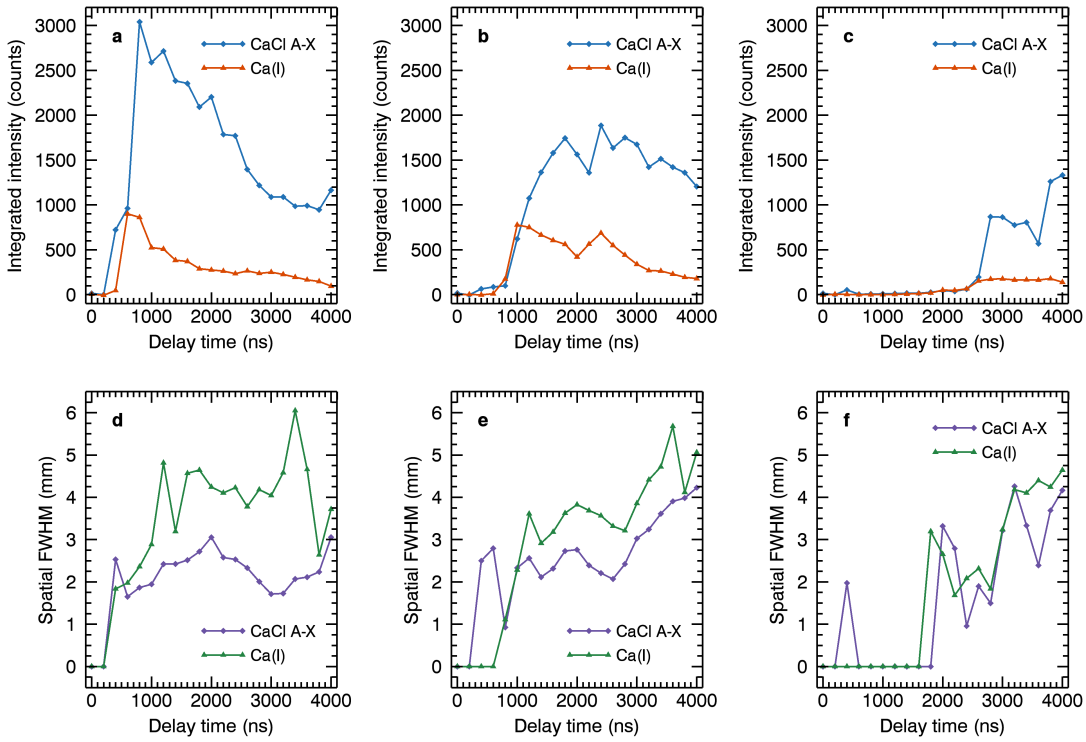

Figure 7.4: Top: Integrated intensity of the CaCl band and the Ca(I) line at 612.2 nm in the plasma of $CaCl_2 \cdot 2\,H_2O$ in dependence of the delay time at a) 1.78 mm, b) 2.28 mm, and c) 2.78 mm above the sample. Bottom: Full width at half maximum of the spatial distributions of the same signals at d) 1.78 mm, e) 2.28 mm, and f) 2.78 mm above the sample.

distributions of the signals. The highest band intensity is observed at 1.78 mm above the sample for a delay time of 800 ns, despite a small FWHM that means that the intensity is concentrated close to the plasma center. The temperature calculated from Ca(II) lines shown in Fig. 4.18 for a $CaCl_2$ sample was still above 10 000 K at this point. This suggests that the plasma center is not the hottest part of the plasma at the delay times at which molecules are formed.

The time evolution of the CaCl band and the Ca(I) line in Fig. 7.4 is very similar. Both signals increase quickly and then decrease slowly over time at 1.78 mm above the sample, whereas the initial rise of the intensity is delayed for measurements at larger distances from the sample. The spatial width changes in the same way, but the Ca(I) signal is consistently wider than the CaCl band. Since neutral Ca is stable at higher temperatures than CaCl in the LTE simulations shown in Fig. 4.10, it is likely that the larger width of the Ca(I) signal indicates that the regions at 2–4 mm distance from the plasma axis are hotter than the center.

In Fig. 7.5, the spatially resolved spectrum for the 80:20 mixture of NaCl and

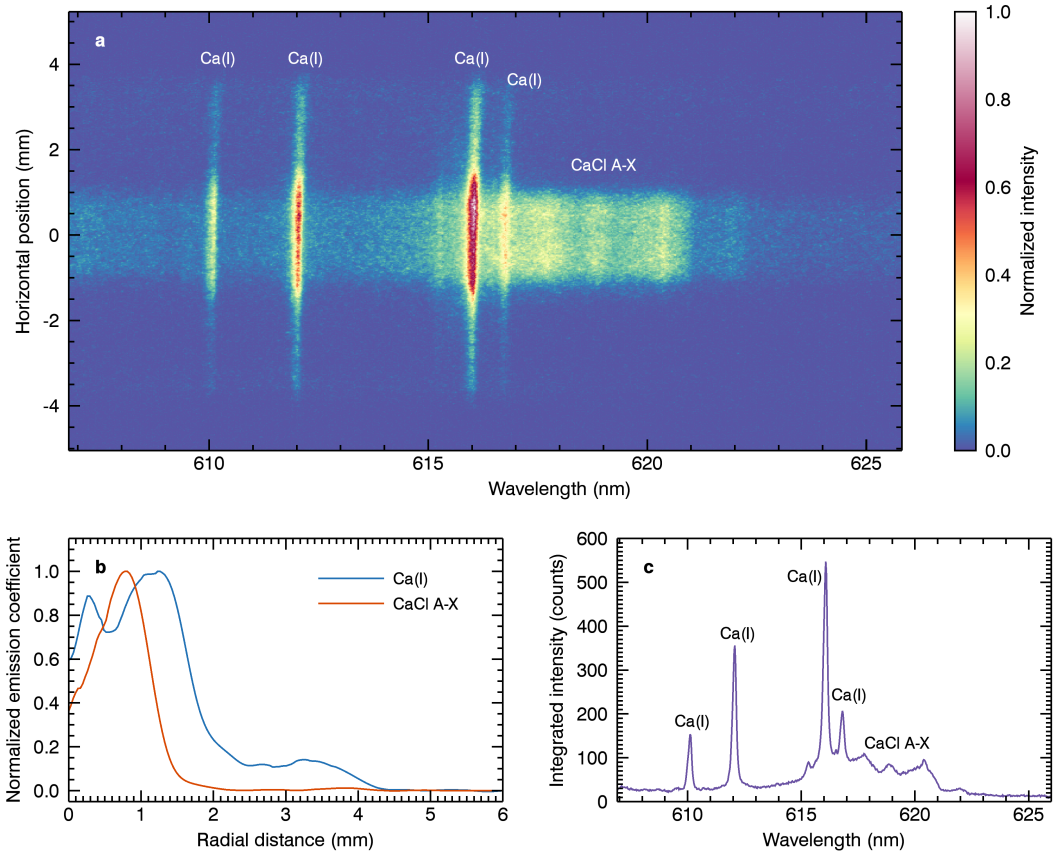

Figure 7.5: a) Spatially resolved spectrum for the mixture of NaCl and $CaSO_4 \cdot 2\,H_2O$ at 1.78 mm above the sample, measured at a delay of 1 µs. b) Radial emission coefficient of the CaCl band and the Ca(I) line at 612.2 nm. c) Spatially integrated spectrum of the measurement.

$CaSO_4 \cdot 2\,H_2O$ is shown for a delay time of 1 µs. In contrast to the $CaCl_2$ measurements, the spatial distribution of the CaCl band intensity shows less distinct regions. While a low intensity can be observed at a distance of 2.5–4 mm from the plasma axis, most of the intensity is found in a single clearly defined region close to the center with a spatial FWHM of about 2 mm. The Ca(I) lines again extend further out with a spatial FWHM of about 3.5 mm. As before, the radial emission distribution of the CaCl band is ring-like around the plasma center, while the Ca(I) lines have a slightly more uniform emission close to the center.

The measurement at 1 µs is shown here because it is highly symmetrical, which is important for the calculation of the radial emission coefficient by Abel inversion. However, measurements at other delay times show the same general behavior, as shown in Fig. 7.6. The CaCl band intensity at low delay times rises more slowly than it does for the $CaCl_2$ sample, which corresponds well to the time-resolved measurements of the $KCl + CaCO_3$ sample shown in Fig. 5.16a. After the signal has appeared, it does not

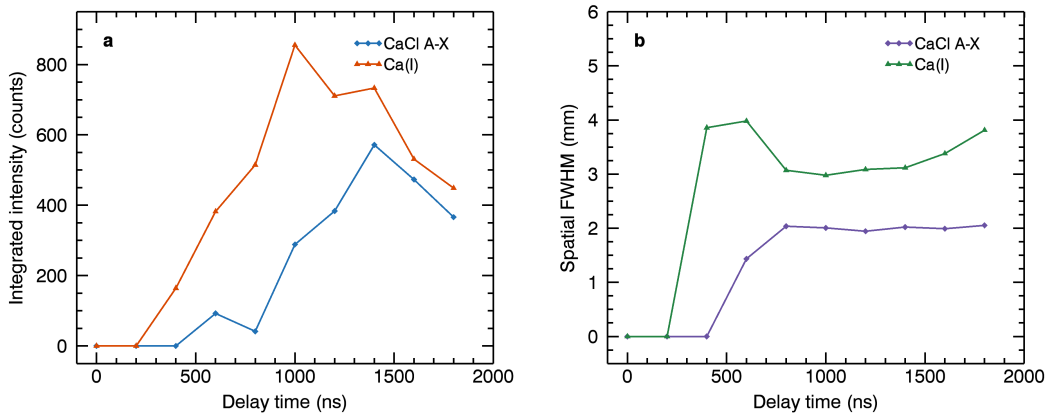

Figure 7.6: a) Integrated intensity of the CaCl band and the Ca(I) line at 612.2 nm in dependence of the delay time. b) Full width at half maximum of the spatial distributions of the intensities of the CaCl band and the Ca(I) line in dependence of the delay time.

change spatially a lot, which can be seen in Fig. 7.6b by the nearly constant spatial width from 800 ns on. Again, the time evolution of the spatial width of the Ca(I) line resembles that of the CaCl band, but is consistently larger.

The spatial distribution of the CaF band intensity was measured with a bandpass filter. The measurements at different delay times are shown in Fig. 7.7. Similarly to the CaCl emission, the CaF emission appears very close to the plasma axis, further

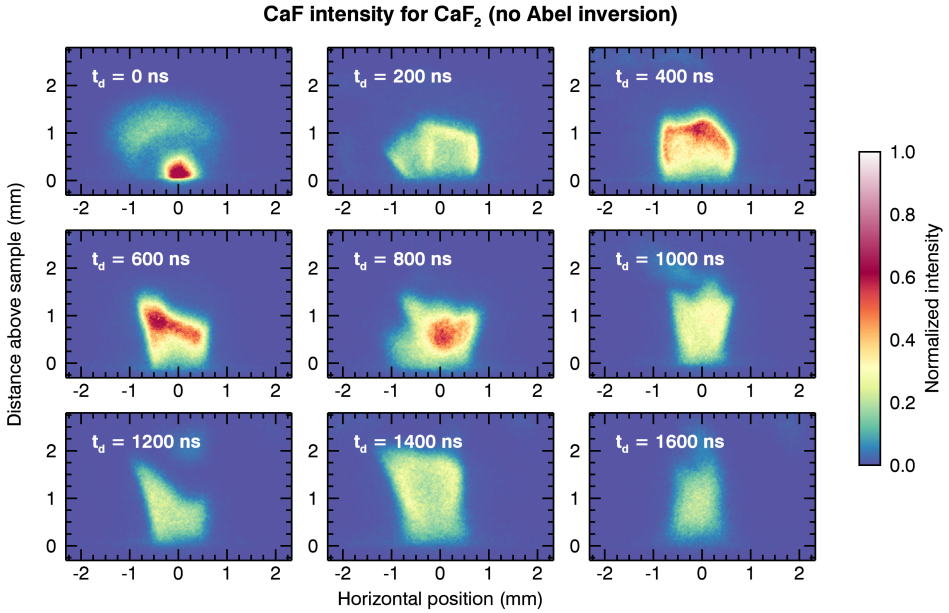

Figure 7.7: Spatial distribution of the CaF band emission at different delay times. Like the CaCl band emission, it is located close to the plasma axis. The two-dimensional spatial information reveals slight asymmetries in several measurements.

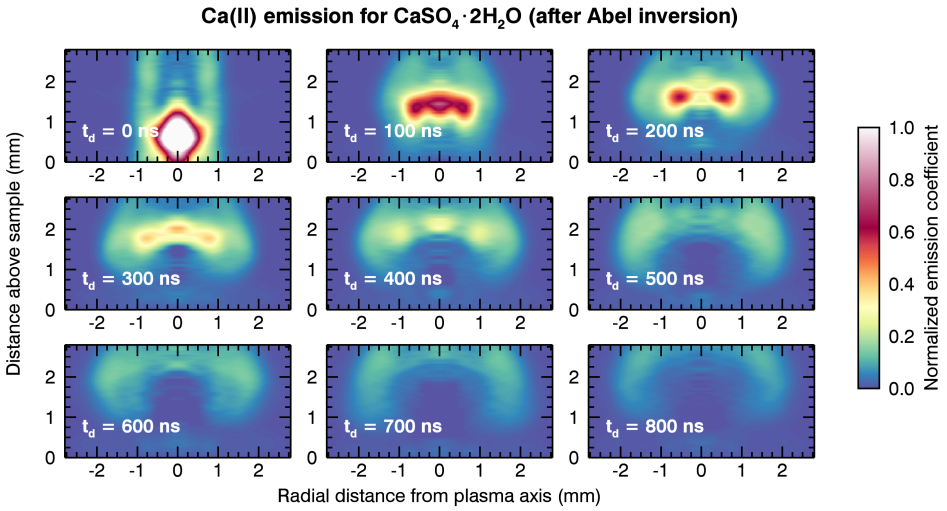

Figure 7.8: Radial emission coefficient of the Ca(II) line at 373.7 nm in the plasma of a $CaSO_4 \cdot 2\,H_2O$ sample at different delay times from 0 ns to 800 ns, measured with a gate width of 100 ns. The emission coefficient is mirrored at the plasma axis to give the impression of a slice through the plasma.

indicating that the temperature at the plasma axis is lower than previously thought. The emission is confined vertically as well as horizontally to a relatively small region in which it mostly stays for the different measurements. The distribution changes slightly every time, however, and is often not symmetric. The signal appears to vary between measurements in a similar way as the CaF band intensity did in the time-resolved measurements of a $CaF_2 + K_2SO_4$ sample in Fig. 5.16d.

7.2.2 Calcium emissions

Figure 7.8 shows the radial emission coefficient of the Ca(II) line at 373.7 nm at different delay times. At 0 ns delay time, the signal is very intense at the plasma center, which indicates a high temperature and a high concentration of Ca^+ ions. The medium intensity seen at greater heights above the sample is likely the result of measurement artifacts, i.e. of other ionized lines that appear in the early stages of the plasma and overlap with the Ca(II) signal. At longer delays, these cannot be seen anymore, and the signal accurately represents the Ca(II) distribution. It can be seen that the intensity moves away from the center of the plasma, forming a ring around the center at 200 ns delay that is found at a height of about 1.7 mm above the sample and at a distance of about 0.6 mm from the plasma axis. At 800 ns, which is close to the delay time where a strong CaCl signal could be observed at the plasma center in Fig. 7.5, the highest Ca(II) signal intensity is found in a thick dome-like layer around the plasma center, while the plasma center is devoid of Ca(II) emission. This supports the theory that the plasma center is rarefied and cools down considerably as the plasma expands and that

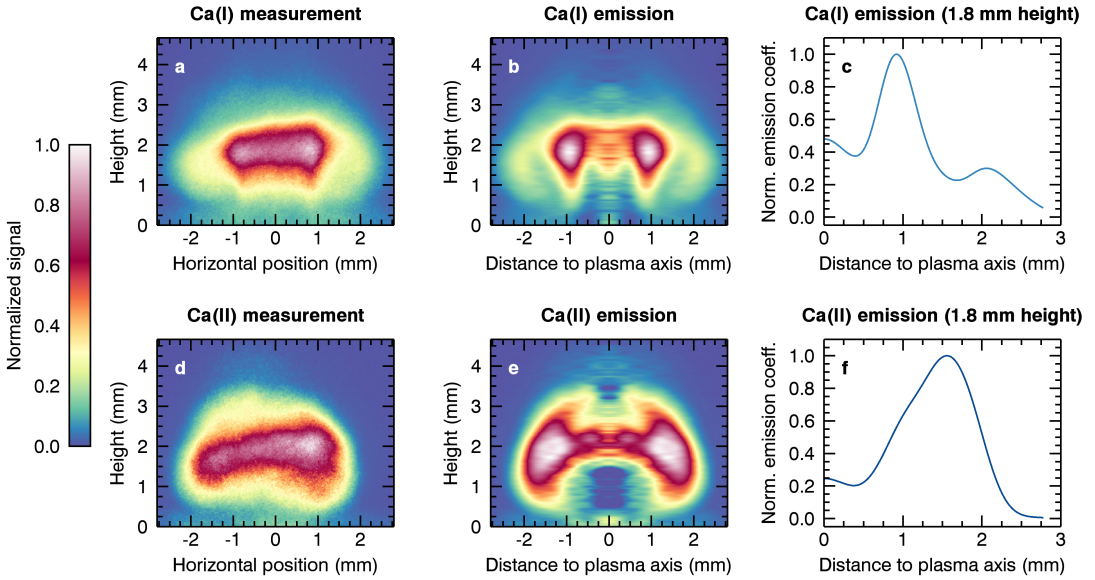

Figure 7.9: Comparison of the emissions of Ca(I) at 431.9 nm and Ca(II) at 373.7 nm in the plasma of a $CaSO_4 \cdot 2\,H_2O$ sample for a delay time of 500 ns and a gate width of 100 ns. The left column (a, d) shows the measured intensity signals, the center column (b, e) shows the emission coefficients calculated by Abel inversion, and the right column (c, f) shows the radial emission coefficients at 1.8 mm height above the sample surface. The emission coefficients in (b) and (d) are mirrored at the plasma axis to give the impression of a slice through the plasma.

higher plasma temperatures are found closer to the plasma front in the later plasma stages. The changes in the signal distribution over time also indicate dynamic changes in the spatial distribution of Ca^+ ions and in the temperature field within the plasma.

Figure 7.9 shows a comparison of the spatial distributions of Ca(I) at 431.9 nm and of Ca(II) at 373.7 nm measured with a delay time of 500 ns and a gate width of 100 ns. The comparison clearly shows a difference in the spatial distributions that is in good agreement with the previous measurements of the molecular emissions. The maximum emission coefficient of neutral Ca(I) at 1.8 mm height above the sample is found at a distance of about 0.9 mm from the plasma axis, while the maximum emission coefficient of Ca(II) at the same height is found at about 1.5 mm distance from the plasma axis. The plasma temperature is therefore higher at 1.5 mm distance than at 0.9 mm. In the two-dimensional emission distributions shown in Fig. 7.9b and d, it can be seen that this seems to be a general trend. However, the temperature also seems to decrease at even larger distances again, as indicated by the Ca(I) emission at distances greater than 2 mm, where the Ca(II) emission has mostly decreased to low values. A low temperature close to the plasma front is to be expected, since the outer layers of the plasma interact with the ambient gas and therefore cool off more quickly.

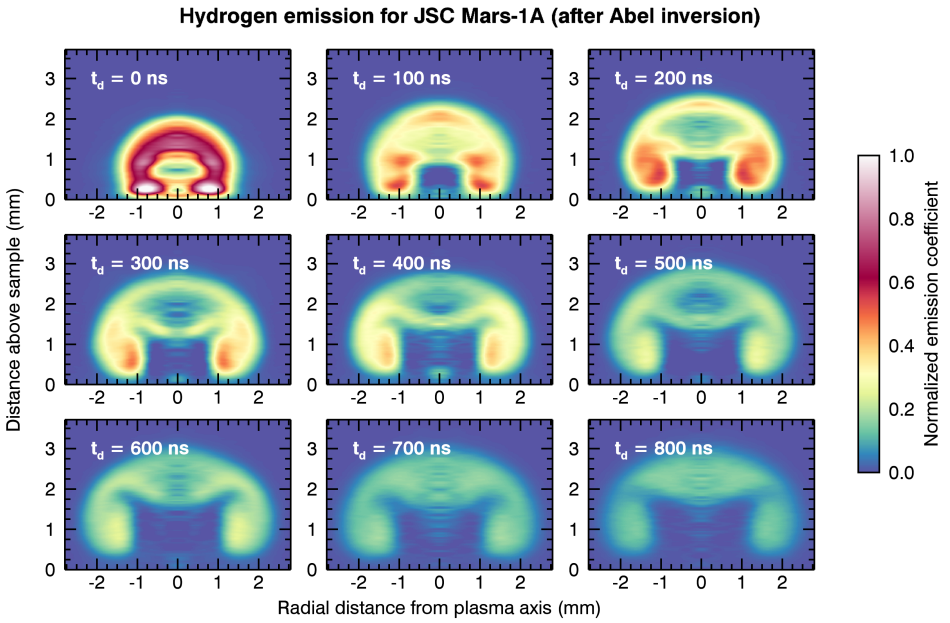

Figure 7.10: Radial emission coefficient of the H_α line in the plasma of a JSC Mars-1A sample at different delay times from 0 ns to 800 ns, measured with a gate width of 100 ns. The emission coefficient is mirrored at the plasma axis to give the impression of a slice through the plasma. It quickly forms a distinct shape that it keeps over time. At the top, the hydrogen emission seems to follow the shock wave of the plasma and potentially also a reflected downward shock wave. At the sides, vortexes appear that speak of the strong movements within the plasma. The size of the emission region increases slightly over time, but the shape remains mostly constant.

7.2.3 Hydrogen emissions

The spatial distribution of the H_α line intensity was very symmetrical for all measurements, so that it was possible to calculate accurate radial emission coefficients for these measurements. The radial emission coefficient of H_α in the plasma of JSC Mars-1A is shown in Fig. 7.10 for different delay times. Even though each delay time was measured at a different position on the sample, which is relatively heterogeneous in the case of the regolith simulant, the time evolution of the emission coefficient does not show strong fluctuations. It has a distinct shape with an apparent vortex slightly above the sample surface at a distance of a few millimeters from the plasma axis. The distance to the plasma axis and the height above the surface increase slightly over time. The top of the emission has a dome-like shape that also slowly expands over time. At early delay times, two arches can be observed, one that bends upwards and one that bends downwards. Both the vortex and the arches suggest that the hydrogen atoms in the plasma are strongly affected by pressure changes within the plasma. Whereas the upward-bending arch is likely related to the outgoing shock wave, the downward-bending arch could

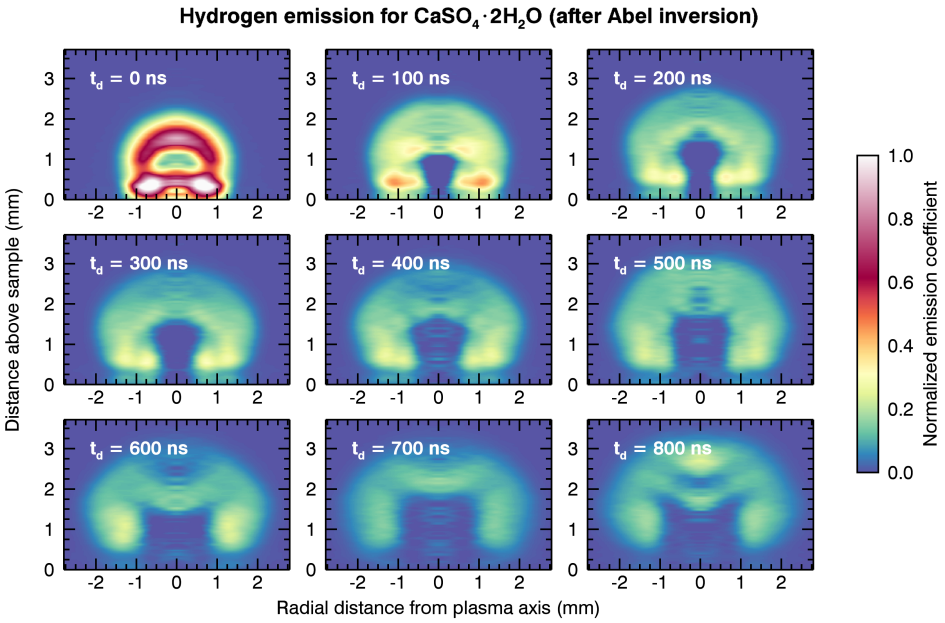

Figure 7.11: Radial emission coefficient of the H_α line in the plasma of a $CaSO_4 \cdot 2\,H_2O$ sample at different delay times from 0 ns to 800 ns, measured with a gate width of 100 ns. The emission coefficient is mirrored at the plasma axis to give the impression of a slice through the plasma. The shape of the emission is very similar to the one observed for the JSC Mars-1A sample.

be related to a shock wave that was reflected back into the plasma from the outgoing shock wave front. The light hydrogen atoms are strongly affected by these pressure changes and accumulate in regions closer to the two shock wave fronts. In comparison, the emissions of the heavier Ca^+ ions shown in Fig. 7.8 did not seem to be dominated by pressure gradients and flows within the plasma in the same way.

After the first 100 ns, there is no hydrogen emission in the center of the plasma close to the sample surface. This could be related to a lower temperature in this region, but this is unlikely at the low delay times at which the effect is first observed. Instead, the strong influence of the shock wave suggests that the hydrogen concentration is much lower at the center. The outgoing shock wave could create a suction that pulls the hydrogen outwards, leading to the accumulation of hydrogen atoms behind the shock wave. The vortex that appears at the lower end of the shock wave front could also be explained by this, as the low pressure at the plasma center creates an inflow of atoms, which are first pulled inwards horizontally along the sample surface and then pulled upwards by the expanding shock wave. This effect is also predicted by simulations of the laser-induced plasma that include dynamic transport mechanisms [134].

The radial emission coefficient of the H_α line in the plasma of a $CaSO_4 \cdot 2\,H_2O$ sample, shown in Fig. 7.11, is very similar to the one shown for JSC Mars-1A. Again, a

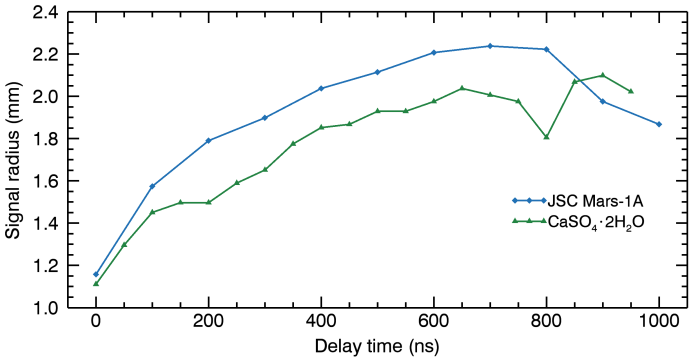

Figure 7.12: Radius of the spatial distribution of the H_α line in dependence of the delay time for the JSC Mars-1A sample and the $CaSO_4 \cdot 2\,H_2O$ sample.

vortex at the side of the plasma plume and arches at the top can be observed, but the features appear later than before and are less clear, because the emission is more spread out. These differences could be related to the different compositions of the samples, which influence the laser ablation process and the strength of the shock wave.

Figure 7.12 shows the radius of the hydrogen signal over time for both samples, measured as the largest radius at which the full width at half maximum is observed. The values are similar for both samples, but the radius is slightly higher for the JSC Mars-1A sample. The measurements clearly show a deceleration due to the atmospheric pressure. After a fast expansion in the first 200 ns, the expansion slows down and eventually stops at about 800 ns. For the hydrogen signal of the JSC Mars-1A sample, a decrease of the radius can be observed at higher delay times, which is related to the fact that the hydrogen signal is only found in small distinct regions at this point.

7.2.4 Atmospheric carbon emissions

The investigated C(III) emission at 229.7 nm in the plasma of the $CaSO_4 \cdot 2\,H_2O$ sample is shown in Fig. 7.13 for different delay times. I confirmed that it is the C(III) signal by repeating the measurement while using air as the ambient gas, in which case the signal disappears. It is surprising that the C(III) signal appears at all in the LIBS plasma, since the second ionization can only be found at high temperatures, while the atmospheric emissions are usually assumed to be located in a colder outer layer of the plasma, in accordance with the measurements made by Aguilera et al. [2]. Here the C(III) signal is located directly at the center of the plasma, which is still the hottest region in the plasma at this early stage. It is likely that this emission can only be observed due to the high temperature in this region, not because of a higher carbon concentration. Potentially the carbon concentration is even reduced at the plasma center due to the expanding plasma that pushes out the ambient gas. In that case

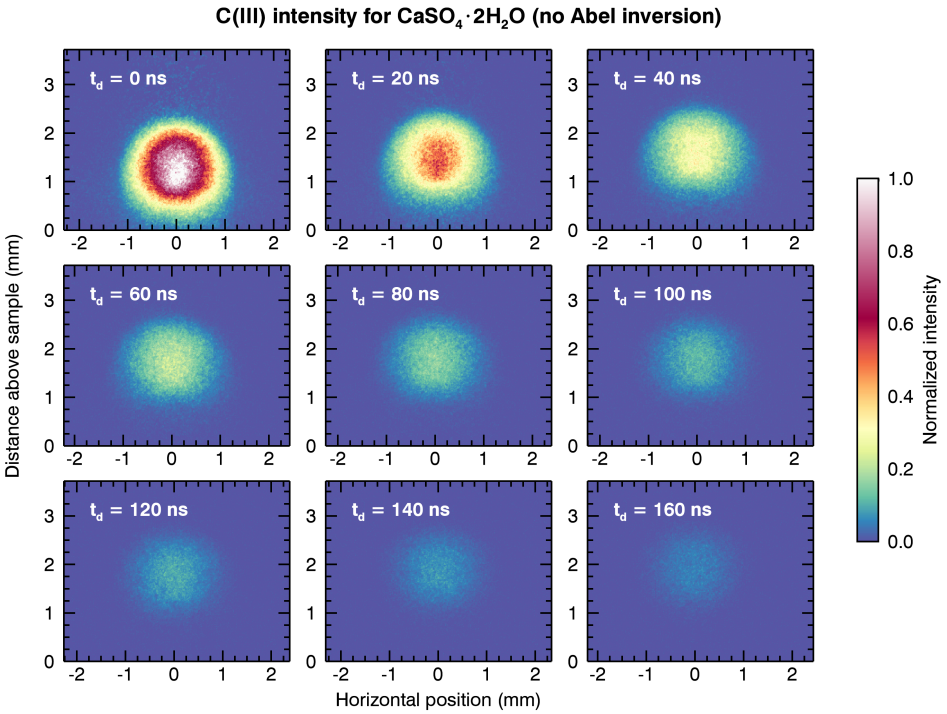

Figure 7.13: Spatial distribution of the C(III) line at 229.7 nm in the plasma of a $CaSO_4 \cdot 2\,H_2O$ sample at different delay times from 0 ns to 160 ns, measured with a gate width of 20 ns and a small aperture.

the measurements show that the temperature in the plasma center is high enough to produce significant C(III) emission even at a delay of 160 ns. However, it can also be observed that the maximum intensity shifts slightly towards higher plasma regions, indicating a shift of the temperature towards the upper plasma layers.

Like the C(III) emission, the C(I) emission is found closer to the center of the plasma than initially expected. The radial emission coefficient of it is shown in Fig. 7.14 for various delay times. At the center of the plasma, there is no C(I) emission. This could mean that the temperature is too high at the center, but since molecular emissions appear very close to the plasma center at similar delay times, another potential explanation is that the carbon is pulled outwards by the expanding plasma shock wave. Without further measurements, this cannot be determined for certain.

At a delay of 300 ns, the radius of the C(I) emission is about 1.5 mm, which is lower than the radius of the hydrogen emission. The carbon emission therefore seems to be relatively close to the plasma center, not in an outer layer. It is surprising that no carbon emission can be found further out, as it indicates that the temperature drops very quickly in the outer layers, where there should be a higher concentration of carbon than in the plasma center. However, it is also possible that the vorticity of the plasma pulls in the ambient gas as the plasma expands outwards. This could explain why a

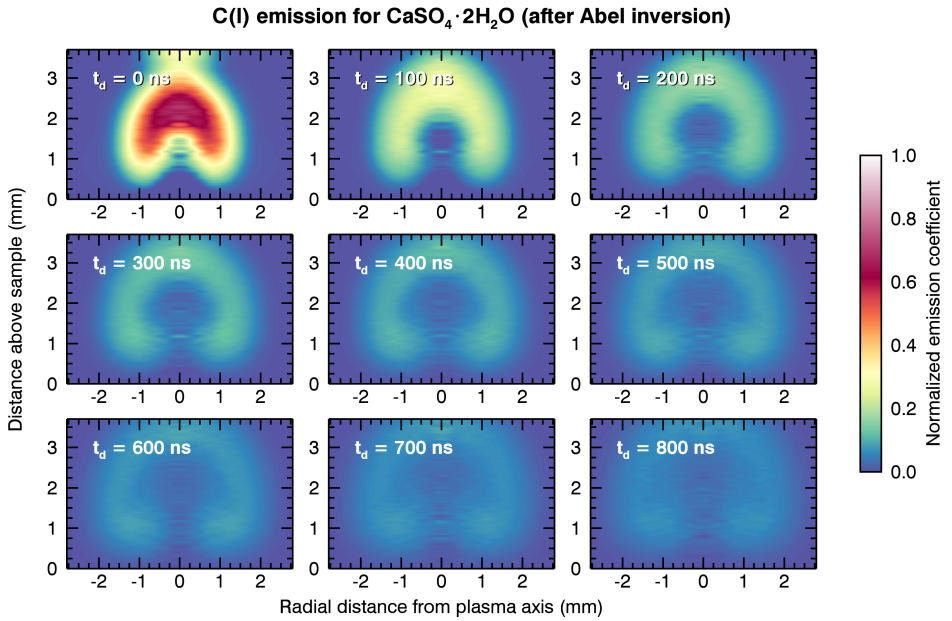

Figure 7.14: Radial emission coefficient of the C(I) line at 247.9 nm in the plasma of a $CaSO_4 \cdot 2\,H_2O$ sample at different delay times from 0 ns to 800 ns, measured with a gate width of 200 ns and a small aperture. The emission coefficient is mirrored at the plasma axis to give the impression of a slice through the plasma.

relatively strong carbon emission is observed within the plasma. The C(I) emission near the surface at delay times of 300–500 ns also resembles a vortex, though it is not as clear as in the case of the hydrogen signal.

Both the C(I) signal and the C(III) signal seem to be blurred. If the C(I) emission is measured with an open aperture, the lack of emission from the plasma center cannot be observed, and even with a small aperture the signal appears more blurred than other observed signals. It is possible that the UV spectral range is not focused correctly by the plasma imaging setup despite the apparent sharpness of the calibration measurements in Chapter 6. In that case, the radius of the C(I) emission will likely be slightly larger, but both signals will still be near or at the plasma center.

7.2.5 Atmospheric and ablated oxygen emissions

The radial emission coefficient of the O(I) triplet at 777.4 nm is shown in Fig. 7.15 for the NaCl sample and for the $CaSO_4 \cdot 2\,H_2O$ sample. The emission is weaker for the $CaSO_4 \cdot 2\,H_2O$ sample than it is for the NaCl sample, which is surprising. No hydrogen was detected in the plasma of the NaCl sample, so that adsorbed water cannot explain this observation. The detected oxygen comes only from the CO_2 in the Mars-analog atmosphere. At delay times of 100 ns or longer, the emission has a dome-like shape for both samples. The emission coefficient is only high in a thin layer at the edge of the

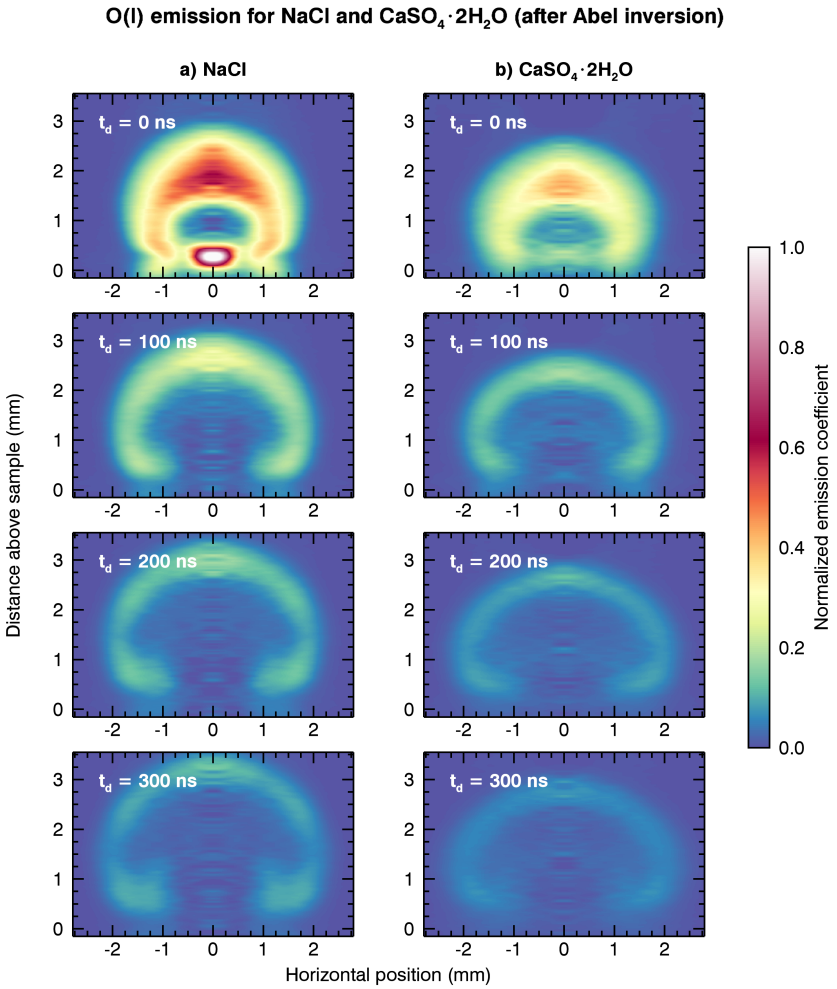

Figure 7.15: Radial emission coefficient of the O(I) triplet at 777.4 nm in the plasma of a) the NaCl sample and b) the $CaSO_4 \cdot 2\,H_2O$ sample at different delay times from 0 ns to 300 ns, measured with a gate width of 200 ns and a small aperture. The emission coefficient is mirrored at the plasma axis to give the impression of a slice through the plasma.

plasma, which visually resembles a shock wave. Near the sample surface, the emission can also be found closer to the plasma axis in a shape that again resembles a vortex. This effect is especially pronounced in the measurement of the NaCl sample at 300 ns delay. The distribution of the O(I) emission is otherwise slightly higher for the NaCl sample, but slightly wider for the $CaSO_4 \cdot 2\,H_2O$ sample. It is unclear whether this is a reproducible effect.

The O(I) distribution resembles the H_α distribution in Fig. 7.11, though there are also differences. The emission in the outer layers is similar in shape, width, and height. The radius of the O(I) emission over time is also similar to that of H_α, see Fig. 7.16. Furthermore, the apparent vortices near the sample surface can be seen again. However, the vortices are weaker, and the distribution of the emission closer to the plasma center

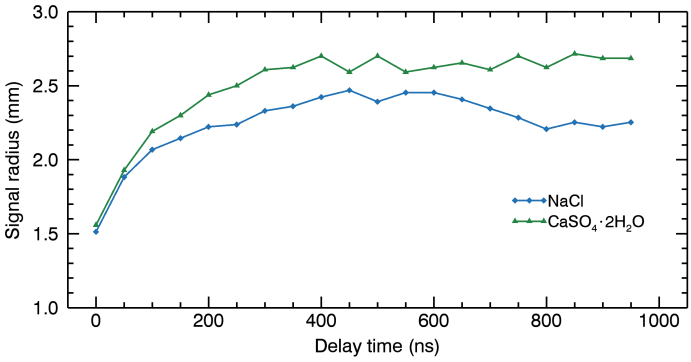

Figure 7.16: Radius of the emission of the O(I) triplet in dependence of the delay time for the NaCl sample and the $CaSO_4 \cdot 2\,H_2O$ sample.

is different. There is no significant emission of the O(I) triplet in the plasma center, whereas a complex distribution with strong emission can be observed for the H_α line. The radius of the O(I) emission in Fig. 7.16 also seems to be generally larger than that of the H_α emission in Fig. 7.12. This could indicate that the shock wave compresses the ambient gas and creates a thin layer of high oxygen concentration in front of the shock wave. However, the C(I) emission had a smaller radius than the H_α emission and was generally found closer to the plasma center, which does not support this theory.

7.2.6 Hydrogen and oxygen next to a barrier

The measurements of the H_α line and the O(I) triplet with a vertical barrier placed on a $CaSO_4 \cdot 2\,H_2O$ sample are shown in Fig. 7.17 for different delay times. For both emissions, the plasma needs to be formed very close to the barrier in order to be able to see an effect. This is in contrast to [119], where an increase of the hydrogen signal was already detected at distances of 3 mm or more. The measurements shown in Fig. 7.17 are therefore the ones that were made closest to the barrier. For the oxygen signal, the distance is 0.25 mm larger because measurements could not be done at the same positions as before. Because the symmetry of the plasma emission is broken by the barrier, no radial emission coefficients were calculated.

The effect of the barrier is similar for both emissions. The plasma does not extend as far out as it does on the other side, where it is not confined by a barrier. However, the emission also does not extend up to the barrier itself. A small gap can be seen between the barrier and the emission, and slightly above the sample an small part of the emission bends back even further, similar to the downward arch that was observed in the hydrogen emission. This indicates that the shock wave is reflected back into the plasma and compresses it in front of the barrier. Due to the compression, the particle concentration and the temperature are increased, causing a local intensity maximum.

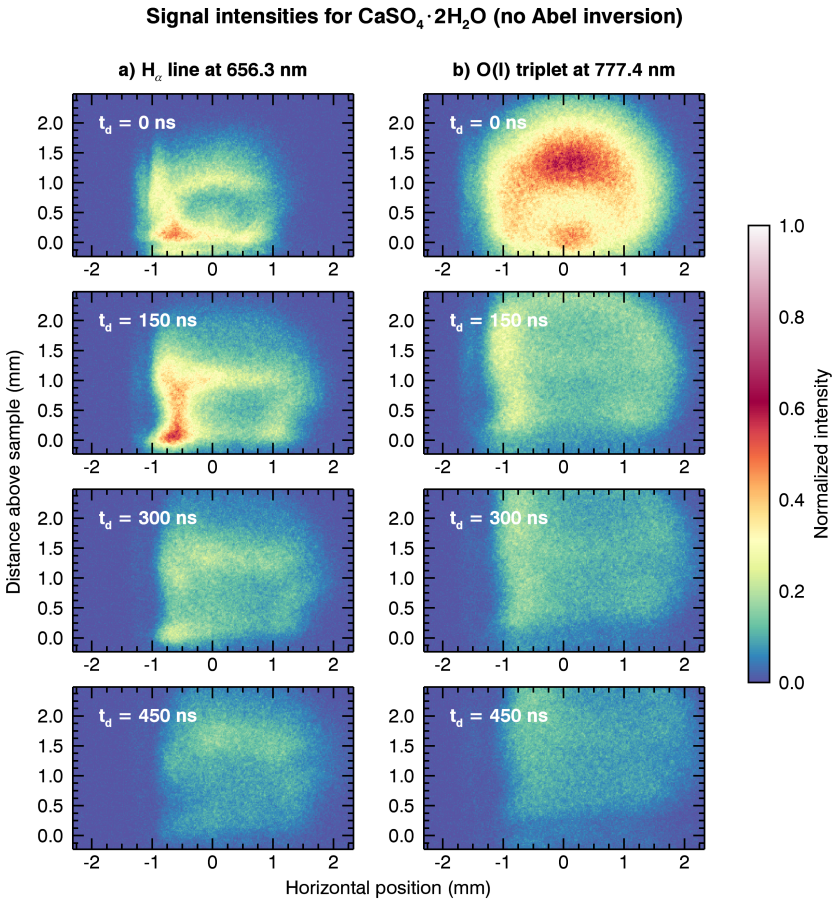

Figure 7.17: Spatial distribution of a) the H_α line and b) the O(I) triplet in the plasma of a $CaSO_4 \cdot 2\,H_2O$ sample next to a vertical barrier at different delay times. The shown measurements were made at a distance of 0.5 mm (a) and a distance of 0.75 mm (b) between laser beam and barrier.

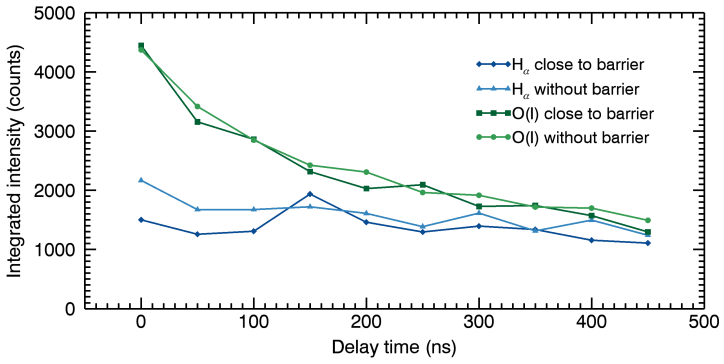

Figure 7.18: Integrated intensity of the emissions of hydrogen and oxygen over time, once with a vertical barrier close to the plasma and once without a vertical barrier.

The spatially integrated intensity is shown in Fig. 7.18 in dependence of the delay time for the measurements close to the barrier and for those far away from the barrier. It can be seen that there is no significant difference in the intensity of these measurements for either of the two signals. The hydrogen signal is even reduced slightly when measured close to the barrier, though this may be explained by a reduction of the laser energy if part of the laser beam was shielded by the barrier. The increase of the hydrogen emission close to a wall that was reported by Rapin et al. [119] could not be reproduced.

7.3 Summary and discussion

The observations made in this chapter indicate that the distributions of the plasma emissions are strongly governed by hydrodynamic processes inside the plasma plume that lead to an unexpected evolution of the temperature inside the plasma. The results seem to support a model of the plasma like the one shown in Fig. 7.19. Here the plasma is initially hot and dense and still has a small diameter (Fig. 7.19a). The highest temperatures are found directly in the plasma center, which is highly ionized so that intense emissions of ionized calcium and carbon can be observed. While the carbon concentration may already be higher in the outer regions of the plasma due to the displacement of the ambient gas by the ablated material, only the plasma center is hot enough to produce intense C(III) emissions. However, as the plasma expands, the distribution of the temperature within the plume drastically changes (Fig. 7.19b). Following the shock wave, the high atomic and ionic concentrations also expand outwards and lead to a higher temperature in the region close to the plasma front, while the rarefaction wave following the outgoing shock wave reduces the number densities at the center. The plasma center cools quickly and turns into a cold plasma region in which molecules such as CaCl and CaF are stable. Close to the sample surface, the plasma expansion is slowed down by drag, while the upwards flow at the plasma center creates a suction that pulls in ambient gas. Vortices form in the lower outer regions of the plasma plume. These vortices can be observed clearly in the hydrogen signal (Fig. 7.10 and Fig. 7.11), since hydrogen is the lightest element and its distribution is most strongly governed by the pressure gradients in the plasma. The same general shape of the plasma emissions can also be observed in the emissions of ionic calcium (Fig. 7.8), atomic carbon (Fig. 7.14), and oxygen (Fig. 7.15). However, oxygen is only found in a thin layer directly at the plasma front, while carbon seems to be found closer to the plasma center. It is possible that the emission of atomic oxygen, which is stable over a larger temperature range than atomic carbon due to its higher ionization energy of 13.6 eV, is governed by the spatial changes in the oxygen concentration, while the emission of atomic carbon, which has a lower ionization energy of 11.3 eV, is more

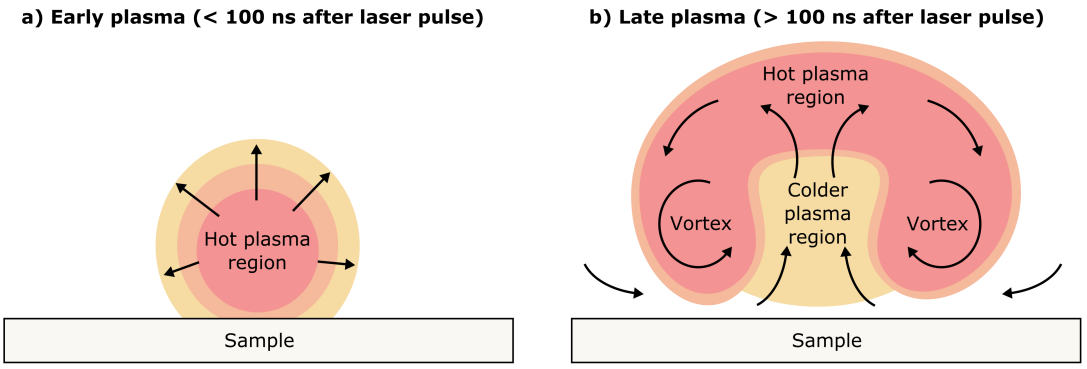

Figure 7.19: Illustration of dynamics and temperature gradients within the early plasma (a) and the late plasma (b) based on the observations in this chapter. The early plasma is dense and hot, with the temperature decreasing sharply from the plasma center. The density of the plasma at later stages is more strongly defined by the pressure gradients within the plasma.

strongly governed by the temperature of the plasma and is therefore found in regions closer to the plasma center. Further measurements of carbon and oxygen emissions from different energy levels and for different samples could be useful to understand these observations better.

While the observations made for the molecular emissions are different from the expectations based on plasma simulations [29, 135, 136], the results correspond well with experimental results by Gaft et al. [50] under terrestrial conditions. The general model for the evolution of the plasma plume proposed here also corresponds very well with two-dimensional hydrodynamic simulations of the plasma plume in terrestrial ambient conditions by Shabanov and Gornushkin [134]. These predicted a strong vorticity within the plasma, especially close to the sample surface, as well as complex temperature distributions affected by outgoing as well as reflected shock waves inside the plasma. However, the simulations were made for terrestrial ambient conditions, resulting in a stronger confinement of the plasma, higher temperatures at the plasma center, and a lower influence of transport mechanisms on the signal distributions. Similar simulations of the plasma in Martian ambient conditions could be promising for an improved understanding of the laser-induced plasma on Mars and as a comparison for future analyses with the plasma imaging setup.

In the final study, the signal distributions of the H_α line and the O(I) triplet were investigated for different distances from a vertical barrier. While the plasma expansion was considerably confined in proximity to the barrier, the signal intensities did not change noticeably. The sevenfold increase of the hydrogen signal close to a barrier that was reported by Rapin et al. [119] could not be reproduced. It is likely that their observed increase of the hydrogen signal is related to the vacuum grease that was

used on the barrier in their experiment, since this grease contains a high amount of hydrogen. This possibility was already considered by the authors and seems to be the most probable explanation considering the results shown here. The implications for the hydrogen analysis on Mars are considerable. Intense hydrogen signals have frequently been observed on Mars, especially at protrusions and in cavities [119, 130]. Rapin et al. [119] proposed that the strong hydrogen signals were caused by geometrical effects instead of higher hydrogen concentrations. Since their results could not be reproduced here, it seems likely that the hydrogen concentration is actually higher in cavities on Mars and could potentially be related to frozen water, which could be more stable in these cavities.

The results of these first studies show that plasma imaging can be an important tool for LIBS. The spatially resolved measurements can be used to check the validity of long-held assumptions in LIBS, for example that of an approximately Gaussian temperature profile from the plasma axis towards the outer plasma regions or the assumed homogeneity of the plasma plume. The Abel inversion is a useful deconvolution technique that has been successfully applied here to many different measurements in order to obtain the radial emission coefficient distribution. The plasma imaging setup is versatile and capable of providing data with a high spatial resolution.

8. Summary and Conclusion

The focus of this thesis was on the investigation of molecular emissions in LIBS and on the analysis and characterization of the laser-induced plasma in Martian atmospheric conditions. The studies that were conducted were intended to further our understanding of LIBS on Mars, to help with the interpretation of Martian LIBS data, and to provide new models for data analysis. As outlined in Chapter 1, I set out to answer three specific questions:

- Which of the molecular emissions that could be observed in Martian LIBS spectra are well-suited for the detection and quantification of chlorine and fluorine?
- What is the relation between the intensity of a molecular emission and the concentrations of the reacting elements?
- How are atomic, ionic, and molecular emissions distributed within the laser-induced plasma, and which processes determine these spatial distributions?

In order to answer the first question, I investigated the most intense molecular emissions of MgCl, CaCl, MgF, and CaF, namely the $\Delta v = 0$ band sequences of the $A^2\Pi – X^2\Sigma^+$ transition. The MgCl and MgF bands were found not to be suitable for detection and quantification purposes due to a very low SNR even at high concentrations of the reactants. The formation of MgCl and MgF also seemed to be less favored in comparison to the formation of CaCl and CaF in the laser-induced plasma, since their intensities quickly decreased as the Ca concentration in the samples increased. CaCl and CaF were found to be well-suited for the detection and quantification of chlorine and fluorine, which could be explained by the high population densities of the excited energy levels as well as the high Franck-Condon factors of the higher vibrational levels in the band sequences, which lead to a significant increase of the total band intensity.

The second question was investigated very closely for the CaCl and CaF bands. It was shown that LTE calculations of the molecular band intensities cannot describe the band intensities of CaCl and CaF accurately. I derived a new theoretical model based on chemical reactions that are only partially balanced, which was able to describe the CaCl and CaF band intensities accurately for many different sets of samples and for different measurement parameters. The non-equilibrium effects are stronger for CaCl, which readily reacts to $CaCl_2$ for higher Cl concentrations. The reaction model enables the calculation of calibration curves for the quantification of chlorine and fluorine, which are especially accurate if the concentrations of the halogens are low and the concentration

of calcium is high. However, an open question remains with regards to the influence of physical matrix effects on the signal intensities. Future studies should focus on samples with similar reactant concentrations, but different material parameters and different surface properties. Furthermore, the parameters ζ and η for the CaCl and CaF bands need to be determined for LIBS instruments on Mars in order to use the molecular emissions for quantification.

The final question was investigated with the plasma imaging setup that was developed in the course of this thesis. The results provide important information that call into question the common assumptions about the laser-induced plasma in Martian atmospheric conditions. These include the assumption that the plasma center is the hottest and most emissive region of the plasma plume. While the plasma center is initially very dense, hot, and emissive in my experiments, the measurements indicate that it has a low temperature and is nearly devoid of atomic and ionic species as soon as 100–200 ns after the laser pulse. The low temperature instead enables the formation of molecular species at the plasma center. Flows and pressure gradients within the plasma seem to be of similar importance to the spatial distributions of plasma emissions as temperature gradients. They especially seem to influence the hydrogen signal distribution. Other atomic and ionic emissions were affected to a lesser degree, potentially due to the higher mass of these elements. The dynamics within the plasma plume and their influence on the plasma parameters is an important field of investigation that should be expanded upon in future studies. This can be crucial to understand which external conditions may lead to changes in the signal intensities of elements that are important in the context of Martian exploration. An investigation of the influence of a vertical barrier on the hydrogen signal could not reproduce a reported increase of the hydrogen signal intensity in close proximity to a barrier [119]. This is relevant for the analysis of hydrogen signals in Martian LIBS spectra. High signal intensities might not be caused by surface effects after all, but could indeed be related to higher hydrogen concentrations.

Since the number of LIBS instruments used for in-situ planetary exploration will increase in the future, it will also become more important to investigate the capabilities and challenges of this analytical technique closely. The results of this thesis have shown that some models that are used for LIBS in terrestrial conditions will lead to incorrect results in different planetary conditions. The development of new models, such as the reaction model presented in this thesis, as well as the employment of new experimental setups, such as the plasma imaging setup, will be crucial for an accurate spectroscopic analysis of extraterrestrial environments.

Bibliography

[1] J. Aguilera and C. Aragón. Temperature and electron density distributions of laser-induced plasmas generated with an iron sample at different ambient gas pressures. *Applied Surface Science*, 197-198:273–280, 2002. doi: 10.1016/S0169-4332(02)00382-3.

[2] J. A. Aguilera, C. Aragón, and J. Bengoechea. Spatial characterization of laser-induced plasmas by deconvolution of spatially resolved spectra. *Applied Optics*, 42(30):5938–5946, 2003. doi: 10.1364/AO.42.005938.

[3] C. C. Allen, K. M. Jager, R. V. Morris, D. J. Lindstrom, M. M. Lindstrom, and J. P. Lockwood. Martian soil stimulant available for scientific, educational study. *Eos, Transactions American Geophysical Union*, 79(34):405–405, 1998. doi: 10.1029/98EO00309.

[4] C. Alvarez-Llamas, J. Pisonero, and N. Bordel. Quantification of fluorine traces in solid samples using CaF molecular emission bands in atmospheric air Laser-Induced Breakdown Spectroscopy. *Spectrochimica Acta Part B: Atomic Spectroscopy*, 123:157–162, 2016. doi: 10.1016/j.sab.2016.08.006.

[5] C. Alvarez-Llamas, J. Pisonero, and N. Bordel. A novel approach for quantitative LIBS fluorine analysis using CaF emission in calcium-free samples. *Journal of Analytical Atomic Spectrometry*, 32(1):162–166, 2017. doi: 10.1039/c6ja00386a.

[6] D. E. Anderson, B. L. Ehlmann, O. Forni, S. M. Clegg, A. Cousin, N. H. Thomas, J. Lasue, D. M. Delapp, R. E. McInroy, O. Gasnault, M. D. Dyar, S. Schröder, S. Maurice, and R. C. Wiens. Characterization of LIBS emission lines for the identification of chlorides, carbonates, and sulfates in salt/basalt mixtures for the application to MSL ChemCam data. *Journal of Geophysical Research: Planets*, 122(4):744–770, 2017. doi: 10.1002/2016JE005164.

[7] C. Aragón and J. Aguilera. Characterization of laser induced plasmas by optical emission spectroscopy: A review of experiments and methods. *Spectrochimica Acta Part B: Atomic Spectroscopy*, 63(9):893–916, 2008. doi: 10.1016/j.sab.2008.05.010.

[8] N. Arnold, J. Gruber, and J. Heitz. Spherical expansion of the vapor plume into ambient gas: An analytical model. *Applied Physics A: Materials Science and Processing*, 69(7):S87–S93, 1999. doi: 10.1007/s003399900183.

[9] V. Babushok, F. DeLucia, P. Dagdigian, J. Gottfried, C. Munson, M. Nusca, and A. Miziolek. Kinetic modeling study of the laser-induced plasma plume of cyclotrimethylenetrinitramine (RDX). *Spectrochimica Acta Part B: Atomic Spectroscopy*, 62(12):1321–1328, 2007. doi: 10.1016/j.sab.2007.10.029.

[10] R. J. M. Bennett. Hönl-London factors for doublet transitions in diatomic molecules. *Monthly Notices of the Royal Astronomical Society*, 147(1):35–46, 2014. doi: 10.1093/mnras/147.1.35.

[11] J. D. Blacic, D. R. Pettit, D. A. Cremers, and N. Roessler. Laser-induced breakdown spectroscopy for remote elemental analysis of planetary surfaces. *International Symposium on Spectral Sensing Research*, 1992.

[12] N. Bloembergen. Laser induced electric breakdown in solids. *IEEE Journal of Quantum Electronics*, 10(3):375–386, 1974. doi: 10.1109/JQE.1974.1068132.

[13] A. Bogaerts and Z. Chen. Effect of laser parameters on laser ablation and laser-induced plasma formation: A numerical modeling investigation. *Spectrochimica Acta Part B: Atomic Spectroscopy*, 60(9-10):1280–1307, 2005. doi: 10.1016/j.sab.2005.06.009.

[14] A. Bogaerts, Z. Chen, R. Gijbels, and A. Vertes. Laser ablation for analytical sampling: what can we learn from modeling? *Spectrochimica Acta Part B: Atomic Spectroscopy*, 58(11):1867–1893, 2003. doi: 10.1016/j.sab.2003.08.004.

[15] R. Brennetot, J. L. Lacour, E. Vors, A. Rivoallan, D. Vailhen, and S. Maurice. Mars analysis by laser-induced breakdown spectroscopy (MALIS): Influence of Mars atmosphere on plasma emission and study of factors influencing plasma emission with the use of Doehlert designs. *Applied Spectroscopy*, 57(7):744–752, 2003. doi: 10.1366/000370203322102816.

[16] M. Capitelli, F. Capitelli, and A. Eletskii. Non-equilibrium and equilibrium problems in laser-induced plasmas. *Spectrochimica Acta Part B: Atomic Spectroscopy*, 55(6):559–574, 2000. doi: 10.1016/S0584-8547(00)00168-3.

[17] B. C. Clark and D. C. Van Hart. The salts of Mars. *Icarus*, 45(2):370–378, 1981. doi: 10.1016/0019-1035(81)90041-5.

[18] B. C. Clark, A. K. Baird, H. J. Rose, P. Toulmin, K. Keil, A. J. Castro, W. C. Kelliher, C. D. Rowe, and P. H. Evans. Inorganic analyses of Martian surface samples at the Viking landing sites. *Science*, 194(4271):1283–1288, 1976. doi: 10.1126/science.194.4271.1283.

[19] S. Clegg, J. Barefield, R. Wiens, S. Sharma, A. Misra, J. Tucker, M. Dyar, J. Lambert, S. Smrekar, and A. Treiman. Venus geochemical analysis by remote laser-induced breakdown spectroscopy (LIBS). *41st Lunar and Planetary Science Conference*, page 1631, 2010.

[20] S. M. Clegg, S. K. Sharma, A. K. Misra, M. D. Dyar, M. H. Hecht, J. Lambert, S. Feldman, N. Dallmann, R. C. Wiens, S. D. Humphries, D. T. Vaniman, E. A. Speicher, M. L. Carmosino, S. E. Smrekar, A. Treiman, A. Wang, S. Maurice, and L. Esposito. Remote laser induced breakdown spectroscopy (LIBS) geochemical investigation under Venus atmospheric conditions. *42nd Lunar and Planetary Science Conference*, page 1568, 2011.

[21] S. M. Clegg, N. Mangold, S. Le Mouélic, A. Olilla, R. Anderson, D. L. Blaney, B. Clark, A. Cousin, M. D. Dyar, B. L. Ehlmann, C. Fabre, O. Forni, J. Lasue, P.-Y. Meslin, S. Schröder, J. B. Sirven, D. T. Vaniman, S. Maurice, R. C. Wiens, and M. S. Team. High calcium phase observations at Rocknest with ChemCam. *44th Lunar and Planetary Science Conference*, page 2087, 2013.

[22] G. Colonna and A. D'Angola. A hierarchical approach for fast and accurate equilibrium calculation. *Computer Physics Communications*, 163(3):177–190, 2004. doi: 10.1016/j.cpc.2004.08.004.

[23] G. Colonna, A. Casavola, and M. Capitelli. Modelling of LIBS plasma expansion. *Spectrochimica Acta Part B: Atomic Spectroscopy*, 56(6):567–586, 2001. doi: 10.1016/S0584-8547(01)00230-0.

[24] D. A. Cremers and L. J. Radziemski. Detection of chlorine and fluorine in air by laser-induced breakdown spectrometry. *Analytical Chemistry*, 55(8):1252–1256, 1983. doi: 10.1021/ac00259a017.

[25] D. A. Cremers and L. J. Radziemski. *Handbook of Laser-induced Breakdown Spectroscopy*. John Wiley & Sons, Ltd, Chichester, UK, 2006. ISBN 9780470092996. doi: 10.1002/0470093013.

[26] D. A. Cremers, E. V. Sevostiyanova, L. Gibson, and R. C. Wiens. LIBS analysis of geological samples at low pressures: Application to Mars, the Moon, and asteroids. *35th Lunar and Planetary Science Conference*, page 1589, 2004.

[27] G. Cristoforetti, A. De Giacomo, M. Dell'Aglio, S. Legnaioli, E. Tognoni, V. Palleschi, and N. Omenetto. Local thermodynamic equilibrium in laser-induced breakdown spectroscopy: Beyond the McWhirter criterion. *Spectrochimica Acta Part B: Atomic Spectroscopy*, 65(1):86–95, 2010. doi: 10.1016/j.sab.2009.11.005.

[28] J. P. Dahl and M. Springborg. The Morse oscillator in position space, momentum space, and phase space. *The Journal of Chemical Physics*, 88(7):4535–4547, 1988. doi: 10.1063/1.453761.

[29] A. De Giacomo and J. Hermann. Laser-induced plasma emission: from atomic to molecular spectra. *Journal of Physics D: Applied Physics*, 50(18):183002, 2017. doi: 10.1088/1361-6463/aa6585.

[30] A. De Giacomo, M. Dell'Aglio, R. Gaudiuso, G. Cristoforetti, S. Legnaioli, V. Palleschi, and E. Tognoni. Spatial distribution of hydrogen and other emitters in aluminum laser-induced plasma in air and consequences on spatially integrated Laser-Induced Breakdown Spectroscopy measurements. *Spectrochimica Acta Part B: Atomic Spectroscopy*, 63(9):980–987, 2008. doi: 10.1016/j.sab.2008.06.010.

[31] A. De Giacomo, R. Gaudiuso, M. Dell'Aglio, and A. Santagata. The role of continuum radiation in laser induced plasma spectroscopy. *Spectrochimica Acta Part B: Atomic Spectroscopy*, 65(5):385–394, 2010. doi: 10.1016/J.SAB.2010.03.016.

[32] B. deB. Darwent. *Bond dissociation energies in simple molecules*. National Bureau of Standards, 1970.

[33] B. Dick. Inverting ion images without Abel inversion: Maximum entropy reconstruction of velocity maps. *Physical Chemistry Chemical Physics*, 16(2):570–580, 2014. doi: 10.1039/c3cp53673d.

[34] F. R. Doucet, P. J. Faustino, M. Sabsabi, and R. C. Lyon. Quantitative molecular analysis with molecular bands emission using laser-induced breakdown spectroscopy and chemometrics. *Journal of Analytical Atomic Spectrometry*, 23(5):694, 2008. doi: 10.1039/b714219f.

[35] G. Dreibus and H. Wänke. Mars, a volatile-rich planet. *Meteoritics*, 20(2):367–381, 1985. doi: 10.1017/CBO9781107415324.004.

[36] G. Dreibus and H. Wänke. Volatiles on Earth and Mars: A comparison. *Icarus*, 71(2):225–240, 1987. doi: 10.1016/0019-1035(87)90148-5.

[37] B. L. Ehlmann and C. S. Edwards. Mineralogy of the Martian surface. *Annual Review of Earth and Planetary Sciences*, 42(1):291–315, 2014. doi: 10.1146/annurev-earth-060313-055024.

[38] J. El Haddad, L. Canioni, and B. Bousquet. Good practices in LIBS analysis: Review and advices. *Spectrochimica Acta Part B: Atomic Spectroscopy*, 101:171–182, 2014. doi: 10.1016/j.sab.2014.08.039.

[39] A. El Sherbini, H. Hegazy, and T. El Sherbini. Measurement of electron density utilizing the Hα-line from laser produced plasma in air. *Spectrochimica Acta Part B: Atomic Spectroscopy*, 61(5):532–539, 2006. doi: 10.1016/j.sab.2006.03.014.

[40] P. Elder, T. Jerrick, and J. W. Birkeland. Determination of the radial profile of absorption and emission coefficients and temperature in cylindrically symmetric sources with self-absorption. *Applied Optics*, 4(5):589–592, 1965. doi: 10.1364/AO.4.000589.

[41] W. E. Ernst, J. O. Schröder, U. Buck, J. Kesper, T. Seelemann, L. E. Berg, and H. Martin. Combined analysis of laser and microwave spectroscopy on CaCl: The A2Π-X2Σ+and B2Σ+-X2Σ+systems. *Journal of Molecular Spectroscopy*, 117(2): 342–354, 1986. doi: 10.1016/0022-2852(86)90159-1.

[42] J. Filiberto and A. H. Treiman. Martian magmas contained abundant chlorine, but little water. *Geology*, 37(12):1087–1090, 2009. doi: 10.1130/G30488A.1.

[43] J. Filiberto, J. Wood, R. Dasgupta, N. Shimizu, L. Le, and A. H. Treiman. Effect of fluorine on near-liquidus phase equilibria of an Fe-Mg rich basalt. *Chemical Geology*, 312-313:118–126, 2012. doi: 10.1016/j.chemgeo.2012.04.015.

[44] O. Forni, M. Gaft, M. J. Toplis, S. M. Clegg, S. Maurice, R. C. Wiens, N. Mangold, O. Gasnault, V. Sautter, S. Le Mouélic, P. Y. Meslin, M. Nachon, R. E. McInroy, A. M. Ollila, A. Cousin, J. C. Bridges, N. L. Lanza, and M. D. Dyar. First detection of fluorine on Mars: Implications for Gale Crater's geochemistry. *Geophysical Research Letters*, 42(4):1020–1028, 2015. doi: 10.1002/2014GL062742.

[45] O. Forni, D. T. Vaniman, L. Le Deit, S. M. Clegg, N. L. Lanza, J. Lasue, D. L. Bish, N. Mangold, R. C. Wiens, P.-Y. Meslin, O. Gasnault, S. Maurice, A. Cousin, M. J. Toplis, H. Newsom, and E. B. Rampe. Fluorine and lithium at the Kimberley Outcrop, Gale Crater. *46th Lunar and Planetary Science Conference*, page 1989, 2015.

[46] O. Forni, M. Nachon, A. Mangold, D. L. Blaney, R. C. Wiens, S. M. Clegg, P.-Y. Meslin, O. Gasnault, S. Maurice, A. Cousin, J. Frydenvand, S. Schwenzer, and J. L. Eigenbrode. Fluorine in the Pahrump Outcrop, Gale Crater: Implications for fluid circulation and alteration. *47th Lunar and Planetary Science Conference*, page 1990, 2016.

[47] O. Forni, P.-Y. Meslin, J. L'Haridon, W. Rapin, M. Nachon, H. Newsom, N. Mangold, O. Gasnault, D. E. Anderson, R. B. Anderson, D. L. Blaney, S. M. Clegg, A. Cousin, E. Dehouck, J. R. Johnson, N. L. Lanza, J. Lasue, S. Maurice, and

R. C. Wiens. Detection of fluorine-rich phases, phosphates and halite in the Stimson-Murray units, Gale crater, Mars. *48th Lunar and Planetary Science Conference*, page 1838, 2017.

[48] O. Forni, P.-Y. Meslin, A. Cousin, S. M. Clegg, N. Mangold, L. Le Deit, O. Gasnault, G. David, M. Nachon, D. L. Blaney, H. E. Newsom, S. Maurice, R. C. Wiens, and M. Gaft. Fluorine on Mars: seven years of detection with ChemCam on-board MSL. *9th International Conference on Mars*, page 6095, 2019.

[49] M. P. Freeman and S. Katz. Determination of a radiance-coefficient profile from the observed asymmetric radiance distribution of an optically thin radiating medium. *Journal of the Optical Society of America*, 53(10):1172, 1963. doi: 10.1364/JOSA.53.001172.

[50] M. Gaft, L. Nagli, N. Eliezer, Y. Groisman, and O. Forni. Elemental analysis of halogens using molecular emission by laser-induced breakdown spectroscopy in air. *Spectrochimica Acta Part B: Atomic Spectroscopy*, 98:39–47, 2014. doi: 10.1016/j.sab.2014.05.011.

[51] P. J. Gasda, E. B. Haldeman, R. C. Wiens, W. Rapin, T. F. Bristow, J. C. Bridges, S. P. Schwenzer, B. Clark, K. Herkenhoff, J. Frydenvang, N. L. Lanza, S. Maurice, S. Clegg, D. M. Delapp, V. L. Sanford, M. R. Bodine, and R. McInroy. In situ detection of boron by ChemCam on Mars. *Geophysical Research Letters*, 44(17):8739–8748, 2017. doi: 10.1002/2017GL074480.

[52] O. Gasnault, J. Mazoyer, A. Cousin, P.-Y. Meslin, J. Lasue, J.-L. Lacour, A. Ollila, G. Berger, O. Forni, S. Maurice, R.-C. Wiens, S. Clegg, and J. Blank. Deciphering sample and atmospheric oxygen contents with ChemCam on Mars. *43rd Lunar and Planetary Science Conference*, page 2888, 2012.

[53] M. A. Gigosos, M. Á. González, and V. Cardeñoso. Computer simulated Balmer-alpha, -beta and -gamma Stark line profiles for non-equilibrium plasmas diagnostics. *Spectrochimica Acta Part B: Atomic Spectroscopy*, 58(8):1489–1504, 2003. doi: 10.1016/S0584-8547(03)00097-1.

[54] F. R. Gilmore, R. R. Laher, and P. J. Espy. Franck–Condon factors, r-centroids, electronic transition moments, and Einstein coefficients for many nitrogen and oxygen band systems. *Journal of Physical and Chemical Reference Data*, 21(5): 1005–1107, 1992. doi: 10.1063/1.555910.

[55] I. B. Gornushkin, S. V. Shabanov, and U. Panne. Abel inversion applied to a transient laser induced plasma: Implications from plasma modeling. *Journal of Analytical Atomic Spectrometry*, 26(7):1457–1465, 2011. doi: 10.1039/c1ja10044k.

[56] H. R. Griem, A. C. Kolb, and K. Y. Shen. Stark broadening of hydrogen lines in a plasma. *Physical Review*, 116(1):4–16, 1959. doi: 10.1103/PhysRev.116.4.

[57] D. Grojo, J. Hermann, and A. Perrone. Plasma analyses during femtosecond laser ablation of Ti, Zr, and Hf. *Journal of Applied Physics*, 97(6):063306, 2005. doi: 10.1063/1.1861519.

[58] J. P. Grotzinger, J. Crisp, A. R. Vasavada, R. C. Anderson, C. J. Baker, R. Barry, D. F. Blake, P. Conrad, K. S. Edgett, B. Ferdowski, R. Gellert, J. B. Gilbert, M. Golombek, J. Gómez-Elvira, D. M. Hassler, L. Jandura, M. Litvak, P. Mahaffy, J. Maki, M. Meyer, M. C. Malin, I. Mitrofanov, J. J. Simmonds, D. Vaniman, R. V. Welch, and R. C. Wiens. Mars Science Laboratory mission and science investigation. *Space Science Reviews*, 170(1-4):5–56, 2012. doi: 10.1007/s11214-012-9892-2.

[59] R. M. Haberle, C. P. McKay, J. Schaeffer, N. A. Cabrol, E. A. Grin, A. P. Zent, and R. Quinn. On the possibility of liquid water on present-day Mars. *Journal of Geophysical Research E: Planets*, 106(E10):23317–23326, 2001. doi: 10.1029/2000JE001360.

[60] D. W. Hahn and N. Omenetto. Laser-induced breakdown spectroscopy (LIBS), part I: Review of basic diagnostics and plasma-particle interactions: still-challenging issues within the analytical plasma community. *Appl. Spectrosc.*, 64(12):335A–366A, 2010. doi: 10.1366/000370210793561691.

[61] D. W. Hahn and N. Omenetto. Laser-induced breakdown spectroscopy (LIBS), part II: Review of instrumental and methodological approaches to material analysis and applications to different fields. *Applied Spectroscopy*, 66(4):347–419, 2012. doi: 10.1366/11-06574.

[62] C. Haisch, R. Niessner, O. I. Matveev, U. Panne, and N. Omenetto. Element-specific determination of chlorine in gases by laser-induced-breakdown-spectroscopy (LIBS). *Fresenius' Journal of Analytical Chemistry*, 356(1):21–26, 1996. doi: 10.1007/s0021663560021.

[63] S. S. Harilal, B. E. Brumfield, and M. C. Phillips. Lifecycle of laser-produced air sparks. *Physics of Plasmas*, 22(6):063301, 2015. doi: 10.1063/1.4922076.

[64] A.-M. Harri, M. Genzer, O. Kemppinen, H. Kahanpää, J. Gomez-Elvira, J. A. Rodriguez-Manfredi, R. Haberle, J. Polkko, W. Schmidt, H. Savijärvi, J. Kauhanen, E. Atlaskin, M. Richardson, T. Siili, M. Paton, M. de la Torre Juarez, C. Newman, S. Rafkin, M. T. Lemmon, M. Mischna, S. Merikallio, H. Haukka, J. Martin-Torres, M.-P. Zorzano, V. Peinado, R. Urqui, A. Lapinette, A. Scodary,

T. Mäkinen, L. Vazquez, N. Rennó, and t. R. S. the REMSMSL Science Team. Pressure observations by the Curiosity rover: Initial results. *Journal of Geophysical Research: Planets*, 119(1):82–92, 2014. doi: 10.1002/2013JE004423.

[65] R. D. Harris, D. A. Cremers, C. Khoo, and K. Benelli. LIBS-based detection of geological samples at low pressures (< 0.0001 Torr) for moon and asteroid exploration. *36th Lunar and Planetary Science Conference*, page 1796, 2005.

[66] J. Hermann, A. Lorusso, A. Perrone, F. Strafella, C. Dutouquet, and B. Torralba. Simulation of emission spectra from nonuniform reactive laser-induced plasmas. *Physical Review E - Statistical, Nonlinear, and Soft Matter Physics*, 92(5):053103, 2015. doi: 10.1103/PhysRevE.92.053103.

[67] G. Herzberg. *Spectra of Diatomic Molecules*. Van Nostrand, 2nd editio edition, 1950. ISBN 0442033850.

[68] S. L. Hess, R. M. Henry, C. B. Leovy, J. A. Ryan, and J. E. Tillman. Meteorological results from the surface of Mars: Viking 1 and 2. *Journal of Geophysical Research*, 82(28):4559–4574, 1977. doi: 10.1029/JS082I028P04559@10.1002/(ISSN)2156-2202.VIKPROJ1.

[69] D. L. Hildenbrand. Dissociation energies and chemical bonding in the alkaline-earth chlorides from mass spectrometric studies. *The Journal of Chemical Physics*, 52(11):5751–5759, 1970. doi: 10.1063/1.1672855.

[70] T. Hirao, P. F. Bernath, C. E. Fellows, R. F. Gutterres, and M. Vervloet. High-resolution Fourier transform study of MgCl: The $A^2\Pi$–$X^2\Sigma^+$ band system. *Journal of Molecular Spectroscopy*, 212(1):53–56, 2002. doi: 10.1006/jmsp.2002.8514.

[71] H. Hönl and F. London. Über die Intensitäten der Bandenlinien. *Zeitschrift für Physik*, 33(1):803–809, 1925. doi: 10.1007/BF01328367.

[72] K. P. Huber and G. Herzberg. *Constants of diatomic molecules*, volume 4. Springer US, Boston, MA, 1979. ISBN 0-442-23394-9. doi: 10.1007/978-1-4757-0961-2_2.

[73] Y. Iida. Effects of atmosphere on laser vaporization and excitation processes of solid samples. *Spectrochimica Acta Part B: Atomic Spectroscopy*, 45(12):1353–1367, 1990. doi: 10.1016/0584-8547(90)80188-O.

[74] T. E. Itina, V. N. Tokarev, W. Marine, and M. Autric. Monte Carlo simulation study of the effects of nonequilibrium chemical reactions during pulsed laser desorption. *Journal of Chemical Physics*, 106(21):8905–8912, 1997. doi: 10.1063/1.473948.

[75] S. E. Jackson and D. Günther. The nature and sources of laser induced isotopic fractionation in laser ablation-multicollector-inductively coupled plasma-mass spectrometry. *Journal of Analytical Atomic Spectrometry*, 18(3):205–212, 2003. doi: 10.1039/b209620j.

[76] K. Y. Kane and D. A. Cremers. An in situ technique for elemental analysis of lunar surfaces. In *Lunar and Planetary Institute, Joint Workshop on New Technologies for Lunar Resource Assessment*, pages 34–35, 1992.

[77] K. Y. Kane and D. A. Cremers. Remote elemental analysis of planetary surfaces using laser-induced breakdown spectroscopy. *23rd Lunar and Planetary Science Conference*, page 651, 1992.

[78] J. M. Keller, W. V. Boynton, S. Karunatillake, V. R. Baker, J. M. Dohm, L. G. Evans, M. J. Finch, B. C. Hahn, D. K. Hamara, D. M. Janes, K. E. Kerry, H. E. Newsom, R. C. Reedy, A. L. Sprague, S. W. Squyres, R. D. Starr, G. J. Taylor, and R. M. Williams. Equatorial and midlatitude distribution of chlorine measured by Mars Odyssey GRS. *Journal of Geophysical Research E: Planets*, 112(3):E03S08. doi: 10.1029/2006JE002679.

[79] A. K. Knight, N. L. Scherbarth, D. A. Cremers, and M. J. Ferris. Characterization of laser-induced breakdown spectroscopy (LIBS) for application to space exploration. *Applied Spectroscopy*, 54(3):331–340, 2000. doi: 10.1366/0003702001949591.

[80] J. Koput. Ab initio prediction of the potential energy surface and vibration-rotation energy levels of $CaCl_2$. *Journal of Physical Chemistry A*, 112(12):2743–2746, 2008. doi: 10.1021/jp711785p.

[81] J. Koput and A. Roszczak. CaF_2 as a quasilinear molecule: The vibrational-rotational energy levels predicted by ab initio quantum chemistry approach. *Journal of Physical Chemistry A*, 108(42):9267–9273, 2004. doi: 10.1021/jp046682k.

[82] S. Kubitza, D. S. Vogt, K. Rammelkamp, U. Böttger, S. Frohmann, P. B. Hansen, S. Schröder, and H.-W. Hübers. A miniaturized Raman/LIBS instrument for in-situ investigation of celestial bodies in pioneering missions. *European Planetary Science Congress*, 2018.

[83] K. J. Laidler. *Chemical Kinetics*. Pearson, 3 edition, 1987.

[84] J. Lasue, R. C. Wiens, S. M. Clegg, D. T. Vaniman, K. H. Joy, S. Humphries, A. Mezzacappa, N. Melikechi, R. E. McInroy, and S. Bender. Remote laser-induced breakdown spectroscopy (LIBS) for lunar exploration. *Journal of Geophysical Research: Planets*, 117(E1), 2012. doi: 10.1029/2011JE003898.

[85] J. Lasue, A. Cousin, P.-Y. Meslin, N. Mangold, R. C. Wiens, G. Berger, E. Dehouck, O. Forni, W. Goetz, O. Gasnault, W. Rapin, S. Schröder, A. Ollila, J. Johnson, S. Le Mouelic, S. Maurice, R. Anderson, D. L. Blaney, B. Clark, S. M. Clegg, C. D'Uston, F. Cécile, N. Lanza, M. B. Madsen, J. Martín-Torres, N. Melikechi, H. Newsom, V. Sautter, and M.-P. Zorzano. Martian Eolian dust probed by ChemCam. *Geophysical Research Letters*, 2018. doi: 10.1029/2018GL079210.

[86] S. Le Mouélic, O. Gasnault, K. E. Herkenhoff, N. T. Bridges, Y. Langevin, N. Mangold, S. Maurice, R. C. Wiens, P. Pinet, H. E. Newsom, R. G. Deen, J. F. Bell, J. R. Johnson, W. Rapin, B. Barraclough, D. L. Blaney, L. Deflores, J. Maki, M. C. Malin, R. Pérez, and M. Saccoccio. The ChemCam Remote Micro-Imager at Gale crater: Review of the first year of operations on Mars. *Icarus*, 249:93–107, 2015. doi: 10.1016/j.icarus.2014.05.030.

[87] X.-y. Liu, G.-q. Li, X.-s. Liu, Y.-k. Mu, Y. Wang, and P.-z. Ding. Gauss numerical inversion for use in computing the radiation field from a cylindrically symmetric radiation source. *Radiation Physics and Chemistry*, 61(2):93–98, 2001. doi: 10.1016/S0969-806X(00)00432-1.

[88] X. L. Mao, W. T. Chan, M. A. Shannon, and R. E. Russo. Plasma shielding during picosecond laser sampling of solid materials by ablation in He versus Ar atmosphere. *Journal of Applied Physics*, 74(8):4915–4922, 1993. doi: 10.1063/1.354325.

[89] C. B. Markwardt. Non-linear least squares fitting in IDL with MPFIT. 2009.

[90] S. Maurice, R. C. Wiens, M. Saccoccio, B. Barraclough, O. Gasnault, O. Forni, N. Mangold, D. Baratoux, S. Bender, G. Berger, J. Bernardin, M. Berthé, N. Bridges, D. Blaney, M. Bouyé, P. Caïs, B. Clark, S. Clegg, A. Cousin, D. Cremers, A. Cros, L. Deflores, C. Derycke, B. Dingler, G. Dromart, B. Dubois, M. Dupieux, E. Durand, L. D'Uston, C. Fabre, B. Faure, A. Gaboriaud, T. Gharsa, K. Herkenhoff, E. Kan, L. Kirkland, D. Kouach, J. L. Lacour, Y. Langevin, J. Lasue, S. Le Mouélic, M. Lescure, E. Lewin, D. Limonadi, G. Manhès, P. Mauchien, C. McKay, P. Y. Meslin, Y. Michel, E. Miller, H. E. Newsom, G. Orttner, A. Paillet, L. Parès, Y. Parot, R. Pérez, P. Pinet, F. Poitrasson, B. Quertier, B. Sallé, C. Sotin, V. Sautter, H. Séran, J. J. Simmonds, J. B. Sirven, R. Stiglich, N. Striebig, J. J. Thocaven, M. J. Toplis, and D. Vaniman. The ChemCam instrument suite on the Mars Science Laboratory (MSL) rover: Science objectives and mast unit description. *Space Science Reviews*, 170(1-4):95–166, 2012. doi: 10.1007/s11214-012-9912-2.

[91] S. Maurice, S. M. Clegg, R. C. Wiens, O. Gasnault, W. Rapin, O. Forni, A. Cousin, V. Sautter, N. Mangold, L. Le Deit, M. Nachon, R. B. Anderson,

N. L. Lanza, C. Fabre, V. Payré, J. Lasue, P.-Y. Meslin, R. J. Léveillé, B. L. Barraclough, P. Beck, S. C. Bender, G. Berger, J. C. Bridges, N. T. Bridges, G. Dromart, M. D. Dyar, R. Francis, J. Frydenvang, B. Gondet, B. L. Ehlmann, K. E. Herkenhoff, J. R. Johnson, Y. Langevin, M. B. Madsen, N. Melikechi, J.-L. Lacour, S. Le Mouélic, E. Lewin, H. E. Newsom, A. M. Ollila, P. Pinet, S. Schröder, J.-B. Sirven, R. L. Tokar, M. J. Toplis, C. D'Uston, D. T. Vaniman, and A. R. Vasavada. ChemCam activities and discoveries during the nominal mission of the Mars Science Laboratory in Gale crater, Mars. *Journal of Analytical Atomic Spectrometry*, 31(4):863–889, 2016. doi: 10.1039/C5JA00417A.

[92] P.-Y. Meslin, L. Cicutto, O. Forni, C. Drouet, W. Rapin, M. Nachon, A. Cousin, J. G. Blank, F. M. McCubbin, O. Gasnault, H. Newsom, N. Mangold, S. Schröder, V. Sautter, S. Maurice, and R. C. Wiens. Calibration of the Fluorine, Chlorine, and Hydrogen Content of Apatites with the ChemCam LIBS Instrument. *47th Lunar and Planetary Science Conference*, page 1703, 2016.

[93] MGS MOLA Team. MOLA Mission Experiment Gridded Data Records, 2003. URL http://pds-geosciences.wustl.edu/missions/mgs/megdr.html.

[94] A. Miotello and R. Kelly. Laser-induced phase explosion: New physical problems when a condensed phase approaches the thermodynamic critical temperature. *Applied Physics A: Materials Science and Processing*, 69(7):S67–S73, 1999. doi: 10.1007/s003390051357.

[95] K. Möller, H. U. Schütze-Pahlmann, J. Hoeft, and T. Törring. Effects of unresolved hyperfine structure in the microwave rotational spectra of the 2Σ-radicals CaBr and CaCl. *Chemical Physics*, 68(3):399–404, 1982. doi: 10.1016/0301-0104(82)87048-1.

[96] E. M. Monge, C. Aragón, and J. A. Aguilera. Space- and time-resolved measurements of temperatures and electron densities of plasmas formed during laser ablation of metallic samples. *Applied Physics A: Materials Science and Processing*, 69(7):S691–S694, 1999. doi: 10.1007/s003390051507.

[97] P. M. Morse. Diatomic molecules according to the wave mechanics. II. Vibrational levels. *Physical Review*, 34(1):57–64, 1929. doi: 10.1103/PhysRev.34.57.

[98] R. S. Mulliken. Report on notation for the spectra of polyatomic molecules. *The Journal of Chemical Physics*, 23(11):1997–2011, 1955. doi: 10.1063/1.1740655.

[99] R. A. Multari and D. A. Cremers. A time-resolved imaging study of Cr(I) emissions from a laser plasma formed on a sample at nonnormal incidence. *IEEE Transactions on Plasma Science*, 24(1):39–40, 1996. doi: 10.1109/27.491680.

[100] M. Nachon, S. M. Clegg, N. Mangold, S. Schröder, L. C. Kah, G. Dromart, A. Ollila, J. R. Johnson, D. Z. Oehler, J. C. Bridges, S. Le Mouélic, O. Forni, R. C. Wiens, R. B. Anderson, D. L. Blaney, J. F. Bell, B. Clark, A. Cousin, M. D. Dyar, B. Ehlmann, C. Fabre, O. Gasnault, J. Grotzinger, J. Lasue, E. Lewin, R. Léveillé, S. McLennan, S. Maurice, P. Y. Meslin, W. Rapin, M. Rice, S. W. Squyres, K. Stack, D. Y. Sumner, D. Vaniman, and D. Wellington. Calcium sulfate veins characterized by ChemCam/Curiosity at Gale crater, Mars. *Journal of Geophysical Research E: Planets*, 119(9):1991–2016, 2014. doi: 10.1002/2013JE004588.

[101] J. Nakagawa, P. J. Domaille, T. C. Steimle, and D. O. Harris. Microwave optical double resonance and reanalysis of the CaF A2Πr-X2Σ band system. *Journal of Molecular Spectroscopy*, 70(3):374–385, 1978. doi: 10.1016/0022-2852(78)90175-3.

[102] NASA. Curiosity Rover - Mars Science Laboratory, 2018. URL https://mars.nasa.gov/msl/mission/rover/.

[103] NASA Jet Propulsion Laboratory. NASA selects investigations for the Mars Science Laboratory, 2004. URL https://www.jpl.nasa.gov/news/news.php?feature=699.

[104] R. Noll. *Laser-Induced Breakdown Spectroscopy*. Springer Berlin Heidelberg, Berlin, Heidelberg, 2012. ISBN 978-3-642-20667-2. doi: 10.1007/978-3-642-20668-9.

[105] V. N. Ochkin. *Spectroscopy of low temperature plasma*. Wiley-VCH Verlag GmbH & Co. KGaA, Weinheim, Germany, 2009. ISBN 9783527627509. doi: 10.1002/9783527627509.

[106] E. A. Ogryzlo, Y. Q. Shen, and P. T. Wassell. The yield of $O_2(b^1\Sigma_g{}^+)$ in oxygen atom recombination. *Journal of Photochemistry*, 25(2-4):389–398, 1984. doi: 10.1016/0047-2670(84)87040-9.

[107] M. M. Osterloo, V. E. Hamilton, J. L. Bandfield, T. D. Glotch, A. M. Baldridge, P. R. Christensen, L. L. Tornabene, and F. S. Anderson. Chloride-bearing materials in the southern highlands of Mars. *Science*, 319(5870):1651–1654, 2008. doi: 10.1126/science.1150690.

[108] M. M. Osterloo, F. S. Anderson, V. E. Hamilton, and B. M. Hynek. Geologic context of proposed chloride-bearing materials on Mars. *Journal of Geophysical Research E: Planets*, 115(10):E10012, 2010. doi: 10.1029/2010JE003613.

[109] P. Outridge, W. Doherty, and D. Gregoire. Ablative and transport fractionation of trace elements during laser sampling of glass and copper. *Spec-*

trochimica Acta Part B: Atomic Spectroscopy, 52(14):2093–2102, 1997. doi: 10.1016/S0584-8547(97)00112-2.

[110] T. Owen, K. Biemann, D. R. Rushneck, J. E. Biller, D. W. Howarth, and A. L. Lafleur. The composition of the atmosphere at the surface of Mars. *Journal of Geophysical Research*, 82(28):4635–4639, 1977. doi: 10.1029/JS082i028p04635.

[111] C. G. Parigger, D. H. Plemmons, and E. Oks. Balmer series H_β measurements in a laser-induced hydrogen plasma. *Applied Optics*, 42(30):5992, 2003. doi: 10.1364/AO.42.005992.

[112] S. Pavlov, E. Jessberger, H.-W. Hübers, S. Schröder, I. Rauschenbach, S. Florek, J. Neumann, H. Henkel, and S. Klinkner. Miniaturized laser-induced plasma spectrometry for planetary in situ analysis – The case for Jupiter's moon Europa. *Advances in Space Research*, 48(4):764–778, 2011. doi: 10.1016/j.asr.2010.06.034.

[113] S. G. Pavlov, S. Schröder, I. Rauschenbach, E. K. Jessberger, and H.-W. Hübers. Low-energy laser induced breakdown spectroscopy for in-situ space missions to solar system bodies without atmospheres. *Planetary and Space Science*, 71(1): 57–63, 2012. doi: 10.1016/j.pss.2012.07.001.

[114] D. Perez and L. J. Lewis. Ablation of solids under femtosecond laser pulses. *Physical Review Letters*, 89(25):255504, 2002. doi: 10.1103/PhysRevLett.89.255504.

[115] D. Perez and L. J. Lewis. Molecular-dynamics study of ablation of solids under femtosecond laser pulses. *Physical Review B - Condensed Matter and Materials Physics*, 67(18):184102, 2003. doi: 10.1103/PhysRevB.67.184102.

[116] L. J. Radziemski and D. A. Cremers. *Laser-induced plasmas and applications*. M. Dekker, 1989. ISBN 0824780787.

[117] A. A. Radzig and B. M. Smirnov. *Reference Data on Atoms, Molecules, and Ions*, volume 31 of *Springer Series in Chemical Physics*. Springer Berlin Heidelberg, Berlin, Heidelberg, 1985. ISBN 978-3-642-82050-2. doi: 10.1007/978-3-642-82048-9.

[118] Y. Ralchenko, A. E. Kramida, J. Reader, and NIST ASD Team. NIST Atomic Spectra Database (version 5.6.1), 2018. URL https://physics.nist.gov/asd.

[119] W. Rapin, B. Bousquet, J. Lasue, P.-Y. Meslin, J.-L. Lacour, C. Fabre, R. Wiens, J. Frydenvang, E. Dehouck, S. Maurice, O. Gasnault, O. Forni, and A. Cousin. Roughness effects on the hydrogen signal in laser-induced breakdown spectroscopy. *Spectrochimica Acta Part B: Atomic Spectroscopy*, 137:13–22, 2017. doi: 10.1016/j.sab.2017.09.003.

[120] W. Rapin, P.-Y. Meslin, S. Maurice, R. Wiens, D. Laporte, B. Chauviré, O. Gasnault, S. Schröder, P. Beck, S. Bender, O. Beyssac, A. Cousin, E. Dehouck, C. Drouet, O. Forni, M. Nachon, N. Melikechi, B. Rondeau, N. Mangold, and N. Thomas. Quantification of water content by laser induced breakdown spectroscopy on Mars. *Spectrochimica Acta Part B: Atomic Spectroscopy*, 130:82–100, 2017. doi: 10.1016/j.sab.2017.02.007.

[121] I. Rauschenbach, E. Jessberger, S. Pavlov, and H.-W. Hübers. Miniaturized laser-induced breakdown spectroscopy for the in-situ analysis of the Martian surface: Calibration and quantification. *Spectrochimica Acta Part B: Atomic Spectroscopy*, 65(8):758–768, 2010. doi: 10.1016/j.sab.2010.03.018.

[122] X. Ren, T. Cai, D. Liu, J. Liu, H. Zhang, Q. Fu, Z. Zhang, and W. Xu. Preliminary scientific exploration programs for Mars Surface Composition Detection Package of China's first Mars exploration. *European Planetary Science Congress*, 12, 2018.

[123] N. O. Rennó, B. J. Bos, D. Catling, B. C. Clark, L. Drube, D. Fisher, W. Goetz, S. F. Hviid, H. U. Keller, J. F. Kok, S. P. Kounaves, K. Leer, M. Lemmon, M. B. Madsen, W. J. Markiewicz, J. Marshall, C. McKay, M. Mehta, M. Smith, M. P. Zorzano, P. H. Smith, C. Stoker, and S. M. Young. Possible physical and thermodynamical evidence for liquid water at the Phoenix landing site. *Journal of Geophysical Research E: Planets*, 114(10):E00E03, 2009. doi: 10.1029/2009JE003362.

[124] S. F. Rice, H. Martin, and R. W. Field. The electronic structure of the calcium monohalides. A ligand field approach. *The Journal of Chemical Physics*, 82(11): 5023–5034, 1985. doi: 10.1063/1.448676.

[125] J. Rostas, N. Shafizadeh, G. Taieb, B. Bourguignon, and M. G. Prisant. The $A^2\Pi$–$X^2\Sigma^+$ system of MgCl. Evidence for predissociation in the $a^2\Pi$ state of MgCl. *Chemical Physics*, 142(1):97–109, 1990. doi: 10.1016/0301-0104(90)89073-Y.

[126] R. Russo. Laser ablation in analytical chemistry – a review. *Talanta*, 57(3): 425–451, 2002. doi: 10.1016/S0039-9140(02)00053-X.

[127] R. E. Russo. Laser ablation. *Applied Spectroscopy*, 49(9):14A–28A, 1995. doi: 10.1366/0003702953965399.

[128] B. Sallé, D. A. Cremers, S. Maurice, and R. C. Wiens. Laser-induced breakdown spectroscopy for space exploration applications: Influence of the ambient pressure on the calibration curves prepared from soil and clay samples. *Spectrochimica Acta Part B: Atomic Spectroscopy*, 60(4):479–490, 2005. doi: 10.1016/j.sab.2005.02.009.

[129] S. Schröder, S. G. Pavlov, I. Rauschenbach, E. K. Jessberger, and H. W. Hübers. Detection and identification of salts and frozen salt solutions combining laser-induced breakdown spectroscopy and multivariate analysis methods: A study for future martian exploration. *Icarus*, 223(1):61–73, 2013. doi: 10.1016/j.icarus.2012.11.011.

[130] S. Schröder, P. Y. Meslin, O. Gasnault, S. Maurice, A. Cousin, R. C. Wiens, W. Rapin, M. D. Dyar, N. Mangold, O. Forni, M. Nachon, S. Clegg, J. R. Johnson, J. Lasue, S. Le Mouélic, A. Ollila, P. Pinet, V. Sautter, and D. Vaniman. Hydrogen detection with ChemCam at Gale crater. *Icarus*, 249:43–61, 2015. doi: 10.1016/j.icarus.2014.08.029.

[131] S. Schröder, K. Rammelkamp, D. S. Vogt, O. Gasnault, and H.-W. Hübers. Contribution of a martian atmosphere to laser-induced breakdown spectroscopy (LIBS) data and testing its emission characteristics for normalization applications. *Icarus*, 2019. doi: 10.1016/j.icarus.2019.02.017.

[132] S. Schröder, D. S. Vogt, K. Rammelkamp, P. B. Hansen, S. Kubitza, P.-Y. Meslin, and H.-W. Hübers. Time-resolved LIBS plasma imaging for an improved understanding of martian LIBS data. *50th Lunar and Planetary Science Conference*, page 2793, 2019.

[133] A. Seiff and D. B. Kirk. Structure of the atmosphere of Mars in summer at mid-latitudes. *Journal of Geophysical Research*, 82(28):4364–4378, 1977. doi: 10.1029/JS082i028p04364.

[134] S. Shabanov and I. Gornushkin. Two-dimensional axisymmetric models of laser induced plasmas relevant to laser induced breakdown spectroscopy. *Spectrochimica Acta Part B: Atomic Spectroscopy*, 100:147–172, 2014. doi: 10.1016/j.sab.2014.08.026.

[135] S. V. Shabanov and I. B. Gornushkin. Modeling chemical reactions in laser-induced plasmas. *Applied Physics A: Materials Science and Processing*, 121(3): 1087–1107, 2015. doi: 10.1007/s00339-015-9445-0.

[136] S. V. Shabanov and I. B. Gornushkin. Anions in laser-induced plasmas. *Applied Physics A: Materials Science and Processing*, 122(7):676, 2016. doi: 10.1007/s00339-016-0175-8.

[137] D. E. Smith, M. T. Zuber, H. V. Frey, J. B. Garvin, J. W. Head, D. O. Muhleman, G. H. Pettengill, R. J. Phillips, S. C. Solomon, H. J. Zwally, W. B. Banerdt, T. C. Duxbury, M. P. Golombek, F. G. Lemoine, G. A. Neumann, D. D. Rowlands, O. Aharonson, P. G. Ford, A. B. Ivanov, C. L. Johnson, P. J. McGovern, J. B.

Abshire, R. S. Afzal, and X. Sun. Mars Orbiter Laser Altimeter: Experiment summary after the first year of global mapping of Mars. *Journal of Geophysical Research: Planets*, 106(E10):23689–23722, 2001. doi: 10.1029/2000JE001364.

[138] P. H. Smith, L. K. Tamppari, R. E. Arvidson, D. Bass, D. Blaney, W. V. Boynton, A. Carswell, D. C. Catling, B. C. Clark, T. Duck, E. DeJong, D. Fisher, W. Goetz, H. P. Gunnlaugsson, M. H. Hecht, V. Hipkin, J. Hoffman, S. F. Hviid, H. U. Keller, S. P. Kounaves, C. F. Lange, M. T. Lemmon, M. B. Madsen, W. J. Markiewicz, J. Marshall, C. P. McKay, M. T. Mellon, D. W. Ming, R. V. Morris, W. T. Pike, N. Renno, U. Staufer, C. Stoker, P. Taylor, J. A. Whiteway, and A. P. Zent. H_2O at the Phoenix landing site. *Science*, 325(5936):58–61, 2009. doi: 10.1126/science.1172339.

[139] P. Sobron, M. Fahey, M. Krainak, A. Misra, F. Rehnmark, A. Wang, A. Yu, K. Zacny, and R. Zeigler. Redeployable sensor probe for in-situ lunar resource mapping from small landers. *50th Lunar and Planetary Science Conference*, page 2749, 2019.

[140] N. Sonine. Recherches sur les fonctions cylindriques et le développement des fonctions continues en séries. *Mathematische Annalen*, 16(1):1–80, 1880. doi: 10.1007/BF01459227.

[141] M. Sparks, D. L. Mills, R. Warren, T. Holstein, A. A. Maradudin, L. J. Sham, E. Loh, and D. F. King. Theory of electron-avalanche breakdown in solids. *Physical Review B*, 24(6):3519–3536, 1981. doi: 10.1103/PhysRevB.24.3519.

[142] B. C. Stuart, M. D. Feit, S. Herman, A. M. Rubenchik, B. W. Shore, and M. D. Perry. Nanosecond-to-femtosecond laser-induced breakdown in dielectrics. *Physical Review B*, 53(4):1749–1761, 1996. doi: 10.1103/PhysRevB.53.1749.

[143] V. Sundararajan. Overview and technical architecture of India's Chandrayaan-2 Mission to the Moon. In *AIAA Aerospace Sciences Meeting*, Reston, Virginia, 2018. American Institute of Aeronautics and Astronautics. ISBN 978-1-62410-524-1. doi: 10.2514/6.2018-2178.

[144] G. J. Taylor, L. M. Martel, S. Karunatillake, O. Gasnault, and W. V. Boynton. Mapping Mars geochemically. *Geology*, 38(2):183–186, 2010. doi: 10.1130/G30470.1.

[145] A. H. Treiman, M. J. Drake, M. J. Janssens, R. Wolf, and M. Ebihara. Core formation in the Earth and Shergottite Parent Body (SPB): Chemical evidence from basalts. *Geochimica et Cosmochimica Acta*, 50(6):1071–1091, 1986. doi: 10.1016/0016-7037(86)90389-3.

[146] USGS Astrogeology Science Center. Mars Viking Global Color Mosaic 925m v1, 2014. URL https://astrogeology.usgs.gov/search/map/Mars/Viking/Color/Mars_Viking_ClrMosaic_global_925m.

[147] J. M. Vadillo and J. Laserna. Laser-induced plasma spectrometry: truly a surface analytical tool. *Spectrochimica Acta Part B: Atomic Spectroscopy*, 59(2):147–161, 2004. doi: 10.1016/j.sab.2003.11.006.

[148] J. M. Vadillo, J. M. Fernández Romero, C. Rodríguez, and J. J. Laserna. Effect of plasma shielding on laser ablation rate of pure metals at reduced pressure. *Surface and Interface Analysis*, 27(11):1009–1015, 1999. doi: 10.1002/(SICI)1096-9918(199911)27:11⟨1009::AID-SIA670⟩3.0.CO;2-2.

[149] J. A. van der Mullen. Excitation equilibria in plasmas; a classification. *Physics Reports*, 191(2-3):109–220, 1990. doi: 10.1016/0370-1573(90)90152-R.

[150] D. Vogt, K. Rammelkamp, S. Schröder, and H. Hübers. Molecular emission in laser-induced breakdown spectroscopy: An investigation of its suitability for chlorine quantification on Mars. *Icarus*, 302:470–482, 2018. doi: 10.1016/j.icarus.2017.12.006.

[151] D. Vogt, S. Schröder, K. Rammelkamp, P. Hansen, S. Kubitza, and H.-W. Hübers. CaCl and CaF emission in LIBS under simulated Martian conditions. *Icarus*, 335:113393, 2020. doi: 10.1016/j.icarus.2019.113393.

[152] D. S. Vogt, S. Frohmann, S. Schröder, K. Rammelkamp, U. Böttger, and H.-W. Hübers. Miniaturized Raman/LIBS instrument for in situ exploration of planetary bodies without atmospheres. *European Planetary Science Congress*, 2017.

[153] O. H. Walters and S. Barratt. The alkaline earth halide spectra and their origin. *Proceedings of the Royal Society A: Mathematical, Physical and Engineering Sciences*, 118(779):120–137, 1928. doi: 10.1098/rspa.1928.0040.

[154] C. M. Western. PGOPHER: A program for simulating rotational, vibrational and electronic spectra. *Journal of Quantitative Spectroscopy and Radiative Transfer*, 186:221–242, 2017. doi: 10.1016/j.jqsrt.2016.04.010.

[155] R. Wiens, S. Maurice, J. Lasue, O. Forni, R. Anderson, S. Clegg, S. Bender, D. Blaney, B. Barraclough, A. Cousin, L. Deflores, D. Delapp, C. Fabre, O. Gasnault, N. Lanza, J. Mazoyer, N. Melikechi, P.-y. Meslin, H. Newsom, A. Ollila, R. Perez, R. Tokar, and D. Vaniman. Pre-flight calibration and initial data processing for the ChemCam laser-induced breakdown spectroscopy instrument on

the Mars Science Laboratory rover. *Spectrochimica Acta Part B: Atomic Spectroscopy*, 82:1–27, 2013. doi: 10.1016/j.sab.2013.02.003.

[156] R. C. Wiens, R. E. Arvidson, D. D. Cremers, M. J. Ferris, J. D. Blacic, F. Seelos IV, and K. Deal. Combined remote mineralogical and elemental identification from rovers: Field and laboratory tests using reflectance and laser-induced breakdown spectroscopy. *Journal of Geophysical Research*, 107(E11):1–14, 2002. doi: 10.1029/2000JE001439.

[157] R. C. Wiens, S. Maurice, B. Barraclough, M. Saccoccio, W. C. Barkley, J. F. Bell, S. Bender, J. Bernardin, D. Blaney, J. Blank, M. Bouyé, N. Bridges, N. Bultman, P. Caïs, R. C. Clanton, B. Clark, S. Clegg, A. Cousin, D. Cremers, A. Cros, L. Deflores, D. Delapp, R. Dingler, C. D'Uston, M. Darby Dyar, T. Elliott, D. Enemark, C. Fabre, M. Flores, O. Forni, O. Gasnault, T. Hale, C. Hays, K. Herkenhoff, E. Kan, L. Kirkland, D. Kouach, D. Landis, Y. Langevin, N. Lanza, F. Larocca, J. Lasue, J. Latino, D. Limonadi, C. Lindensmith, C. Little, N. Mangold, G. Manhes, P. Mauchien, C. McKay, E. Miller, J. Mooney, R. V. Morris, L. Morrison, T. Nelson, H. Newsom, A. Ollila, M. Ott, L. Pares, R. Perez, F. Poitrasson, C. Provost, J. W. Reiter, T. Roberts, F. Romero, V. Sautter, S. Salazar, J. J. Simmonds, R. Stiglich, S. Storms, N. Striebig, J. J. Thocaven, T. Trujillo, M. Ulibarri, D. Vaniman, N. Warner, R. Waterbury, R. Whitaker, J. Witt, and B. Wong-Swanson. The ChemCam instrument suite on the Mars Science Laboratory (MSL) rover: Body unit and combined system tests. *Space Science Reviews*, 170(1-4):167–227, 2012. doi: 10.1007/s11214-012-9902-4.

[158] R. C. Wiens, S. Maurice, and F. R. Perez. The SuperCam remote sensing instrument suite for the Mars 2020 rover: a preview. *Spectroscopy*, 32(5):50–55, 2017.

[159] C. H. Wu, H. R. Ihle, and K. A. Gingerich. A mass spectrometric study of the alkaline earth diatomic molecules. Dissociation energies of Mg_2, Ca_2 and CaLi. *International Journal of Mass Spectrometry and Ion Physics*, 47(C):235–238, 1983. doi: 10.1016/0020-7381(83)87178-2.

[160] S. Yalçin, D. R. Crosley, G. P. Smith, and G. W. Faris. Influence of ambient conditions on the laser air spark. *Applied Physics B: Lasers and Optics*, 68(1): 121–130, 1999. doi: 10.1007/s003400050596.

[161] Y. B. Zel'dovich and Y. P. Raizer. *Physics of shock waves and high-temperature hydrodynamic phenomena*. Dover Publications, Inc., Mineola, New York, 2002. ISBN 0486420027. doi: 10.1115/1.3607836.

List of Figures

List of Tables

List of Publications

Peer-reviewed publications (first author)

- D. Vogt, K. Rammelkamp, S. Schröder, and H. Hübers. Molecular emission in laser-induced breakdown spectroscopy: An investigation of its suitability for chlorine quantification on Mars. *Icarus*, 302:470–482, 2018. doi: 10.1016/j.icarus.2017.12.006.

- D. Vogt, S. Schröder, K. Rammelkamp, P. Hansen, S. Kubitza, and H.-W. Hübers. CaCl and CaF emission in LIBS under simulated Martian conditions. *Icarus*, 335: 113393, 2020. doi: 10.1016/j.icarus.2019.113393.

Peer-reviewed publications (co-author)

- K. Rammelkamp, S. Schröder, S. Kubitza, D. S. Vogt, S. Frohmann, P. B. Hansen, U. Böttger, F. Hanke, and H.-W. Hübers. Low-level LIBS and Raman data fusion in the context of in situ Mars exploration. *Journal of Raman Spectroscopy*, 2019. ISSN 0377-0486. doi: 10.1002/jrs.5615.

- S. Schröder, K. Rammelkamp, F. Hanke, I. Weber, D. S. Vogt, S. Frohmann, S. Kubitza, U. Böttger, and H.-W. Hübers. Effects of pulsed laser and plasma interaction on Fe, Ni, Ti, and their oxides for LIBS Raman analysis in extraterrestrial environments. *Journal of Raman Spectroscopy*, 2019. ISSN 0377-0486. doi: 10.1002/jrs.5650.

- S. Schröder, K. Rammelkamp, D. S. Vogt, O. Gasnault, and H.-W. Hübers. Contribution of a martian atmosphere to laser-induced breakdown spectroscopy (LIBS) data and testing its emission characteristics for normalization applications. *Icarus*, 2019. doi: 10.1016/j.icarus.2019.02.017.

Oral presentations at conferences

- D. S. Vogt, S. Kilian, K. Rammelkamp, S. Schröder, A. Cousin, O. Forni, and H.-W. Hübers. Detection of chlorine via atomic and molecular emission in high-resolution time-resolved LIBS spectra under Martian conditions. *International LIBS*, 2016.

- D. S. Vogt, S. Frohmann, S. Schröder, K. Rammelkamp, U. Böttger, and H.-W. Hübers. Miniaturized Raman/LIBS instrument for in situ exploration of planetary bodies without atmospheres. *European Planetary Science Congress*, 2017.

- D. S. Vogt, S. Frohmann, S. Kubitza, P. B. Hansen, K. Rammelkamp, S. Schröder, and H.-W. Hübers. Time-resolved spectral imaging of LIBS plasma at low pressures for the exploration of Solar System bodies. *European Planetary Science Congress*, 2018.

- D. S. Vogt, K. Rammelkamp, P. B. Hansen, S. Kubitza, S. Frohmann, S. Schröder, and H.-W. Hübers. Molecular emissions in the laser-induced plasma in simulated Martian conditions — calibration models and new insights from plasma imaging. *NASLIBS at SciX*, 2019 (upcoming invited talk).

Poster presentations at conferences

- D. S. Vogt, K. Rammelkamp, S. Schröder, and H.-W. Hübers. Suitability of molecular emission in laser-induced breakdown spectroscopy for the quantification of chlorine under Martian conditions. *48th Lunar and Planetary Science Conference*, 2017.

- S. Schröder, D. S. Vogt, K. Rammelkamp, P. B. Hansen, S. Kubitza, P.-Y. Meslin, and H.-W. Hübers. Time-resolved LIBS plasma imaging for an improved understanding of martian LIBS data. *50th Lunar and Planetary Science Conference*, 2019 (corresponding author).

- D. S. Vogt, S. Schröder, K. Rammelkamp, P. B. Hansen, S. Kubitza, and H.-W. Hübers. Investigation of MgCl, MgF, CaCl, and CaF emission in LIBS for the quantification of chlorine and fluorine in Martian atmospheric conditions. *9th International Conference on Mars*, 2019.

Acknowledgments

I would like to express my deep gratitude to Prof. Dr. Heinz-Wilhelm Hübers for his support and his guidance during the course of this thesis, especially in the final months leading up to the submission of the thesis. His critical questions and his constructive suggestions improved my research greatly. I also want to thank him for the lab space and the equipment that he provided to our group.

Furthermore, I would like to thank Dr. Susanne Schröder, who headed the Junior Research Group that I was part of. Thanks to her trust in my abilities, I was able to do research in a field that excites me. She always encouraged me to dig deeper and helped me to define the scientific questions that would be of interest to the planetary science community. Since being part of her group and having her as my supervisor would not have been possible without the DLR VO-R Junior Research Group initiative, I would also like to thank Prof. Dr. Hansjörg Dittus for launching this project and for the generous funding we received for our research.

I also want to express my gratitude towards my colleagues Kristin Rammelkamp, Simon Kubitza, Peder Bagge Hansen, and Dr. Sven Frohmann. Each of them supported me a lot by helping me with my measurements, by suggesting papers that could interest me, by discussing my research and offering helpful advice, or by helping me in the development of the plasma imaging setup. Likewise, I want to thank the whole Terahertz and Laser Spectroscopy department for providing a great work environment in these last three years.

Finally, I would like to thank my family and my friends for their support throughout my study, but especially during the last year.

Statutory Declaration

I declare that I have completed the thesis independently using only the aids and tools specified. I have not applied for a doctor's degree in the doctoral subject elsewhere and do not hold a corresponding doctor's degree. I have taken due note of the Faculty of Mathematics and Natural Sciences PhD Regulations, published in the Official Gazette of Humboldt-Universität zu Berlin no. 42 on July 11 2018.

Berlin, August 23, 2019

David Sebastian Vogt